

# Investigation of the interplay between Electron-Cyclotron waves, suprathermal electrons and turbulence in tokamak plasmas

Présentée le 3 novembre 2023

Faculté des sciences de base  
SPC - Physique du Tokamak TCV  
Programme doctoral en physique

pour l'obtention du grade de Docteur ès Sciences

par

**Jean Arthur CAZABONNE**

Acceptée sur proposition du jury

Prof. V. Savona, président du jury  
Dr S. Coda, directeur de thèse  
Dr E. Westerhof, rapporteur  
Dr S. Freethy, rapporteur  
Dr J.-Ph. Hogge, rapporteur



閑さや 岩にしみ入 蟬の声

*shizukasa ya iwa ni shimi-iru semi no koe*

*Deep silence —*

*seeping into rocks,*

*the shrill of cicadas.*

---

Haiku,

Matsuo Bashō (1644-1694)

À mes parents, mon frère.

À toi aussi Camille, et aux fourmis qui se rêvent cigales.







# Abstract

Electron-Cyclotron waves are routinely used in tokamaks to heat the plasma and to drive current through the electron channel. Their unique ability to drive very localized current renders them the main foreseen tool for neoclassical tearing mode mitigation in future large fusion devices, such as ITER. This application is critical to avoid dangerous disruptions, which can damage the tokamak components, e.g. the vacuum vessel or the coils. However, experimental characterizations of the wave power deposition have led to the conclusion that numerical simulations, using either ray-tracing or quasilinear drift-kinetic codes, tend to predict an overly narrow power deposition profile and to overestimate the current drive efficiency, as well as the total driven current. This thesis focuses on understanding the discrepancy between experiments and simulations, to improve the predictive capabilities of the numerical toolkit. In particular, efforts have been placed in investigating the interplay between the injected waves, the suprathermal electrons and the missing ingredient in the codes usually used to simulate electron-cyclotron wave propagation and absorption: turbulence. Two phenomena are proposed to explain this discrepancy: the beam broadening caused by its scattering through density fluctuations, and the wave-enhanced transport of suprathermal electrons, transporting electrons away from the resonance location.

A first part of the thesis is dedicated to the study of turbulent transport enhancement by the electron-cyclotron wave absorption. The wave-accelerated electrons emit hard X-rays through Bremsstrahlung, which can be measured in TCV using the Hard X-Ray Spectrometer. It is then possible to perform forward modeling of a discharge thanks to the synthetic diagnostic embedded in the quasilinear bounce-average drift-kinetic Fokker-Planck solver LUKE. It is shown, by analyzing experimental data, that the radial transport of fast electrons increases with the injected wave power. This is further confirmed by matching experimental and synthetic hard X-ray data, tuning an ad-hoc radial diffusion coefficient in LUKE. This increase of transport is associated with a measured increase of density and temperature fluctuation level. A new electron-cyclotron heating and current-drive source has been developed for the global flux-driven gyro-kinetic code ORB5, simulating turbulent transport from first principles and showing an increase of electron transport with wave power.

On the other hand, beam scattering is also studied, using a full-wave propagation solver, coupled to LUKE to estimate the impact of beam broadening on the wave power deposition profile. Dedicated scenarios have been developed in TCV to minimize and maximize this

## Abstract

---

impact, respectively. Even though the impact of beam broadening is expected to be important in large fusion devices like ITER, it is shown that, for the tested TCV configurations, this phenomenon is not sufficient to explain the gap between experimental and synthetic hard X-ray data.

This thesis provides tools and an analysis framework for a better understanding of the underlying mechanisms behind the suprathermal electron distribution broadening, which is potentially symptomatic of a diminished accuracy in the electron-cyclotron wave power deposition and of a degraded current-drive efficiency.

**keywords:** Tokamak physics, Electron-Cyclotron current drive, Electron-Cyclotron heating, Hard X-ray spectrometry, Turbulent transport, Suprathermal electrons, Bounce-average drift-kinetic, Flux-driven gyro-kinetic, Full-wave propagation, Quasilinear wave absorption.

# Résumé

Les ondes cyclotroniques électroniques sont couramment utilisées dans les tokamaks pour chauffer le plasma et générer du courant. Leur capacité à générer du courant de manière très localisée font d'elles le principal outil envisagé pour atténuer les modes de déchirement néoclassiques dans les futures grandes installations de fusion, comme ITER. Cette application est critique pour éviter une brutale interruption de la décharge plasma pouvant entraîner une destruction matérielle, notamment au niveau de l'enceinte à vide ou des bobines. Cependant, la caractérisation expérimentale du dépôt de puissance des ondes a mené à la conclusion que les simulations, utilisant aussi bien du tracé de rayons que des codes cinétiques quasi-linéaires gyro-moyennés, tendent à prédire un profil de dépôt de puissance trop fin ainsi qu'une trop grande efficacité de génération de courant et un courant plasma total trop élevé. Ce travail de thèse se concentre sur la compréhension de cet écart entre les observations expérimentales et les simulations, afin d'améliorer les capacités prédictives des outils numériques. En particulier, des efforts ont été déployés pour tenter de comprendre l'inter-influence entre les ondes envoyées dans le plasma, les électrons suprathermiques, et l'ingrédient manquant des outils habituellement utilisés pour calculer la propagation des ondes cyclotroniques électroniques : la turbulence. Deux phénomènes sont proposés pour expliquer la différence observée : l'élargissement du faisceau d'onde lorsqu'il traverse le plasma turbulent, et l'augmentation du transport turbulent indirectement causée par l'absorption des ondes par le plasma.

Une première partie de cette thèse est consacrée à l'étude du renforcement du transport turbulent par l'absorption des ondes cyclotroniques électroniques. Les électrons accélérés par les ondes émettent des rayons X durs par Bremsstrahlung, qui peuvent être mesurés par spectrométrie rayons X durs dans TCV. Il est ensuite possible de simuler une décharge plasma et l'émission associée de rayons X durs grâce au diagnostic synthétique inclus dans le code LUKE, qui résout l'équation de Fokker-Planck quasi-linéaire gyro-moyennée et moyennée sur les orbites. Il est montré en analysant les données expérimentales que le transport radial des électrons suprathermiques augmente avec la puissance de l'onde injectée, ce qui est confirmé par les simulations LUKE pour lesquelles on utilise un transport radial ad hoc, ajusté pour que les données synthétiques correspondent aux données expérimentales de spectrométrie rayons X durs. Cette augmentation du transport est associée à une augmentation mesurée expérimentalement du niveau de fluctuation de la densité et de la température du plasma. Une nouvelle source de chauffage et de génération de courant par ondes cyclotroniques

## Résumé

---

électroniques a été développée pour le code gyro-cinétique global piloté par les flux ORB5, qui calcule le transport turbulent premier principe, et qui montre également une augmentation du transport des électrons avec la puissance de l'onde absorbée.

D'un autre côté, la diffusion du faisceau d'onde dans un plasma turbulent est également étudiée au moyen d'un code résolvant l'équation d'onde, couplé à LUKE pour estimer l'impact de l'élargissement du faisceau sur le dépôt de puissance de l'onde. Des scénarios dédiés ont été développés à TCV pour maximiser et minimiser cet effet. Même s'il est attendu que l'impact de l'élargissement du faisceau soit important dans les futures machines de grande taille comme ITER, il apparaît que cet effet n'est pas suffisant pour expliquer l'écart entre les observations expérimentales et les données synthétiques des rayons X durs.

Ce travail de thèse apporte des outils et une grille d'analyse pour mieux comprendre les mécanismes sous-jacents à l'élargissement de la distribution des électrons suprathermiques, qui est potentiellement symptomatique d'une précision amoindrie de la déposition de la puissance de l'onde et d'une efficacité de génération de courant dégradée.

**Mots clés:** Physique du tokamak, Génération de courant par ondes cyclotroniques électroniques, Chauffage par ondes cyclotroniques électroniques, Spectrométrie rayons X durs, Transport turbulent, Électrons suprathermiques, Cinétique gyro-moyennée moyennée sur les orbites, Gyro-cinétique pilotée par les flux, Propagation par résolution de l'équation d'onde, Absorption d'onde quasi-linéaire.

# Contents

<b>Abstract (English/Français)</b>	<b>i</b>
<b>1 Introduction</b>	<b>1</b>
1.1 The role of controlled nuclear fusion in the context of anthropic climate change	1
1.2 The path to controlled fusion: tokamaks and stellarators	4
1.2.1 The nuclear fusion process	4
1.2.2 Technical solutions: tokamaks and stellarators	7
1.2.3 The road to fusion and remaining challenges: ITER and DEMO	9
1.3 Principle of Electron-Cyclotron resonant heating and current drive	11
1.4 Thesis motivation and outline	14
1.4.1 Motivation: understanding the discrepancy between experiments and simulations	14
1.4.2 Thesis outline	18
<b>2 TCV: the Tokamak à Configuration Variable</b>	<b>21</b>
2.1 General description and research overview	21
2.2 Heating and current-drive systems	22
2.2.1 NBH: Neutral Beam Heating	22
2.2.2 ECRH/CD: Electron-Cyclotron Resonant Heating and Current Drive	23
2.3 Main plasma diagnostics	25
2.3.1 TS: the Thomson Scattering diagnostic	26
2.3.2 CXRS: the Charge eXchange Recombination Spectroscopy	27
2.3.3 Passive spectroscopy: measuring the whole electromagnetic spectrum	28
2.3.4 Magnetic probes and equilibrium reconstruction	29
2.4 Fluctuation diagnostics	29
2.4.1 Brief introduction to the main turbulence modes in tokamaks	29
2.4.2 TPCI: the Tangential Phase Contrast Imaging diagnostic	31
2.4.3 CECE: the Correlation Electron-Cyclotron Emission diagnostic	32
2.4.4 SPR: the Short Pulse Reflectometer	32
2.5 HXRS: the Hard X-Ray Spectrometer	33
2.5.1 Measuring Hard X-Rays emitted through electron Bremsstrahlung	33
2.5.2 General description of the spectrometer	34
2.5.3 Cadmium-telluride photodiodes	35

## Contents

---

2.5.4	Acquisition and signal processing chain . . . . .	40
2.5.5	Tomographic capabilities . . . . .	45
2.5.6	Synthetic diagnostic . . . . .	47
<b>3</b>	<b>Numerical tools</b>	<b>51</b>
3.1	Wave propagation solvers . . . . .	51
3.1.1	COMSOL: the full-wave model . . . . .	51
3.1.2	C3PO: the ray-tracing code . . . . .	55
3.1.3	WKBeam: the wave-kinetic equation solver . . . . .	70
3.2	Wave absorption and Fokker-Planck solvers . . . . .	71
3.2.1	LUKE: the bounce-averaged drift-kinetic Fokker-Planck solver . . . . .	72
3.2.2	ORB5: the global flux-driven gyro-kinetic code . . . . .	81
<b>4</b>	<b>Electron transport enhancement by Electron-Cyclotron waves</b>	<b>95</b>
4.1	Introduction . . . . .	95
4.2	Experimental setup . . . . .	96
4.2.1	Diagnostics . . . . .	96
4.2.2	Electron-Cyclotron power modulation and conditional averaging . . . . .	99
4.3	Numerical tools . . . . .	103
4.4	Experimental suggestion of turbulent transport enhancement by EC waves . . . . .	106
4.4.1	Transport of fast electrons suggested by Hard X-Ray Spectrometer measurement . . . . .	106
4.4.2	Increased turbulence during high-power Electron-Cyclotron phase from experimental measurements . . . . .	112
4.5	Transport studies with experimentally constrained LUKE simulations . . . . .	117
4.6	First principles transport analysis with ORB5 . . . . .	123
4.7	Conclusion . . . . .	135
<b>5</b>	<b>Electron-Cyclotron beam scattering by density fluctuations</b>	<b>137</b>
5.1	Introduction . . . . .	137
5.2	Density fluctuation measurement and modeling . . . . .	137
5.3	Numerical tools for wave propagation and absorption, and for comparison with experiments . . . . .	140
5.4	Full-Wave numerical studies and beam broadening regimes . . . . .	140
5.5	Experimental study: to assess the discrepancy between observations and simulations . . . . .	146
5.5.1	Experimental setup . . . . .	146
5.5.2	Methodology for the ECCD cases and justification . . . . .	148
5.5.3	COMSOL-LUKE simulations of experimental cases . . . . .	151
5.6	Conclusions . . . . .	155
<b>6</b>	<b>Conclusion and outlook</b>	<b>159</b>
6.1	Conclusions . . . . .	159

6.2 Outlook and future works . . . . .	160
<b>A The TCV X2 launcher geometry</b>	<b>163</b>
A.1 Definitions of the different frames . . . . .	163
A.1.1 TCV Cartesian frame . . . . .	163
A.1.2 TCV cylindrical frame . . . . .	163
A.1.3 Launcher cylindrical frame . . . . .	163
A.2 Definitions . . . . .	164
A.2.1 Definitions of launcher angles . . . . .	164
A.2.2 Definition of launcher's geometrical parameters . . . . .	164
A.3 Ray initial position and direction on mirror 4 . . . . .	165
A.4 Conversion from launcher angles to TORAY/C3PO angles . . . . .	166
<b>B Analytic equilibrium generation</b>	<b>169</b>
B.1 Poloidal magnetic flux calculation . . . . .	170
B.2 Magnetic field and pressure calculations . . . . .	172
B.3 Gradient-controlled profiles . . . . .	173
B.4 Surface- and volume-averaged quantities . . . . .	175
B.5 Verification with an ITER configuration . . . . .	177
B.6 LUKE equilibrium reconstruction . . . . .	177
B.7 Alternative inputs convenient for density fluctuation generation . . . . .	178
<b>C Coordinate systems for describing phase space</b>	<b>179</b>
C.1 Description of the configuration space . . . . .	179
C.2 Description of the velocity space . . . . .	180
<b>D Polarization for 2D ECCD configurations in COMSOL</b>	<b>181</b>
<b>Bibliography</b>	<b>185</b>
<b>Acknowledgements</b>	<b>207</b>
<b>Curriculum Vitae</b>	<b>211</b>





# 1 Introduction

*Le fléau n'est pas à la mesure de  
l'homme, on se dit donc que le fléau  
est irréel, c'est un mauvais rêve qui  
va passer.*

---

La Peste,  
Albert Camus (1913-1960)

## 1.1 The role of controlled nuclear fusion in the context of anthropic climate change

Anthropic climate change is attested from what is one of the most important works of cross-fields synthesis of scientific literature ever performed in science history, produced by the Intergovernmental Panel on Climate Change (IPCC). The IPCC consists of three working groups (WG) of international experts, focusing on the science basis of climate change (WGI), on assessing the vulnerability of natural and economical systems to climate change (WGII) and on providing, without prescribing, mitigation perspectives based on different probable scenarios (WGIII). This tremendous work is constantly updated and gathered in the sixth edition of the Assessment Report (AR6), separated in three different reports from each working group [Intergovernmental Panel on Climate Change (IPCC) 2023a,c,b].

In the light of these reports, it is unambiguously true that the present climate change is driven by recent human activity, releasing an anomalous amount of greenhouse gases and leading to a quick and sudden global warming with respect to the characteristic geological timescales (*high confidence*, see point A.1 of [Intergovernmental Panel on Climate Change (IPCC) 2023d]). The global surface temperature measured between 2011-2020 is 1.1°C higher than the 1850-1900 average, *likely* due to radiative forcing from mixed greenhouse gases, in particular carbon dioxide (mainly from coal, oil and gas burning) and methane (mainly

from cattle farming). This is illustrated by figure 1.1, showing the acceleration of greenhouse gases emission together with global temperature increase. The global warming will *more likely than not* continue in the near term (2021-2040), reaching at least  $1.5^{\circ}\text{C}$  (see point B.1 of [Intergovernmental Panel on Climate Change (IPCC) 2023d]). Mitigating the anthropic climate change is of prime importance for the human species, since it directly endangers coastal settlement, as well as food and clean water supply. It also causes global health issues, due to extreme heat waves for instance, particularly affecting urban areas (*high confidence*, see point A.2 of [Intergovernmental Panel on Climate Change (IPCC) 2023d]). Note that 55% of the world population lives in urban areas (2018 estimation from the United Nation), and 40% of the population lives within 100 km of the coasts (2017 estimation from the United Nation). It is worth noticing that human impact is not limited to climate change, but also concerns general soil, air and water pollution from chemicals, heavy metals and plastics, which can potentially induce global health issues together with ecosystem destruction.

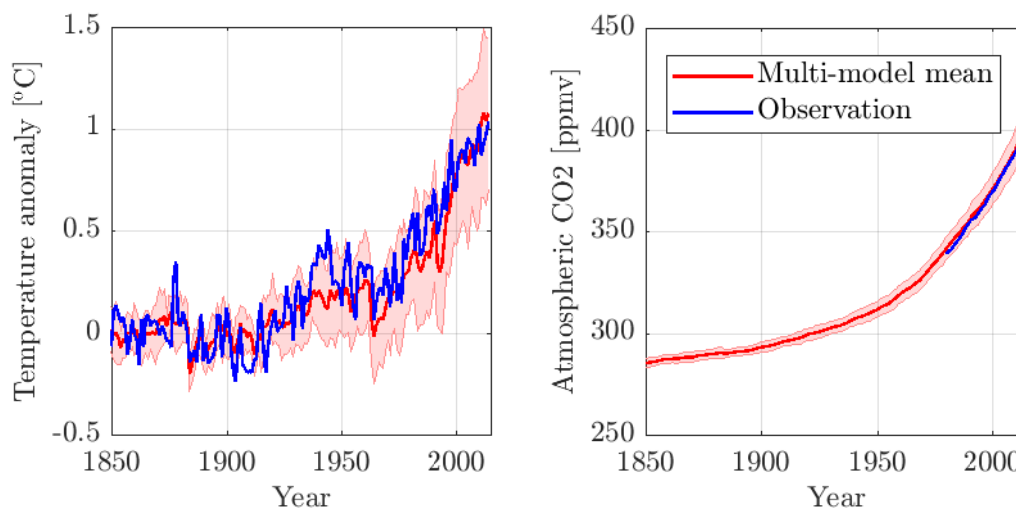


Figure 1.1: *Left*: Global surface temperature anomaly with respect to the 1850-1900 average global temperature. *Right*: Atmospheric CO<sub>2</sub> concentration. Both are shown from multi-model averaged as well as direct observations. The data set used to produce this picture comes from [Gier and Bock 2023], in [Eyring et al. 2021], and is available under CC-BY 4.0 license (<https://creativecommons.org/licenses/by/4.0>).

The increased greenhouse gases emission is caused by the rapid industrialization and globalization of human economic systems, leading to an increased utilization of energy. In 2019, around 80% of the primary energy used in the world was fossil, i.e. energy from carbon-based fuels which are generated by the slow natural decay of dead plants and animals (e.g. oil, gas, coal) [International Energy Agency 2021]. Carbon dioxide is naturally emitted from fossil fuel combustion. However, energy utilization is closely related to the Human Development Index (HDI), which is the geometrical average between three indicators of health (life expectancy at birth), education (averaged years of schooling of more than 25 years-old adults) and standard of living (gross national incomes per capita), established by the United Nations. The HDI is plotted against the total energy supply (TES, consists of the sum of production and imports,

## 1.1 The role of controlled nuclear fusion in the context of anthropic climate change

subtracting the exports and storage) per capita in figure 1.2. One can see that, until a certain value of TES per capita, the HDI strongly increases with the energy supply per capita, and then saturates. This means that it is necessary to increase the energy supply of the countries with the lowest HDI, to improve the population well-being as well as worldwide equality. Drawing a simplified picture, the energy supply is directly related to the development of the economy (the gross domestic product scales strongly with the total energy supply), which in turn potentially affects the development of state infrastructures such as schools, hospitals and transports (all of them also requiring energy to work), thus increasing the HDI. At the same time, it is necessary to reduce the energy utilization of the countries in the saturation area, first to compensate for the required increased energy supply of the low-HDI countries, then to mitigate the climate change. This saturation phenomenon could be imputed to many different (and sometimes interconnected) causes that can vary significantly from one country to another: a heavily carbon-based energy supply or carbon-dependent industry, an over-use of energy or an energy management style predicated on infinite access to resources, but also, for instance, difficult local weather conditions (e.g. extreme cold or extreme heat requiring heavy use of air conditioning). This balance in energy supply between low and high-HDI countries is also fair, as it has been established *with high confidence* that countries which historically contributed the least to the climate change, so countries with low energy supply and therefore low carbon emission, are among the countries that suffer the most from its adverse consequences (see point A.2 of [Intergovernmental Panel on Climate Change (IPCC) 2023d]). This situation perfectly illustrates the socioeconomic and geopolitical complexity of efficiently addressing climate change.

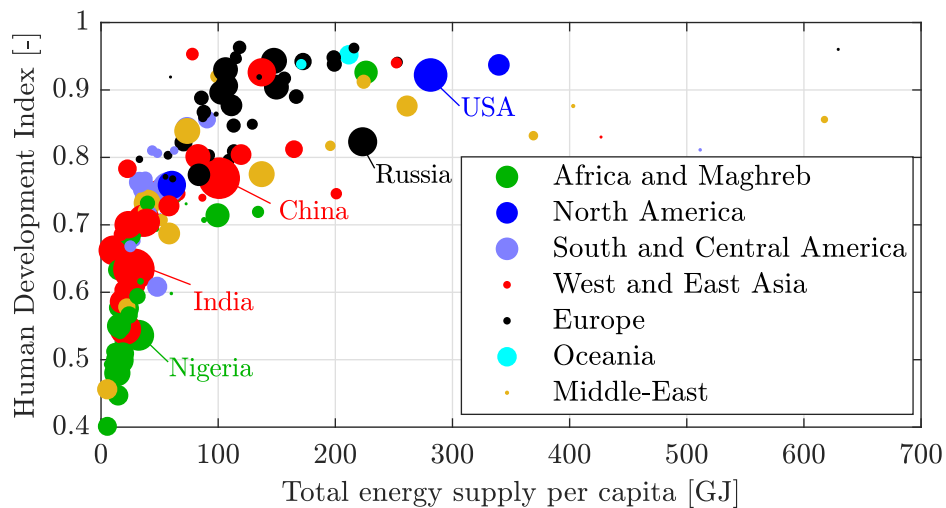


Figure 1.2: Human development index (HDI) as a function of total energy supply (TES) per capita. Data for the TES are 2019 data from [International Energy Agency 2021], under CC-BY 4.0 license (<https://creativecommons.org/licenses/by/4.0>), while data for the HDI are 2020-2021 data from [UNDP (United Nations Development Programme) 2022]. The marker size is proportional to the logarithm of the population in millions.

It has been shown with *high confidence* that the climate change could be efficiently slowed

down by rapidly and consistently reducing human-driven greenhouse gases emission (see point B.1 of [Intergovernmental Panel on Climate Change (IPCC) 2023d]). In particular, in 2019, 63% of the world electricity was generated by burning fossil fuels and electricity represented 19.7% of the total final consumption of energy, which is dominated by direct combustion of fossil fuels (40.4% of oil, 16.4% of natural gas and 9.5% of coal), e.g. for heat and transportation [International Energy Agency 2021]. Reducing the greenhouse gases emission of electricity generation can be achieved by increasing the use of renewable energy generation means (e.g. photovoltaic cells, wind turbines, dams for hydroelectricity) or of nuclear power plants to replace standard carbon-based generation means. Other sectors, such as transport and industry, could also be further electrified.

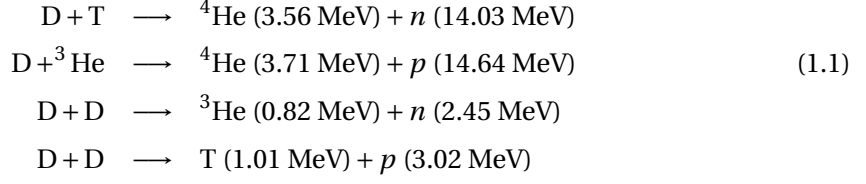
Fission power plants were developed after the Second World War, primarily in the USA, where the first reactor to produce electricity was built in 1951. Their main advantage is their low carbon footprint with respect to other types of power plants, even though it is partly offset by the long construction and decommissioning phases, but at the cost of long-lasting nuclear waste production and critical safety management of the nuclear fission chain reaction. In this context, controlled nuclear fusion can play a major role, as it does not rely on a chain reaction, and therefore does not present a risk of reaction runaway. Contrary to fission power plants, it does not produce long-lasting nuclear waste either. Moreover, the fuel (deuterium and tritium) can be produced on-site from hydrogen, rendering the technology more accessible in theory, as the main resource is more equally distributed across the world than uranium, or even coal or oil. However, with regard to the urgency of mitigating climate change, the long term development timescale of the first nuclear fusion reactor demonstrator DEMO, for now planned for 2050 [Federici et al. 2014], means that nuclear fusion cannot be foreseen as a direct transition energy supply, but rather as a long-term low-carbon base-load energy supply.

## 1.2 The path to controlled fusion: tokamaks and stellarators

### 1.2.1 The nuclear fusion process

Although it is not common on Earth, nuclear fusion reactions are a type of reaction which occurs frequently in nature, as it is the main underlying process that explains stellar longevity. The nuclear fusion reaction consists of two or more atomic nuclei fusing together into another heavier nucleus, eventually releasing subatomic particles such as protons or neutrons. For light elements, such as hydrogen, deuterium, tritium or helium, this reaction converts the energy stored within the nuclear binds into kinetic energy carried by the reaction products. In that case, the mass of the products is lighter than the mass of the reactants, the mass defect originating from the difference in nuclear binding energy between the separated reactants and the combined products. Part of the kinetic energy of the fusion products is then converted to heat via inelastic collisions. The main nuclear fusion reactions considered for fusion devices

are [Heidbrink and Sadler 1994, 1995]



Significant nuclear fusion rates require extreme conditions. Indeed, for the two nuclei to actually interact, it is necessary to overcome the strong repulsive Coulomb force acting between them. In practice, this Coulomb barrier can be breached by quantum tunneling, still requiring a high energy gap between the projectile (labeled  $p$ ) and the target (labeled  $t$ ). Typically, the fusion cross-section  $\sigma_{fus}^{pt}$  can be expressed as [Gamov and Critchfield 1949; Hutchinson 1987]

$$\sigma_{fus}^{pt} = \frac{A_5^{pt} + A_2^{pt} \left[ (A_4^{pt} - A_3^{pt} E_p)^2 + 1 \right]^{-1}}{E_p \left[ \exp \left( A_1^{pt} E_p^{-0.5} \right) - 1 \right]} \tag{1.2}$$

where the cross section is expressed in barns ( $1 \times 10^{-28} \text{ m}^2$ ) and the projectile energy  $E_p$  is in keV, assuming the target at rest. The coefficients  $A_1^{pt}$ ,  $A_2^{pt}$ ,  $A_3^{pt}$ ,  $A_4^{pt}$  and  $A_5^{pt}$  are the Duane coefficients, given in [Huba 2016] for each relevant fusion reactions. These typical cross-sections are shown in figure 1.3. It can be noticed that the fusion reaction with the highest cross-section at lower energies is the deuterium-tritium reaction, peaking at energy around 113 keV. This implies that, in theory, extreme temperatures (around  $1.3 \times 10^9 \text{ K}$ ) are required for maximum fusion reaction rate. In practice, the target temperature for the future fusion devices is of the order of 10 keV, which is still around  $120 \times 10^6 \text{ K}$ . Indeed, the optimum temperature maximizing the fusion reaction rate is lower than the temperature maximizing the fusion cross-section, meaning that the target temperature is closer to this optimum value.

At such high temperatures, the matter is in plasma state, in which atoms are dissociated into free ions and electrons, but the matter remains statistically neutral, the so-called quasi-neutrality state. A plasma is defined by a characteristic length over which an external electric field is screened, such that over this length, the plasma quasi-neutrality is ensured. This characteristic length is the so-called Debye length  $\lambda_D = \sqrt{\epsilon_0 T_e / (e^2 n_e)}$ , with  $n_e$  and  $T_e$  the electron density and temperature,  $e$  the elementary charge and  $\epsilon_0$  the vacuum permittivity. This means that the plasma state is only defined for a characteristic size much greater than the Debye length. For the screening to be efficient, the number of particles within a Debye sphere must be large  $n_e \lambda_D^3 \gg 1$ . In an analogous way, an external electric field applied to the plasma is screened over a characteristic time scale. This typical time scale is the reciprocal of the plasma frequency  $\omega_{p,e} = \sqrt{e^2 n_e / (\epsilon_0 m_e)}$  with  $m_e$  the electron mass, which characterizes the electron collective self-oscillations. This implies that the quasi-neutral plasma state is defined only for time scales, in particular the electron-neutral collision time scale, much greater than  $2\pi / \omega_{p,e}$ .

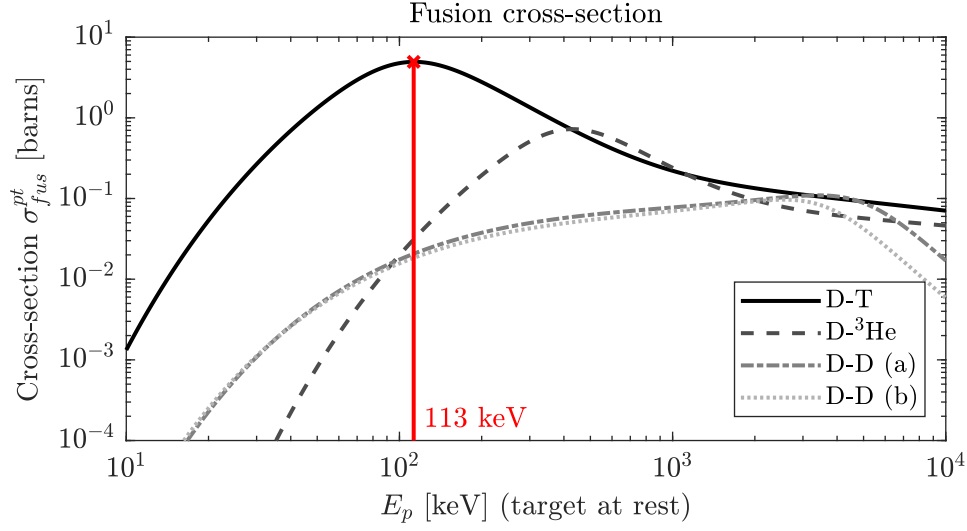


Figure 1.3: Fusion cross-sections for the fusion reactions described in equation 1.1, namely deuterium-tritium, deuterium-helium and the two branches of deuterium-deuterium, computed using equation 1.2.

Plasmas can be sorted into different categories, depending on their density and temperature. Examples of different plasma types are shown in figure 1.4.

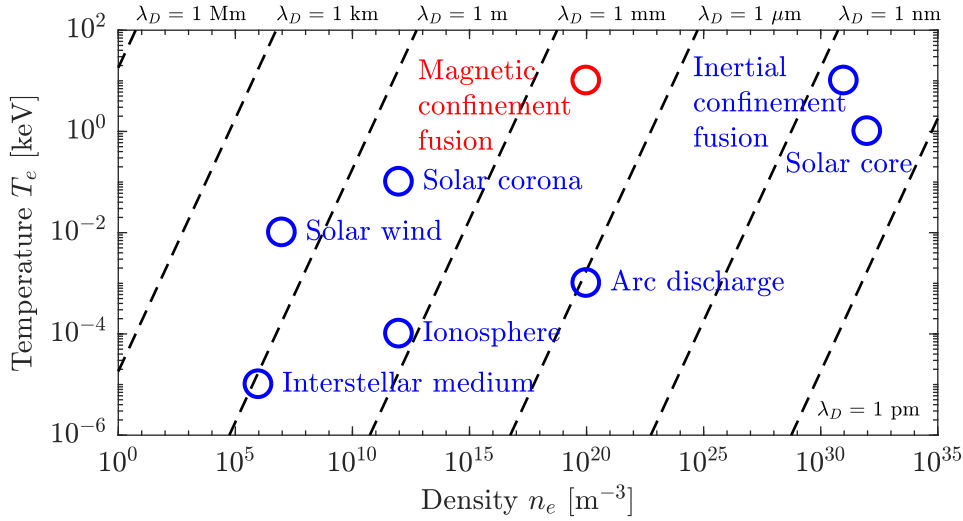


Figure 1.4: Different types of plasma, depending on electron temperature and density. Values are just indicative.

However, temperature is not the only parameter to play with to increase the fusion reaction rate. Indeed, the total number of fusion reactions integrated within a given volume is [Hutchinson 1987; Heidbrink and Sadler 1994, 1995]

$$R_{fus}^{pt} = \iiint n_p(\mathbf{x}) n_t(\mathbf{x}) \langle \sigma_{fus}^{pt} v \rangle d^3x \quad (1.3)$$

where  $\mathbf{x}$  is the position vector,  $n_p$  and  $n_t$  are the projectile and target ion densities and  $\langle \sigma_{fus}^{pt} v \rangle$  is the reaction rate in  $m^3/s$  given by

$$\langle \sigma_{fus}^{pt} v \rangle = \frac{\iint |\mathbf{v}_p - \mathbf{v}_t| \sigma_{fus}^{pt}(|\mathbf{v}_p - \mathbf{v}_t|) f_p(\mathbf{x}, \mathbf{v}_p) f_t(\mathbf{x}, \mathbf{v}_t) d\mathbf{v}_p d\mathbf{v}_t}{\iint f_p(\mathbf{x}, \mathbf{v}_p) f_t(\mathbf{x}, \mathbf{v}_t) d\mathbf{v}_p d\mathbf{v}_t} \quad (1.4)$$

with  $f_p$  and  $f_t$  the projectile and target ion distribution functions, and  $\mathbf{v}_p$  and  $\mathbf{v}_t$  the projectile and target ion velocities. For Maxwellian distributions, the reaction rate reduces to a function of the different ion temperatures. This means that the absolute fusion rate also scales directly with the reactive volume and with the square of the reactant density (assuming equally distributed projectiles and targets). In the case of standard stars such as the Sun, the plasma temperature in the core is relatively low with respect to the target temperature for a fusion device ( $15 \times 10^6$  K or 1.3 keV), but the core density is extremely high ( $9 \times 10^{31} \text{ m}^{-3}$  assuming the core composition is only protons), which compensates for the lower fusion cross-section. On Earth, it is not yet possible to reach such high densities for a sufficiently large volume over a sufficiently long time, so the target temperature in future fusion reactors needs to match as much as possible the optimum fusion temperature, in order to maximize the fusion reaction rate. External heating systems are therefore required to improve the fusion performance until ignition is reached. Ignition refers to the plasma self-sustaining phase in which the fusion rate is sufficiently high for the ion fusion products to transfer enough of their kinetic energy (of the order of 1 MeV) to the reactants via collisions, thus maintaining a steady-state high fusion rate. The ignited plasma is then often referred to as a burning plasma.

### 1.2.2 Technical solutions: tokamaks and stellarators

High temperature plasmas cannot be handled mechanically, and need to be confined to allow for steady-state operation and for the extraction of heat and of the fusion products kinetic energy. In particular, charged particles can be magnetically confined, while the neutrons produced by the different fusion reactions (see equation 1.1) are not affected by the magnetic field. These neutrons are free to escape any magnetic trap, and must be stopped in neutron damping materials (such as water) to convert their kinetic energy into heat. Heat can then be used to generate electricity, as it is done in conventional fission, gas or coal power plants.

The principle of magnetic confinement fusion is predicated on the fact that charged particles (ions and electrons) are subject to Laplace-Lorentz forces in presence of external electric and magnetic fields,  $\mathbf{E}$  and  $\mathbf{B}$ . The equation of motion of a particle  $s$  of mass  $m_s$  and charge  $q_s$  is given by

$$\frac{d(m_s \mathbf{v})}{dt} = q_s (\mathbf{E} + \mathbf{v} \times \mathbf{B}) \quad (1.5)$$

where  $\mathbf{v}$  is the particle velocity. Considering only an external magnetic field  $\mathbf{B}$  and assuming



$\mathbf{B} = B\mathbf{e}_\parallel$ , it is possible to write  $\mathbf{v} = \mathbf{v}_\perp + v_\parallel \mathbf{e}_\parallel$ . Projecting equation 1.5 yields

$$\frac{d(m_s v_\parallel)}{dt} = 0, \quad (1.6)$$

$$\frac{d(m_s \mathbf{v}_\perp)}{dt} = q_s \mathbf{v}_\perp \times \mathbf{B}, \quad (1.7)$$

meaning that charged particles follow a uniform motion along the magnetic field lines, and a circular motion in the perpendicular direction, around the field lines. This so-called cyclotron motion is characterized by the radius of the circular motion, or Larmor radius  $\rho_{L,s} = |v_\perp|/\Omega_{c,s}$ , where the cyclotron frequency  $\Omega_{c,s} = |q_s|B/m_s$  corresponds to the particle rotation frequency around the magnetic field lines. From equation 1.7, one can see that ions and electrons rotate in opposite directions around the field lines.

A naive approach to charged particle confinement would therefore be to close the magnetic field lines on themselves to create a toroidal magnetic trap. However, any additional external force applied to the particles  $\mathbf{F}_s$  will generate particle drifts of velocity  $\mathbf{v}_{d,\mathbf{F}_s} = \mathbf{F}_s \times \mathbf{B}/(q_s B^2)$ , and the bending of the magnetic field lines introduces forces due to the magnetic field curvature and inhomogeneity. Some of these drifts, such as the  $\mathbf{E} \times \mathbf{B}$  drift, are independent of the sign of the charge, but others, such as magnetic-field-curvature and magnetic-gradient drifts, depend on the sign of the charge and therefore induce a charge separation. In particular, the magnetic field curvature induces a vertical charge separation in a purely toroidal magnetic field, leading to a direct loss of confinement over time. It is thus necessary to impose at least an additional poloidal magnetic field to compensate the charge separation initiated by these vertical drifts.

Two main technical solutions to magnetic confinement fusion have been designed and are currently studied as serious candidates for future fusion reactors. A first concept is the *stellarator* (contraction of stellar generator). The stellarator principle was initially developed in the USA, during the 50s-60s, at Princeton University [Shafranov 1980]. It consists of a twisted toroidal device featuring a complex drift-compensating helical magnetic configuration, generated using a superposition of different magnetic fields without relying on an external electric field. In principle, such a configuration allows for continuous operation. The main disadvantage of the stellarator design is the complexity of the coil engineering, as each coil requires a unique 3D shape to provide the required magnetic field. Due to their complex design, it is also difficult to optimize the robustness of the coils with respect to the Lorentz forces arising from the high current flowing into them. Finally, optimizing the magnetic configuration requires significant computer resources. These are the main reasons why the second design was initially preferred for the development of fusion machines.

This second concept is the *tokamak* (Russian acronym for *toroidalnaïa kamera s magnitnymi katouchkami*, or toroidal chamber with magnetic coils in English), which was born in the 50s in the ex-USSR, with the first tokamak T-1 starting operation in 1958 at Kurchatov Institute, in Moscow [Smirnov 2009]. In a tokamak, the poloidal magnetic field is generated by an inductive current flowing toroidally, directly induced by the central solenoid, which is absent from the

## 1.2 The path to controlled fusion: tokamaks and stellarators

stellarator device. The toroidal field can thus be generated by relatively simple poloidal-shaped coils. This comes with two main advantages: the conception simplicity and an initial source of heat to reach better fusion performances, often referred to as Ohmic heating. However, since it relies on induction, it requires a transient magnetic field from the central solenoid, which precludes steady-state operation by design. Additional toroidal current sources are therefore necessary to palliate this intrinsic intermittency in view of power-plant operation. The last, but not least, disadvantage of tokamaks with respect to stellarators is its sensitivity to disruptive events, either from vertical displacement events or caused by unstable growing MHD modes, leading to a partial or complete loss of the usually large toroidal plasma current (absent from stellarator plasmas) which can then severely damage the structure of the machine. Tokamaks however possess significant advantages over stellarators, such as better neoclassical (collisional) confinement for instance, which render them the most plausible reactor concept at the moment. A detailed comparison of common points and differences between tokamak and stellarator can be found in [Helander et al. 2012]. The two configurations are illustrated in figure 1.5. Different tokamaks have been built across the world, and a non-comprehensive list is provided in table 1.1.

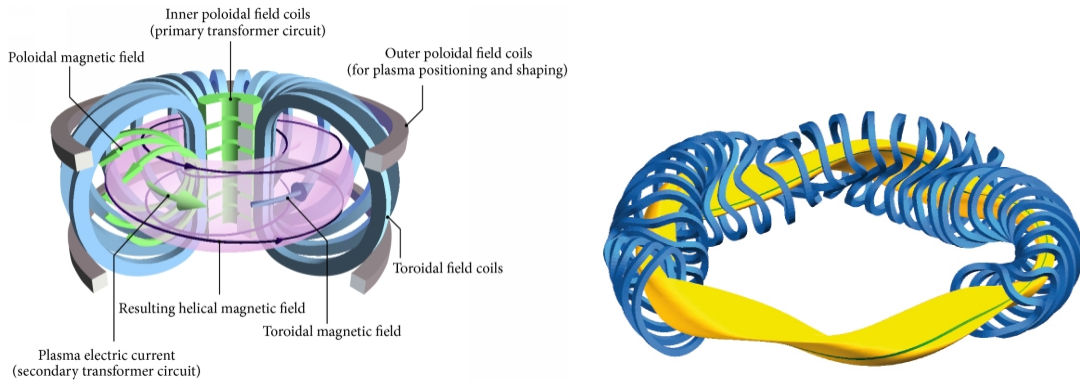


Figure 1.5: *Left*: example of a tokamak configuration, with the toroidal field coils in blue, the central solenoid in green and the plasma in purple. A magnetic field line is highlighted in black. Credits: [Zhang et al. 2014], CC BY 4.0 (<https://creativecommons.org/licenses/by/4.0>), via Wikimedia Commons. *Right*: example of a stellarator configuration, with the coils in blue and the plasma in yellow. A magnetic field line is highlighted in green. Credits: Max-Planck Institut für Plasmaphysik, CC BY 3.0 (<https://creativecommons.org/licenses/by/3.0>), via Wikimedia Commons.

### 1.2.3 The road to fusion and remaining challenges: ITER and DEMO

Confining the plasma is a necessary but not sufficient condition to reach the ignition state, which also requires a sufficiently high plasma pressure. In fact, the required condition to fulfill to get a burning plasma takes the form of a criterion on the triple product of plasma ion density  $n_i$ , ion temperature  $T_i$  and energy confinement time  $\tau_E$ , the so-called Lawson criterion [Lawson 1957]

$$n_i T_i \tau_E \geq 10^{21} \text{ m}^{-3} \cdot \text{keV} \cdot \text{s}. \quad (1.8)$$

## Chapter 1. Introduction

Table 1.1: Examples of tokamaks built across the world, with indicative parameters given for comparison.

Tokamak	Major axis $R_0$	Minor axis $a$	Max. magnetic field $B_0$	Max. plasma current $I_p$	Location
TCV	0.88 m	0.25 m	1.54 T	1 MA	Switzerland
ASDEX-Upgrade	1.65 m	0.80 m	3.10 T	2 MA	Germany
DIII-D	1.67 m	0.67 m	2.20 T	2 MA	USA
JET	2.96 m	1.25 m	3.45 T	4.8 MA	UK
WEST	2.5 m	0.50 m	3.70 T	1 MA	France
EAST	1.85 m	0.45 m	3.50 T	1 MA	China
ITER <sup>†</sup>	6.20 m	2.00 m	5.30 T	15 MA	France

<sup>†</sup>Planned, construction started but it is not finished.

The energy confinement time  $\tau_E$  is the characteristic time over which the plasma loses its stored energy  $W$ , the energy balance therefore reading  $dW/dt = P_{in} - W/\tau_E$  with  $P_{in}$  the injected power by external means. Experimentally, the energy confinement time can be estimated by

$$\tau_E = \frac{3 \langle n_e T_e + n_i T_i \rangle}{2 P_{in} - dW/dt} V \quad (1.9)$$

with  $V$  the plasma volume. Extrapolating the energy confinement time to all machines and plasma parameters is challenging, as it depends on complex transport phenomena, including neoclassical transport, caused by the various particle orbits and collisions, and turbulent transport. The most common extrapolation method consists of using multi-machine empirical scaling laws, such as the IPB98(y,2) scaling law [ITER Physics Expert Group on Confinement and Transport et al. 1999], but this often lacks physical insight. Another method is to use physics-based scaling laws, assuming a given transport model, taking the risk that it may be over-simplifying or specific to a given regime. These different scaling laws are extensively compared to one another to assess their robustness, see [Stroth et al. 2020] for instance, but one of the main common feature of all these studies is that the energy confinement time scales positively with the plasma volume.

For power-plant operation, it is important to maximize the triple product  $n_i T_i \tau_E$  to values above the Lawson criterion. However, in tokamaks, MHD stability constrains the accessible plasma pressure and plasma current [Troyon et al. 1984]. An independent limit also appears on the operational plasma density, with complex non-linear dependencies on other plasma parameters [Greenwald 2002]. Therefore, the plasma volume has been identified as a key parameter to increase the energy confinement time, and thus the triple product. This is why the International Thermonuclear Experimental Reactor (ITER), a tokamak under construction in the South-East of France and a collaborative project between China, the EU, India, Japan, Russia, South Korea and the USA, scales up in volume by a factor 10 with respect to the biggest existing tokamak, the Joint European Torus (JET) (see table 1.1). Indeed, ITER aims at demonstrating the feasibility of a deuterium-tritium fusion gain  $Q = 10$  in pulsed operation and  $Q = 5$  in steady-state operation, meaning that the fusion output power is more than 10 (or 5 respectively) times larger than the power injected into the plasma (this does not take

into account the machine efficiency). Other ITER missions are to assess nuclear safety in a tritium environment, as well as to test concepts of tritium breeding blankets, necessary to fuel the deuterium-tritium reaction in a future reactor. ITER is merely a first step toward a fusion reactor, as it aims at providing a proof of concept, while the actual fusion reactor demonstrator is left for the future device DEMO. A status of the construction progress of ITER can be found in [Bigot 2022], and the complete research plan is available in [ITER Organization 2018]. In addition to the physical challenges that ITER will have to face to reach the foreseen fusion performances, many engineering challenges will have to be tackled, in particular challenges involving material sciences. For instance, ITER will have to assess material resistance to a high energy neutron flux as well as to extreme heat fluxes in long-lasting steady-state operation.

As already mentioned, optimizing fusion performance would require reaching the target plasma temperature of 10 to 20 keV, and steady-state tokamak operation would require sustaining the toroidal plasma current by external means. Different technologies can be used for both purposes, such as neutral beam injection and wave-power transfer to the plasma.

### 1.3 Principle of Electron-Cyclotron resonant heating and current drive

A very efficient tool for coupling external power to the plasma is to use external waves that are absorbed by different mechanisms, such as resonant or collisional absorption. The main difficulty is to generate waves that fulfill the relevant dispersion relations in the plasma, which is described by a non-homogeneous refractive index. A particularly efficient resonant wave-plasma coupling can be achieved with Electron-Cyclotron (EC) waves, reviewed in detail in [Prater 2004]. These waves are electromagnetic waves, in the range of microwaves for typical tokamaks and stellarators, which interact resonantly with the electrons in the plasma as follows

$$\omega - k_{\parallel} v_{\parallel} - \frac{n\Omega_{c,e}}{\gamma} = 0 \quad (1.10)$$

with  $\omega$  the wave frequency,  $k_{\parallel}$  its parallel wave-number with respect to the magnetic field,  $v_{\parallel}$  the parallel velocity of electrons,  $\Omega_{c,e}$  the electron cyclotron frequency,  $n$  the harmonic number and  $\gamma$  the relativistic Lorentz factor. This means that the wave resonates with the different harmonics of the relativistic electron cyclotron motion, and that the waves accelerate electrons in the perpendicular direction. For a given EC wave frequency, the contour of the resonance location in the velocity space  $(v_{\perp}, v_{\parallel})$  is an ellipse given by [Prater 2004]

$$\frac{v_{\perp}^2}{v_{Te}^2} = \left(1 - \frac{\omega^2}{n^2\Omega_{c,e}^2}\right) \frac{c^2}{v_{Te}^2} + 2N_{\parallel} \frac{\omega^2}{n^2\Omega_{c,e}^2} \frac{c}{v_{Te}} \frac{v_{\parallel}}{v_{Te}} - \left(1 + N_{\parallel}^2 \frac{\omega^2}{n^2\Omega_{c,e}^2}\right) \frac{v_{\parallel}^2}{v_{Te}^2} \quad (1.11)$$

with  $v_{Te} = \sqrt{k_B T_e / m_e}$  the electron thermal velocity and  $N_{\parallel}$  the parallel refractive index. A key advantage of EC waves is that, as electromagnetic waves, they can propagate in vacuum, meaning that it is possible to have the wave generator (gyrotrons in this case) far away from

## Chapter 1. Introduction

---

the extreme tokamak environment, and that no physical components need to be brought close to the hot plasma boundary. The other main advantage of EC waves is that the resonance is, at first order, located in a narrow region of the plasma determined by the resonant magnetic field for each harmonics.

For  $k_{\parallel} = 0$ , at a given radial location, the resonance is located at a constant velocity  $v$  in velocity space. For heating applications, this value of  $v$  at the location at which the wave absorption occurs is often above the thermal velocity. The bulk electrons are then pumped from the bulk distribution to higher velocities, along the resonance location in velocity space, distorting the electron distribution function. The hole thus created is filled efficiently thanks to fast thermal collisional relaxation. When the wave is injected in steady-state, the wave power deposition and collisions balance and the electron distribution function deformation is sustained. In the  $k_{\parallel} = 0$  case, a plateau is generated in the electron distribution function, increasing the electron temperature. This is the so-called Electron-Cyclotron Resonant Heating (ECRH).

In the case of finite  $k_{\parallel}$ , the resonance is Doppler shifted in phase space, resulting in a non-symmetric wave power deposition in phase space, which generates a non-symmetric distortion of the electron distribution function. If the accelerated electrons remain untrapped by the non-homogeneous magnetic field, a net parallel current is driven in the direction opposite to that of the Doppler-shifted resonance location (because of their negative charge, electrons travel opposite to the current). This is the so-called Fisch-Boozer current-drive mechanism. On the other hand, if the accelerated electrons become trapped, they will start bouncing back and forth, thus generating a defect in the electron distribution function in the direction of the Doppler-shifted resonance location, and driving a net current in that same parallel direction. This is the so-called Ohkawa mechanism and is usually a minor effect. These processes are responsible for the so-called Electron-Cyclotron Current Drive (ECCD) mechanism, and are illustrated in figure 1.6. Both ECRH and ECCD typical resonances are illustrated in figure 1.7, and are further described in section 3.2.2.

The accessibility of the EC waves to the plasma depends on the plasma refractive index, and on the wave polarization, yielding different resonance and cutoff conditions. Therefore, the wave accessibility to the plasma is not the same depending on whether the wave is launched from the low- or the high-field side. For the sake of simplicity, the  $k_{\parallel} = 0$  case is considered. In this configuration, two different polarization modes propagate: the ordinary mode (O-mode), with a wave electric field aligned with the background magnetic field, and the extraordinary mode (X-mode), with a wave electric field perpendicular to both the background magnetic field and the propagation direction. Neglecting thermal effects, it is possible to write a simplified form of the refractive index  $N_{O/X}$

$$N_O = \sqrt{P} ; N_X = \sqrt{\frac{S^2 - D^2}{S}} \quad (1.12)$$

### 1.3 Principle of Electron-Cyclotron resonant heating and current drive

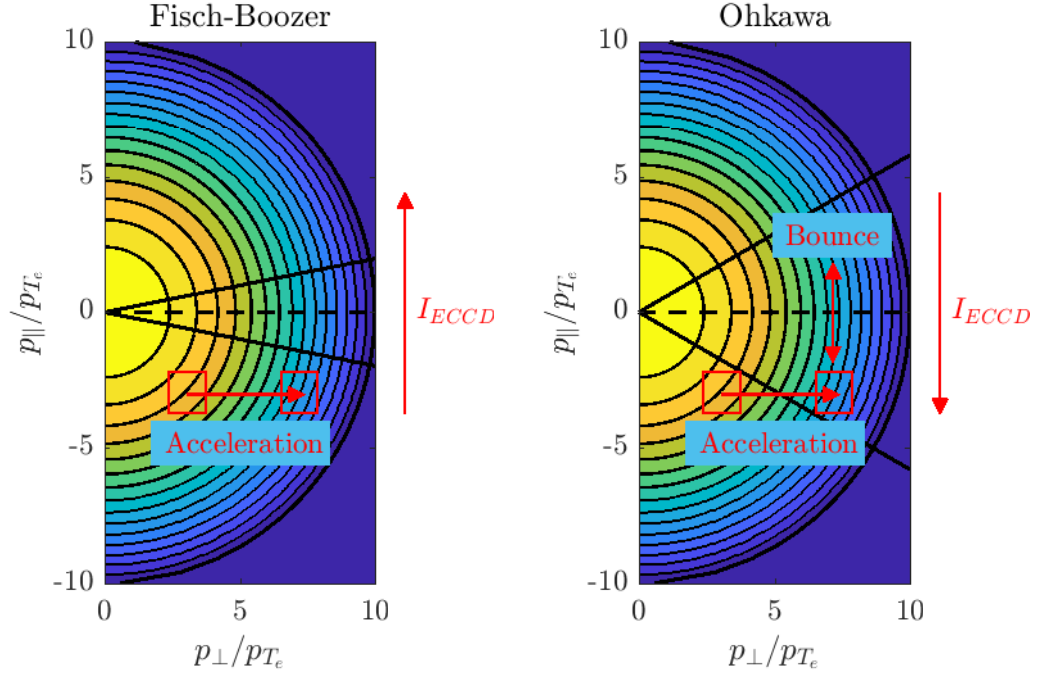


Figure 1.6: Fish-Boozer Electron-Cyclotron current drive mechanism (*left*) and Ohkawa mechanism (*right*). The trapped particles are located within the black straight lines. The color map indicates the electron distribution function.

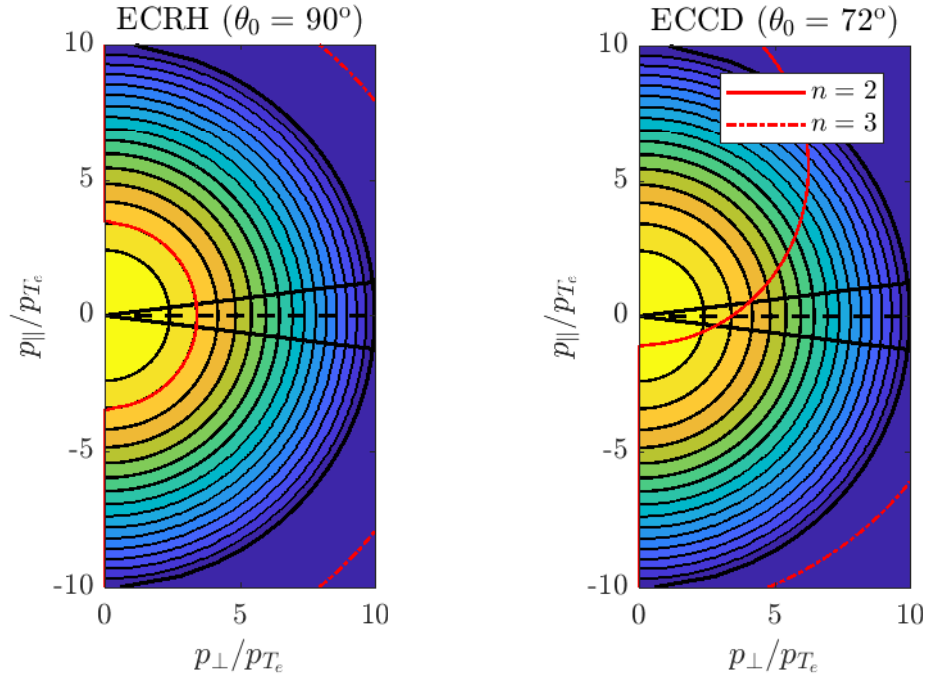


Figure 1.7: Example of the resonance location in velocity space calculated with equation 1.11, using  $B = 1.51$  T,  $T_e = 1.8$  keV and  $\omega/(2\pi) = 82.7$  GHz, for harmonics  $n = 2$  and  $3$ . *Left* shows an ECRH configuration and *right* an ECCD configuration, with  $\theta_0$  the angle between the magnetic field and the wavevector and  $N_{\parallel} = \cos(\theta_0)$ .

with  $P$ ,  $S$  and  $D$  the Stix coefficients [Stix 1992], defined by

$$\begin{aligned} P &= 1 - \frac{\omega_{p,e}^2}{\omega^2} & ; & \quad S = 1 - \frac{\omega_{p,e}^2}{\omega^2 - \Omega_{c,e}^2} \\ D &= \frac{\Omega_{c,e}}{\omega} \frac{\omega_{p,e}^2}{\omega^2 - \Omega_{c,e}^2} & ; & \quad Q = P - S = \frac{\Omega_{c,e}^2}{\omega^2 - \Omega_{c,e}^2} \end{aligned} \quad (1.13)$$

with  $\omega_{p,e}$  the plasma frequency and  $\Omega_{c,e}$  the electron cyclotron frequency. The expression of the refractive index is generalized in section 3.2.2 (see equation 3.68), and the EC wave polarization in section 3.1.1. From this simplified form of the refractive index, it is possible to draw the Clemmov-Mullaly-Allis (CMA) diagram for both polarization modes, showing the resonances and the cutoffs in the 2D  $(\omega_{p,e}^2, \Omega_{c,e}^2)$  space, or equivalently in the  $(n_e, B^2)$  space. This is illustrated in figure 1.8. It can be seen that O-mode can propagate only up to a critical electron density  $n_c = \omega^2 \epsilon_0 m_e / e$ . Accessibility is more complex for X-mode: launching from the low-field side makes the first EC harmonic inaccessible, and the second or third harmonics need to be used instead. On the other hand, it is possible to reach the first harmonic from the high-field side, but this configuration is unpractical due to the limited space in the high-field side of tokamaks. However, for such an approach, the X-mode can propagate to higher densities than the O-mode. In the example shown in figure 1.7, at a given frequency and close to the wave absorption location, the higher order EC harmonic resonance tend to involve electrons at higher velocities than the lower harmonics, meaning that there are less targets for wave absorption for these higher order harmonics than for the lower one. In practice, treating the absorption of the different modes and harmonics is complicated, and thermal effects need to be considered. Typically, O1 (launched with frequency  $\omega$ ) and X2 (launched with frequency  $2\omega$ ) resonate at the same plasma location and show similar absorption behavior, but, in that particular case, X2-mode can travel through higher densities. In comparison, O2 and X3 modes show weaker absorption [Prater 2004].

## 1.4 Thesis motivation and outline

### 1.4.1 Motivation: understanding the discrepancy between experiments and simulations

As mentioned in section 1.3, Electron-Cyclotron (EC) waves are routinely used in tokamaks (e.g. TCV, ASDEX-Upgrade or JET), and even in stellarators such as W-7X, to drive current and increase the electron temperature. In particular, the ability of EC waves to drive current in a narrow region of the plasma turns them into the main foreseen tool for magnetohydrodynamic (MHD) mode stabilization. When unstable, resistive MHD modes such as Neoclassical tearing Modes (NTM) generate linearly growing and non-linearly saturating magnetic islands at rational values of the safety factor, hampering the magnetic confinement of the plasma and degrading the overall performance of fusion devices, potentially leading to disruption in high

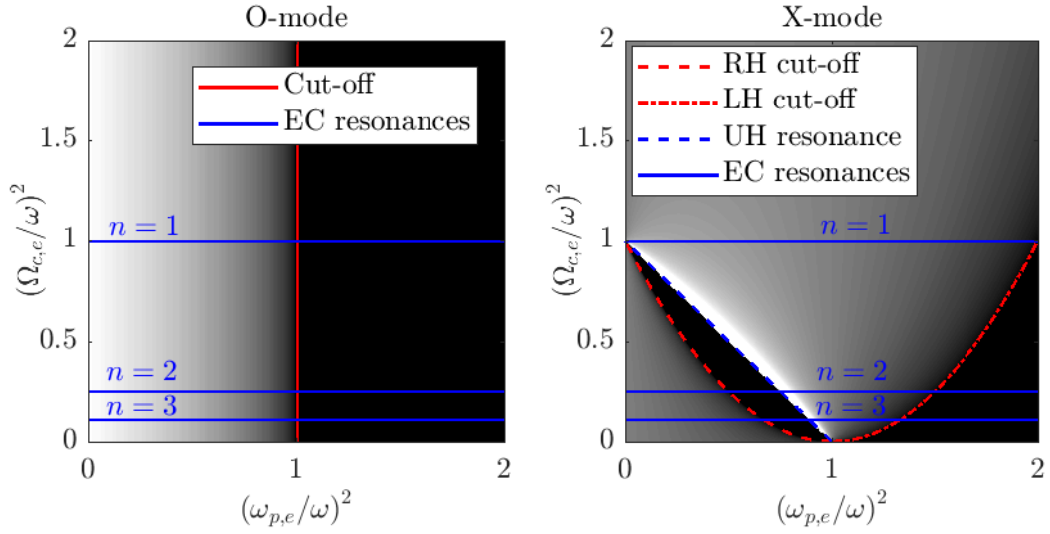


Figure 1.8: CMA diagram for EC waves, assuming  $k_{\parallel} = 0$ , for O-mode polarization (*left*) and X-mode polarization (*right*), both launched with a frequency  $\omega$ . The EC resonances are shown for harmonics  $n = 1, 2$  and  $3$ . For the X-mode polarization, UH stands for upper hybrid, RH and LH for right-hand and left-hand respectively. The color map represents the real part of the refractive index (white is 1 and black is 0).

pressure devices such as ITER [Haye 2006]. These magnetic islands can be seen as heat short-circuits leading to a flattening of the temperature profile within the core. This flattening of the temperature, and so of the pressure, decreases the pressure-gradient-driven current, the so-called bootstrap current. This reduction of the bootstrap current then further destabilizes the NTM. Therefore, NTMs can be stabilized by driving current inside the magnetic islands to compensate for this missing bootstrap current. Such techniques have been developed and tested for NTM prevention and stabilization in real conditions in TCV [Kong et al. 2019]. Even though advanced control techniques help to gain in efficiency, MHD mode mitigation using EC waves still requires a high level of accuracy in the power deposition location.

However, comparisons between linear estimations of the power deposition profile and experimental data have suggested that the actual power deposition profile might be broader than numerical expectations. In TCV, the measured hard X-ray emissivity profile, which is used as a proxy for the suprathermal electron density (the hard X-rays being emitted by suprathermal electron Bremsstrahlung), is broader and flatter than what can be expected from the EC power deposition profile obtained by ray tracing, in particular for off-axis power deposition locations [Coda et al. 2003a]. This apparent discrepancy has been further confirmed by recent studies led in the DIII-D tokamak, for which direct inversions of the EC power deposition profile from electron temperature measurements have been performed, showing that the measured power deposition profile is broader than the ray-tracing estimation by a factor ranging from 1.6 to 3.6 [Slief et al. 2023]. The same study also concludes that, in ITER, considering the total EC power available, full NTM suppression is achievable only if the power deposition profile is broader by less than a factor 2.4 with respect to ray-tracing estimations. Different mechanisms have been proposed to explain this discrepancy, based on the missing key ingredient of both linear



ray-tracing and quasilinear drift-kinetic codes: turbulence.

The aim of this thesis is to better characterize those mechanisms, both experimentally and numerically. In particular, two potential mechanisms are studied: the radial broadening of the suprathermal electron distribution after the EC beam absorption due to turbulent transport enhancement by the EC waves, and the broadening of the EC beam traveling through the turbulent edge density before its absorption.

### **Enhancement of the transport of suprathermal electrons by the EC waves**

The comparisons between expected EC power deposition profiles and hard X-ray emissivity profiles lead to the conclusion that suprathermal electrons exist in regions of the plasma where wave-plasma interaction is negligible, suggesting that these fast electrons accelerated by the EC waves might be transported away from the resonance location [Coda et al. 2003a]. In TCV, the estimation of the EC driven current is highly overestimated by forward quasilinear drift-kinetic modeling, and matching simulated and experimental current, as well as measured and synthetic hard X-ray spectra, requires the addition of ad-hoc radial transport of fast electrons [Nikkola et al. 2003; Choi et al. 2020a]. This additional ad-hoc transport has also proven to be necessary to reproduce experimental results in the DIII-D tokamak [Harvey et al. 2002]. Simulations performed for ITER has shown that this transport limits the achievable current-drive efficiency [Bertelli and Westerhof 2009].

To study this potential transport enhancement by the EC waves, one can proceed to perturbative transport studies [Cardozo 1995; Ryter et al. 2010]. By using a power-modulated heating source in a quasi steady-state plasma, it is possible to study its dynamical response to this perturbation and to deduce some transport-related properties such as diffusion or convection coefficients. Historically, this technique has been widely used to study electron heat transport in tokamaks such as DIII-D (EC waves) [Jahns et al. 1986], TFR (EC waves) [TFR and FOM-ECRH 1988], TCA (Alfvén waves) [Joye et al. 1988], JET (Ion-Cyclotron waves) [Gambier et al. 1990] and DITE (EC waves) [Cox et al. 1993], but also in stellarators such as W7-A (EC waves) [Hartfuss et al. 1986]. A multi-machine analysis [Ryter et al. 2001], including ASDEX, TCV, RTP and TCU (EC waves), Tore Supra (fast wave electron heating) and JET (combination of Ion-Cyclotron heating and neutral beam heating) has shown that electron heat transport in the core is governed by turbulent transport, except near the magnetic axis (inside the  $q = 1$  surface) where MHD activity dominates. In stellarators, the radial transport of suprathermal electrons is associated with neoclassical effects enhanced by the toroidal asymmetry (orbits, trapped particles) [Murakami et al. 2000]. However, in ECRH experiments performed in W7-X, it has been found that turbulent transport dominates over neoclassical transport in predominantly electron heating scenarios [Beurskens et al. 2021b].

This perturbative technique has been applied in TCV to study particle transport instead of heat transport, using power-modulated EC waves in MHD-quiescent plasmas [Choi et al. 2020a]. From bounce-averaged drift-kinetic simulations of these experiments, including ad-hoc radial

transport, it has been found that an electron radial diffusion coefficient directly proportional to the plasma-wave interaction diffusion coefficient, and so which relates to the local power deposition (that also depends on the distribution gradient), provides the best agreement between simulations and experimental measurements. Plasma turbulence could explain the enhanced electron transport, considering that EC wave absorption may change the local electron temperature absolute value and gradient, as well as the ion-to-electron temperature ratio, which are all key parameters determining the turbulence regime and properties [Garbet et al. 2004a].

### **Beam scattering through the turbulent edge of tokamak plasmas**

The second possible explanation, which does not exclude the first one, is the scattering of the EC beam passing through the fluctuating plasma refractive index before its absorption. This scattering results in an average beam broadening that may affect the power deposition profile. Analytical and numerical work has been performed to better understand the microwave beam broadening by turbulent plasma density, using different approaches such as quasi-optics [Bertelli et al. 2010; Sysoeva et al. 2015; Tretinnikov et al. 2021], statistical Fokker-Planck formalism [Tsironis et al. 2009; Hizanidis et al. 2010], ray tracing coupled to a drift-kinetic Fokker-Planck solver [Decker et al. 2012; Peysson et al. 2012], wave-kinetic equation solver [Weber et al. 2015], benchmarked against full-wave simulations [Snicker et al. 2017a,b; Köhn et al. 2018], proper full-wave simulations in tokamak-relevant conditions [Holland et al. 2023], or simulations of the effect of single-blob [Ram et al. 2013] and multi-blob [Ioannidis et al. 2017] density structures on a microwave beam. These numerical studies tend to conclude that the effect of wave scattering on the beam broadening may be important, particularly in large-sized tokamak like ITER or DEMO, where the wave travels over a distance of meters before reaching the absorption location. Quantifying this effect is still challenging, as it highly depends on the properties of the density fluctuations. For the ITER equatorial launchers in the baseline H-mode scenario, one can expect from 20 % to 150 % of beam broadening [Snicker et al. 2017b]. A multi-model approach has also been proposed to study neoclassical tearing mode mitigation using EC waves in a turbulent plasma, concluding that, for ITER-relevant configurations, the damping time of the NTM is up to four times longer in the presence of edge-localized density blobs because of the turbulence-induced beam refraction and diffraction [Tsironis et al. 2021]. Part of these studies focus mainly on the beam broadening but not on the resulting power deposition profile, which also depends on the wave injection configuration.

Recently, effort has been placed in the experimental characterization of the impact of edge-localized density fluctuations on the beam broadening. Experimental studies on the toroidal device TORPEX [Chellaï et al. 2018b] and on TCV [Chellaï et al. 2018a; Chellaï et al. 2021] in the case of non-absorbed, fully-transmitted microwave beam, with the support of a full-wave propagation solver, have shown a correlation between the transmitted EC power and the density fluctuations. In TCV specifically, it has been related to a combination of Scrape-Off Layer (SOL) turbulence, using experimentally validated fluid simulations performed with

the global Braginskii solver (GBS) code [Chellaï et al. 2018a], and core turbulence calculated by gradient-driven gyro-kinetic simulations [Chellaï et al. 2021]. It was shown that core turbulence, even though of relatively lower amplitude than edge turbulence, can account for up to 50 % of the measured transmitted power deposition broadening. In DIII-D, the beam broadening has been experimentally evidenced by analyzing the temperature perturbation induced by the EC beam, fitting the heat transport with a model taking into account the beam width, estimated through a full-wave model [Brookman et al. 2017, 2021, 2023]. In that case, edge density fluctuations have been characterized using both beam emission spectroscopy measurements and fluid simulations [Brookman et al. 2023].

### 1.4.2 Thesis outline

The work performed throughout this thesis can be subdivided in different goals and tasks, as follows:

- The maintenance and calibrations of the hard X-ray spectrometer installed in TCV, as well as the development of a set of user-friendly functions to make the diagnostic data more easily accessible, so they can be used in studies other than those presented in this thesis. A detailed description of the diagnostic is given in section 2.5. The rest of chapter 2 describes the main features of TCV, its heating systems and its main diagnostics, as well as the fluctuation diagnostics used for the presented work.
- The development of numerical tools dedicated to the study of the interplay between waves, turbulence and suprathermal electrons, which is the object of the entire chapter 3. In particular, ray-tracing routines have been improved to take into account varying refractive index and non-Gaussian beams, and then benchmarked against full-wave simulations. A benchmark of a realistic Electron-Cyclotron source developed for flux-driven gyro-kinetic codes is also proposed. This development has led to two co-authored publications [Donnel et al. 2021, 2022].
- The study of the dynamical response of the plasma to an Electron-Cyclotron wave pulse, to investigate the turbulent transport enhancement induced by the waves. This work was initiated by Dr Dahye Choi, leading to one co-authored publication [Choi et al. 2020a], and is significantly extended in chapter 4. In particular, transport studies have been extended to different background heating power levels and different current-drive conditions, adding an experimental analysis of turbulence and, for the first time, first principles flux-driven gyro-kinetic simulations to directly assess the impact of the Electron-Cyclotron waves on electron transport. This work has been published in *Plasma Physics and Controlled Fusion* [Cazabonne et al. 2023].
- The study of the impact of edge-localized density fluctuations on Electron-Cyclotron beam scattering and power deposition profile broadening in TCV. This work follows earlier efforts by Dr Oulfa Chellaï in a scenario featuring non-absorbed top-launched

Electron-Cyclotron beam [Chellaï et al. 2018a; Chellaï et al. 2021]. The case of efficiently absorbed waves, relevant to the practical application of ECRH in a reactor, is developed in chapter 5. Full-wave numerical studies are performed, scanning relevant parameters such as the fluctuation correlation length and the width of the turbulent layer, to identify different beam broadening regimes as in [Snicker et al. 2017a]. Then, simulations of experimental cases are performed to assess the actual impact of the beam broadening on the power deposition profile in TCV shots for which the beam is completely absorbed. This work has been submitted for publication in *Nuclear Fusion*.

General conclusions are drawn in chapter 6. Finally, the list of appendices providing technical details is:

- Appendix A: details the EC low-field side launchers installed on TCV.
- Appendix B: describes the analytic equilibrium generation method based on [Cerfon and Freidberg 2010].
- Appendix C: describes the different coordinate systems used in the different codes.
- Appendix D: details the EC wave polarization projected in the Cartesian frame of COM-SOL, for equatorial ECCD.



## 2 TCV: the *Tokamak à Configuration Variable*

*Le macchine, diceva, sono effetto dell'arte, che è scimmia della natura, e di essa riproducono non la forme ma la stessa operazione. Egli mi spiegò così i portenti dell'orologio, dell'astrolabio e del magnete. Ma all'inizio temetti che si trattasse di stregoneria, e finì di dormire certe notti serene in cui egli si poneva (tenendo in mano uno strano triangolo) a osservare le stelle.*

---

Il Nome Della Rosa,  
Umberto Eco (1932-2016)

### 2.1 General description and research overview

The *Tokamak à Configuration Variable* (TCV) is medium-sized tokamak, with a major radius  $R = 0.89$  m, a minor radius  $a = 0.25$  m, a maximum magnetic field on axis  $B_0 \sim 1.54$  T, a maximum plasma current  $I_p = 1$  MA, a maximum plasma elongation  $\kappa = 2.8$  and a triangularity which ranges from  $\delta = -0.6$  to  $\delta = +0.9$  [Hofmann et al. 1994]. The inner walls of the vacuum vessel are paved with graphite tiles.

TCV possesses 16 toroidal field coils, made of copper. These non-superconducting coils are water-cooled. TCV plasmas last only up to 3 s, which is sufficiently short to ensure safe usage of the copper coils. One of the unique features of TCV is its set of 16 poloidal field coils, which allows the formation of a wide range of plasma shapes, from positive and negative triangularity to exotic shapes such as doublets and "jellyfish" plasmas. These shaping capabilities are illustrated in figure 2.1. Figure 2.2 shows a 3D model of TCV, with the different coils and

structures. Finally, TCV is also equipped with a high power-density heating system, using external Electron-Cyclotron waves and neutral beam injection, in addition to the standard Ohmic heating of tokamak devices.

The research fields covered on TCV are summarized in [Coda et al. 2019] and [Reimerdes et al. 2022]. In particular, the recent development of the divertor baffles contributes to extending the studies of plasma edge physics and plasma heat exhaust, which is one of the main focus points of the machine program [Reimerdes et al. 2017, 2021]. A second field of research is the high confinement mode, so-called H-mode, which is the expected working regime for ITER, as well as alternative high confinement modes and high performance scenarios, such as ELM-free regimes. The flexibility of TCV also allows the study of the operational limits for larger devices and of potential solutions to overcome these limits, such as benign plasma termination and runaway electron beam generation and mitigation for instance. Finally, a significant contribution to the fusion community is provided by the development and testing of efficient real-time control systems.

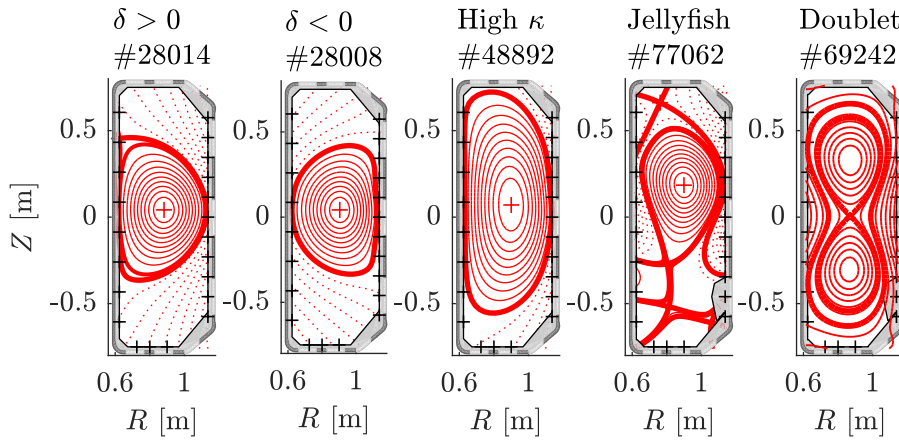


Figure 2.1: Examples of TCV shaping capabilities, where  $\delta$  is the triangularity and  $\kappa$  the elongation.

## 2.2 Heating and current-drive systems

As mentioned in section 2.1, the other unique feature of TCV is the high power density of its heating system.

### 2.2.1 NBH: Neutral Beam Heating

Auxiliary heating capabilities of TCV come partly from two neutral beam injectors (NBI), totaling a maximum of 2.3 MW additional power [Karpushov et al. 2023]. The first NBI injects up to 1.3 MW of 30 keV particles (D or H) and is mainly used for heating purposes. The second NBI injects faster particles, between 50 and 60 keV, up to 1 MW, and is also used for heating.

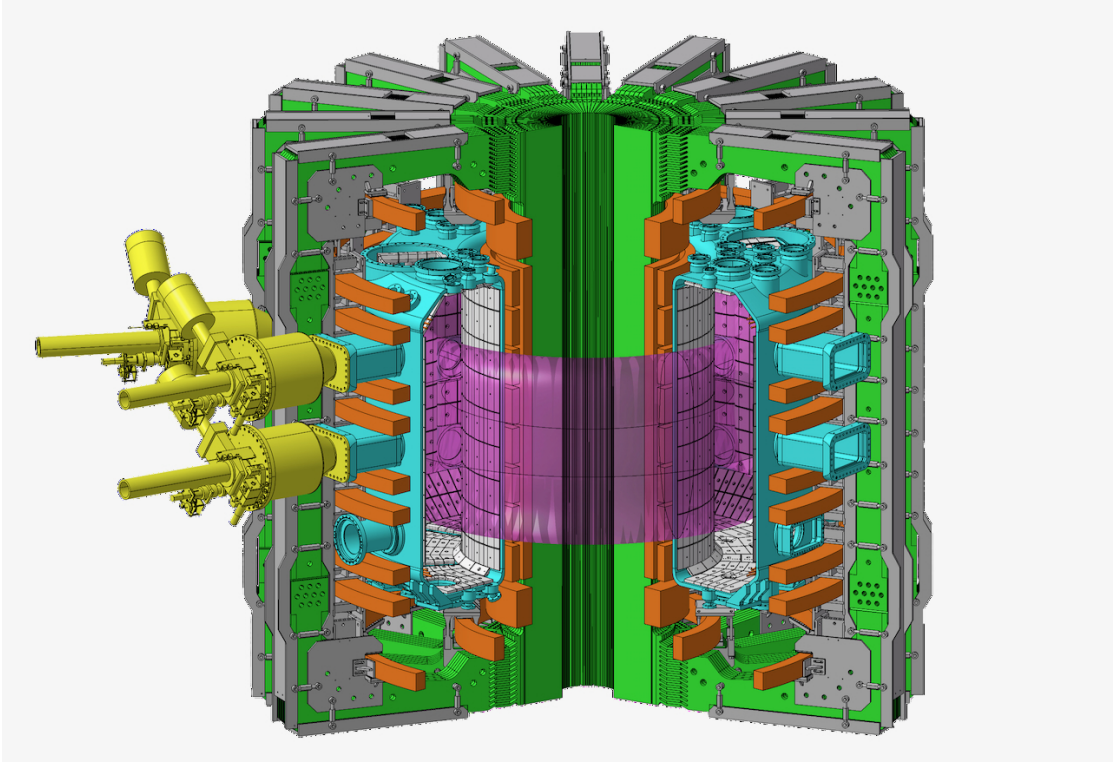


Figure 2.2: 3D model of TCV, showing the vacuum vessel in cyan and the carbon tiles inside the vessel in light gray, the toroidal field coils in green, the poloidal field and Ohmic coils in orange and the Electron-Cyclotron wave low-field side launchers in yellow. The plasma is drawn for illustration in light purple. *Courtesy of M. Toussaint.*

This second beam is especially suited for fast ion studies. As shown in figure 2.3, the two beams face each other, leading to a non-negligible beam-beam D-D fusion interaction. Combined with the increased beam-plasma interaction of the second beam, this effect increases the neutron emission rate by ten times with respect to single-beam operation, which requires the development of additional neutron shielding in TCV [Weisen et al. 2023].

Neutral beam heating mainly acts on ions: fast neutrals ionized within the plasma, fueling the plasma with fast ions, which then exchange momentum with bulk ions and electrons through collisions. The collision drag of bulk electrons by fast ions implies that, in standard single-beam operation, both the ion and electron temperatures increase and usually are of the same order.

### 2.2.2 ECRH/CD: Electron-Cyclotron Resonant Heating and Current Drive

TCV is equipped with a total of 6 gyrotrons, which generate up to 4.5 MW of microwave power. Two of these gyrotrons, G1 and G2, are 82.7 GHz 750 kW gyrotrons, which aim to launch X-polarized Electron-Cyclotron (EC) waves from the low-field side, that will be absorbed at the second cyclotron harmonic location within the plasma (later referred to as X2 EC beams).



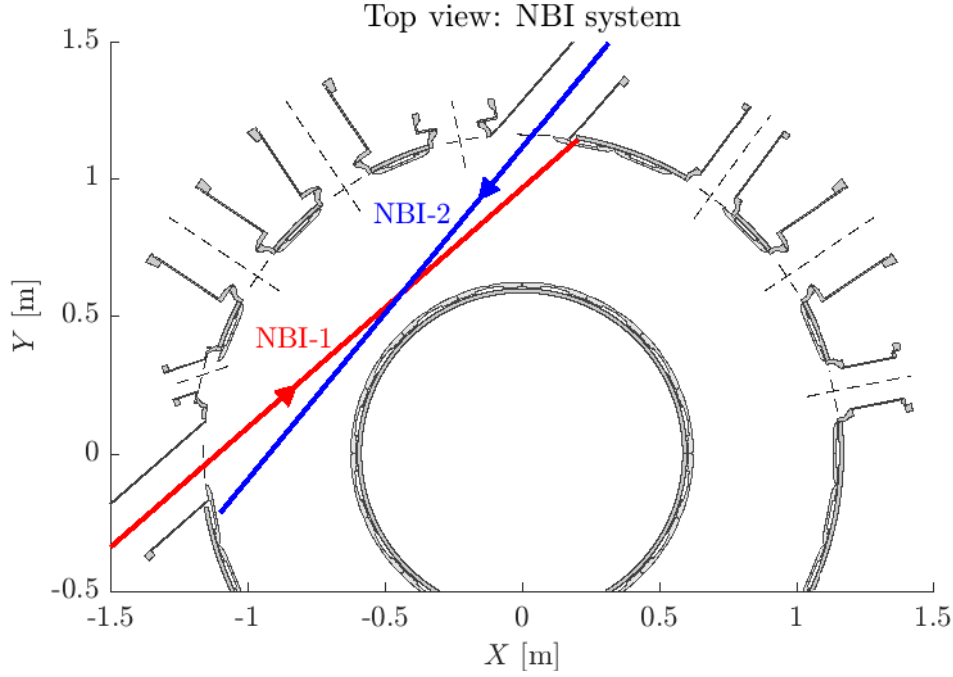


Figure 2.3: Top view of the neutral beam injection system of TCV. The path of the first beam (30 keV, 1.3 MW) is shown in red and the path of the second beam (50-60 keV, 1MW) is shown in blue.

G1 and G2 are the only available gyrotrons with proven, safe, power-modulation capabilities. A second pair of gyrotrons, G7 and G9, are 118 GHz 500 kW gyrotrons, generating EC waves that will be absorbed at the third electron cyclotron harmonic location in the plasma (later referred to as X3 EC beams). Finally, a set of two dual-frequency X2/X3 gyrotrons have been installed in TCV, with 84/126 GHz frequency for a 900/1000 kW power respectively. The EC beam each generates can be injected either from the low-field side or from the top of the machine, directly along the X3 resonance surface [Hogge et al. 2020].

Waveguides are used to transfer the EC waves from the gyrotrons to the launchers, which consists of a set of mirrors, with two degrees of freedom in their movement to allow targeting specific locations for the wave absorption. In total, 6 launchers (L1, L2, L4, L5, L10 and L11) are available, as shown in figure 2.4. The possible routing between gyrotrons and launchers is described in table 2.1. The low-field side launchers, which have been used in the experiments performed for this thesis (see chapters 4 and 5), consist of three fixed mirrors and one steerable mirror at the end of the transmission line, which can be tilted to tune the angle between the beam and the horizontal axis in the launcher frame, so-called the launching poloidal angle  $\theta_L$ . The whole launcher can turn on itself by an angle called the launcher toroidal angle  $\phi_L$ . A detailed schematics of these low-field side launchers is given in appendix A, as well as the conversions to other angular systems.

EC heating increases the electron temperature (see section 1.3), but contrary to the fast ions transferring momentum to the bulk electrons through collisions when using neutral beam heating, the collisional momentum transfer of fast electrons to bulk ions is negligible. The

latter therefore can only be heated by bulk electrons through collisions, but this equipartition is rather weak at the low densities required for X2 heating; thus, the ion temperature does not increase with X2 EC waves.

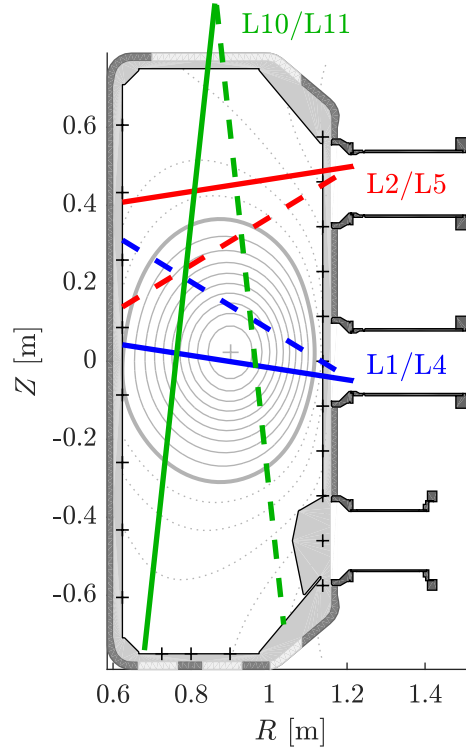


Figure 2.4: TCV EC launching system.

Table 2.1: Possible routing between gyrotrons (G1 to G11) and launchers (L1 to L11).

	L1	L2	L4	L5	L10	L11
G1	✓					
G2		✓				
G7				✓		
G9			✓			
G10				✓	✓	
G11			✓			✓

## 2.3 Main plasma diagnostics

Since the ion plasma temperature in the core of TCV is of the order of 1 keV (approximately 12 millions Kelvins), probing the plasma core relies mainly on spectroscopic diagnostics. These diagnostics can be separated into two main categories: active spectroscopy, using externally launched electro-magnetic radiations, and passive spectroscopy measuring the electro-magnetic radiations emitted by the plasma itself.

### 2.3.1 TS: the Thomson Scattering diagnostic

In TCV, the main diagnostic to measure the electron density and temperature profiles is the incoherent Thomson Scattering (TS) diagnostic [Blanchard et al. 2019; Arnichand et al. 2019]. This diagnostic consists of an active spectroscopic system, using three Nd:YAG infrared lasers of wavelength  $1.06 \mu\text{m}$ . These laser are launched vertically through the plasma, from the bottom of the machine, with a repetition rate of 20 Hz each. They can be launched sequentially to reach a 60 Hz sampling rate over the whole plasma discharge. It is also possible to use custom trigger times to increase the temporal resolution for a specific time slice of the discharge.

The electrons along the laser path are accelerated by the oscillations of the laser electric field, leading to the incoherent scattering of the electro-magnetic radiation. A part of the scattered light, which travels in all directions, is measured by a set of optical fibers installed on the low-field side of the machine, carrying the light to spectrometers where the measured spectra are analyzed. The broadening of the scattered light spectrum is a proxy for the electron temperature, while the total scattered power relates to the electron density. This means that absolute calibration of the spectrometers is necessary to infer the electron density. Such calibrations are performed regularly in TCV, using dedicated discharges. The spectrometer lines of sight are illustrated in figure 2.5, as well as the probed plasma volumes, which delineate the laser path.

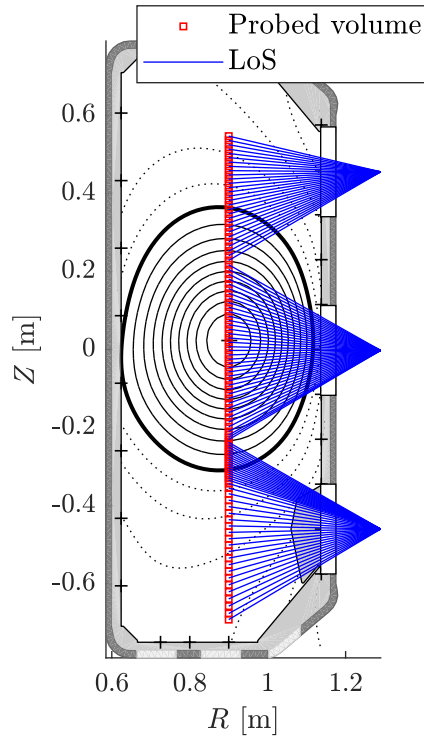


Figure 2.5: Poloidal view of lines of sight (LoS) of the Thomson Scattering diagnostic, with the associated probed volumes corresponding to the laser path.

### 2.3.2 CXRS: the Charge eXchange Recombination Spectroscopy

The Charge eXchange Recombination Spectroscopy (CXRS) diagnostic installed in TCV is an active spectroscopy system and is the main diagnostic to infer ion properties [Marini 2017]. It uses a low-power neutral beam injector as an actuator, the so-called Diagnostic Neutral Beam Injector (DNBI), inducing charge exchange recombination between the intrinsic carbon VI+ impurities and the injected neutral hydrogen along the beam path. The charge exchange recombination process consists of the transfer of an electron from the neutral to the target ion.

The target ion is then in an excited state, and relaxes to the ground state by emitting photons. The photons are emitted following a chain of characteristic emission lines and the CXRS diagnostic looks at one of these specific emission lines. From the spectral analysis of the measured light, it is possible to infer the carbon VI+ density and temperature profiles, as well as the ion toroidal velocity. It is assumed that all ion species share the same temperature. Using the independent electron density measurement, it is therefore possible to estimate the main ion density and a lower bound for the effective charge, neglecting the population of impurities other than carbon VI+.

The CXRS consists of three main systems, looking at the beam path on the low-field side, both horizontally and vertically, and looking at the beam path on the high-field side. These systems, as well as the DNBI path, are illustrated in figure 2.6.

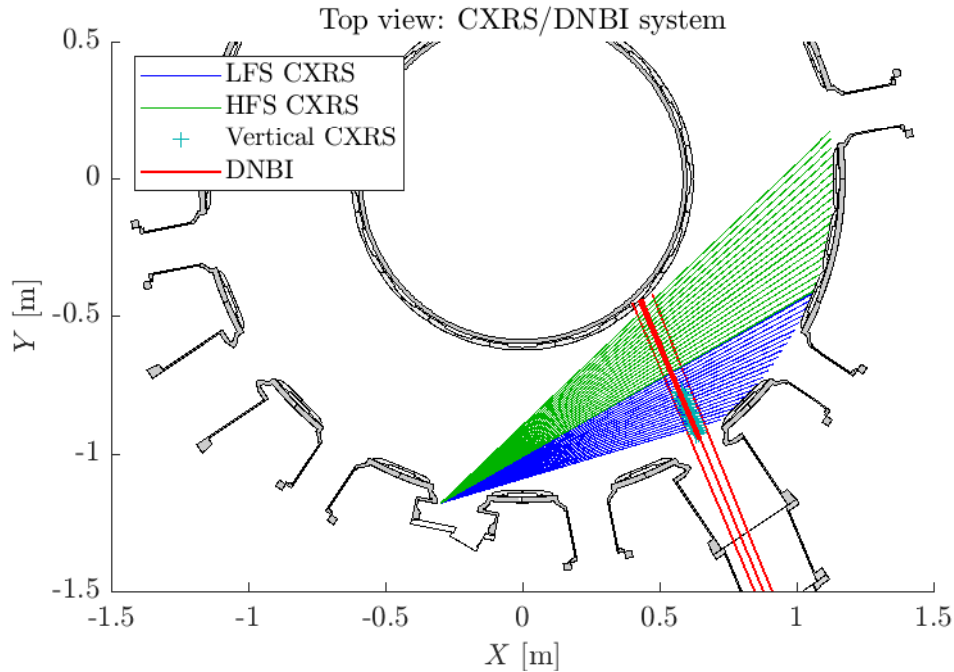


Figure 2.6: Top view of the different CXRS systems installed in TCV, working with the DNBI.

### 2.3.3 Passive spectroscopy: measuring the whole electromagnetic spectrum

TCV is equipped with a set of passive spectroscopy diagnostics, covering almost the whole electro-magnetic radiation spectrum, from microwaves to gamma rays. These different diagnostics serve different purposes, from measuring the heat flux on the tokamak tiles to estimating the suprathermal electron Bremsstrahlung. A summary is offered in table 2.2. In particular, the hard X-ray spectrometer (HXRS) is described in detail in section 2.5, as it is the main diagnostic used throughout the present thesis.

Another diagnostic that has been used for this work is the XTe diagnostic, which infers the central electron temperature from soft X-ray measurements. The XTe is made of 4 vertically viewing photodiodes, each shielded differently. This allows one to use a total of 6 different channel-to-channel ratios to estimate the central electron temperature, with a 10 kHz sampling rate. This fast sampling rate of the electron temperature is the main advantage of the XTe over the TS diagnostic. However, it lacks radial resolution and the estimation of the temperature is based on a model assuming a Maxwellian electron distribution. This leads to a potential error in the estimation of the absolute temperature value when heating the plasma with EC waves.

Table 2.2: Summary of the electro-magnetic spectrum covering by TCV spectroscopic diagnostics.

Radiation type	Frequency	Wavelength	Energy	TCV diagnostics	Measured physical properties
Gamma rays	$\geq 30$ EHz	$\leq 10$ pm	$\geq 124$ keV	LaBrDoRE (planned), PMTX	Runaway electron Bremsstrahlung or collisions with the walls
Hard X-rays	3 EHz - 30 EHz	100 pm - 10 pm	12.4 keV - 124 keV	HXRS, PMTX	Suprathermal electron Bremsstrahlung (in- and ex-vessel)
Soft X-rays	30 PHz - 3 EHz	10 nm - 100 pm	124 eV - 12.4 keV	XTe, RADCAM (SXR)	Thermal electron Bremsstrahlung, electron temperature
Ultraviolet	790 THz - 30 PHz	380 nm - 10 nm	2.75 eV - 124 eV	RADCAM (AXUV)	Total radiated power
Visible	400 THz - 790 THz	750 nm - 380 nm	1.98 eV - 2.75 eV	DSS, GPI, MANTIS, FASTCAM	Impurity content, divertor chemical content, edge density turbulence
Infrared	300 GHz - 400 THz	1 mm - 750 nm	1.24 meV - 1.98 eV	MANTIS, VIR/HIR	Runaway electron synchrotron emission, power deposition on TCV tiles
Microwaves	3 GHz - 300 GHz	100 mm - 1 mm	12.4 $\mu$ eV - 1.24 meV	VECE, CECE	Thermal and supra-thermal electron-cyclotron emission, electron temperature and fluctuations

### 2.3.4 Magnetic probes and equilibrium reconstruction

In TCV, magnetic pick-up coils are used to measure the variation of the poloidal component of the magnetic flux, tangential to the vacuum vessel, with a default 10 kHz sampling rate. These time variations of magnetic flux induce a voltage within the pick-up coils, which is measured. The magnetic measurement system consists of 4 poloidal arrays within the vacuum vessel, each made of 38 evenly spaced magnetic probes, with the equipped poloidal sectors being spaced by  $90^\circ$ . Another set of 6 toroidal arrays is also available within the vacuum vessel, each made of 16 or 8 magnetic probes. Finally, poloidal flux loops are wound outside the vacuum vessel, paired with the poloidal magnetic probes, measuring the poloidal magnetic flux with a 2 kHz sampling rate.

The flux loop probes are used to estimate the poloidal magnetic flux and its time derivatives, which produces a measurement of the loop voltage at the plasma edge. On the other hand, the magnetic probes are used to control the plasma shape in real time. By integration of the signal from a given poloidal array of magnetic probes, it is also possible to estimate the total plasma current.

These measurements are used as input to the equilibrium reconstruction code LIUQE [Moret et al. 2015]. They define the boundary conditions for the equilibrium reconstruction, which provides the 2D poloidal magnetic flux inside the vacuum vessel, the plasma safety factor, elongation, triangularity, etc. The principle of the equilibrium reconstruction is, in the cylindrical basis  $(R, Z, \phi)$ , to find a function  $\psi_P(R, Z)$  for the poloidal magnetic flux which satisfies the ideal magnetohydrodynamic pressure balance. This problem takes the form of the Grad-Shafranov equation

$$\Delta^* \psi_P = -4\pi^2 \mu_0 R \left( R \frac{\partial p}{\partial \psi_P} - \frac{T}{\mu_0 R} \frac{\partial T}{\partial \psi_P} \right) \quad (2.1)$$

where  $p(\psi_P)$  is the plasma pressure function and  $T(\psi_P) = RB_\phi(\psi_P)$  is the current function with  $B_\phi$  the toroidal magnetic field. The functions  $p$  and  $T$  are arbitrary functions that also need to be identified, constrained by the experimental data. The modified Laplacian reads

$$\Delta^* = R \frac{\partial}{\partial R} \left( R \frac{\partial}{\partial R} \right) + \left( \frac{\partial}{\partial Z} \right)^2. \quad (2.2)$$

## 2.4 Fluctuation diagnostics

### 2.4.1 Brief introduction to the main turbulence modes in tokamaks

The hot plasma in tokamaks is usually not a quiet medium, and turbulence of magnetic field or plasma pressure tends to arise naturally due, for instance, to a destabilizing combination of charged particle drifts and local gradients. A diverse zoology of electrostatic and electromagnetic turbulent modes co-exists, for all sorts of wavelengths and frequencies. Turbulence has a significant impact at many levels of the physical interpretation of experimental and numerical

results (e.g on Electron-Cyclotron beam scattering or on particle transport), and it is therefore important to be able to characterize it.

The main modes responsible for turbulent transport in the core of tokamak plasmas result from electrostatic drift-wave microinstabilities [Horton 1999; Garbet et al. 2004a]. The principle of drift-wave generation and propagation is illustrated for electrons in figure 2.7, in a simplified case excluding magnetic field gradient and curvature effects. The pressure gradient, driven either by the density or temperature gradient, or both, generates a particle drift, the so-called diamagnetic drift. Generally speaking, for a particle of species  $s$  with charge  $q_s$ , the diamagnetic drift velocity reads

$$\mathbf{v}_{d,F_s} = \frac{1}{q_s} \frac{\mathbf{F}_s \times \mathbf{B}}{B^2} \quad (2.3)$$

with  $\mathbf{F}_s$  the force responsible for the drift and  $B$  the magnetic field, meaning that the drift direction is perpendicular to both the drive force and the magnetic field directions. In the particular case of pressure-gradient-driven diamagnetic drifts,  $\mathbf{F}_s = -\nabla p_s / n_s$  with  $\nabla p_s$  the pressure gradient and  $n_s$  the particle density. As shown in figure 2.7.a), in non-homogeneous plasmas, the diamagnetic drift results from the finite averaged guiding center velocity at a given position. These drifts are in opposite directions for ions and electrons, and therefore create a charge separation. As described in figure 2.7.b), this means that a perturbation of the electric potential  $\delta\phi_E$  is associated to a given electron density perturbation propagating in the  $\mathbf{k}_d$  direction. This electric field perturbation in turn induces an  $\mathbf{E} \times \mathbf{B}$  drift that sustains the electron density perturbation, which propagates in the diamagnetic velocity direction  $\mathbf{v}_{d,e} = \nabla p_e \times \mathbf{B} / (en_e B^2)$ .

The same principles apply in tokamaks, with the addition of  $\nabla B$ -driven drifts. On the high-field side,  $\nabla B$  and  $\nabla p$  are in opposite directions, and the perturbation is stabilized, whereas on the low-field side, the magnetic field gradient destabilizes the perturbation which then grows before it saturates due to various saturation mechanisms, such as the turbulence shearing by  $\mathbf{E} \times \mathbf{B}$  flows [Villard et al. 2002]. Modes that are driven by the ion temperature gradients are simply called Ion Temperature Gradient modes (ITG), while electron-temperature-gradient-driven modes are called Electron Temperature Gradient modes (ETG). The typical fluctuation correlation length for ITG modes is of the order of the sonic Larmor radius, while it is of the order of the electron Larmor radius for ETG, making ETG much more challenging to experimentally characterize or to simulate with gyro-kinetic codes because of the required high spatial and temporal resolution in both cases, the main constraints being the intrinsic diagnostic limitations and the numerical cost respectively.

The other type of microinstabilities that dominates in tokamak plasma is the Trapped Electron Mode (TEM), which is driven unstable by the resonant interaction between the bouncing motion of trapped electrons and an electrostatic perturbation. These modes are also mainly localized on the low-field side, as it is where the trapping of electrons mainly occurs, due to the non-homogeneous magnetic field. The characteristic fluctuation correlation length of TEM

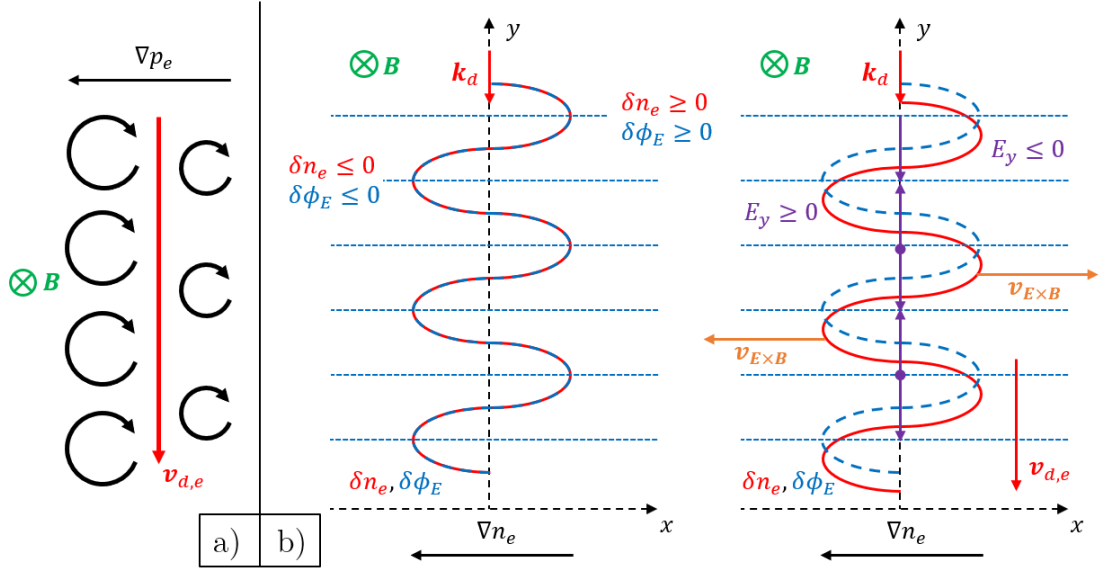


Figure 2.7: Illustration of the drift wave generation mechanism from the electron pressure gradient  $\nabla p_e$ , for a homogeneous background magnetic field *a*), and principles of drift wave propagation, from an initial density perturbation  $\delta n_e$  propagating in the  $\mathbf{k}_d$  direction and the associated electric potential perturbation  $\delta\phi_E$  *b*). The perturbation  $\delta\phi_E$  induces an electric field  $E_y$  with the associated cross-field drift, sustaining the density perturbation propagating in the electron diamagnetic direction  $\mathbf{v}_{d,e} = \nabla p_e \times \mathbf{B} / (en_e B^2)$ .

scales similarly to the one of the ITG modes. A detailed introduction to these microinstabilities is given in chapter 2.6 of [Merlo 2016].

### 2.4.2 TPCI: the Tangential Phase Contrast Imaging diagnostic

In TCV, core and inner edge turbulence properties can be measured by Tangential Phase Contrast Imaging (TPCI) [Marinoni et al. 2006]. A 7-cm wide CO<sub>2</sub> infrared laser ( $\lambda_0 = 10.6 \mu\text{m}$ ) beam is sent through the plasma, propagating in a straight line with a large toroidal component. Density fluctuations perpendicular to the beam propagation scatter the laser light, leading to perturbations of its phase. The scattered and unscattered components of the light are processed by an internal-reference interferometer: the beam is focused on a reflective phase plate introducing a delay in its unscattered component by means of a groove placed on the focal point (the scattered light is focused away from the focal point and thus not on the groove) and both components are then imaged onto a matrix of photodiodes, generating a time-dependent interference pattern. This time-dependent signal is proportional to the fluctuating phase shift of the scattered beam, and so to the line-integrated density fluctuations. A rotatable mask placed on the focal plane allows for a selection of the probed wave-vector. Since turbulent eddies are mostly field-aligned and the measurement is only sensitive to fluctuations perpendicular to the laser beam propagation, the filtered line-integrated scattered signal actually corresponds to a short path over which the wave vector is perpendicular to both the laser beam and the plasma magnetic field. The mask thus permits selecting the



probed location along the laser beam (the farther away it probes from the point of tangency to the magnetic field, the longer the integrated line of sight). The currently installed TPCI diagnostic is able to resolve ion scale turbulence (from 7.0 cm down to 0.1 cm), but an upgrade is underway to resolve electron scale turbulence. An example of a TPCI configuration is shown in the left-hand plot of figure 4.2.

### 2.4.3 CECE: the Correlation Electron-Cyclotron Emission diagnostic

The Correlation Electron-Cyclotron Emission (CECE) diagnostic is a powerful tool to measure electron temperature fluctuations in TCV [Fontana et al. 2017]. It consists of a set of antennas (two fixed and one steerable antennas on the low field side) measuring the microwaves emitted by the cyclotron motion of electrons, which is related to the electron temperature. Different radiometer channels corresponding to different frequencies are available, close enough so that they probe the same fluctuating structure but at different spatial locations. These channels can be coupled with only one antenna at the time. The cross-correlation analysis between the different channels reduces the noise by suppressing the uncorrelated part, allowing the measurement to resolve low electron temperature fluctuations ( $\leq 0.5\%$ ) and permitting an estimate of the radial correlation length of fluctuating structures ( $k_\theta = 0.3\text{ cm}^{-1}$  for the low field side antenna used in the present study, but up to  $k_\theta = 1.12\text{ cm}^{-1}$  in optimal conditions, using the steerable antenna). However, the use of the CECE diagnostic is limited in the case of high power EC wave coupling to the plasma. Indeed, microwaves from the EC beam itself are in the same range of frequencies as microwaves from cyclotron emission of the plasma electrons, thus polluting the measured signal. The configuration of the CECE antennas can nonetheless be optimized to maximize the signal-to-noise ratio. An example of CECE configuration is presented in the right-hand plot of figure 4.2.

### 2.4.4 SPR: the Short Pulse Reflectometer

In TCV, the profile of the root-mean-square (RMS) relative density fluctuation level  $[\delta n_e / \bar{n}_e]_{RMS}$  be measured by Short-Pulse Reflectometry (SPR) [Molina Cabrera et al. 2019]. The SPR diagnostic sends short pulses or wave-trains ( $\leq 1\text{ ns}$ ) at varying microwave frequencies (50 GHz to 75 GHz), with a high repetition rate and with either O- or X-polarization. When the microwave pulse reaches the cutoff in the plasma, it bounces back to the radiometer where it is measured, with a sampling rate of 32 Gsamples/s. The statistical properties of the pulse delay are analyzed to infer information about the plasma density fluctuations: in particular, the RMS fluctuation level can be inferred from the RMS value of the delay [Krutkin et al. 2023]. For O-mode waves, the cutoff depends only on the plasma density, so the analysis of the reflected pulse shape and delay gives direct information on the position of a given density layer. X-mode polarization is used to probe the edge of the plasma as it is reflected at lower plasma density than O-mode. However, the analysis is more challenging as the cutoff for X-mode depends on both the plasma density and the magnetic field. An example of the plasma area probed by the SPR is shown in figure 5.1.

## 2.5 HXRS: the Hard X-Ray Spectrometer

### 2.5.1 Measuring Hard X-Rays emitted through electron Bremsstrahlung

The absorption of externally launched waves, such as Electron-Cyclotron or Lower-Hybrid waves, by tokamak plasmas is one of the main tools to increase its temperature and to drive current. In particular, Electron-Cyclotron waves (frequency of the order of 100 GHz) are used as they can target accurately a narrow region of the electron distribution in real and velocity space, allowing for accurate heating and current drive for complex plasma scenario development or local plasma instability mitigation. The wave-plasma interaction results in the generation of a suprathermal tail in the electron distribution. Those fast electrons emit a Hard X-Ray (HXR) continuum by Bremsstrahlung, with typical energies ranging from 10 keV to 1 MeV. Fast electron Bremsstrahlung diagnostics are thus a powerful tool to infer the non-thermal electron distribution by experimentally constraining numerical simulations.

Measuring Hard X-Rays in a tokamak environment is particularly challenging, especially because of the strong magnetic fields (around 1.5 T in TCV and 3.45 T in JET) and high-energy neutron flux. Different techniques have been developed throughout the years. A first class of HXR diagnostics are scintillators, absorbing incoming photons and re-emitting photons by fluorescence. Usually, a photo-multiplier is added to increase the signal output. Different technologies have been implemented in tokamaks, such as bismuth germanate  $\text{Bi}_4\text{Ge}_4\text{O}_{12}$  (BGO) scintillators in DIII-D [James et al. 2010, 2011] and JET [Plyusnin et al. 2019] or sodium iodide (NaI) scintillators in J-TEXT [Ma et al. 2017]. These scintillators are now progressively being replaced by new lanthanum(III) bromide ( $\text{LaBr}_3$ ) such as in FT-2 [Shevelev et al. 2016], JET [Rigamonti et al. 2018; Plyusnin et al. 2019], ASDEX [Nocente et al. 2018], EAST [Zhou et al. 2019] and Aditiya [Purohit et al. 2020]. In DIII-D, a novel cerium doped yttrium aluminum perovskite (YAP:Ce) scintillator has been recently developed [Dal Molin et al. 2021]. Scintillators are mainly used for runaway electron studies (energies higher than 1 MeV).

A second class of HXR spectrometer is based on the use of compact solid-state photodiodes, mainly dedicated to suprathermal electron studies (energies between 10 keV and 1 MeV). In particular, cadmium telluride (CdTe) photodiodes have been used in HXR cameras, starting at Tore Supra [Peysson and Imbeaux 1999; Peysson et al. 2001] (recently updated for WEST [Barbui et al. 2021]) and spreading to other tokamaks such as TCV [Gnesin et al. 2008] and more recently J-TEXT [Yang et al. 2018], EAST [Cao et al. 2020] and HL-2A [Zhang et al. 2021]. The main advantages of CdTe detectors over scintillators are their compactness and their reduced sensitivity to neutrons (due to the small size of each diode, of the order of  $1\text{ cm}^3$ ) and indifference to magnetic fields, thus requiring less shielding.

However, spectral analysis for very high photon energy ( $\geq 1\text{ MeV}$ ) is challenging for every type of materials and detectors. In particular, this type of CdTe diodes cannot be used for quantitative runaway studies, as it relies on photoelectric effects, which is no longer the dominant physical effect at high impinging photon energy (in CdTe, Compton scattering

becomes dominant over photoelectric effect for energies  $\geq 300$  keV).

### 2.5.2 General description of the spectrometer

The TCV HXRS is made of 4 distinct cameras totaling 101 (97 + 4 blind detectors) CdTe photodiodes. Each camera is uniquely designed to take the least space while fitting on its TCV port, and consists of an array of 24 (or 25) photodiodes of  $2 \times 2 \times 2$  mm size, manufactured by the Eurorad company. The different lines of sight (1 per diode) are defined by a tungsten fan-shaped collimator with uniform angular spacing [Gnesin et al. 2008]. As shown in figure 2.8, the full set of cameras covers a complete poloidal section of the plasma, enabling 2D tomographic studies. The spacing between the different lines of sight on the top-bottom and left-right midplane axes is  $3 \pm 2$  cm on average. The four cameras are labeled C2 (top), C4 (upper Low-Field Side), C5 (equatorial Low-Field Side) and C7 (bottom). Both C4 and C5 can be turned by  $90^\circ$  to cover a toroidal view. A picture of a camera (here C2) and its collimator is shown in figure 2.9. The final assembly is shielded by a 2-cm thick tungsten shield to ensure that no photon from outside the lines of sight will reach the diodes. The properties of CdTe diodes are discussed in section 2.5.3.

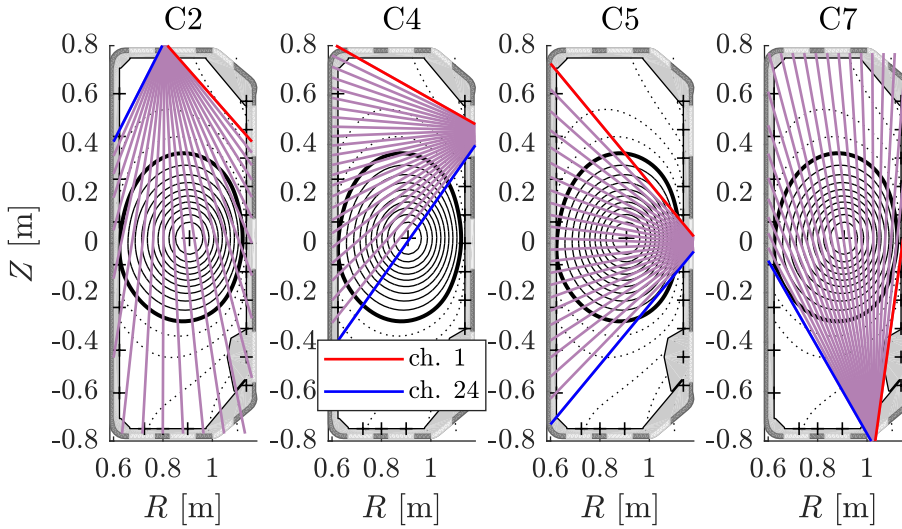


Figure 2.8: Poloidal view of the TCV vessel, showing the TCV HXRS lines of sight for each camera. An example of a TCV plasma equilibrium (#74304) is shown as well. Channel 1 is indicated in red and channel 24 in blue for each camera.

The initial design of the HXRS [Gnesin et al. 2008] was directly inspired by the Tore Supra spectrometer [Peysson et al. 2001], which had been lent to TCV in the past to perform experiments with Electron-Cyclotron waves [Coda et al. 2003a]. The main differences between the TCV and Tore Supra systems are the more flexible individual-channel collimation of the former and the fact that the TCV HXRS uses digital pulse processing, providing a greater flexibility and an easier optimization in the post-processing method compared to fast, but fixed, analog

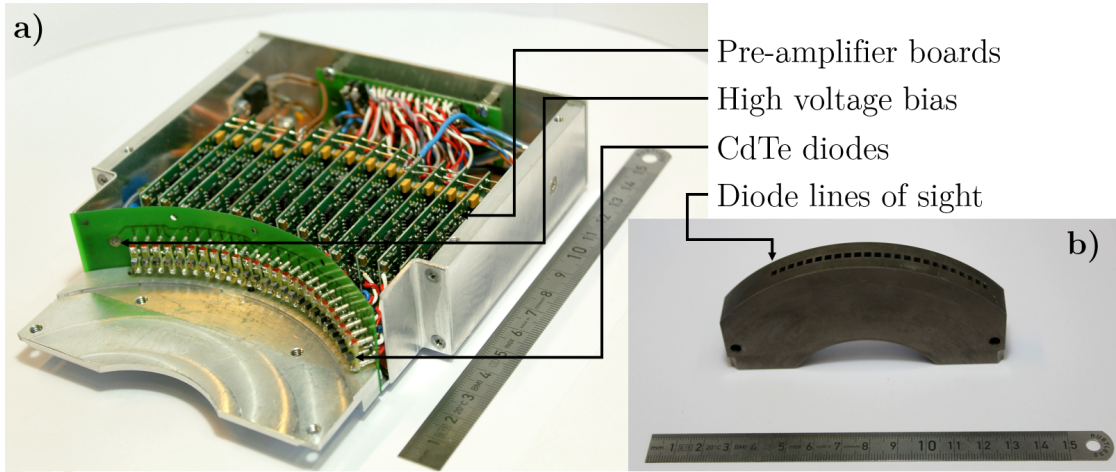


Figure 2.9: *a)* Picture of the inside casing of the C2 HXRS camera, *b)* picture of the tungsten collimator of the C2 HXRS camera, defining a fan-shape array of line of sights

pulse-processing [Kamleitner et al. 2014].

The complete acquisition chain is illustrated in figure 2.10. Photodiodes are biased to collect the electric charge generated from photoelectric interaction, thus generating an electric current. The signal is integrated, shaped and amplified by the embedded pre-amplification boards before being sent to the analog-to-digital converter (ADC) via the bitbus unit, which also provides electrical power to the camera and a clock and trigger to the ADC. Then, the raw voltage time traces are stored in a dedicated computer. Line-integrated raw data can be accessed and treated afterwards, using digital pulse processing and pulse height analysis (PHA) [Kamleitner et al. 2014], sorting pulses by amplitude, to create photon energy spectra. This post-treatment consists of analyzing and counting multiple single-detection events, rather than analyzing a continuous signal. The signal processing chain is further detailed in section 2.5.4. It is also possible to use tomographic algorithms to deconvolve energy and position and recover 2D HXR emission profiles, which is discussed in section 2.5.5

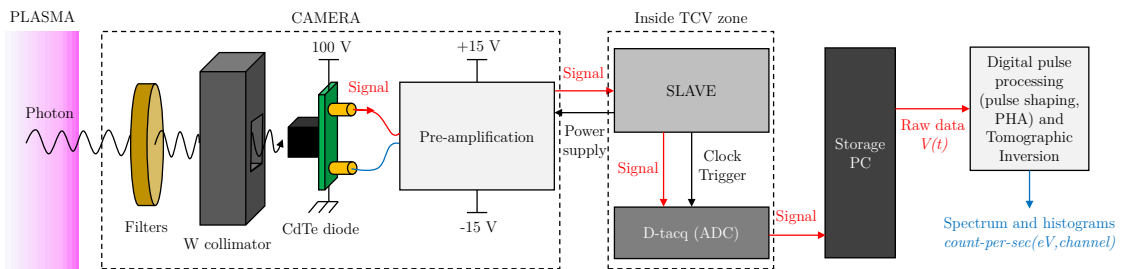


Figure 2.10: Illustration of the TCV HXRS signal acquisition and treatment chain.

### 2.5.3 Cadmium-telluride photodiodes

Cadmium telluride photodiodes are solid-state semiconductor crystals of the II-VI category, forming a p-n junction. They are used both in research and in industry for medical applications

(X ray imaging), astrophysics and photo-voltaic solar cells. They have been brought to the tokamak world by Tore Supra, enabling better understanding of the suprathermal electron physics, measuring HXR from electron Bremsstrahlung emission, related to Lower-Hybrid wave heating and current drive [Peysson and Imbeaux 1999].

Photons can interact in different ways within a semiconductor depending on their energy. They can undergo complete absorption (photoelectric effect), creating a photo-electron of kinetic energy equal to the photon energy, minus the binding energy of the electron. This photo-electron almost instantaneously loses its energy by Coulomb collisions within the semiconductor lattice, creating many hole-electron pairs, and so a charge, that can be collected by applying an electric field to the semiconductor. This principle is illustrated in figure 2.11.

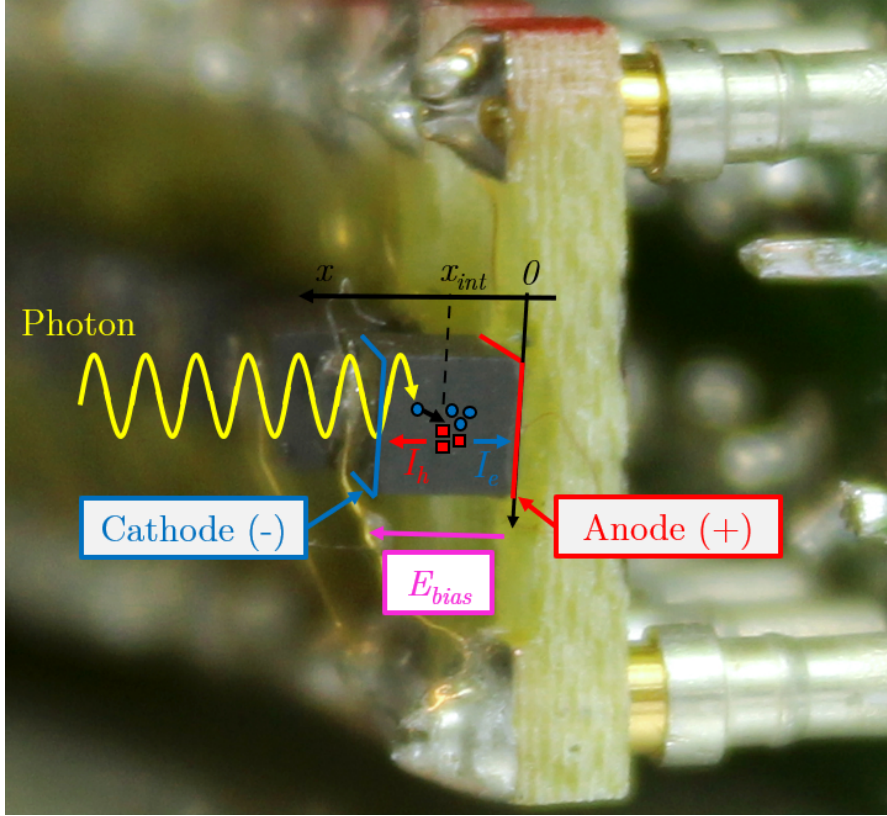


Figure 2.11: Picture of a CdTe photo-diode mounted on a HXR camera. The electron current (flow of particles) is labeled  $I_e$ , the hole current is labeled  $I_h$ , the bias electric field is labeled  $E_{bias}$  and  $x_{int}$  is the distance of the interaction location from the anode.

The collected charge  $Q(t)$  can be expressed from the total current  $I(t)$  generated by the charge carrier displacement, taking into account both electron and hole contributions. The current for a given charge  $q$  before collection can be expressed as follows [Knoll 2000], assuming a pure photoelectric effect in a detector of length  $L_{det}$  and that all the charge carriers (of density

$n_0$ ) are instantaneously generated at the same location in the detector

$$I_q = en_0 A_{det} \mu_q E_{bias} = q \frac{E_\gamma}{\epsilon_p} \frac{\mu_q E_{bias}}{L_{det}} \quad (2.4)$$

where  $A_{det}$  is the cross-section of the detector,  $\epsilon_p$  is the energy required to generate a hole-electron pair,  $E_\gamma$  is the incoming photon energy,  $\mu_q$  the charge mobility in the semiconductor and  $E_{bias}$  the bias electric field. Thus, the total current generated is expressed as follow

$$\frac{I(t)}{E_\gamma} = \begin{cases} (I_e + I_h)/E_\gamma & \text{if } t \leq \tau_{D,e} \\ I_h/E_\gamma & \text{if } \tau_{D,e} \leq t \leq \tau_{D,h} \\ 0 & \text{if } t \geq \tau_{D,h} \end{cases} \quad (2.5)$$

where  $\tau_{D,e}$  and  $\tau_{D,h}$  are respectively the electron ( $e$ ) and hole ( $h$ ) charge collection times, the so-called charge drift times, in the semiconductor (see figure 2.13), and assuming that  $\tau_{D,h} \leq \tau_{D,e}$ . This is the time it takes for a given charge  $q$  to reach the respective electrode (cathode for holes and anode for electrons), depending on the charge mobility  $\mu_q$  in the semiconductor, the bias voltage applied between the electrodes  $V_{bias}$  (or electric field  $E_{bias}$ ) and the distance from the relevant electrode to the location where the photon is absorbed  $x_{abs}$ . It is given by  $\tau_{D,q} = x_{abs}/(\mu_q E_{bias})$ . In CdTe, complete charge collection is limited by the longer hole collection time. On average, for a 2-mm-long CdTe diode biased with 100 V, the hole collection time is  $\langle \tau_{D,h} \rangle_x = 2 \mu\text{s}$ , meaning that a maximum of  $f_{i,max} = 500 \text{ kHz}$  impinging photon frequency is allowed to avoid pile-up. The TCV HXRS is also equipped with selectable filters, used both as high- and low-cut energy filters, to help reduce the impinging photon frequency, depending on plasma scenario. Two wheels with 6 positions each are mounted in front of each camera, totaling 36 configurations. The filter positions are described in table 2.3. An example of how filters affect the detection efficiency is pictured in figure 2.12.

Table 2.3: TCV HXRS selectable filter positions

Position	Wheel A	Wheel B
1	-	-
2	0.15 mm (Al)	0.03 mm (Al)
3	1.50 mm (Al)	0.60 mm (Al)
4	0.30 mm (Fe)	0.15 mm (Fe)
5	0.80 mm (Fe)	0.50 mm (Fe)
6	2.50 mm (Fe)	1.50 mm (Fe)

By integration, the total generated charge (after a time  $t = \max(\tau_{D,e}, \tau_{D,h})$ ) in the semiconductor by a photon is  $I_e \tau_{D,e} + I_h \tau_{D,h} = en_0 A_{det} L_{det} = e E_\gamma / \epsilon_p$ , so is directly proportional to the energy of the incoming photon  $E_\gamma$ . To measure the charge, the output CdTe current (or the associated proportional voltage) has to be integrated. This is done using analog circuits and described in section 2.5.4.

However, the charge collection may be incomplete due to charge trapping within the semiconductor. This is characterized by the charge mean free path before trapping, or trapping length,



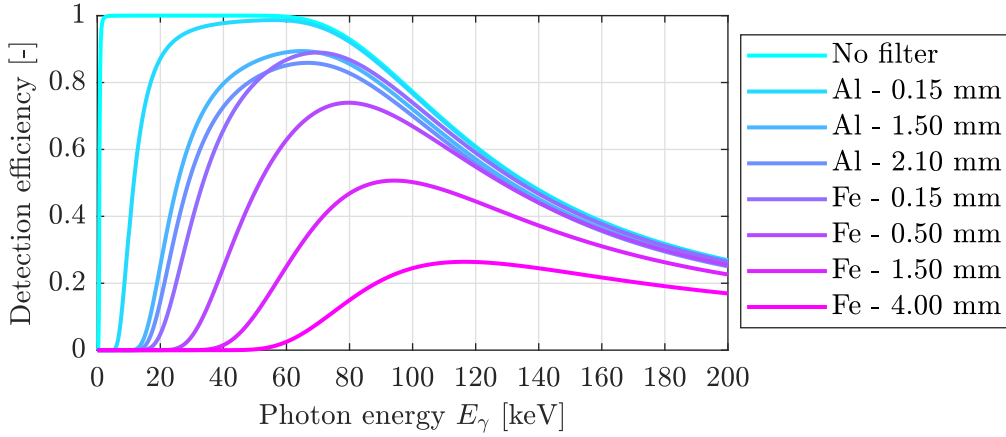


Figure 2.12: Example of CdTe detection efficiency as a function of photon energy, computed for different filter materials and thicknesses, not taking into account the Beryllium window between the vacuum vessel and the camera.

$\lambda_{T,q}$  (see figure 2.13). If the trapping length is short compared to the detector size, the charge collection will be partial. For a given photon energy, this leads to a tail on the low energy side of the Gaussian photo-peak (see figure 2.15). The charge collection efficiency  $\eta$  is shown in figure 2.13 for a 2-mm CdTe detector with 100 V applied between the electrodes. The charge collection efficiency is calculated as follows [Gnesin 2011]

$$\eta = \frac{\lambda_{T,e}}{L_{det}} \left[ 1 - \exp\left(\frac{-x_{int}}{\lambda_{T,e}}\right) \right] + \frac{\lambda_{T,h}}{L_{det}} \left[ 1 - \exp\left(\frac{L_{det} - x_{int}}{\lambda_{T,h}}\right) \right] \quad (2.6)$$

where  $x_{int}$  is the photon energy deposition location with respect to the anode. Putting the cathode on the side of the photon flux improves the detection efficiency [Gnesin 2011].

Other interaction processes occur in CdTe diodes: elastic (Rayleigh) and inelastic (Compton) scattering. Compton scattering results in a collected charge corresponding to only a fraction of the impinging photon energy, leading to uncertainty in the energy determination. In CdTe, for impinging photon energy above 1 MeV, the photon can also create an electron-positron pair. As shown in figure 2.14 showing the mass attenuation in CdTe, these phenomena limit the energy range over which the detector is most useful to  $\sim 200$  keV ( $\sim 30$  % of Compton scattering). This, added to the fact that collimation is lost at very high photon energy, preclude straightforward quantitative studies of runaway electrons with CdTe spectrometers.

The lower energy bounds, around 20 keV, is a direct consequence of the electronic noise (see figure 2.15), as the measured charge is very small ( $\sim 250e$  C/keV). Also, in a metallic environment such as in Tore Supra/WEST, the  $K_\alpha$  emission lines of the different components (typically Cr, Mn, Ni, Fe, Cu) are between 10 and 20 keV [Peysson and Imbeaux 1999].

The diode calibration procedure consists of exposing each diodes to a well-known line-

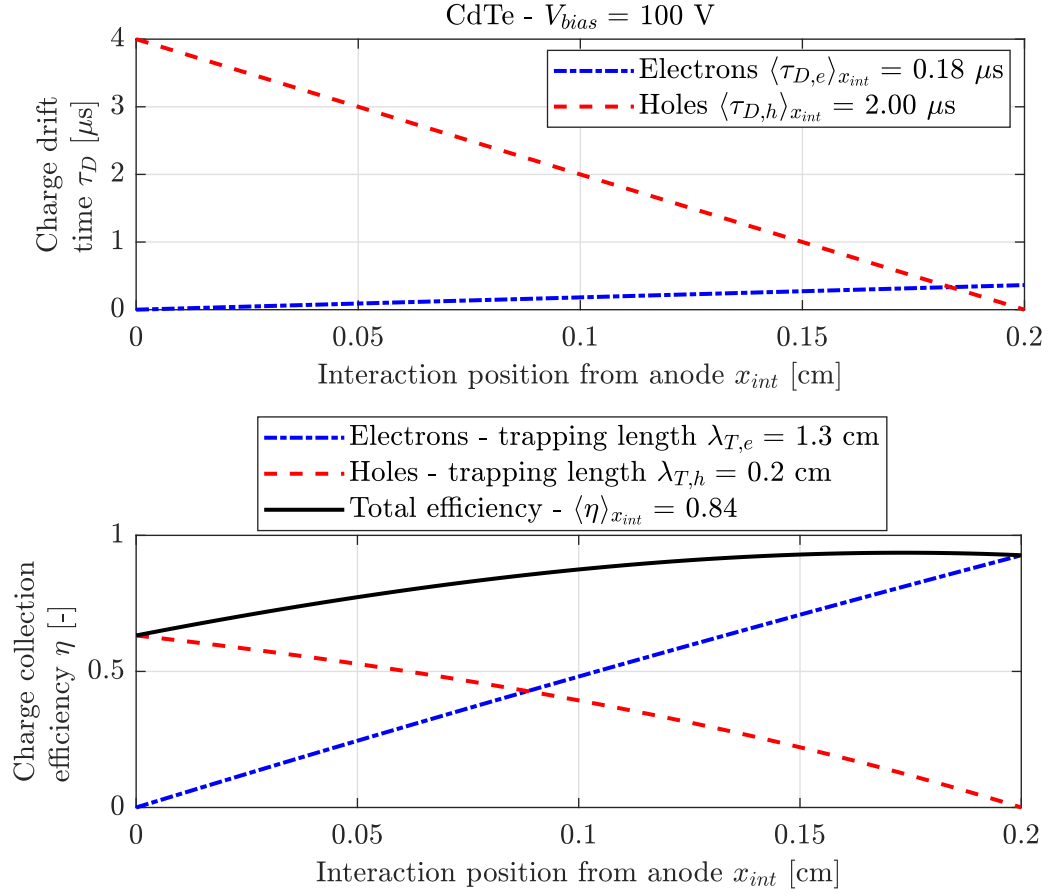


Figure 2.13: Charge collection time (*top*) and charge collection efficiency (*bottom*) for a 2-mm-thick CdTe detector, with a bias voltage of 100V. Data for electron and hole mobility are taken from [Gnesin 2011], data for electron and hole mobility-trapping time product (so-called  $\mu\tau$  product,  $\lambda_T = \mu\tau E_{bias}$ ) are taken from [Strauss 1977].

emitting HXR source, and collecting photons for each energy bin, to obtain a photon count histogram. From this histogram, photo-peaks can be identified, depending on the photon source, and fitted with a Gaussian. These Gaussian fits allow one to convert the measured voltage into a measured energy, while the full-width at half-maximum of the peaks gives the energy resolution. This is illustrated in figure 2.15. Each diode is calibrated using an Am-241 source (one photo-peak at 59.54 keV), showing an average resolution for the HXRS of  $8.0 \pm 0.7$  keV at 59.54 keV. A detailed model for the CdTe response function, calibrated with multiple HXR sources, has also been developed at TCV [Choi et al. 2020b].



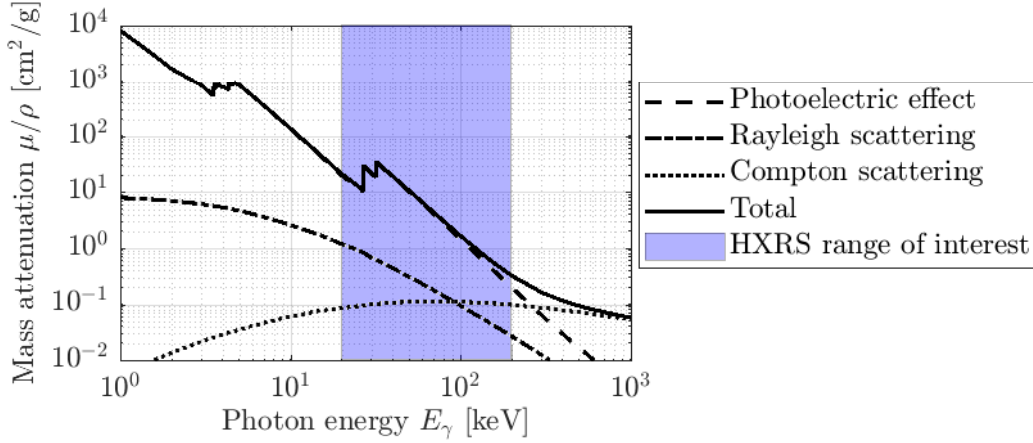


Figure 2.14: Mass attenuation for photons in cadmium telluride. Cross-sections for photoelectric effects are taken from [Scofield 1973], cross-sections for Rayleigh and Compton scattering are taken from [Hubbell et al. 1975]. The typical range of the TCV HXRS is represented in blue.

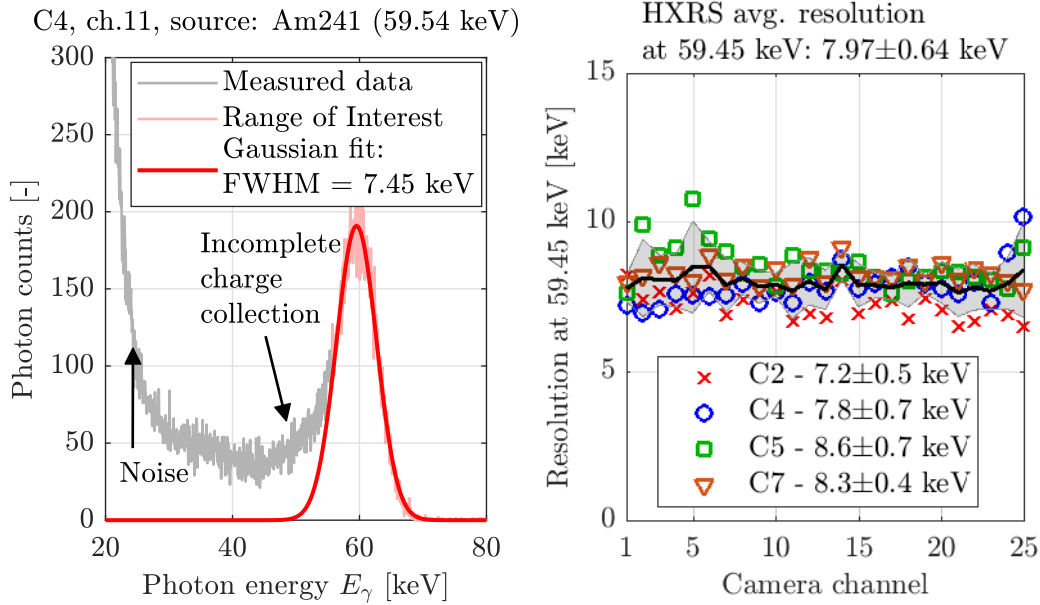


Figure 2.15: Example of a measured photon spectrum for diode calibration, with the photo-peak fitted as a Gaussian (*left*) and full-width at half-maximum of the Gaussian photo-peaks measured for each channel of each camera (*right*), using an Am-241 source (HXRS peak at 59.54 keV).

## 2.5.4 Acquisition and signal processing chain

### Embedded analog pre-amplification

The output signal from the photodiodes is directly treated by the embedded analog filtering amplifiers. First, their role is to integrate the detector output current  $I_{det}$ , to measure the collected charge, which is proportional to the impinging photon energy. On the other hand, for the signal to be detectable, it needs to be amplified to levels compatible with the analog-to-digital converter range and binning. The signal is also shaped to avoid pile-up issues,

which can saturate the ADC. Finally, the signal is turned into a differential output at the end of the electronic circuit, to reduce the noise from power supply and grounding. The simplified electronic scheme is depicted in figure 2.16, where the sub-circuits used to clean the DC inputs  $V_{bias}$  and  $V_{DD}$ , as well as the operational amplifier power supplies, have been removed for clarity. The first stage consists of a composite integrator, which integrates and shapes the signal. It convolutes the signal with an exponential decay of characteristic time  $\tau_{int} = R_2 C_2 = 5 \mu s$  so that, when the photodiode receives a high frequency of impinging photons, the ADC is less likely to saturate. The second stage consists of two amplifiers in series with high-pass filters to cut out the DC components from the previous stage, with a total gain of  $G_{amp} = (R_6/R_5)^2 = 48$  (for frequencies  $f \gg 408$  Hz). Finally, the signal is split into two branches one of which is inverted, creating a pair of differential outputs  $V_{out}^+$  and  $V_{out}^-$ .

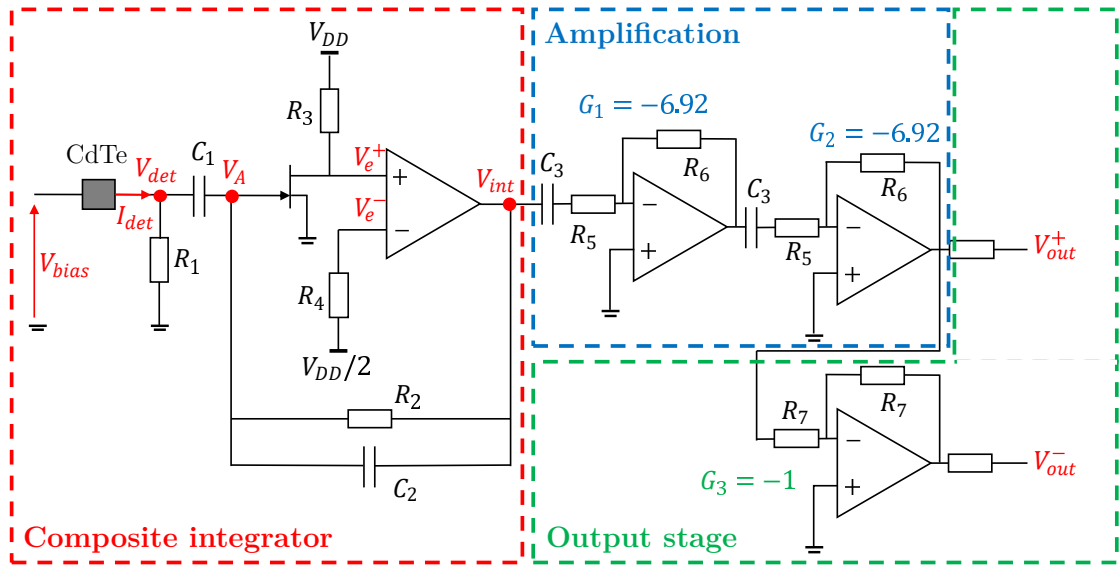


Figure 2.16: Schematic view of the TCV HXRS embedded electronics (for one channel), highlighting the 3 stages of pre-amplification: integration, amplification and inversion. The first operational amplifier is supplied with  $\pm 5$  V, while the others are supplied with  $\pm 12$  V.

The complete electronic circuit is characterized by its transfer function and associated Bode diagram. The transfer function in Fourier space of the integrator  $H_{int}(i\omega) = V_{int}/I_{det}$  is obtained by applying Millman's theorem to  $V_A$  and  $V_{det}$  in the small signal approximation. This means that a given signal  $V$  is decomposed into a DC component  $V_{DC}$  and a time-varying component  $\tilde{V}(t)$  with  $V_{DC} \gg \tilde{V}(t)$ . The DC components are therefore static and only the time-varying components are considered. This yields

$$\tilde{V}_A = \frac{\tilde{V}_{int} + i\omega C_1 Z_{eq} \tilde{V}_{det}}{1 + i\omega C_1 Z_{eq}} \quad (2.7)$$

$$\tilde{V}_{det} = \frac{i\omega R_1 C_1 \tilde{V}_A + R_1 \tilde{I}_{det}}{1 + i\omega R_1 C_1} \quad (2.8)$$

where  $Z_{eq}$  is an equivalent impedance given by  $Z_{eq} = R_2/(1 + i\omega R_2 C_2)$ . The N-channel Junction

Field Effect Transistor (JFET) is characterized by its forward transfer admittance  $|y_{fs}|$ . The JFET amplifies the variations in  $V_A$  (the gate-source voltage) in the form of a drain-source current  $-|y_{fs}|V_A$ . The DC component of  $V_e^+$  is adjusted by the feedback loop imposing the DC component of  $V_A$  such that  $V_e^+ = V_{DD} - |y_{fs}|R_3 V_A = V_e^- = V_{DD}/2$ . In the small signal approximation, the variations in  $V_{int}$ , related to the variation in  $V_e^+$ , are then given by

$$\tilde{V}_{int} = G_{OA} \tilde{V}_e^+ = -G_{OA} |y_{fs}| R_3 \tilde{V}_A \quad (2.9)$$

with  $G_{OA} = 1$  the gain of the operational amplifier. Combining equations 2.7, 2.8 and 2.9 leads to

$$H_{int}(i\omega) = \frac{-i\omega G_{OA} |y_{fs}| R_3 R_1 C_1 Z_{eq}}{(1 + i\omega R_1 C_1) \left[ 1 + G_{OA} |y_{fs}| R_3 + i\omega C_1 Z_{eq} \left( 1 - \frac{i\omega R_1 C_1}{1 + i\omega R_1 C_1} \right) \right]} \quad (2.10)$$

The transfer functions of the different inverting amplifiers are given by

$$H_{amp}(i\omega) = -\frac{R_6}{R_5} \times \frac{i\omega R_5 C_3}{1 + i\omega R_5 C_3}. \quad (2.11)$$

The total transfer function is then given by the product of all sub-transfer functions, and the transfer function in the time domain  $h(t)$  is given by the inverse Fourier transform of  $H(i\omega) = V_{out}/I_{det}$ , which reads

$$h(t) = \frac{1}{\sqrt{2\pi}} \int_{-\infty}^{+\infty} H(i\omega) e^{+i\omega t} d\omega. \quad (2.12)$$

Finally, the time response of the circuit  $V_{out}(t)$  to any input  $I_{det}(t)$  can be calculated from  $V_{out}(t) = h(t) * I_{det}(t)$ , where  $*$  is the convolution product, i.e.  $(h * I_{det})(t) = \int_{-\infty}^{+\infty} h(t - \tau) I_{det}(\tau) d\tau$ . The Bode diagram of the complete pre-amplifier is shown in figure 2.17.

### Analog-to-digital conversion

The signal is digitized after its pre-amplification by a D-tacq analog-to-digital converter. The signal is binned with a 14-bit resolution but stored with a 16-bit resolution, corresponding to a  $\pm 4$  V range, with a sampling frequency  $f_s$  of 12 MHz. This means that a signal of frequency up to  $f_{max} = f_s/2 = 6$  MHz can be measured. The complete ADC system of the HXRS is made of two D-tacq modules, each composed of three 16-channels boards (labeled from HXRS001 to HXRS006), totaling 96 channels (for 97 viewing and 4 blind photodiodes). Each channel is calibrated using an external waveform generator ( $\pm 3$  V 10 kHz sine wave), as the offset and the range slightly drift over time from factory calibrations. Calibration results are shown in figure 2.18.

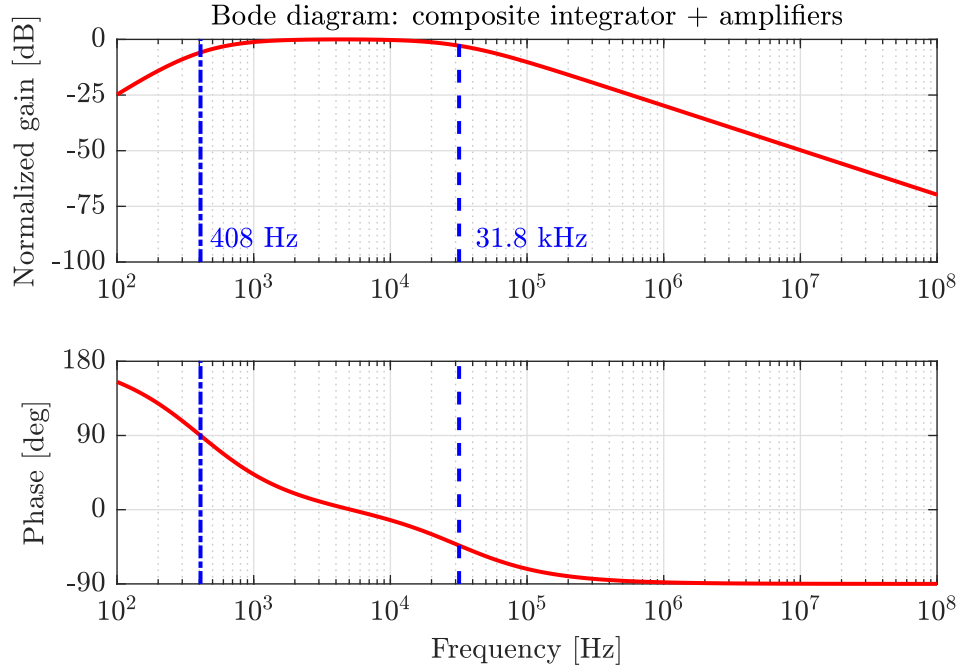


Figure 2.17: Bode diagram of the embedded electronics of the TCV HXRS cameras, showing the normalized gain and the phase.

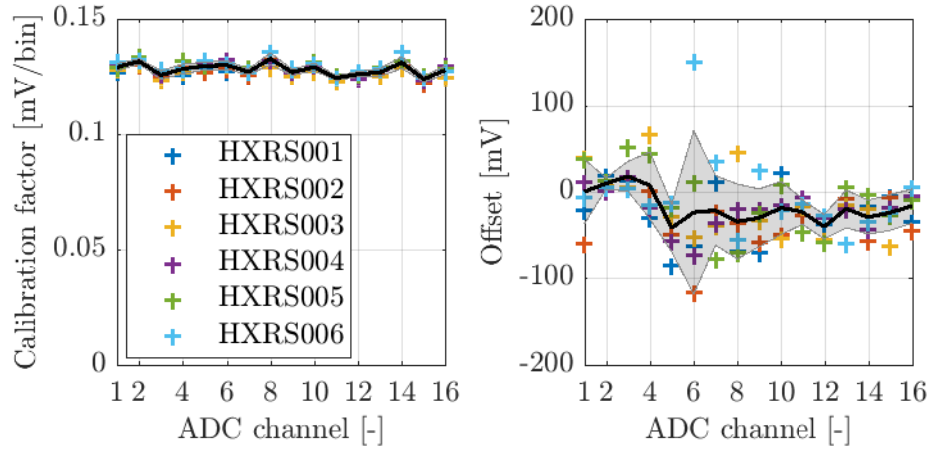


Figure 2.18: ADC calibration results, using a  $\pm 3$  V 10 kHz sine wave. Calibration factor from amplitude measurements using unbalanced output from the waveform generator (*left*) and offset from measurements using balanced output from the waveform generator (*right*).

### Digital pulse processing

The shaped and amplified time traces from the photodiodes can be post-treated to sort photons by energy within a given set of time windows, thus generating time-averaged HXR energy spectra for each HXRS channel. In TCV, this post-processing is fully digital, and the digital pulse processing methods are detailed and benchmarked in depth in [Kamleitner et al. 2014]. The principle of digital pulse processing is illustrated in figure 2.19. It consists of two main steps. First, pulses corresponding to impinging photons are detected by digital

filtering of the raw time traces, using a dynamic threshold. This means that the local maxima are identified as pulses only if they are separated by minima with a maximum-to-minimum ratio over a given threshold. For noise rejection, only peaks with energy exceeding another given threshold are taken into account. The estimation of the pulse height, and so of the photon energy, is performed by another digital filtering of the raw signal and the signal level is evaluated at times corresponding to the detected peaks. The main pulse processing method used on TCV has been optimized for high-frequency HXR detection (labeled *opt4na* in [Kamleitner et al. 2014]). In this case, the filtering method is the same for the pulse detection and the pulse height analysis and the filter consists of convoluting the raw signal with an optimized trapezoidal window. The filter parameters have been optimized to reduce the response to input noise, to give the expected response to input pulses and to work best with impinging photon frequency from 100 to 400 kHz. These optimized parameters have been obtained by least square minimization of a cost function that takes into account noise and output pulse shape [Kamleitner et al. 2014]. An example of pulse response is given in figure 2.20.

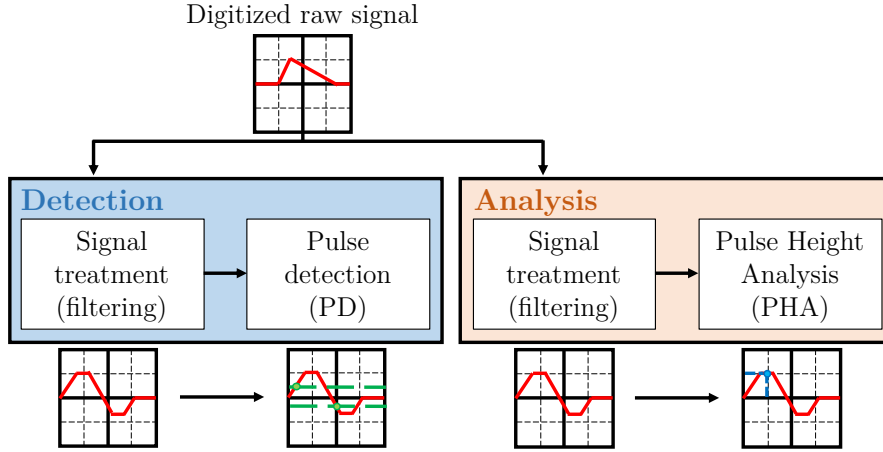


Figure 2.19: Scheme of the HXRS digital pulse processing principle as performed in TCV.

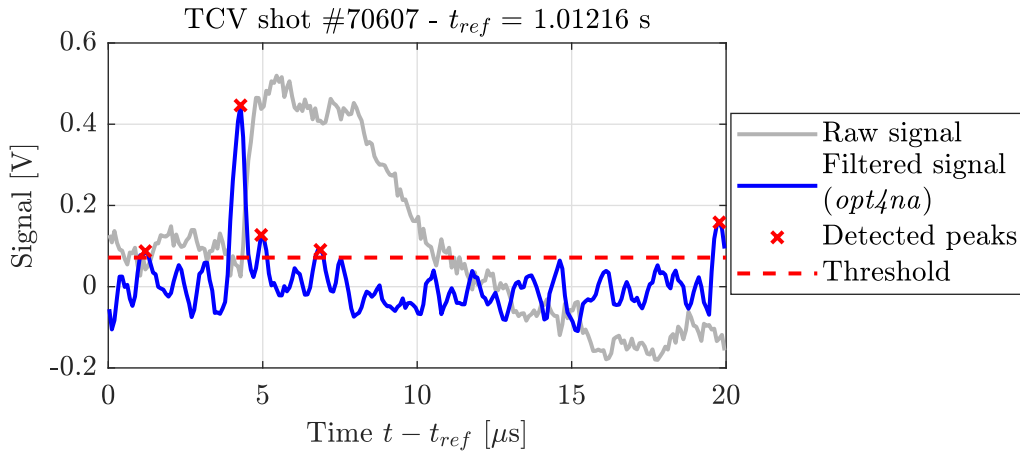


Figure 2.20: Raw HXRS signal processing, using the *opt4na* method (optimized trapezoidal filter) [Kamleitner et al. 2014] for pulse detection and analysis.

The main properties and characteristics of the HXRS are summarized in table 2.4.

Table 2.4: Summary of the hard X-ray spectrometer characteristics installed at TCV.

Detector	Type Size Manufacturer Energy range Energy resolution <sup>c</sup> Collected charge Pile-up limit <sup>d</sup>	Solid-state CdTe 2 × 2 × 2 mm Eurorad 20 <sup>a</sup> -200 <sup>b</sup> keV 8.0 ± 0.7 keV ~ 250e C/keV 500 kHz
Camera <sup>†</sup>	Number Labels <sup>e</sup> Lines of sight Collimation Shielding Possibility of toroidal view Filters	4 C2, C4, C5, C7 24 (25 for C4) + 1 blind Fan-shape tungsten collimator with uniform angular spacing 2-cm thick tungsten C4, C5 36 combinations of Al and/or Fe <sup>f</sup>
Pre-amplifier	Type Gain Integration time Low cutoff frequency	Analog 48 5 μs 408 Hz
ADC	Sampling rate Resolution Range	12 MHz 14 bits (stored at 16 bits) ±4 V
Signal Treatment <sup>††</sup>	Type Filter Detection PHA	Digital Optimized trapezoidal filter <i>opt4na</i> Dynamic threshold <sup>g</sup> Level evaluation

<sup>a</sup> Electronic noise limit;

<sup>b</sup> 30 % of Compton scattering, becomes dominant at ~ 300 keV;

<sup>c</sup> From calibrations at 59.54 keV;

<sup>d</sup> From average charge collection time;

<sup>e</sup> See figure 2.8;

<sup>f</sup> Two filter wheels per camera with 6 position each, see table 2.3;

<sup>g</sup> Find the local maxima and count them as pulses if they are separated by a minimum with a given minimum-to-maximum ratio;

<sup>†</sup> [Gnesin et al. 2008]; <sup>††</sup> [Kamleitner et al. 2014].

### 2.5.5 Tomographic capabilities

The HXRS provides a line-integrated measurement of the photon count rate, but since its lines of sight cover a complete poloidal section, it is possible to perform a tomographic inversion of the data to recover an estimation of the local emissivity  $\epsilon_{HXRS}$ . For a given chord  $l$  measuring the line-integrated brightness  $I_{HXRS,l}$ , the tomographic problem can be reduced to inverting

the integral

$$I_{HXR,l} = C_l \int_{s_l} \epsilon_{HXR} ds \quad (2.13)$$

where  $s$  is the coordinate along the line of sight of length  $s_l$  and  $C_l$  is a calibration factor. There are many different methods available to invert this integral, from the simple Abel inversion to minimum Fisher regularization and maximum likelihood method. These different methods are detailed in section 2.6 of [Kamleitner 2015] and section 2.2 of [Choi 2020], which also presents a benchmark of the multiple methods for different expected shapes of 2D emissivity profiles.

The particular method which has been applied in the work performed for the present thesis is the minimum Fisher regularization, which is described in detail in [Anton et al. 1996] and [Choi 2020]. With this method, the plasma is discretized in pixels, assuming homogeneous emissivity within a given pixel. This means that the pixels should be small enough to minimize the error, but not too small as the available number of measurements is limited. In TCV, this spatial discretization can be based either on a Cartesian coordinate system (square or rectangle pixels) or on a flux grid (trapezoidal pixels). For  $N_p$  pixels, the discretized tomographic problem for each line of sight  $l$  reads

$$I_{HXR,l} = \sum_{p=1}^{N_p} T_{lp} \epsilon_{HXR,p} \quad (2.14)$$

where  $T_{lp}$  is the length element of the line of sight  $l$  within the pixel  $p$ . Combining all the  $N_l$  available lines of sight, it is possible to write the discretized tomographic inversion problem in a matrix form  $I_{HXR} = \mathbb{T} \cdot \epsilon_{HXR}$  where  $\mathbb{T}$  is the  $N_l \times N_p$  matrix of length elements for each line of sight and each pixel. A direct inversion of  $\mathbb{T}$  is almost impossible in tokamaks due to the low number of available lines of sight, leading to too many unknowns (the local values of emissivity) with respect to the available number of equations (the line integrated measurements) [Anton et al. 1996; Choi 2020].

The minimum Fischer regularization is one of the different methods used to overcome this difficulty. In principle, it consists of a modified least-square minimization, where the functional to be minimized reads

$$\chi^* = ||\mathbb{T} \cdot \epsilon_{HXR} - I_{HXR}||^2 + \alpha_R R(\epsilon_{HXR}) \quad (2.15)$$

with the first term of the right-hand side corresponding to the standard least-square minimization. The second term represents the additional constraints on the fit, to avoid over-fitting of the solution, where  $R$  is the regularizing functional and  $\alpha_R$  is the regularization parameter governing the relative weights of the goodness of the fit (first term on the right-hand side) and of the additional requirements. This parameter has to be found iteratively, by computing solutions to equation 2.15 for a given  $\alpha_R$  and estimating the error with respect to a target error. If the error is above the target error, new solutions to equation 2.15 are computed for a new value of  $\alpha_R$ , until the error finally matches the target error. The minimum Fisher regularization

method uses the Fisher information as a regularizing functional

$$R(\epsilon_{HXR}) = \int \frac{1}{\epsilon_{HXR}} \left( \frac{\partial \epsilon_{HXR}}{\partial x} \right)^2 dx \quad (2.16)$$

where the standard deviation  $\sigma_\epsilon$  of the probability distribution function  $\epsilon_{HXR}(x)$  is an input parameter that controls the target error, following the Cramer-Rao inequality  $\sigma_\epsilon^2 \geq 1/R(\epsilon_{HXR})$  (see [Anton et al. 1996] and reference therein for more details). An example of tomographic reconstruction of 2D hard X-ray emissivity is shown in figure 2.21, using a flux-based discretization and a target error  $\sigma_\epsilon = 0.07$ .

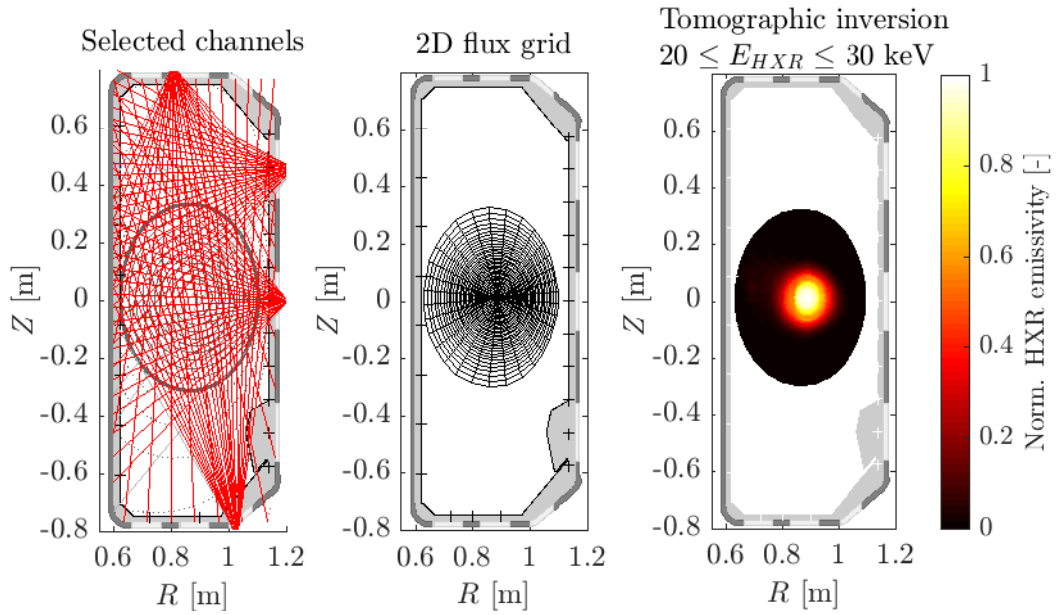


Figure 2.21: Tomographic reconstruction of 2D hard X-ray emissivity from HXRS data, using a flux-based discretization for the minimum Fisher regularization method and a target error  $\sigma_\epsilon = 0.07$ . TCV shot #73217 has been used, between 1.10 and 1.25 s.

### 2.5.6 Synthetic diagnostic

In TCV, the HXRS has been used to perform studies of the suprathermal electron population during Electron-Cyclotron heating and current drive experiments. A first research field is the study of suprathermal electron dynamics (generation, relaxation and transport), using modulated EC power cycles and conditionally averaged HXRS data to increase the photon count rate statistics, as in [Kamleitner et al. 2015; Choi et al. 2020a] and as described in chapter 4. This work was initiated in TCV using a HXR camera on loan from Tore Supra [Coda et al. 2003a,b; Nikkola et al. 2003]. Another field of research for which the HXRS has been used is the study of suprathermal-electron driven magneto-hydro-dynamic (MHD) instabilities [Kamleitner et al. 2015; Choi et al. 2019]. All these studies require the reconstruction of the non-thermal distribution of electrons.



Recovering the non-thermal electron distribution in configuration and velocity space from fast electron Bremsstrahlung data is not possible in the absence of functional constraints, as the photon is emitted from a given electron within a continuum of energies, up to the total kinetic electron energy. This is the main reason why its determination relies heavily on simulations. A synthetic diagnostic is implemented within the fast electron Bremsstrahlung module R5-X2 [Peysson and Decker 2008], embedded in the 3D bounce-averaged drift-kinetic Fokker-Planck solver LUKE [Peysson and Decker 2014]. LUKE, coupled to the ray-tracing code C3PO [Peysson et al. 2012] which solves the Electron-Cyclotron wave propagation, provides the electron distribution from which the fast electron Bremsstrahlung is computed by R5-X2. LUKE and C3PO are both described in detail in sections 3.2.1 and 3.1.2 respectively. As detailed in [Peysson and Decker 2008], from the non-thermal electron distribution function  $f_e(\mathbf{x}, \mathbf{p}, t)$  in the configuration and momentum space  $(\mathbf{x}, \mathbf{p})$  and the Bremsstrahlung differential cross-section  $d\sigma_B^{es}/(dt dE_\gamma d\Omega)$  from collisions between electrons and particles of species  $s$  (including electrons), with  $E_\gamma$  the photon energy and  $\Omega$  the solid angle, it is possible to estimate the plasma contribution to the effective photon energy spectrum arriving at a detector, excluding the contribution from the walls, by

$$\frac{dN_{E_\gamma}}{dt dE_\gamma} \simeq \int_{l_{min}}^{l_{max}} G_D \left[ \sum_s \frac{d(N_{E_\gamma}^{es}/dV)}{dt dE_\gamma d\Omega} \right] dl \quad (2.17)$$

with  $l$  the length of the line of sight,  $V$  the plasma volume,  $G_D$  a geometrical factor and

$$\frac{d(N_{E_\gamma}^{es}/dV)}{dt dE_\gamma d\Omega} = n_s \iiint \frac{d\sigma_B^{es}}{dt dE_\gamma d\Omega} v f_e(\mathbf{x}, \mathbf{p}, t) d\mathbf{p} \quad (2.18)$$

with  $n_s$  the density of species  $s$  and  $v$  the particle velocity. The associated pulse energy spectrum measured by the detector is found by taking into account the detector response

$$\frac{dN_E}{dt dE} = \int_0^{+\infty} \eta_A(E_\gamma) (1 - \eta_D(E_\gamma)) G(E_\gamma, E) \frac{dN_{E_\gamma}}{dt dE_\gamma} dE_\gamma \quad (2.19)$$

where  $E$  is the pulse energy and  $dN_E/(dt dE)$  is the pulse count rate per energy,  $\eta_A(E_\gamma)$  is the fraction of photons transmitted to the detector and  $1 - \eta_D(E_\gamma)$  is the fraction of photons stopped within the effective detector volume. The detector response function is modeled by the normalized response function  $G(E_\gamma, E)$ , which satisfies  $\int_0^{+\infty} G(E_\gamma, E) dE_\gamma = 1$ . In practice, this response function is a complex model, including all types of light-matter interaction processes, such as photoelectric effect, Compton scattering and pair production. For the HXRS installed in TCV, a calibration-based model is preferred for the detector response function over an analytical model, for which the simplifications can otherwise lead to substantial errors in the simulated spectra. This calibration-based model, described in [Choi et al. 2020b], consists of measuring the photon energy spectrum of the cadmium telluride photodiodes for a set of different well-known hard X-ray sources, and to fit these experimental spectra to obtain a semi-empirical model for  $G(E_\gamma, E)$ , which is implemented in R5-X2.

Data from HXRS and R5-X2 can be directly compared, as the TCV geometry and the HXRS chord geometry are both included in the code. The determination of the non-thermal distribution of electrons is then found by matching synthetic data with experimental data. Different parameters can be used to constrain the simulations. Some experimental parameters have a significant error bar, such as the effective charge or the loop voltage. On the other hand, in TCV, the current density is measured only at the edge, and the determination of its complete profile may rely on different assumptions (this particular point is addressed in section 3.2.1). Finally, the free parameter which can be adjusted in LUKE is the ad-hoc radial transport of fast electrons (usually of diffusive form). An example is shown in figure 2.22. In that case, the diffusive transport model is chosen to be directly proportional to the wave diffusion in phase space, as done in [Choi et al. 2020a] and in chapter 4, with a normalization factor  $D_{r0}$ . The raw signal of a channel of a given HXRS camera is shown, with the associated measured and synthetic photon energy spectra, as well as the reconstructed electron distribution function, integrated over the pitch angle  $\xi$ .

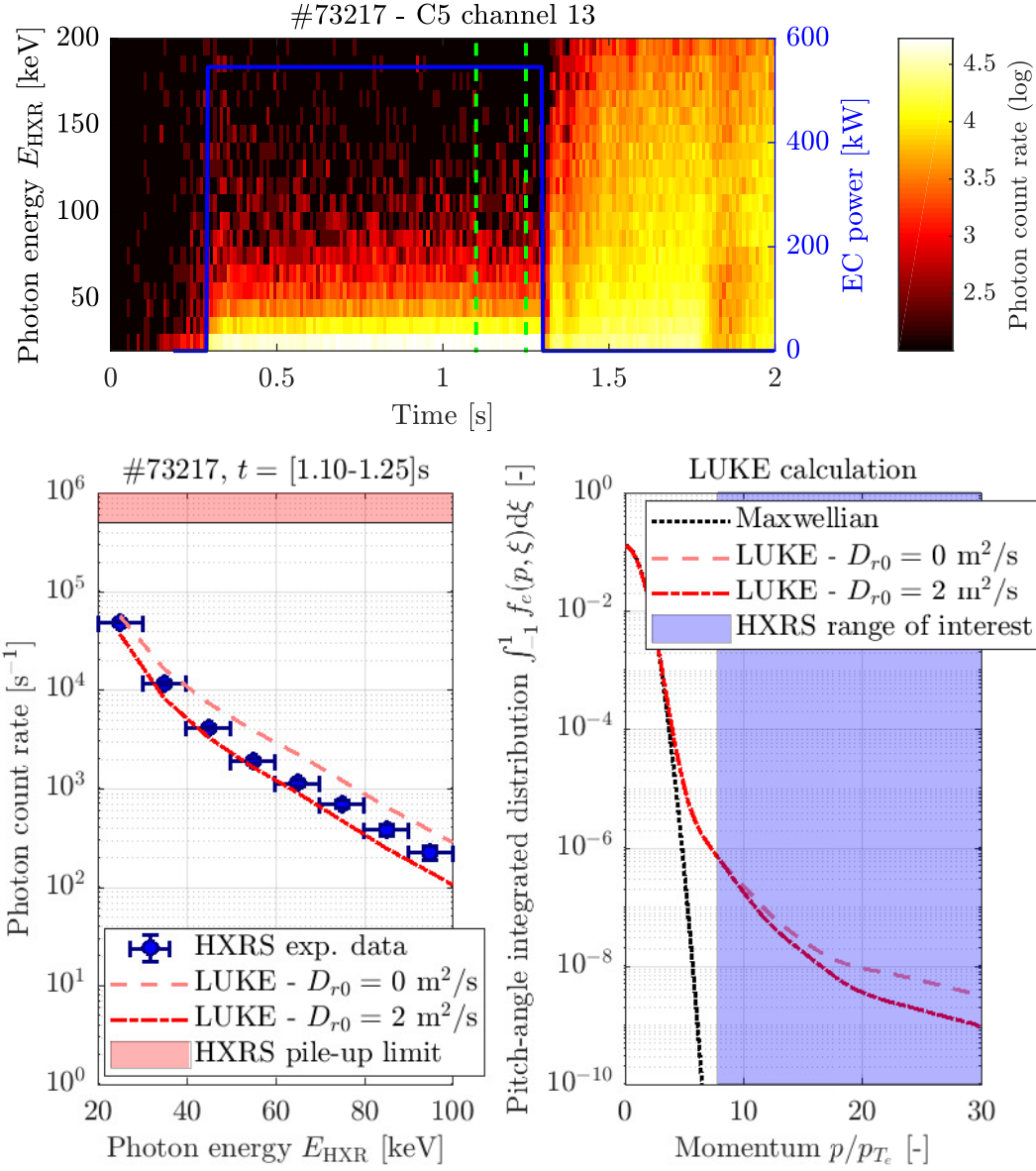


Figure 2.22: Experimentally constrained drift-kinetic simulation for TCV shot #73217. HXRS count rate from channel 13 of camera C5, viewing the magnetic axis (*top*), HXR spectra for the same channel, compared with synthetic diagnostic calculation (*bottom-left*) and associated electron distribution function  $f_e$  at maximum EC wave absorption location, calculated by LUKE and integrated over pitch-angle  $\xi$  (*bottom-right*).

## 3 Numerical tools

### 3.1 Wave propagation solvers

Electron-Cyclotron (EC) wave propagation in tokamaks can be treated in many different ways, using different tools like asymptotic geometric-optic ray tracing (e.g. C3PO [Peysson et al. 2012]), quasi-optical beam tracing based on the paraxial approximation (e.g. TORBEAM [Poli et al. 2001, 2018]), the complex eikonal method (e.g. GRAY [Farina 2007]), a wave-kinetic solver (e.g. WKBeam [Weber et al. 2015]) or even full-wave codes (e.g. IPF-FDMC [Köhn et al. 2008] or EMIT-3D [Williams et al. 2014]), each having their strengths and their limitations. An overview and a benchmark of different ray-tracing and beam-tracing codes for an ITER configuration can be found in [Prater et al. 2008], and in [Figini et al. 2012] for European codes. The development and testing of new features of the ray-tracing code C3PO was required to achieve the studies presented in chapters 4 and 5. Results of this development are presented here. Therefore, the section dedicated to the ray-tracing code C3PO is substantially longer than the other sections, dedicated to the other codes.

#### 3.1.1 COMSOL: the full-wave model

##### The full-wave equation

The most direct way to solve the wave propagation is to explicitly solve the wave equation. Combining Maxwell-Faraday and Maxwell-Ampère's equations, the so-called full-wave equation for the wave electric field  $\mathbf{E}$  thus reads [Stix 1992]

$$\nabla \times (\nabla \times \mathbf{E}) + \mu_0 \frac{\partial}{\partial t} \left( \mathbf{j} + \varepsilon_0 \frac{\partial \mathbf{E}}{\partial t} \right) = 0 \quad (3.1)$$

where  $\mu_0$  is the vacuum permeability,  $\varepsilon_0$  the vacuum permittivity and  $\mathbf{j}$  the plasma current density. To solve equation 3.1, it is necessary to express the current density in terms of the electric field. Considering the displacement current density in a dielectric medium (the plasma in this case), which reads  $\partial \mathbf{D} / \partial t = \mathbf{j} / \varepsilon_0 + \partial \mathbf{E} / \partial t$  with the displacement electric field defined by

$\mathbf{D} = \bar{\bar{\epsilon}} \cdot \mathbf{E}$ , it leads to

$$\nabla \times (\nabla \times \mathbf{E}) + \frac{1}{c^2} \frac{\partial^2}{\partial t^2} (\bar{\bar{\epsilon}} \cdot \mathbf{E}) = 0 \quad (3.2)$$

where  $c$  is the speed of light in vacuum and  $\bar{\bar{\epsilon}}$  is the dielectric tensor. The problem closure is achieved by defining the dielectric tensor, or equivalently, by choosing the terms to be kept in Ohm's law. Indeed, the dielectric tensor has been defined in terms of the current contribution from each species  $s$ , as  $\mathbf{j} = \sum_s \mathbf{j}_s$ , and these current densities can be estimated using Ohm's law, choosing to keep (or not) plasma rotation and Hall effects or to consider classical or neoclassical conductivity for instance.

The Radio-Frequency module of COMSOL Multiphysics® (hereafter referred to simply as COMSOL) provides a finite-element solver allowing the resolution of the full-wave equation governing the evolution of the time Fourier series of the EC beam electric field  $\tilde{\mathbf{E}}(\mathbf{x}, \omega)$  [COMSOL]

$$\nabla \times (\nabla \times \tilde{\mathbf{E}}(\mathbf{x}, \omega)) - \frac{\omega^2}{c^2} \bar{\bar{\epsilon}}(\mathbf{x}, \omega) \cdot \tilde{\mathbf{E}}(\mathbf{x}, \omega) = \mathcal{S} \quad (3.3)$$

with  $\omega$  is the beam pulsation,  $\mathbf{x}$  the position vector and  $\mathcal{S}$  a source term. In this case, the dielectric tensor is reduced to its Hermitian part  $\bar{\bar{\epsilon}}_H$  ( $\bar{\bar{\epsilon}}_H = \bar{\bar{\epsilon}}_H^\dagger$ , where  $^\dagger$  is the conjugate transpose), so the model is limited to treating the EC beam propagation, but not its absorption (dissipative effects are only included in the anti-Hermitian part) [Bornatici et al. 1983]. Thermal effects appear at first order only close to the resonance, which is very localized in space for an EC beam launched from the low-field side. In that case, the propagation of an EC wave can be efficiently modeled with the cold plasma dielectric tensor [Prater 2004; Westerhof 1997]. This approximation may no longer be valid for EC waves launched along the resonant layer, as is the case for top-launched X3 beams in TCV. Plasma rotation effects, as well as the ion contribution to the current, are dropped, and classical Spitzer conductivity is considered. The cold plasma dielectric tensor for a general magnetic field in Cartesian coordinates has been derived by Dr. O. Maj and implemented in COMSOL by Dr. O. Chellaï [Chellaï et al. 2018a; Chellaï et al. 2021]. It reads

$$\bar{\bar{\epsilon}}_H = \begin{pmatrix} S(1 - b_1^2) + Pb_1^2 & +iDb_3 + Qb_1b_2 & -iDb_2 + Qb_1b_3 \\ -iDb_3 + Qb_2b_1 & S(1 - b_2^2) + Pb_2^2 & +iDb_1 + Qb_2b_3 \\ +iDb_2 + Qb_3b_1 & -iDb_1 + Qb_3b_2 & S(1 - b_3^2) + Pb_3^2 \end{pmatrix} \quad (3.4)$$

where  $b_1$ ,  $b_2$  and  $b_3$  are the normalized components of the magnetic field in an arbitrary Cartesian coordinate system, and  $P$ ,  $S$ ,  $D$  and  $Q$  are the Stix coefficients [Stix 1992], defined in equation 1.13.

The computational cost of such simulations limits the calculation to 2D configurations only. So, only ECRH and 2D-limited ECCD configurations can be treated (e.g. ECCD beam propagating on the equatorial midplane). This high computational cost is partly due to the fact that a mesh size such that  $L_{mesh} \leq \lambda_0/5$  is necessary to avoid numerical diffraction of the beam on the mesh itself [Chellaï et al. 2018a]. On the other hand, full-wave simulations can be used regardless of the characteristic length of the plasma non-homogeneity with respect to the beam size  $w$  or the beam wavelength  $\lambda_0$ .

### Boundary conditions: Gaussian beam and absorbing walls

The source term  $\mathcal{S}$  in equation 3.3 stands for the initial conditions, and is set to a Gaussian beam electric field. In TCV, the X2 EC beams launched from the low-field side are Gaussian beams at the launching point on the launcher mirror [Alberti et al. 2017], with a typical beam waist radius in vacuum  $w_0^V = 0.0188$  m. The Gaussian electric field for a beam propagating in the  $s_{\parallel}$  direction, transverse to the  $s_{\perp}$  direction, is

$$E(s_{\parallel}, s_{\perp}) = E_0 \frac{w_0^V}{w(s_{\parallel})} \exp\left(-\frac{s_{\perp}^2}{w^2(s_{\parallel})}\right) \exp\left(-i \frac{k_0 s_{\perp}^2}{2R_C(s_{\parallel})}\right) \exp(-i(k_0 s_{\parallel} - \phi_0(s_{\parallel}))) \quad (3.5)$$

where  $E_0$  is the electric field amplitude at the beam waist,  $k_0$  is the wavenumber,  $w$  is the beam half-width (radius at which the amplitude is  $1/e$  of the amplitude on the propagation axis),  $R_C$  is the curvature radius of the phase front ( $R_C \leq 0$  for a convergent or focusing beam with these conventions) and  $\phi_0$  is the phase shift of the beam, which is the delay between the beam and the corresponding plane wave. The Gaussian beam half-width  $w$  relates to the beam standard deviation  $\sigma_b$  and to the beam full-width at half maximum  $FWHM_b$  through  $w = \sqrt{2}\sigma_b = FWHM_b/(2\sqrt{\ln 2})$ . The beam half-width, the curvature radius of the phase front and the beam phase shift are defined by

$$w(s_{\parallel}) = w_0^V \sqrt{1 + \left(\frac{s_{\parallel} - s_{w_0}^V}{s_R}\right)^2} \quad (3.6)$$

$$R_C(s_{\parallel}) = (s_{\parallel} - s_{w_0}^V) \left[ 1 + \left(\frac{s_R}{s_{\parallel} - s_{w_0}^V}\right)^2 \right] \quad (3.7)$$

$$\phi_0(s_{\parallel}) = \tan^{-1} \left( \frac{s_{\parallel} - s_{w_0}^V}{s_R} \right) \quad (3.8)$$

with  $s_{w_0}^V$  the position of the beam waist along the beam path and  $s_R$  the so-called Rayleigh range, which corresponds to the distance along the beam path over which the beam width increases by a factor  $\sqrt{2}$  with respect to the beam waist,

$$s_R = \frac{\pi(w_0^V)^2}{\lambda_0} N \quad (3.9)$$

where  $\lambda_0$  is the wavelength of the beam in vacuum and  $N$  the refractive index, which, for EC waves, depends on the local magnetic field  $B$ , the local electron density  $n_e$  and the wave polarization. The expression for the refractive index  $N_{O/X}(\theta_0)$  for both the 0- and the X-polarization mode of EC waves is given hereafter in equation 3.68, where  $\theta_0$  is the angle between the wavevector  $\mathbf{k}$  and the magnetic field  $\mathbf{B}$ .

For EC waves launched in the poloidal plane, the polarization mode is given by the direction of the beam electric field with respect to the background plasma magnetic field (linear polarization). For O-mode polarization, the wave electric field is in the same direction than the plasma

magnetic field, perpendicular to the propagation direction. For the X-mode polarization, the wave electric field is perpendicular to both the propagation direction and the plasma magnetic field. Generally speaking, for oblique propagation with respect to the magnetic field, the polarization is elliptical in the plane perpendicular to the propagation direction, and the wave electric field satisfies [Stix 1992; Prater 2004]

$$\frac{iE_x}{E_y} = \frac{N_{O/X}^2(\theta_0) - S}{D} \quad (3.10)$$

where the wave electric field  $E$  is projected in the  $(x, y, z)$  Cartesian basis, with  $\mathbf{B}$  along the  $z$ -axis and  $\mathbf{k}$  in the  $(x, z)$ -plane. The Stix coefficients  $D$  and  $S$  are as defined in equation 1.13.

The Gaussian beam equation described above (equation 3.5) is valid for a homogeneous refractive index (homogeneous plasma or vacuum), but the vacuum-to-plasma transition is not treated, nor is the propagation inside a plasma of varying refractive index. In COMSOL, the Gaussian beam equation is only used at a given position to initiate the electric field.

The other boundaries of the COMSOL computational domain are set to absorbing boundary conditions. Indeed, as beam absorption by the plasma is not treated in COMSOL, and because X2 beams are fully absorbed at first pass within TCV plasmas, wall reflections need to be avoided in COMSOL simulations. However, perfectly absorbing boundary conditions for every beam incident angle present a challenge, and existing methods such as the so-called perfectly matched layer require a very specific geometry to work [Berenger 1996]. Instead, a method based on the Sommerfeld radiation condition is used in COMSOL, the so-called scattering boundary condition (SBC). For a given non-homogeneous Helmholtz equation  $(\nabla^2 + k_0^2)E = \mathcal{S}$  with  $\mathcal{S}$  the bounded source of energy, the Sommerfeld radiation condition states that an electric field  $E$  solution to this Helmholtz equation is radiating if

$$\lim_{r \rightarrow \infty} \sqrt{r} \left( \frac{\partial}{\partial r} - i k_0 \right) E(r) = 0 \quad (3.11)$$

with  $r$  the distance from the source. This condition is exactly non-reflecting for boundaries that are localized infinitely away from the source. It has been adapted in COMSOL to deal with boundaries localized at a finite distance from the source. The first order SBC is given by

$$\mathbf{n} \cdot (\nabla E) - i k_0 E = 0 \quad (3.12)$$

where  $\mathbf{n}$  is the unit vector perpendicular to the boundary. The second order SBC is given by

$$\mathbf{n} \cdot (\nabla E) - i k_0 E - \frac{i}{2k_0} \nabla_t^2 E = 0 \quad (3.13)$$

with  $\nabla_t^2$  the Laplacian taken tangentially along the boundary. The reflection coefficient for second order SBC, which is the condition used in COMSOL simulations, is less than 10 % for incident angle below  $75^\circ$  (normal incidence being an angle of  $0^\circ$ ) [Frei 2015]. Detailed tests and characterization of the COMSOL full-wave model are available in chapter 4.2.2 of

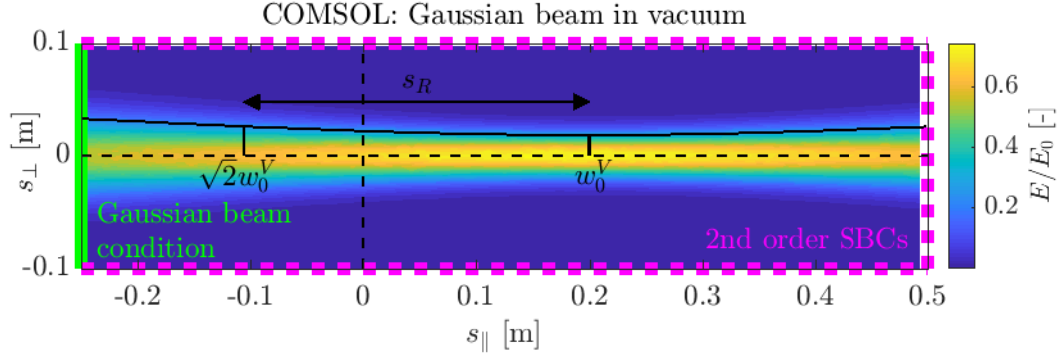


Figure 3.1: Example of a Gaussian beam propagating in vacuum, using the full-wave code COMSOL, showing Gaussian beam properties and the boundary conditions used for the simulation.

[Chellai 2019]. An example of a simple COMSOL simulation of a Gaussian beam propagating in homogeneous plasma is shown in figure 3.1 to illustrate the boundary conditions and the Gaussian beam properties.

### 3.1.2 C3PO: the ray-tracing code

#### Principle

Ray tracing is a very common tool to solve the wave propagation and its linear absorption, as it is fast and flexible, and is often coupled to other codes that need at least an EC wave propagation solver, such as drift-kinetic Fokker-Planck solvers (e.g. LUKE [Peysson and Decker 2014]). The ray-tracing code C3PO, described in depth in [Peysson et al. 2012], solves the following Hamiltonian system to propagate the optical rays

$$\begin{aligned} \frac{d\mathbf{x}}{dt} &= - \frac{\partial \mathcal{D}_H}{\partial \mathbf{k}} / \frac{\partial \mathcal{D}_H}{\partial \omega} \\ \frac{d\mathbf{k}}{dt} &= \frac{\partial \mathcal{D}_H}{\partial \mathbf{x}} / \frac{\partial \mathcal{D}_H}{\partial \omega} \end{aligned} \quad (3.14)$$

where  $\mathbf{x}$  is the position vector of the ray,  $\mathbf{k}$  is the wavevector and  $\mathcal{D}_H$  is the Hermitian part of the dispersion relation  $\mathcal{D}$ , the anti-Hermitian part  $\mathcal{D}_A$  being related to the wave absorption, such that  $\mathcal{D} = \mathcal{D}_H + i\mathcal{D}_A$ . The dispersion relation  $\mathcal{D}$  corresponds to the determinant of the dispersion tensor  $\bar{\bar{D}}$ , defined by the Fourier-expanded wave equation in configuration space and time  $(\mathbf{k}, \omega)$

$$\begin{aligned} \bar{\bar{D}}(\mathbf{k}, \omega) \cdot \tilde{\mathbf{E}}(\mathbf{k}, \omega) &= \mathbf{N} \times \mathbf{N} \times \tilde{\mathbf{E}}(\mathbf{k}, \omega) + \bar{\bar{\epsilon}}(\mathbf{k}, \omega) \cdot \tilde{\mathbf{E}}(\mathbf{k}, \omega) \\ &= \left( \mathbf{N}\mathbf{N} - \bar{\bar{I}}N^2 + \bar{\bar{\epsilon}}(\mathbf{k}, \omega) \right) \cdot \tilde{\mathbf{E}}(\mathbf{k}, \omega) = 0 \end{aligned} \quad (3.15)$$

where  $\bar{\bar{I}}$  is the unit identity tensor and  $\mathbf{N} = c\mathbf{k}/\omega$  is the refractive index. Therefore,  $\bar{\bar{D}} = \mathbf{N}\mathbf{N} - \bar{\bar{I}}N^2 + \bar{\bar{\epsilon}}$ . Non-trivial solutions to equation 3.15 are found by solving  $\mathcal{D} = \det \bar{\bar{D}} = 0$ .



The weak wave damping approximation considered in the ray-tracing approach, reading  $|D_{A,ij}|/|D_{H,ij}| \ll 1$ , allows to treat separately the wave propagation and the wave damping. As already mentioned above, the weak damping approximation is valid for EC waves propagating away from the resonance location [Westerhof 1997], and only the zeroth order in  $|D_{A,ij}|/|D_{H,ij}|$  of equation 3.15 is kept to solve the propagation, which is equivalent to consider only the Hermitian part of  $\mathcal{D}$ , and similar to take the cold plasma dielectric tensor  $\bar{\bar{\epsilon}}_H$  as described in section 3.1.1. The wave absorption is treated by expanding equation 3.15 to higher order in  $|D_{A,ij}|/|D_{H,ij}|$ , thus retaining thermal effects. Assuming that the wave frequency  $\omega$  and the parallel wavevector  $N_{\parallel}$  are given real quantities, the wave (or ray) absorption coefficient is proportional to the imaginary part of the perpendicular wavevector with respect to the magnetic field  $N_{\perp}$ , which reads

$$\Im(N_{\perp}) = \frac{c}{\omega} \frac{P_{dis}}{2\Pi_{\perp}} \quad (3.16)$$

with the dissipated power  $P_{dis}$  defined by

$$P_{dis} = \frac{\epsilon_0 \omega}{2} \tilde{\mathbf{E}}^* \cdot \bar{\bar{D}}_A \cdot \tilde{\mathbf{E}} \quad (3.17)$$

and the density of the energy flow carried by the waves given by

$$\Pi = \frac{\epsilon_0 c}{4} \frac{\partial}{\partial \mathbf{N}} \left( \tilde{\mathbf{E}}^* \cdot \bar{\bar{D}}_H \cdot \tilde{\mathbf{E}} \right). \quad (3.18)$$

The perpendicular component of  $\Pi$  is then given by  $\Pi_{\perp} = ||\Pi \times \mathbf{b}||$ , with  $\mathbf{b}$  the direction of the magnetic field. Different types of dispersion relation, or equivalently different models of dielectric tensor, can be used in C3PO, from vacuum and cold plasma to kinetic models, eventually taking into account collisional damping [Peysson et al. 2012]. In all cases, the dispersion relation is linearized, thus allowing for linear damping calculation only.

In the high frequency limit, which is equivalent to assume that  $\lambda_0$  is much smaller than the beam width  $w$ , which is then assumed to be much smaller than any plasma non-homogeneity characteristic length  $L_f$ , it is possible to perform an asymptotic expansion of the solution to the wave equation, and to write the wave electric field as  $E(\mathbf{x}, t) = A_E(\mathbf{x}) \exp(i\kappa_L S(\mathbf{x}, t, \mathbf{k}, \omega))$  where  $S(\mathbf{x}, t, \mathbf{k}, \omega)$  is the so-called eikonal function,  $A_E(\mathbf{x})$  is the slowly varying amplitude of the field and  $\kappa_L$  is the ratio of characteristic gradient lengths, such that  $\kappa_L^{-1} = L_S/L_{A_E} = (\nabla S)^{-1} \times (\nabla A_E/A_E) \ll 1$ . The spatial ordering is further constrained by the fact that the eikonal function is identified to  $\mathbf{k} = \nabla S$ , meaning that  $S$  is also slowly varying in space, which translates to  $\nabla \cdot \mathbf{k} \ll k^2$  [Cardinali et al. 2007]. Injecting this ansatz into the wave equation reduces it to its asymptotic form, the eikonal equation. To the lowest order, the eikonal function  $S(\mathbf{x}, t, \mathbf{k}, \omega)$  satisfies  $\mathcal{D}_H(\mathbf{x}, t, \mathbf{k}, \omega) = 0$ . In geometric optics, as it is the case for C3PO, the eikonal function is a real function while, in quasi-optics, the eikonal function is a complex function with an imaginary part that relates to the beam electric field profile [Choudhary and Felsen 1973; Farina 2007]. The approximation made to perform this expansion is the so-called Wentzel-Kramer-Brillouin (WKB) approximation.

As stated in [Peysson et al. 2012], the eikonal function  $S$  being independent of the path in phase-space,  $\mathbf{k}$  and  $\mathbf{x}$  components are canonical conjugates, as well as  $\omega$  and  $t$ . This allows one to write the Hamiltonian system 3.14 to which  $\mathbf{k}$  and  $\mathbf{x}$  are solutions. The resulting six ordinary differential equations are then solved in C3PO using the Runge-Kutta-Fehlberg method, after decoupling the geometrical and the physical effects, making the calculation fast and adapted to the 3D tokamak geometry. However, contrary to full-wave codes, the WKB approximation constraints the ordering of the different characteristic lengths and  $\lambda_0 \ll w \ll L_f$  needs to be satisfied. This may be an issue when considering edge density fluctuations as, in that case,  $L_f$  scales as  $5\text{--}10 \rho_{L,s}$ , with  $\rho_{L,s} = c_s/\Omega_{c,i}$  the sonic Larmor radius where the sound speed is  $c_s = \sqrt{k_B T_e/m_i}$  and the ion cyclotron frequency is  $\Omega_{c,i} = q_i B/m_i$  [Rhodes et al. 2002; Carter 2006; Nespoli et al. 2017], meaning that it is possible to have  $L_f \sim \lambda_0$  (order of millimeters). On the other hand, the time evolution of the plasma equilibrium and fluctuations is considered much longer than the wave propagation time and period, meaning that, for a time scale  $t$  relevant to the wave propagation problem,  $\partial \mathcal{D}_H / \partial t = 0$  and  $\omega$  is a constant of the wave motion. An example of C3PO ray-tracing calculation for TCV is shown in figure 3.2.

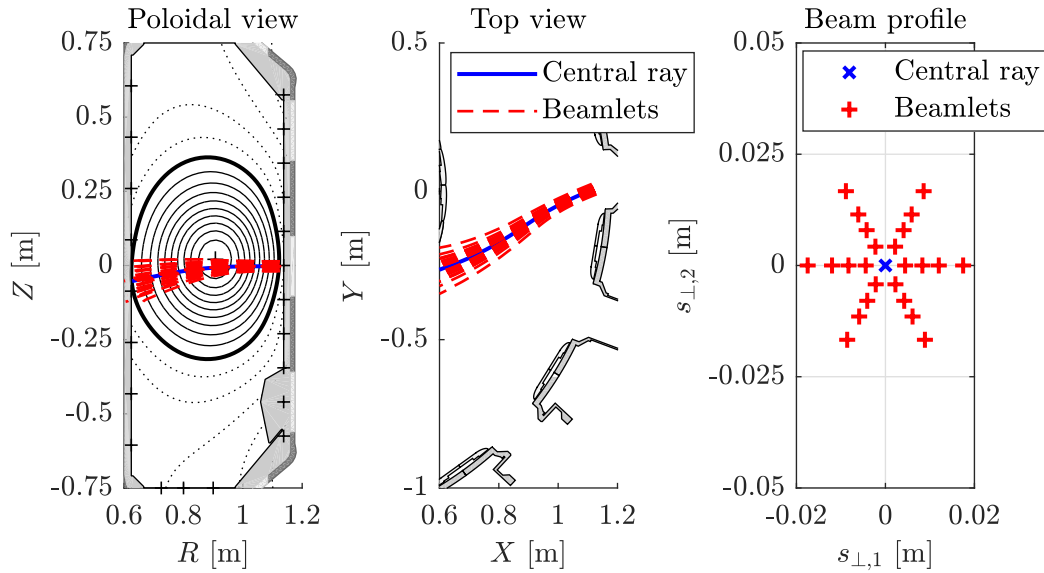


Figure 3.2: C3PO calculation for the beam propagation displayed in a poloidal view (*left*) and a top view (*center*) for a typical TCV geometry. The *right* panel shows the beam discretization (beam cross-section transverse to its propagation direction) into multiple power tubes spread around a central ray (solution of equation system 3.14).

### Quasi-optical beam width estimation

In C3PO, the total beam power is evenly spread among several power tubes, so-called beamlets, each carrying the same fraction of the total power. The beamlets are radially and azimuthally spread around the central ray, thus generating a matrix of  $N_r \times N_\phi$  power tubes, where  $N_r$  and  $N_\phi$  are the radial and azimuthal numbers of power tubes respectively. This multi-ray power spreading is shown in figure 3.2. The distance between the beamlets and the central ray is

constrained by the width of the beam power profile (proportional to the square of the beam electric field). Initially, in C3PO, this beam width was estimated from Gaussian beam theory in vacuum, using an equation similar to equation 3.6. This method lacks an estimation of the beam width that takes into account the local changes in refractive index.

A new method has been proposed to estimate the beam width, presented at the 47th conference on plasma physics of the European Physical Society [Cazabonne et al. 2021], to take into account the vacuum-to-plasma boundary and the gradient of refractive index in the plasma, as well as its poloidal curvature. This work has been motivated by the studies of the impact of the beam width on the wave power deposition profile, requiring a more realistic model for the beam width estimation. This new model is based on the quasi-optical paraxial beam equation. Some ingredients are still missing for C3PO to be a complete beam tracing, namely the consideration of the angle of incidence of the beam onto the flux surfaces, the toroidal curvature of the refractive index and the anisotropy of the beam width. Nevertheless, this model represents a significant improvement over the old one.

Quasi-optics is an approach used to treat electromagnetic wave propagation when the dimensions of the optical elements (lenses, mirror, etc) are larger than the beam wavelength, but the beam wavelength is not negligible compared to these elements. Gaussian beam modes are solutions of the paraxial wave equation [Goldsmith 1998]

$$\frac{\partial^2 u}{\partial s_{\perp}^2} + \frac{1}{s_{\perp}} \frac{\partial u}{\partial s_{\perp}} - i k_0 \frac{\partial u}{\partial s_{\parallel}} = 0 \quad (3.19)$$

where  $u$  is the complex amplitude of the mode,  $k_0$  the wavenumber,  $s_{\parallel}$  is the direction of propagation and  $s_{\perp}$  the transverse direction. It is the zeroth order expansion of the wave equation with respect to a small parameter corresponding to the transverse-to-longitudinal characteristic length ratio, meaning that the variations along the propagation axis are small compared to the transverse variations. This so-called paraxial approximation reads  $w \ll L_d$  where  $L_d = kw^2$  is the characteristic diffraction length [Lax et al. 1975]. This expansion of the wave equation is performed within the WKB approximation and is valid if the characteristic space scale of the beam amplitude variation is much longer than the beam wavelength ( $w \gg \lambda_0$ ) [Goldsmith 1998]. This is the case in tokamaks, where the beam has a wavelength of order 1 mm, whereas the space scale variation of the refractive index ranges from millimeters to centimeters, depending on density gradient and magnetic field profile. A solution of equation 3.19 is

$$u(s_{\perp}, s_{\parallel}) = A_u(s_{\parallel}) \exp\left(-i k_0 \frac{s_{\perp}^2}{2q_u(s_{\parallel})}\right) \quad (3.20)$$

where  $A_u(s_{\parallel})$  and  $q_u(s_{\parallel})$  are two complex functions to be determined, and  $q_u$  is often called the complex beam parameter, carrying information about the beam width and the curvature radius of the phase front. Changes in local refractive index have been taken into account in the beam width calculation using a step-wise refractive index to simulate the gradient. The principle is illustrated in figure 3.3. A recursive chain of ray transfer matrices has been

applied to the Gaussian beam complex parameter  $q_u$  to estimate the width of the beam at each step through the plasma, modeling each plasma slice as a focusing or defocusing lens, depending on the orientation of its curvature. The complete theory can be found in chapter 3 of [Goldsmith 1998].

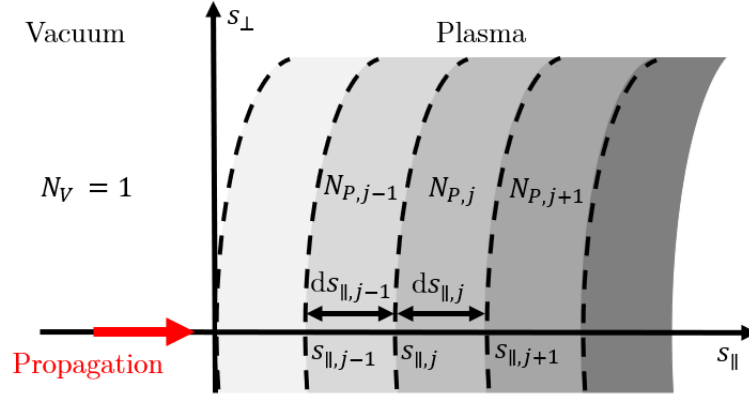


Figure 3.3: Decomposition of the plasma refractive index gradient into a step-wise function for beam width calculation.

In C3PO, it is assumed that the ray travels into vacuum until it reaches the last-closed flux surface on the plasma. The position at which the ray enters the plasma is set to  $s_{\parallel,0} = 0$ . The complex Gaussian beam parameter at the interface on the vacuum side is

$$q_{u,V}(0) = -s_{w_0}^V + i \frac{\pi(w_0^V)^2}{\lambda_0} \quad (3.21)$$

where  $s_{w_0}^V$  is the position of the vacuum beam waist along the beam path  $s_{\parallel}$ , estimated knowing the distance from the beam launcher to the beam waist and the position of the plasma in the vessel. It is positive if the waist is inside the plasma.

The propagation of a beam through a given optical object, such as a given dielectric medium or a lens, can be modeled by a matrix operation that transforms the input beam electric field into the output field, or, in the case of quasi-optics, the complex beam parameter. Such a matrix is a so-called transfer matrix. Thanks to the continuity in Maxwell's equations at the boundary of two different media, it is then possible to treat a layered medium, such as a plasma of varying refractive index, as a chain of transfer matrices, which corresponds to the individual layer transfer matrices multiplied together. For an interface between a first medium of index  $N_{P,j-1}$  and a second medium of index  $N_{P,j}$ , with a curvature radius  $R_{i,j-1 \rightarrow j}$  (positive for a concave surface with respect to the incoming ray, so negative for a ray entering a typical tokamak plasma from the outside), the transfer matrix is

$$M_{i,j-1 \rightarrow j} = \begin{pmatrix} 1 & 0 \\ \frac{N_{P,j} - N_{P,j-1}}{N_{P,j} R_{i,j-1 \rightarrow j}} & \frac{N_{P,j-1}}{N_{P,j}} \end{pmatrix}, \quad (3.22)$$

while the transfer matrix for a beam traveling over a distance  $ds_{\parallel,j-1}$  in a homogeneous medium is simply given by

$$M_{i,ds_{\parallel,j-1}} = \begin{pmatrix} 1 & ds_{\parallel,j-1} \\ 0 & 1 \end{pmatrix}. \quad (3.23)$$

It can be noticed that for a plane interface one has  $R_{i,j-1 \rightarrow j} \rightarrow \infty$ , and so, in that particular case, the transfer matrix is simplified. In the model used in C3PO, only the poloidal curvature is considered, assuming that the toroidal curvature is negligible with respect to the poloidal one and to the transverse size of the beam. First, the vacuum-to-plasma interface is considered. The complex beam parameter at the interface, on the plasma side, is

$$q_{u,P}(s_{\parallel,0}) = \frac{M_{i,V \rightarrow P}^{(11)} q_{u,V}(0) + M_{i,V \rightarrow P}^{(12)}}{M_{i,V \rightarrow P}^{(21)} q_{u,V}(0) + M_{i,V \rightarrow P}^{(22)}} \quad (3.24)$$

where the  $M_{i,V \rightarrow P}^{(jk)}$  are the elements of the transfer matrix for the vacuum-plasma interface, given by

$$M_{i,V \rightarrow P} = \begin{pmatrix} 1 & 0 \\ \frac{N_{P1} - N_V}{N_{P1} R_{i,V \rightarrow P}} & \frac{N_V}{N_{P1}} \end{pmatrix}. \quad (3.25)$$

Then, the complex Gaussian beam parameter at a location  $s_{\parallel,j}$  is computed recursively, assuming that it is traveling over a distance  $ds_{\parallel,j-1}$  in a medium of index  $N_{P,j-1}$  until it reaches the next medium of index  $N_{P,j}$ . The transfer matrix for a step through the plasma is then

$$\begin{aligned} M_{t,j-1 \rightarrow j} &= \begin{pmatrix} 1 & 0 \\ \frac{N_{P,j} - N_{P,j-1}}{N_{P,j} R_{i,j-1 \rightarrow j}} & \frac{N_{P,j-1}}{N_{P,j}} \end{pmatrix} \begin{pmatrix} 1 & ds_{\parallel,j-1} \\ 0 & 1 \end{pmatrix} \\ &= \begin{pmatrix} 1 & ds_{\parallel,j-1} \\ \frac{N_{P,j} - N_{P,j-1}}{N_{P,j} R_{i,j-1 \rightarrow j}} & \frac{N_{P,j} - N_{P,j-1}}{N_{P,j} R_{i,j-1 \rightarrow j}} ds_{\parallel,j-1} + \frac{N_{P,j-1}}{N_{P,j}} \end{pmatrix} \end{aligned} \quad (3.26)$$

and the complex Gaussian beam parameter is

$$q_{u,P}(s_{\parallel,j}) = \frac{M_{t,j-1 \rightarrow j}^{(11)} q_{u,P}(s_{\parallel,j-1}) + M_{t,j-1 \rightarrow j}^{(12)}}{M_{t,j-1 \rightarrow j}^{(21)} q_{u,P}(s_{\parallel,j-1}) + M_{t,j-1 \rightarrow j}^{(22)}}. \quad (3.27)$$

The width of the beam inside the plasma is evaluated taking the imaginary part of the complex Gaussian beam parameter

$$w(s_{\parallel}) = \sqrt{\frac{\lambda_0}{\pi N_P(s_{\parallel}) \operatorname{Im}\left(-\frac{1}{q_{u,P}(s_{\parallel})}\right)}}. \quad (3.28)$$

This approach can be seen as an intermediate step from multiple ray tracing toward beam tracing and fully quasi-optical approaches. The beam-tracing code TORBEAM [Poli et al. 2001] is also based on the paraxial expansion of the wave equation. It solves the propagation of a central ray together with additional ordinary differential equations for the imaginary

part of the phase of the wave, which directly relates to transverse beam properties (beam width and phase front curvature radius), assuming  $L_f \gg w \gg \lambda_0$ . On the other hand, the model used in GRAY [Farina 2007] is directly based on the complex eikonal equation, which is, as described in the previous section, another asymptotic limit to the wave equation under the WKB approximation [Choudhary and Felsen 1973; Goldsmith 1998]. It adds a partial differential equation as a closure to the standard multiple-ray-tracing system of ordinary differential equations, using an extended dispersion function that keeps information on the complex eikonal function, via the so-called quasi-optical terms.

#### Benchmark against full-wave model in simplified configurations

The quasi-optical transfer matrix model for the beam width estimation has been benchmarked against full-wave calculations. This benchmark is first performed in a simplified geometry, in a simulation box identical to what is described in figure 3.1. The beam first travels into vacuum from  $s_{\parallel} = -0.25$  m to  $s_{\parallel} = 0$  m, and then into the plasma until  $s_{\parallel} = 0.5$  m. The plasma is defined by a constant background magnetic field  $B_0$ , and an elliptic electron density map, centered in  $(s_{\parallel,c}, s_{\perp,c})$  and defined by

$$n_e(s_{\parallel}, s_{\perp}) = (n_{e,0} - n_{e,1}) \left( 1 - \frac{(s_{\parallel} - s_{\parallel,c})^2}{R_{\parallel}^2} - \frac{(s_{\perp} - s_{\perp,c})^2}{R_{\perp}^2} \right) + n_{e,1} \quad (3.29)$$

where  $n_{e,0}$  and  $n_{e,1}$  are the maximum and minimum electron density respectively,  $R_{\parallel}$  and  $R_{\perp}$  the parallel and the perpendicular radii, with the ellipticity defined by  $\kappa = R_{\parallel}/R_{\perp}$ . The beam propagates in the  $s_{\parallel}$  direction and is X-polarized, with its electric field  $E$  in the  $s_{\perp}$  direction, satisfying  $\mathbf{k}_0 \perp \mathbf{E} \perp \mathbf{B}_0$ . Two quantities are defined to compare the transfer matrix model (labeled *TM*) with the full-wave simulations (labeled *FW*): the correlation between the different beam width calculations  $\zeta(\sigma_b)$ , and the averaged relative gap  $\langle g \rangle(\sigma_b)$  between the same quantities, defined by

$$\zeta(\sigma_b) = \frac{\int_{s_{\parallel,0}}^{s_{\parallel,end}} \sigma_{b,FW}(s_{\parallel}) \sigma_{b,TM}(s_{\parallel}) ds_{\parallel}}{\sqrt{\int_{s_{\parallel,0}}^{s_{\parallel,end}} |\sigma_{b,FW}(s_{\parallel})|^2 ds_{\parallel} \int_{s_{\parallel,0}}^{s_{\parallel,end}} |\sigma_{b,TM}(s_{\parallel})|^2 ds_{\parallel}}} \quad (3.30)$$

and

$$\langle g \rangle(\sigma_b) = \left\langle \frac{|\sigma_{b,FW}(s_{\parallel}) - \sigma_{b,TM}(s_{\parallel})|}{\sigma_{b,FW}(s_{\parallel})} \right\rangle_{s_{\parallel}} \quad (3.31)$$

where  $\sigma_b$  is the standard deviation of the beam transverse profile.

A list of the scans that have been performed in this configuration is given in table 3.1. The background magnetic field is kept constant to simplify the analysis of the scans and the control of the general parameters, such as the curvature of the refractive index. The first scan S#1.1 is a scan in spatial resolution  $ds_{\parallel}$ , as the transfer-matrix model relies on the step-wise discretization of the plasma refractive index. Results are shown in figure 3.4. Even though a coarser spatial resolution reduces the agreement between the transfer-matrix model and the

full-wave simulations, one can see that it has a rather small impact. Using a coarse resolution (e.g.  $ds_{\parallel} = 1$  cm), the maximum averaged gap is around 3.5 % only, for a correlation always above 0.999. On the other hand, it is not necessary to increase the resolution dramatically as the improvement on both the gap and the correlation tends to saturate.

Table 3.1: List of scans performed in the simplified geometry to compare the transfer-matrix model with the full-wave simulations. The equilibrium parameters are  $n_{e,1} = 1e17 \text{ m}^{-3}$ ,  $(s_{\parallel,c}, s_{\perp,c}) = (0.25, 0)$  m and  $B_0 = 1.5$  T, for a beam frequency  $f_b = 82.7$  GHz. The angle of incidence of the beam on the plasma surface is  $\alpha_{in}$  ( $\alpha_{in} = 90^\circ$  corresponds to normal incidence) and  $\kappa \rightarrow \infty$  corresponds to flat density surfaces.

Scan #	Scanned parameter	$n_{e,0}$	$\kappa = R_{\parallel}/R_{\perp}$	Resolution $ds_{\parallel}$	$\alpha_{in}$
S#1.1	$ds_{\parallel}$	$2e19 \text{ m}^{-3}$	1	$10^{-3} - 10^{-1} \text{ m}$	$90^\circ$
S#1.2	$n_{e,0}$	$1e19 - 3e19 \text{ m}^{-3}$	1	$10^{-3} \text{ m}$	$90^\circ$
S#1.3	$\kappa$	$2e19 \text{ m}^{-3}$	0.5-2	$10^{-3} \text{ m}$	$90^\circ$
S#1.4 <sup>a</sup>	$\kappa$	$2e19 - 3e19 \text{ m}^{-3}$	0.5- $\infty$	$10^{-3} \text{ m}$	$90^\circ$
S#1.5	$\alpha_{in}$	$2e19 - 3e19 \text{ m}^{-3}$	$\infty$	$10^{-3} \text{ m}$	$45^\circ - 90^\circ$

<sup>a</sup>This scan is performed excluding curvature effects in the transfer-matrix model;

The two main parameters that are taken into account by the transfer-matrix model are the changes in refractive index and the effect of the poloidal curvature on the beam width. Figure 3.5 shows the beam width profile for two different background density. The beam width is compared in the case of flat density surfaces (no curvature) and in the case of circular density surface (using equation 3.29 with  $R_{\parallel} = R_{\perp} = 0.25$  m). First, a very good agreement is found between the transfer-matrix model and the full-wave simulations. However, a difference tends to appear at higher density (smaller refractive index) and the transfer-matrix model overestimates the beam width. Since the different effects are cumulative, this difference increases over the path. Then, by comparing the beam width to a Gaussian beam in vacuum, it is shown that the effect of the refractive index curvature dominates over the effect of refractive index gradient, as the plasma behaves like a focusing or defocusing lens, even though the refractive index gradient still broadens the beam in a cumulative way, leading to a non-negligible impact for a long beam path into the plasma. Results of scans in density (S#1.2) and curvature radius (S#1.3) are shown in figure 3.4. This confirms the good agreement between the transfer-matrix model and the full-wave simulations, with a slightly degraded agreement at high density and strong curvature. Indeed, strong curvature, or equivalently small curvature radius, can break the initial assumption that the characteristic size of the lens is larger or of the same order than the beam width.

The transfer-matrix model is valid for a beam impinging with a perpendicular angle of incidence on the refractive index curved surfaces. Properly taking into account the impact of non-normal incidence would need further development. The relative impact of the angle of incidence  $\alpha_{in}$  with respect to curvature has been investigated comparing the full-wave calculation with the transfer-matrix model, without including poloidal curvature effects in the transfer-matrix model. First, the curvature radius has been decreased by increasing the inverse elongation to see the impact of neglecting the poloidal curvature (scan S#1.4) and then, the angle of incidence has been varied for flat refractive index surfaces to see the impact of the

non-normal incidence (scan S#1.5). Results of scans S#1.4 and S#1.5 are shown in figure 3.6. This highlights the fact that excluding poloidal curvature has a stronger impact on the beam width estimation than neglecting the angle of incidence. An example of beam width profile for a tilted slab is shown in figure 3.7. It can be noticed that the main impact of the angle of incidence is on beam refraction, which is already taken into account by the ray-tracing code.

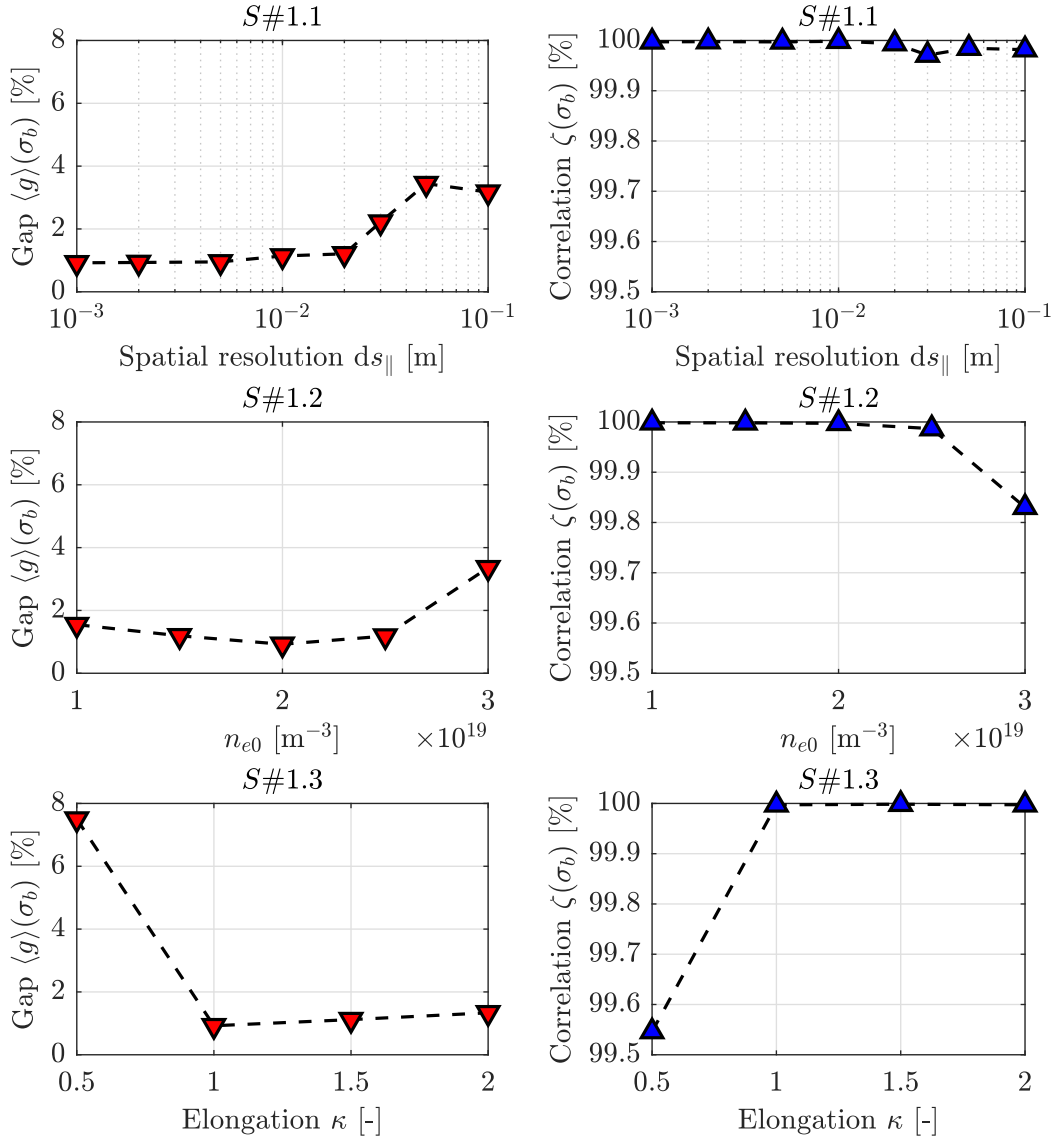


Figure 3.4: Average gap  $\langle g \rangle$  (left, see equation 3.31) and correlation  $\zeta$  (right, see equation 3.30) of the beam standard deviation  $\sigma_b$  between the transfer-matrix model and the full-wave simulations, for scans S#1.1, S#1.2 and S#1.3 (see table 3.1).



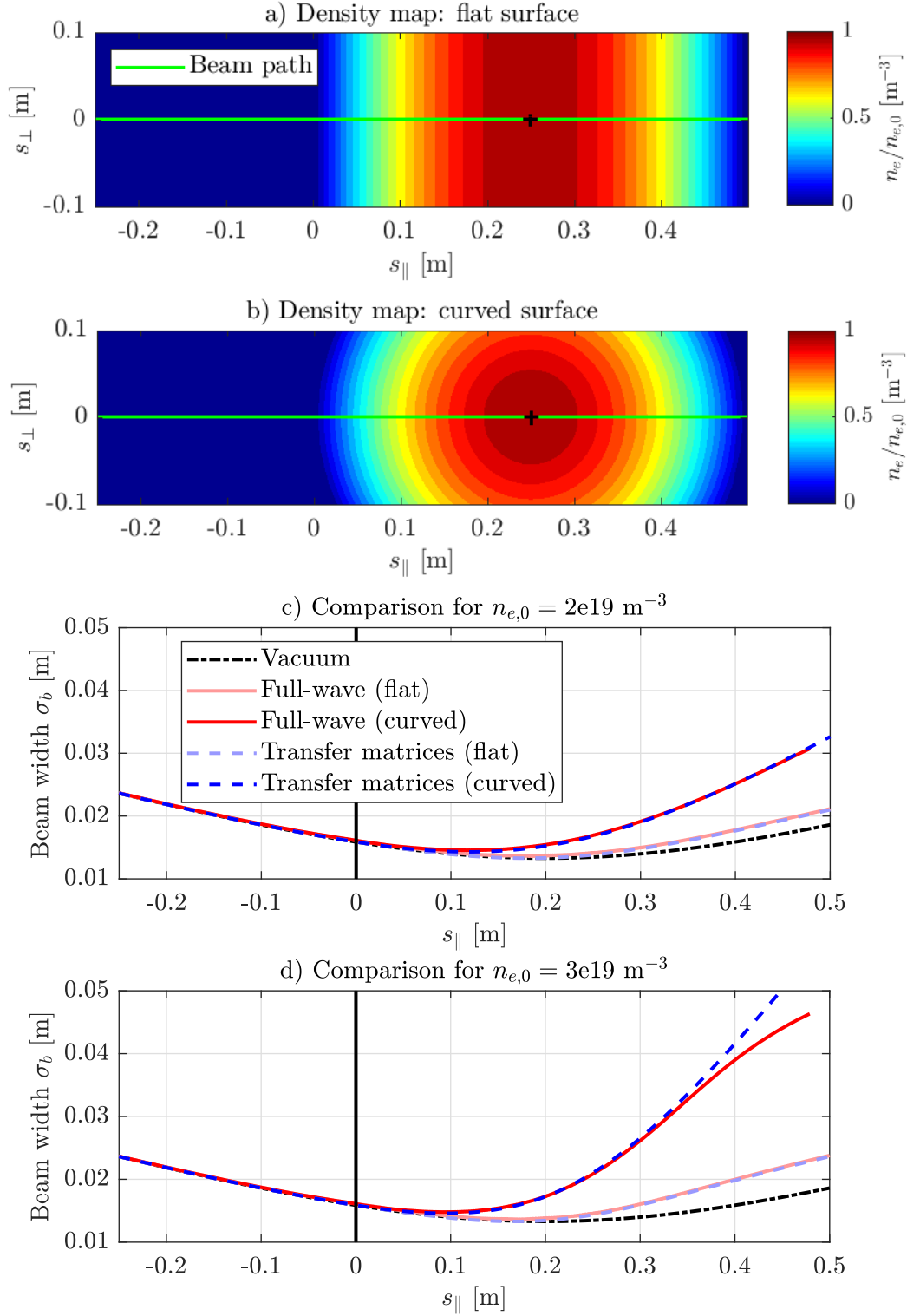


Figure 3.5: Examples of comparison between the transfer-matrix model and the full-wave simulations, for simplified geometry, illustrated in panels *a*) (flat density surfaces) and *b*) (curved density surfaces).

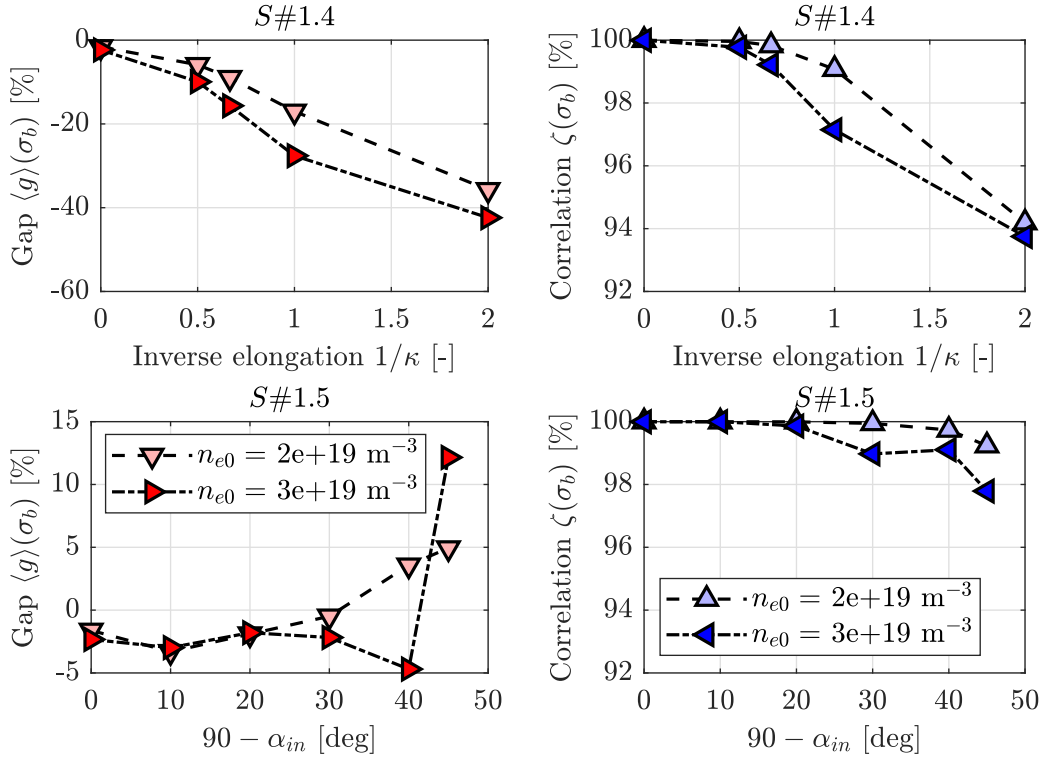


Figure 3.6: Average gap  $\langle g \rangle$  (left, see equation 3.31) and correlation  $\zeta$  (right, see equation 3.30) of the beam standard deviation  $\sigma_b$  between the transfer-matrix model and the full-wave simulations, for scans S#1.4 and S#1.5 (see table 3.1).

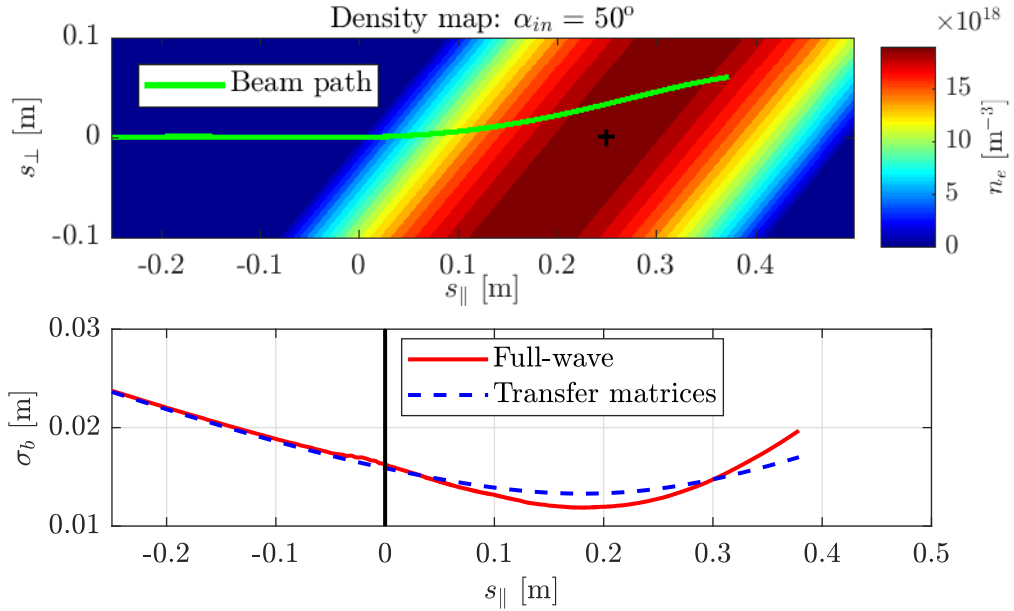


Figure 3.7: Example of comparison between the transfer-matrix model and the full-wave simulation (bottom), for a tilted slab density (top).

### Benchmark against full-wave model in TCV-relevant configurations

The benchmark against full-wave simulations has been extended to TCV-relevant configurations, to assess the improvement that the transfer-matrix model represents with respect

to the previous Gaussian-beam-in-vacuum model. An analytic equilibrium has been generated, using analytic solutions to the Grad-Shafranov equation based on Solov'ev profiles, as described in [Cerfon and Freidberg 2010] and detailed in appendix B. Assuming a deuterium plasma without impurities, i.e  $n_e = n_i = n$ , the following input parameters have been set: the major radius is  $R_0 = 0.88$  m, the plasma minor radius on the horizontal midplane is  $a = 0.24$  m, the plasma elongation is  $\kappa = 1.6$  and the triangularity is  $\delta = 0$ , the magnetic field on axis is  $B_0 = 1.5$  T, the gradient of total pressure, which is constant, is  $\nabla_{\psi_{P,n}} p = -4806.5$  Pa (with the normalized poloidal flux  $\psi_{P,n} = \psi_P / \psi_{P0}$ ), the pressure at the edge is  $p_1 = 1201.6$  Pa, the ion-to-electron temperature ratio is  $T_i / T_e = 1$ , the density at the edge is  $n_1 = 0.5 \times 10^{19} \text{ m}^{-3}$  and the density on axis is  $n_0 = 2.5 \times 10^{19} \text{ m}^{-3}$ , the power dependency of the density in  $\psi_{P,n}$  is  $\gamma_n = 1$  and the free parameter  $A$ , adjusting the pressure-current balance, is  $A = 0$ . The density profile can be written

$$n_e(\psi_{P,n}) = (n_0 - n_1)(1 - \psi_{P,n}) + n_1 \quad (3.32)$$

while the temperature is constant over the whole plasma. In any case, in the cold plasma limit, the temperature profile is not important when studying the beam propagation. Values of  $n_1$  and  $n_0$  have been changed, keeping the pressure unchanged, to scan the density gradient  $\nabla_{\psi_{P,n}} n_e$  and the average density  $\langle n_e \rangle_{\psi_{P,n}}$ . The other scanned parameters are the poloidal launching angle of the beam  $\theta_L$ , defined as the angle between the inward horizontal axis  $-\mathbf{e}_R$  and the propagation direction of the beam projected in the poloidal plane  $\mathbf{e}_{k_\perp} = \mathbf{e}_k - \mathbf{e}_k \cdot \mathbf{e}_\phi$ , and the injection height of the beam with respect to the magnetic axis position  $Z_L - Z_p$ . These scans are illustrated in figure 3.8 and summarized in table 3.2. In all cases, the beam is launched in pure ECRH ( $k_\parallel = 0$ ), with a frequency of 82.7 GHz. These scans have been designed to cover a wide range of situations while changing the inhomogeneity characteristic scale length, within a typical TCV parameter range.

Table 3.2: List of scans performed in the TCV-like geometry to compare the transfer-matrix and the beam-in-vacuum models with the full-wave simulations. The analytic equilibrium is generated using the method developed in [Cerfon and Freidberg 2010], for a beam frequency  $f_b = 82.7$  GHz.

Scan #	Scanned parameter	$\langle n_e \rangle_{\psi_{P,n}}$	$\nabla_{\psi_{P,n}} n_e$	$\theta_L$	$Z_L - Z_p$
S#2.1	$\langle n_e \rangle_{\psi_{P,n}}$	$1.0\text{--}3.0 \times 10^{19} \text{ m}^{-3}$	$-2.0 \times 10^{19} \text{ m}^{-3}$	$20^\circ$	0.25 m
S#2.2	$\nabla_{\psi_{P,n}} n_e$	$1.5 \times 10^{19} \text{ m}^{-3}$	$-3.0 \times 10^0 \text{ m}^{-3}$	$20^\circ$	0.25 m
S#2.3	$\theta_L$	$1.5 \times 10^{19} \text{ m}^{-3}$	$-2.0 \times 10^{19} \text{ m}^{-3}$	$0\text{--}40^\circ$	0.25 m
S#2.4	$Z_L - Z_p$	$1.5 \times 10^{19} \text{ m}^{-3}$	$-2.0 \times 10^{19} \text{ m}^{-3}$	$0^\circ$	0.02-0.35 m

Results of average relative gap  $\langle g \rangle$  and correlation  $\zeta$  for the beam full-width at half maximum are shown in figure 3.9, for all scans described in table 3.2. It has to be noted that results for the central ray position match very well between C3PO and COMSOL, with correlations for the beam position,  $\zeta(R)$  and  $\zeta(Z)$ , being always over 99 %, and a maximum averaged absolute gap of the order of few millimeters. Overall, the implementation of the transfer-matrix beam width model improved the matching between C3PO and the full-wave model, when compared to the previous beam-in-vacuum model. There are only two cases in which the old model gives similar results than the new transfer-matrix model: the  $\theta_L = 0^\circ$  case of the S#2.3 scan,

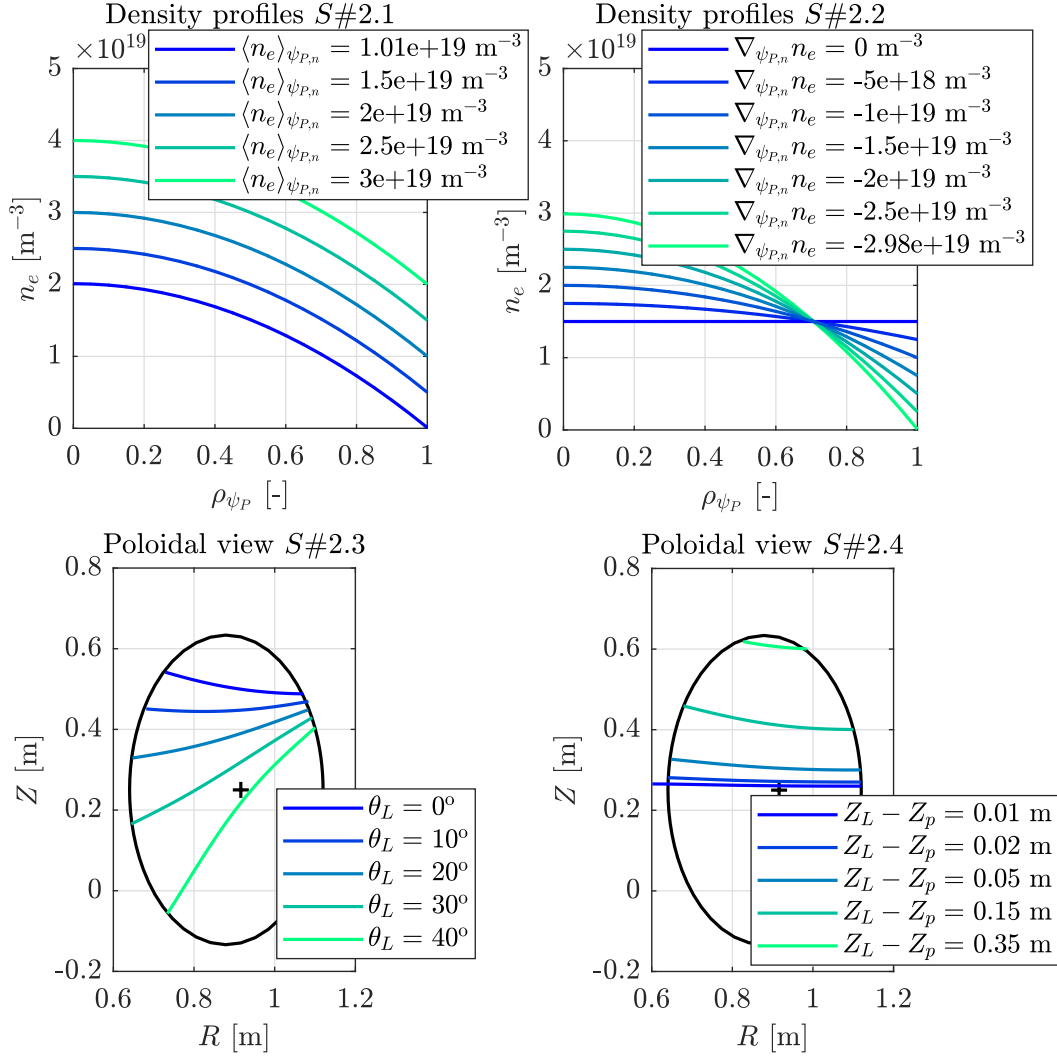


Figure 3.8: Density profiles and beam path for the different scans described in table 3.2.

and the  $Z_L - Z_p = 0.35 \text{ m}$  case of the  $S\#2.4$  scan. In both cases, the beam propagates over a short path within the plasma last-closed flux surface, with an incidence on the flux surfaces far from the normal incidence, which is the worst case scenario for the validity of the transfer-matrix model. However, the agreement with the full-wave code remains very good, and, for these particular cases, the transfer-matrix model does not represent an improvement nor a degradation with respect to the old model. It is worth noticing that the transfer-matrix model does improve the determination of the beam width in cases where the plasma refractive index is significantly different from one, i.e. at higher averaged density, or when it is changing over a shorter characteristic length, i.e. at steeper density gradient.

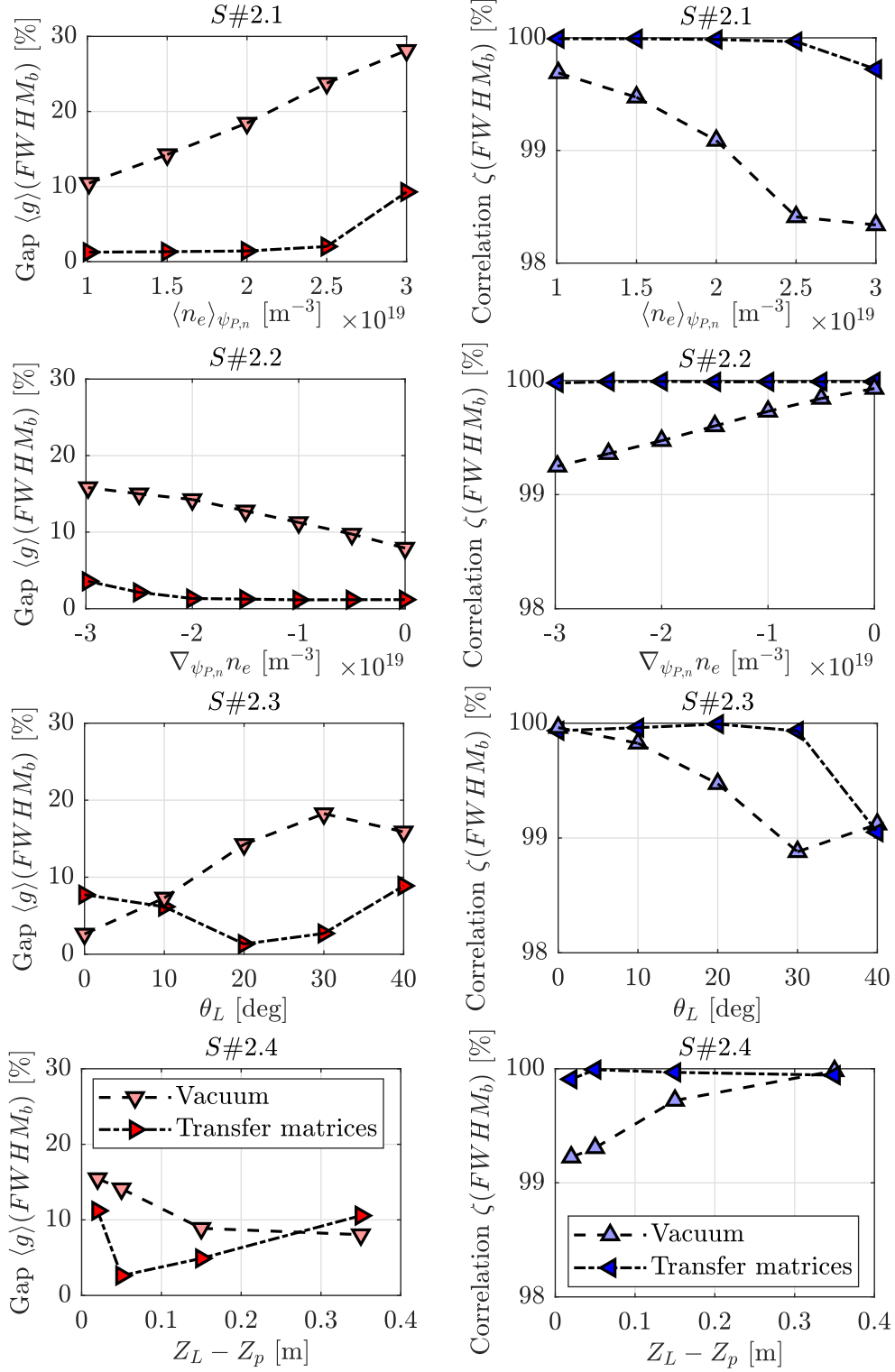


Figure 3.9: Average gap  $\langle g \rangle$  (left, see equation 3.31) and correlation  $\zeta$  (right, see equation 3.30) of the beam full-width at half-maximum  $FWHM_b$  between the transfer-matrix model and the full-wave simulations and between the beam-in-vacuum model and the full-wave model, for scans S#2.1, S#2.2, S#2.3 and S#2.4 (see table 3.2).

### Custom Lorentzian beam width model

Overall, the transfer-matrix model represents a significant improvement in estimating the beam width for the ray tracing code C3PO, but it is still limited to treating Gaussian beam propagation. However, it has been shown in [Köhn et al. 2018; Snicker et al. 2017a] and it is shown in detail in chapter 5 that, in the presence of density fluctuations leading to beam scattering, the beam profile can be distorted from a Gaussian to a Lorentzian profile. Moreover, the transfer-matrix model is not able to treat diffraction effects arising from the beam scattering off density fluctuation structures smaller than the local beam width. Analytical models derived from wave-kinetic theory are available to treat this particular diffraction effect, based on density fluctuation parameters. They can be found in [Sysoeva et al. 2015] for O-mode and in [Tretinnikov et al. 2021] for X-mode, but they are limited to Gaussian beam profiles, which corresponds to the diffusive beam broadening regime described in [Snicker et al. 2017a], while it is shown in chapter 5 that TCV plasmas are more likely to be in the superdiffusive beam broadening regime, where the beam profile is expected to be Lorentzian. Therefore, this new model can be used to calculate a more realistic beam propagation in a quiet plasma, or when the fluctuations of the refractive index are neglected. However, its limitations, coupled to the intrinsic limitation of C3PO in spatial ordering, mean that other tools are required for accurate modeling of a beam propagating through a turbulent refractive index.

The ray-tracing code C3PO is coupled to the bounce-averaged drift-kinetic code LUKE, described below in section 3.2.1, which enables the calculation of the non-thermal electron distribution function in the presence of EC waves. Knowing the distribution function, it is possible to compute the fast electron Bremsstrahlung and directly compare the numerical results to the hard X-ray measurements from the HXRS (see section 2.5). So, to experimentally assess the impact of density-fluctuation-induced beam scattering, it is necessary to be able to provide a non-Gaussian beam width profile to LUKE. A custom beam width model has been added to the ray-tracing code C3PO, with either a Gaussian or a Lorentzian profile. Thus, the full-wave-calculated beam width can be used as an input for the drift-kinetic calculation. This model acts on the radial spreading of the power tubes around the central ray, so the power profile corresponding to either a Gaussian (by default in C3PO) or a Lorentzian beam profile is recovered. The power profile  $P$  is such that  $P \propto E^2$ , so the radial distance  $dr_j$  between the central ray and the  $j$ th power tube reads

$$dr_j = \sigma_b \sqrt{\ln \left( \frac{2N_r}{2(N_r - j) + 1} \right)} \quad (3.33)$$

for a Gaussian beam profile, with  $j$  the ray index and  $N_r$  the radial number of rays, and

$$dr_j = \frac{FWHM_b}{2} \sqrt{\frac{N_r}{(N_r - j) + 1} - 1} \quad (3.34)$$

for a Lorentzian beam profile. A comparison between the expected power profile and the

ray discretization is shown in figure 3.10 for the Lorentzian model, where the normalized power density has been estimated within each ring of surface  $S_{P,j} = \pi(dr_{j+1}^2 - dr_j^2)$ . It can be seen that a good agreement is found for a sufficiently high number of rays. Typically, a radial number of ray  $N_r \geq 18$  is recommended to accurately take into account the effect of the Lorentzian profile (less than 5 % of error on the beam width determination). This custom beam width capabilities in C3PO represents an efficient way of coupling COMSOL full-wave calculation to the drift-kinetic code LUKE, assuming an azimuthally symmetric beam profile. These simulations are later referred to as COMSOL-LUKE simulations.

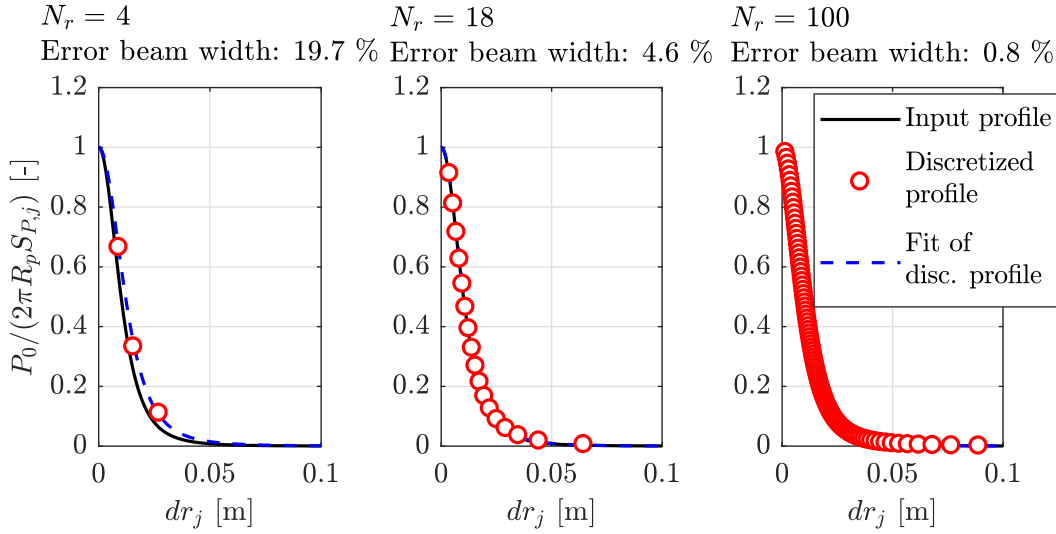


Figure 3.10: Beam power profile reconstruction implemented in C3PO for Lorentzian beam profile (see equation 3.34), for different values of the radial number of rays  $N_r$ . The error on beam width (here on  $FWHM_b$ ) is deduced from the fit of the discretized profile. For the Lorentzian model, the first power tube is at the central ray position.

### 3.1.3 WKBeam: the wave-kinetic equation solver

A last tool, which is planned to be used in a future work to propagate EC waves, is the wave-kinetic code WKBeam, described in details in [Weber et al. 2015], based on the theory developed by [McDonald 1991]. It consists of an alternative beam-tracing method, but instead of taking asymptotic solutions to the wave equation in the form of either the solution to the paraxial wave equation or the complex eikonal ansatz, a solution to the steady-state wave-kinetic equation is computed. The general form of the wave kinetic equation in the  $(\mathbf{x}, \mathbf{k})$  phase space reads [McDonald 1991]

$$\frac{\partial A}{\partial t} + \{A, H\} = \mathcal{S}(\mathbf{x}, \mathbf{k}) \quad (3.35)$$

where  $\{\cdot, \cdot\}$  is the Poisson bracket operator,  $A$  is the wave action density (the transported quantity) defined by the ratio of the wave power density to the wave angular frequency  $\omega$ ,  $H$  is the Hamiltonian of the system, defined by the solution of the cold plasma dispersion relation  $\mathcal{D}_H(\mathbf{x}, t, \mathbf{k}, \omega) = 0 \implies \omega = H(\mathbf{x}, \mathbf{k}, t)$ , and  $\mathcal{S}(\mathbf{x}, \mathbf{k})$  are the source terms, which also

include dissipating effects such as the wave absorption. In steady-state and under the paraxial and the WKB approximations, the wave-kinetic equation solved in WKBeam reduces to [Weber et al. 2015]

$$\begin{cases} \{H, w_u\} &= -2\gamma_u w_u + \mathcal{S}_{sc} \\ H w_u &= 0 \text{ (constraint)} \end{cases} \quad (3.36)$$

where  $w_u$  is the scalar Wigner function that directly relates to the wave electric field power density (the transported quantity). This time, the Hamiltonian of the system  $H$  is the eigenvalue of the Hermitian part of the dispersion tensor  $\bar{\bar{D}}_H$  with the beam angular frequency  $\omega$  considered as a parameter. Thus,  $H = \mathbf{e}_E^\dagger \cdot \bar{\bar{D}}_H \cdot \mathbf{e}_E$  where  $\mathbf{e}_E$  is the electric field polarization vector. The wave absorption is described by the anti-Hermitian part of the dielectric tensor  $\gamma_u = \mathbf{e}_E^\dagger \cdot \bar{\bar{\epsilon}}_A \cdot \mathbf{e}_E$ .

It has been shown that this method, even though it relies on the WKB approximation, is able to treat the average effects of the density fluctuations on the beam refraction and diffraction by describing these fluctuations with the scattering operator  $\mathcal{S}_{sc}$ . The scattering operator depends on the statistical properties of the density fluctuation level and size, assuming that these fluctuations are frozen with respect to the beam propagation [Weber et al. 2015]. This approach is valid under the Born approximation, meaning that it is possible to treat the density fluctuations as a stochastic perturbation of the dielectric tensor  $\delta\epsilon$ , such that the wave electric field  $\mathbf{E}$ , solution of the wave equation  $(\bar{\bar{D}} - \delta\epsilon) \cdot \mathbf{E} = 0$ , can be expanded in an asymptotic series where the lowest order corresponds to the solution in a quiet plasma and the higher orders are random fields corresponding to the fluctuating contribution. The scattering operator  $\mathcal{S}_{sc}$ , built from this expansion, introduces fluctuation-driven random kicks in the ray position in phase space  $(\mathbf{x}, \mathbf{k})$ . Solving the system 3.36 provide a set of rays that samples the distribution of the electric field power density. It is then possible to use a Monte-Carlo method to solve the statistically averaged beam propagation in a turbulent medium. WKBeam is able to treat diffraction effects from first principles, and is therefore not limited to Gaussian beam profile in the presence of density fluctuations.

### 3.2 Wave absorption and Fokker-Planck solvers

The resonant absorption of the EC waves by the plasma occurs for a given group of particles, depending on the frequency of their cyclotron gyration around the local magnetic field lines and, therefore, is localized both in configuration space and velocity space. To accurately model the response of the plasma to the wave absorption, it is necessary to include the information about the velocity distribution of particles, and so, to adopt a kinetic description of the plasma. Different tools are used throughout this work to describe the kinetic evolution of the plasma, with different levels of assumptions. The first tool is the bounce-averaged drift-kinetic Fokker-Planck solver LUKE [Peysson and Decker 2014], described in section 3.2.1, and the second tool is the global flux-driven gyro-kinetic code ORB5 [Lanti et al. 2020], described in section 3.2.2. As for the wave propagation solvers, they all have their strengths and limitations and represents complementary approaches to the same problem. In particular, it is possible to



directly compare LUKE results with experimental data, while it is not possible for ORB5 yet, but ORB5 is able to simulate turbulent transport from first principles while LUKE, by construction in LUKE, lacks this capability.

### 3.2.1 LUKE: the bounce-averaged drift-kinetic Fokker-Planck solver

#### The Fokker-Planck equation

The drift-kinetic code LUKE [Peysson and Decker 2014] solves the linearized bounce-averaged drift-kinetic Fokker-Planck equation for the distribution of electrons  $f_e$ . The general form of the kinetic description of the plasma is a transport equation describing the evolution of a particle distribution function in the 7D (6D + time) space  $(\mathbf{x}, \mathbf{p}, t)$ , with  $\mathbf{x}$  the position in real space and  $\mathbf{p} \equiv m\mathbf{v}$  the momentum of a particle of velocity  $\mathbf{v}$  and mass  $m$  (which can be the apparent relativistic mass  $m \equiv \gamma m_0$ , with  $\gamma$  the Lorentz factor). For the electron distribution function  $f_e(\mathbf{x}, \mathbf{p}, t)$ , this equation, also known as the Boltzmann equation, reads

$$\frac{\partial f_e}{\partial t} + \{f_e, H_e\} = \sum_s \mathcal{C}(f_e, f_s) \quad (3.37)$$

where  $f_e$  is the electron distribution function,  $H_e$  the Hamiltonian for electrons and  $\{\cdot, \cdot\}$  the Poisson brackets. Using the Hamiltonian system of equations linking the canonical conjugate coordinates  $\mathbf{x}$  and  $\mathbf{p}$ , it is possible to write  $\{f_e, H_e\} = \mathbf{v} \cdot \nabla_{\mathbf{x}} f_e + \mathbf{F}_L \cdot \nabla_{\mathbf{p}} f_e$ , where the Lorentz-Laplace force  $\mathbf{F}_L = q_e(\mathbf{E} + \mathbf{v} \times \mathbf{B})$  relates to the electric and magnetic fields  $\mathbf{E}$  and  $\mathbf{B}$ , with  $q_e$  the charge of the electron. The collisions between electrons and species  $s$  are described by the collision operator  $\mathcal{C}(f_e, f_s)$ . There are many steps from the 7D Boltzmann equation to the 3D bounce-averaged drift-kinetic Fokker-Planck equation solved by LUKE. The derivation is described in great details in [Decker and Peysson 2004] and summarized in [Peysson and Decker 2014]. A summary with the main underlying hypotheses is also provided hereafter.

First, the path from the Boltzmann equation to the drift-kinetic equation is detailed. The electric field is expressed as the sum of a background steady-state macroscopic field  $\bar{\mathbf{E}}(\mathbf{x})$  and a time-varying component representing the externally launched waves, expanded in Fourier series  $\tilde{\mathbf{E}}_{\mathbf{k}}$  (and similarly for the magnetic field)

$$\begin{aligned} \mathbf{E}(\mathbf{x}, t) &= \bar{\mathbf{E}}(\mathbf{x}) + \int \tilde{\mathbf{E}}_{\mathbf{k}} \exp(i(\mathbf{k} \cdot \mathbf{x} - \omega t)) d\mathbf{k} \\ \mathbf{B}(\mathbf{x}, t) &= \bar{\mathbf{B}}(\mathbf{x}) + \int \tilde{\mathbf{B}}_{\mathbf{k}} \exp(i(\mathbf{k} \cdot \mathbf{x} - \omega t)) d\mathbf{k} \end{aligned} \quad (3.38)$$

with  $\mathbf{k}$  and  $\omega$  the wave vector and the wave angular frequency. In LUKE, the Fokker-Planck equation is solved at time scales of the order of the characteristic time for collisions and particle orbit bounce, which are the primary time scales for treating the effect of the wave absorption on the electron distribution, as it is governed by the balance between the wave momentum transfer rate and the collisional slowing down. The kinetic equation is then averaged over the faster time scales, namely the wave oscillation time scale  $2\pi/\omega$  and the

gyro-motion time scale  $2\pi/\Omega_{c,e}$ , with  $\Omega_{c,e}$  the electron cyclotron pulsation. Performing the time-averaging over the wave oscillation time scale yields

$$\frac{\partial \bar{f}_e}{\partial t} + \mathbf{v} \cdot \nabla_{\mathbf{x}} \bar{f}_e + q_e (\bar{\mathbf{E}} + \mathbf{v} \times \bar{\mathbf{B}}) \cdot \nabla_{\mathbf{p}} \bar{f}_e = \sum_s \mathcal{C}(\bar{f}_e, \bar{f}_s) - \int_0^{2\pi/\omega} \sum_{\mathbf{k}} [q_e (\bar{\mathbf{E}}_{\mathbf{k}} + \mathbf{v} \times \bar{\mathbf{B}}_{\mathbf{k}}) \cdot \nabla_{\mathbf{p}} f_e] dt \quad (3.39)$$

with the wave-oscillation-period averaged distribution function  $\bar{f}_e = \int_0^{2\pi/\omega} f_e dt$ . The time  $t$  in equation 3.39 is implicitly assumed to be longer than the wave oscillation period, i.e.  $t \gg 2\pi/\omega$ . It is possible to define the wave-plasma interaction operator  $\mathcal{Q}(\bar{f}_e)$  by

$$\mathcal{Q}(\bar{f}_e) = - \int_0^{2\pi/\omega} \sum_{\mathbf{k}} [q_e (\bar{\mathbf{E}}_{\mathbf{k}} + \mathbf{v} \times \bar{\mathbf{B}}_{\mathbf{k}}) \cdot \nabla_{\mathbf{p}} f_e] dt \quad (3.40)$$

which corresponds to the so-called quasilinear term, as it depends on the wave fields and on the linear response of the plasma to these perturbative fields. This operator and its expression are the object of the next subsection. Assuming a strong magnetic field, i.e.  $\Omega_{c,e} \gg \nu_c$  and  $\Omega_{c,e} \gg \tau_b^{-1}$  where  $\nu_c$  is the collision frequency and  $\tau_b$  is the particle bounce characteristic time, the distribution function can be expanded with respect to the small parameter  $\delta_t \sim 1/(\tau_b \Omega_{c,e}) \sim \nu_c/\Omega_{c,e}$  in  $\bar{f}_e = \bar{f}_{e,0} + \bar{f}_{e,1} + O(\delta_t^2)$ . From the zeroth order in  $\delta_t$  of equation 3.39, it is possible to state that  $\bar{f}_{e,0}$  is independent of the gyro-angle  $\varphi$ , and so, of the gyro-motion (the velocity space can be projected as  $(p_{\parallel}, p_{\perp}, \varphi)$ , where the parallel and perpendicular directions are with respect to the magnetic field  $\bar{\mathbf{B}}$ ). The first order of equation 3.39 reads

$$\frac{\partial \bar{f}_{e,0}}{\partial t} + \mathbf{v} \cdot \nabla_{\mathbf{x}} \bar{f}_{e,0} + q_e \bar{\mathbf{E}} \cdot \nabla_{\mathbf{p}} \bar{f}_{e,0} + q_e (\mathbf{v} \times \bar{\mathbf{B}}) \cdot \nabla_{\mathbf{p}} \bar{f}_{e,1} = \sum_s \mathcal{C}(\bar{f}_{e,0}, \bar{f}_{s,0}) + \mathcal{Q}(\bar{f}_{e,0}) \quad (3.41)$$

Equation 3.41 is then averaged over the gyro-motion. The gyro-averaged distribution is given by  $\tilde{f}_{e,0} = \int_0^{2\pi} \bar{f}_{e,0} d\varphi$  and the velocity of the particle guiding center by  $\mathbf{v}_{GC} = \int_0^{2\pi} \mathbf{v} d\varphi$ . By definition, the gyro-motion term  $q_e (\mathbf{v} \times \bar{\mathbf{B}}) \cdot \nabla_{\mathbf{p}} \bar{f}_{e,1}$  averages out to zero. The remaining electric field term reduces to its parallel component with respect to the magnetic field, which can be expressed in the form of an operator  $\mathcal{E}(\tilde{f}_{e,0}) = -q_e \bar{E}_{\parallel} \partial \tilde{f}_{e,0} / \partial p_{\parallel}$ . This operator translates the effects of the induced Ohmic electric field. Using the fact that the distribution  $\tilde{f}_{e,0}$  is independent of the gyro-angle, the gyro-averaged kinetic equation, or so-called drift-kinetic equation, that describes the transport of the 6D (5D + time) distribution function  $\tilde{f}_{e,0}(\mathbf{x}, p_{\parallel}, p_{\perp}, t)$ , reads

$$\frac{\partial \tilde{f}_{e,0}}{\partial t} + \mathbf{v}_{GC} \cdot \nabla_{\mathbf{x}} \tilde{f}_{e,0} = \sum_s \mathcal{C}(\tilde{f}_{e,0}, \tilde{f}_{s,0}) + \mathcal{Q}(\tilde{f}_{e,0}) + \mathcal{E}(\tilde{f}_{e,0}). \quad (3.42)$$

The drift-kinetic approximation is similar to assuming the electron Larmor radius tends to zero, meaning that zero width electron banana orbits are considered and that some neoclassical effects are excluded from the drift-kinetic simulations (e.g. the bootstrap current calculation). For axisymmetric configurations, such as ripple-free tokamaks, the 6D (5D + time) space  $(\mathbf{x}, p_{\parallel}, p_{\perp}, t)$  reduces to the 5D (4D + time) one  $(\rho_{\psi_p}, \theta, p_{\parallel}, p_{\perp}, t)$  where  $\rho_{\psi_p}$  is the poloidal-flux-based normalized radius and  $\theta$  is the poloidal angle. A description of the different coordinate

systems, for configuration space and velocity space, is given in appendix C.

The drift kinetic equation 3.42 can be expanded with respect to the small parameter  $\delta_D \equiv \tau_p/\tau_D \ll 1$ , where  $\tau_p$  is the transit time of passing particles, or equivalently the time it takes for a passing particle to complete one toroidal turn, and  $\tau_D$  is the characteristic drifting time of particles, assuming the guiding center velocity can be expressed as  $\mathbf{v}_{GC} = v_{\parallel} \mathbf{e}_{\parallel} + \mathbf{v}_D$  with  $v_{\parallel}$  the fast velocity along the magnetic field lines and  $\mathbf{v}_D$  the slower drift of the particles. The small parameter  $\delta_D$  can be expressed in terms of the plasma minor radius  $a$  and the electron Larmor radius  $\rho_{L,e}$  as  $\delta_D \sim \rho_{L,e}/a \ll 1$ . Under this small drift approximation, the distribution function is expanded in  $\tilde{f}_{e,0} = \tilde{f}_{e,00} + \tilde{f}_{e,01} + O(\delta_D^2)$  and the first order Fokker-Planck equation reads

$$\frac{\partial \tilde{f}_{e,00}}{\partial t} + v_{s\theta} \frac{\partial \tilde{f}_{e,00}}{\partial s_{\theta}} = \sum_s \mathcal{C}(\tilde{f}_{e,00}, \tilde{f}_{s,00}) + \mathcal{Q}(\tilde{f}_{e,00}) + \mathcal{E}(\tilde{f}_{e,00}) \quad (3.43)$$

where  $s_{\theta}$  is the poloidal distance along a given magnetic flux surface, or equivalently the length along a poloidal magnetic field line, and  $v_{s\theta} = v_{\parallel}(\mathbf{e}_{\parallel} \cdot \mathbf{e}_{s\theta})$  is the poloidal component of the parallel velocity due to the shearing of the magnetic field lines, or, equivalently, due to the poloidal component of the total magnetic field. In the low collision regime, i.e. when  $\nu^* \equiv \tau_b \nu_c^{eff} \ll 1$  with  $\tau_b = \int v_{s\theta}^{-1} ds_{\theta}$  the bounce characteristic time of particle (half a bounce period for trapped particles or a complete orbit period for passing particles) and  $\nu_c^{eff} = (R_p/a)\nu_c$  the effective collision frequency (particle detrapping frequency due to collisions), it is found that  $\partial \tilde{f}_{e,00}/\partial s_{\theta} = 0$ , meaning that the distribution function  $\tilde{f}_{e,00}$  is constant along the magnetic field lines. This low collision approximation translates the fact that the parallel motion of particles is fast enough with respect to the collision characteristic time so they can complete several orbits before being kicked onto another orbit trajectory by collisions.

Finally, the Fokker-Planck equation 3.43 is bounce-averaged. The bounce-averaging operator reads

$$\langle \cdot \rangle_b = \frac{1}{\tau_b} \left[ \frac{1}{2} \sum_{\sigma=\pm 1} \right] \int_{s_{\theta,min}}^{s_{\theta,max}} \frac{ds_{\theta}}{v_{s\theta}} \quad (3.44)$$

where the sum over  $\sigma = \text{sign}(v_{\parallel})$  applies only to trapped particles and  $s_{\theta,min}$  and  $s_{\theta,max}$  are the positions on the poloidal flux surface at maximum magnetic field. By construction, this operator exactly cancels the guiding-center term of the drift-kinetic equation  $\langle \mathbf{v}_{GC} \cdot \nabla_{\mathbf{x}} \tilde{f}_{e,0} \rangle_b = 0$ . Using the fact that, in the low collisionality regime,  $\tilde{f}_{e,00}$  is constant along the magnetic field lines, the bounce-averaging allows to solve the Fokker-Planck equation only at the poloidal location  $\theta_0$ , corresponding to the poloidal location of the minimum magnetic field  $\bar{B}_0(\rho_{\psi_p}) = \bar{B}(\rho_{\psi_p}, \theta_0) = \min_{\theta}(\bar{B}(\rho_{\psi_p}, \theta))$ . In practice, LUKE solves the quasilinear bounce-averaged Fokker-Planck equation on the 3D grid  $(\rho_{\psi_p}, p, \xi = p_{\parallel}/p)$  (see appendix C). The poloidal angle dependency is removed by solving Fokker-Planck equation for the pitch-angle cosine  $\xi_0(\rho_{\psi_p}) = \xi(\rho_{\psi_p}, \theta_0)$  only. By using the kinetic energy, proportional to  $p^2$ , which is a constant of the motion and the magnetic moment, proportional to  $(1 - \xi^2)/B$ , which is an adiabatic invariant, it is possible to calculate the pitch-angle cosine at any other location by  $1 - \xi^2 = (1 - \xi_0^2) \bar{B}(\rho_{\psi_p}, \theta) / \bar{B}_0(\rho_{\psi_p})$ , and to project the distribution function at these locations

[Peysson and Decker 2014]. The 4D (3D + time) bounce-averaged Fokker-Planck equation in  $(\rho_{\psi_p}, p_{\parallel}, p_{\perp}, t)$  space, which can be projected in the  $(\rho_{\psi_p}, p, \xi, t)$  space, is then

$$\frac{\partial}{\partial t} \langle \tilde{f}_{e,00} \rangle_b = \sum_s \langle \mathcal{C}(\tilde{f}_{e,00}, \tilde{f}_{s,00}) \rangle_b + \langle \mathcal{Q}(\tilde{f}_{e,00}) \rangle_b + \langle \mathcal{E}(\tilde{f}_{e,00}) \rangle_b + \langle \mathcal{S}(\tilde{f}_{e,00}) \rangle_b \quad (3.45)$$

where  $\langle \tilde{f}_{e,00} \rangle_b(\rho_{\psi_p}, p_{\parallel}, p_{\perp}, t)$  is the bounce-averaged distribution function and  $\langle \mathcal{S}(\tilde{f}_{e,00}) \rangle_b$  is an optional additional ad-hoc radial transport term, which is used to emulate the missing ingredients in LUKE, such as turbulent transport. The use of this transport term is detailed in chapter 4. The bounce-averaged Fokker-Planck equation 3.45 can be rewritten as

$$\left\langle \frac{\partial f_e}{\partial t} \right\rangle_b = \left\langle \sum_s \mathcal{C}(f_e, f_s) + \mathcal{Q}(f_e) + \mathcal{E}(f_e) + \mathcal{S}(f_e) \right\rangle_b \quad (3.46)$$

defining  $f_e \equiv \tilde{f}_{e,00}$  for the rest of section 3.2.1 to lighten the notations, and recalling that this equation has been obtained by averaging the Boltzmann equation 3.37 over the fast time scales (wave oscillation period  $t \gg 2\pi/\omega$  and cyclotron frequency  $t \gg 2\pi/\Omega_{c,e}$ ), expanding it under the small drift approximation and in the low collision regime ( $\rho_{L,e}/a \ll \nu^* \ll 1$ ), and bounce-averaging it. In LUKE, the collision operators (electron-ion and electron-electron) are linearized, meaning that equation 3.45 is linear too, or quasilinear when the wave operator is considered.

From the conservation of the number of particles, it is possible to write the Fokker-Planck equation in a flux conservative form in the 3D phase space  $(\rho_{\psi_p}, p_{\parallel}, p_{\perp})$

$$\left\langle \frac{\partial f_e}{\partial t} + \sum_{\mathcal{O}} \nabla \cdot \mathbf{S}_{\mathcal{O}}(f_e) \right\rangle_b = 0 \quad (3.47)$$

where the fluxes  $\mathbf{S}_{\mathcal{O}}$  associated with the operators  $\mathcal{O}$  (typically  $\mathcal{C}$ ,  $\mathcal{Q}$ ,  $\mathcal{E}$  and  $\mathcal{S}$ ) are expressed in a diffusive-convective form

$$\mathbf{S}_{\mathcal{O}}(f_e) = -\mathbb{D}_{\mathcal{O}} \cdot \nabla f_e + \mathbf{V}_{\mathcal{O}} f_e \quad (3.48)$$

with  $\mathbb{D}_{\mathcal{O}}$  the diffusion tensor and  $\mathbf{V}_{\mathcal{O}}$  the convection velocity. For an operator  $\mathcal{O}$  acting in the velocity space  $(p, \xi = p_{\parallel}/p)$  only, it is possible to write  $\mathcal{O} = \nabla_{\mathbf{p}} \cdot \mathbf{S}_{\mathcal{O},\mathbf{p}}$  with  $\mathbf{S}_{\mathcal{O},\mathbf{p}} = (S_{\mathcal{O},p}, S_{\mathcal{O},\xi})$  and

$$S_{\mathcal{O},p} = -D_{\mathcal{O}}^{pp} \frac{\partial f_e}{\partial p} + \frac{\sqrt{1-\xi^2}}{p} D_{\mathcal{O}}^{p\xi} \frac{\partial f_e}{\partial \xi} + V_{\mathcal{O}}^p f_e \quad (3.49)$$

$$S_{\mathcal{O},\xi} = -D_{\mathcal{O}}^{\xi p} \frac{\partial f_e}{\partial p} + \frac{\sqrt{1-\xi^2}}{p} D_{\mathcal{O}}^{\xi\xi} \frac{\partial f_e}{\partial \xi} + V_{\mathcal{O}}^{\xi} f_e \quad (3.50)$$

where the coefficients  $D_{\mathcal{O}}^{pp}$ ,  $D_{\mathcal{O}}^{p\xi}$ ,  $D_{\mathcal{O}}^{\xi p}$  and  $D_{\mathcal{O}}^{\xi\xi}$  are the components of the diffusion tensor  $\mathbb{D}_{\mathcal{O},\mathbf{p}}$  in the  $(p, \xi)$  velocity space, and  $V_{\mathcal{O}}^p$  and  $V_{\mathcal{O}}^{\xi}$  are the components of the convection velocity vector  $\mathbf{V}_{\mathcal{O},\mathbf{p}}$ .

The linear collision operator takes the form of a diffusive-convective flux in velocity space only  $\mathcal{C}(f_e, f_s) = \nabla \cdot (\mathbb{D}_{\mathcal{C}, \mathbf{p}}^{es} \cdot \nabla_{\mathbf{p}} f_e - \mathbf{V}_{\mathcal{C}, \mathbf{p}}^{es} f_e)$ . In the  $(p, \xi)$  space, it reads

$$\mathbb{D}_{\mathcal{C}, \mathbf{p}}^{es} = \begin{pmatrix} A_{\mathcal{C}}^{es} & 0 \\ 0 & B_{\mathcal{C}}^{es} \end{pmatrix} ; \quad \mathbf{V}_{\mathcal{C}, \mathbf{p}}^{es} = \begin{pmatrix} V_{\mathcal{C}, p}^{es} \\ 0 \end{pmatrix}. \quad (3.51)$$

For the electron-electron collisions, the coefficients  $A_{\mathcal{C}}^{es}$ ,  $B_{\mathcal{C}}^{es}$  and  $V_{\mathcal{C}, p}^{es}$  are derived from a linearized relativistic operator [Braams and Karney 1989], while for the electron-ion collisions, the linearized non-relativistic operator assumes a Maxwellian distribution for the ions [Karney 1986]. A detailed derivation is available in [Decker and Peysson 2004]. This operator is responsible for the Maxwellian relaxation (or thermalization) of the distribution function. It is important to note that, in the presence of another source term like the quasilinear flux from external wave absorption by the plasma, some dissipation of the energy has to be introduced in the simulation so that the electron temperature and density profiles remain as prescribed and the simulation can converge, since the profiles are not self-consistently calculated. This energy dissipation is naturally introduced through the linearized electron-electron collision operator, which is momentum conserving but not energy conserving.

The bounce-averaged electric Ohmic field operator reduces to a purely convective operator in velocity space, while the ad-hoc additional transport term can take the form of a diffusive-convective operator in configuration space  $\mathcal{S} = \nabla_{\mathbf{x}} \cdot \mathbf{S}_{\mathcal{S}}$  with  $\mathbf{S}_{\mathcal{S}} = -\mathbb{D}_r \cdot \nabla_{\mathbf{x}} f_e + \mathbf{V}_r f_e$ . In the 3D space  $(\rho_{\psi_p}, p_{\parallel}, p_{\perp})$ , it reads

$$\mathbb{D}_r = D_{r0} g_D(\rho_{\psi_p}, p_{\parallel}, p_{\perp}) \begin{pmatrix} 1 & 0 & 0 \\ 0 & 0 & 0 \\ 0 & 0 & 0 \end{pmatrix} ; \quad \mathbf{V}_r = V_{r0} g_V(\rho_{\psi_p}, p_{\parallel}, p_{\perp}) \begin{pmatrix} 1 \\ 0 \\ 0 \end{pmatrix}. \quad (3.52)$$

The models  $g_D$  and  $g_V$  and values  $D_{r0}$  and  $V_{r0}$  for the diffusion tensor and convection velocity are set by the user. This operator acts as a radial transport of electrons.

The quasilinear diffusive operator accounting for the plasma-wave interaction is detailed in the next subsection. An illustration of the electron distribution function calculated by LUKE, including different operators in the Fokker-Planck equation, is given in figure 3.11. When no Ohmic electric field nor external waves are acting on the plasma, the distribution remains Maxwellian under the influence of collisions. The Ohmic electric field shifts the distribution in the  $\pm p_{\parallel}$  direction, depending on its own direction. This shift increases gradually with the particle momentum  $p$ , as the collisionality decreases. For EC waves, the absorption is localized in velocity space around the resonance location [Prater 2004]. The EC waves give a kick to the electrons in the  $p_{\perp}$  direction, pumping particles from the bulk up to suprathermal energies. The hole generated in the distribution by the EC waves is filled due to collisional transport (see section 1.3 and [Prater 2004] for details on the different mechanisms).

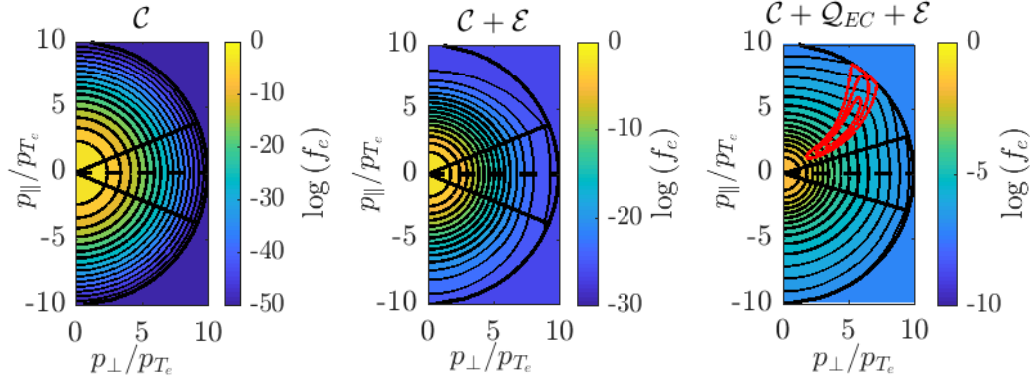


Figure 3.11: Electron distribution function in  $(p_{\parallel}, p_{\perp})$  velocity space from LUKE simulations, using different operators: collisions only (*left*), collisions and Ohmic electric field (*center*) and collisions, Ohmic electric field and EC waves (*right*). Parallel and perpendicular momenta are normalized to the thermal momentum  $p_{T_e}$ . The red contour on the *right* panel represents the wave-related diffusion coefficient. Note that here, the EC wave is oriented in counter-ECCD.

### The quasilinear wave operator

As stated in the previous subsection, the wave-plasma interaction operator, defined by equation 3.40, can be written in the form a quasilinear diffusive Fokker-Planck operator. This formalism has been initially developed by [Kennel and Engelmann 1966], and augmented with relativistic effects by [Lerche 1968]. Two main hypotheses are made to develop this formalism. First, an infinite uniform medium is considered. This approximation is valid in a typical non-uniform tokamak plasmas, provided the plasma profiles and magnetic field do not vary much within the range of the plasma-wave interaction area. This is the case for an EC wave propagating obliquely with respect to the resonance layer, for which the wave absorption takes place in a narrow region of the plasma [Prater 2004]. On the other hand, the distribution is assumed to evolve slowly with respect to the wave propagation time, which justifies the fast time scale averaging needed to obtain the Fokker-Planck equation 3.46, which is then solved by LUKE. The detailed derivation of the quasilinear wave-plasma interaction is available in [Decker and Peysson 2004; Koch 2006; Donnel et al. 2021], and a summary is adapted from [Donnel et al. 2021] in this thesis.

For EC waves, the quasilinear wave-plasma interaction operator  $\mathcal{Q}_{EC}$  can be written as [Koch 2006]

$$\mathcal{Q}_{EC} = \sum_{n=-\infty}^{+\infty} \mathcal{Q}_{EC,n} = \sum_{n=-\infty}^{+\infty} [\nabla_{\mathbf{p}} \cdot (\mathbb{D}_{EC,n} \cdot \nabla_{\mathbf{p}} f_e)] \quad (3.53)$$

with  $n$  the wave harmonic number. For a monochromatic wave of angular frequency  $\omega$ , by expressing the wave electric field  $\tilde{\mathbf{E}}$  as a Fourier series, similarly to what is done in equations 3.38, one obtains

$$\tilde{\mathbf{E}}(\mathbf{x}, t) = \iiint \tilde{\mathbf{E}}_{\mathbf{k}}(\mathbf{k}, \omega) \exp(i\mathbf{k} \cdot \mathbf{x} - \omega t) \frac{d^3 k}{(2\pi)^3} \quad (3.54)$$

and the diffusion coefficient  $\mathbb{D}_{EC,n}$  in the  $(p_{\parallel}, p_{\perp})$  velocity space reads

$$\mathbb{D}_{EC,n} = \pi e^2 \lim_{V_k \rightarrow 0} \frac{1}{V_k} \iiint |\Pi_n^{\dagger} \tilde{\mathbf{E}}_{\mathbf{k}}|^2 \mathbf{s}_n \mathbf{s}_n^T \delta \left( \omega - k_{\parallel} v_{\parallel} - \frac{n\Omega_{c,e}}{\gamma} \right) \frac{d^3 k}{(2\pi)^3} \quad (3.55)$$

with  $V_k$  the integral volume in  $k$  space and where  $^T$  stands for transpose and  $^{\dagger}$  for conjugate transpose. The  $\delta$  function is such that  $\delta(0) = 1$  and represents the resonance condition for the wave-plasma energy transfer. The direction of diffusion in velocity space is given by the dyadic product  $\mathbf{s}_n \mathbf{s}_n^T$  with the vector  $\mathbf{s}_n$  defined by

$$\mathbf{s}_n = \begin{pmatrix} s_n^{\parallel} \\ s_n^{\perp} \end{pmatrix} = \begin{pmatrix} k_{\parallel} v_{\perp} / \omega \\ n\Omega_{c,e} / (\gamma \omega) \end{pmatrix} \quad (3.56)$$

so that

$$\mathbb{D}_{EC,n} = D_{EC,n} \mathbf{s}_n \mathbf{s}_n^T = D_{EC,n} \begin{pmatrix} (s_n^{\parallel})^2 & s_n^{\parallel} s_n^{\perp} \\ s_n^{\perp} s_n^{\parallel} & (s_n^{\perp})^2 \end{pmatrix} = \begin{pmatrix} D_{EC,n}^{\parallel\parallel} & D_{EC,n}^{\parallel\perp} \\ D_{EC,n}^{\perp\parallel} & D_{EC,n}^{\perp\perp} \end{pmatrix} \quad (3.57)$$

with  $D_{EC,n}$  the diffusion coefficient. In the Cartesian basis  $(\mathbf{e}_x, \mathbf{e}_y, \mathbf{e}_{\parallel})$ , the electric field projection reads

$$\Pi_n^{\dagger} \tilde{\mathbf{E}}_{\mathbf{k}} = J_{n-1}(\rho_e) \frac{\tilde{E}_{\mathbf{k},+}}{\sqrt{2}} + J_{n+1}(\rho_e) \frac{\tilde{E}_{\mathbf{k},-}}{\sqrt{2}} + \frac{v_{\parallel}}{v_{\perp}} J_n(\rho_e) \tilde{E}_{\mathbf{k},\parallel} \quad (3.58)$$

where  $J_n$  is the  $n$ th Bessel function of first kind and the argument  $\rho_e = k_{\perp} v_{\perp} \gamma / \Omega_{c,e}$  accounts for the finite Larmor radius effects. These electron Larmor radius effects are kept in the expression of the diffusion coefficient, even though the drift-kinetic approximation is assumed in the Fokker-Planck equation solved by LUKE. Allowing  $\rho_e$  to go to zero would lead to all the terms but  $J_0$  vanishing, making the treatment of the absorption of harmonics  $n \geq 2$  impossible. The electric field components  $\tilde{E}_{\mathbf{k},+}$  and  $\tilde{E}_{\mathbf{k},-}$  are the left-handed and right-handed polarized components, respectively, defined by

$$\tilde{E}_{\mathbf{k},\pm} = \frac{\tilde{E}_{\mathbf{k},x} \pm i \tilde{E}_{\mathbf{k},y}}{\sqrt{2}}. \quad (3.59)$$

In LUKE, the flux resulting from the EC wave quasilinear diffusion is then bounce-averaged.

The transferred power from/to the plasma to/from the waves is given by the time variation of the electron relativistic kinetic energy, which corresponds to the second order moment of the electron distribution function [Koch 2006], the zeroth order being the electron density  $n_e(\mathbf{x}, t) = \int f_e(\mathbf{x}, \mathbf{p}, t) d\mathbf{p}$  and the first order the electron current density  $\mathbf{j}_e(\mathbf{x}, t) = q_e \int \mathbf{p} f_e(\mathbf{x}, \mathbf{p}, t) d\mathbf{p}$ . It is then possible to write the general expression

$$\begin{aligned} \frac{\partial P_{EC,n}}{\partial V} &= \frac{\partial}{\partial t} \int (\gamma - 1) m_e c^2 f_e(\mathbf{x}, \mathbf{p}, t) d\mathbf{p} \\ &= \int (\gamma - 1) m_e c^2 [\nabla_{\mathbf{p}} \cdot (\mathbb{D}_{EC,n} \cdot \nabla_{\mathbf{p}} f_e(\mathbf{x}, \mathbf{p}, t))] d\mathbf{p} \end{aligned} \quad (3.60)$$

with  $\partial P_{EC,n} / \partial V$  the transferred power density (in W/m<sup>3</sup>) due to the plasma interaction with

the  $n$ th harmonic of the EC wave. From equation 3.60, it is possible to see that the deposited power depends on the distribution function, which depends on the deposited power through the wave electric field dependence of the diffusion tensor, the wave damping changing the amplitude of the electric field. For substantially distorted distributions, i.e. for high absorbed power density leading to non-Maxwellian distributions, this non-linear dependency becomes important, and self-consistency is required in the calculation of the deposited power. In LUKE, this is achieved by iteratively calculating the distribution function in a convergence loop. This is the object of the next subsection.

#### Calculation modes

The calculation of the electron distribution function performed by LUKE relies on a main convergence loop over the power deposition profile. This is illustrated in figure 3.12, by the red box labeled *LUKE - RF loop*. An initial Maxwellian electron distribution function is assumed in order to estimate the linear power deposition profile  $P_{abs}^L$  from the ray-tracing results. This result is used to provide a first estimate of the quasilinear diffusion coefficient  $D_{EC,n}$ , which is injected in the Fokker-Planck equation to provide the distorted electron distribution function. This new distribution is then used to estimate the quasilinear wave power deposition profile  $P_{abs}^{QL}$ . Starting from this point, the electron distribution function and the quasilinear wave power deposition profile are iteratively calculated until a convergence on the power deposition is reached (the default criterion is a relative gap below 1 % between two consecutive calculated power deposition profiles).

The default calculation mode of LUKE is the time-asymptotic mode, which considers a radially constant loop voltage profile, meaning that the induced electric field has diffused and completely relaxed over time. In this limit, the electric field operator  $\mathcal{E}$  is calculated from the input loop voltage  $V_{loop}$ . For this type of simulations, the plasma current is not constrained, and can be used to compare the simulations and the experiments. In TCV, this loop voltage is given by magnetic probe measurements and is a proxy for the Ohmic electric field at the edge of the plasma.

However, the hypothesis of fully diffused electric field is not always valid, in particular in the case of an intermittent current source, for instance for fast power-modulated ECCD as in [Choi et al. 2020a] and in chapter 4. The other calculation limit implemented in LUKE for such cases is the frozen current density mode. In this mode, illustrated in figure 3.12 by the green box labeled *LUKE - Ohmic loop*, the total plasma current  $I_p$  or the plasma current density profile  $j_p$  is constrained by the user, and the electric field profile  $E_{||}$  is automatically and iteratively adjusted so the current constraint is matched. In that case, it is not possible to use the measured current to compare experiments and simulations, and other observables have to be found. An example is hard X-ray measurements from fast electron Bremsstrahlung or microwave measurements of emitted radiation from the cyclotron motion of electrons. In LUKE, a synthetic diagnostic for the HXRS diagnostic is used, using the fast electron Bremsstrahlung module R5-X2 [Peysson and Decker 2008], which estimates the line-integrated hard X-ray



emission from the non-thermal electron distribution function calculated by LUKE, taking into account the HXRS geometry and a cadmium telluride photodiode response model based on experimental calibration [Choi et al. 2020b]. It is important to recall that, in LUKE, the width of the banana orbits is considered infinitely small; therefore, no neoclassical effects such as bootstrap current are included in the simulations. It is then important to remove the bootstrap current contribution from the experimental measurements before comparing with LUKE in the time-asymptotic mode, or before constraining the frozen-current mode.

LUKE runs in steady-state, but it is also possible to run dynamical simulations. These dynamical simulations are performed by solving the Fokker-Planck equation, initiating the calculation at a given time step with the calculated distribution function from the previous time step, the first time step being initiated by a Maxwellian distribution function, as for the steady-state simulations. The calculation at each time step then follows the calculation scheme given in figure 3.12. As described in [Decker et al. 2012], this means that, at each time step, the RF convergence loop ensures that the wave energy transport equation is solved consistently with the distribution function, assuming an instantaneous response of the EC wave damping to any change in the distribution function. Because the wave power propagation time is very short, the RF convergence loop is independent of the kinetic equation time evolution.

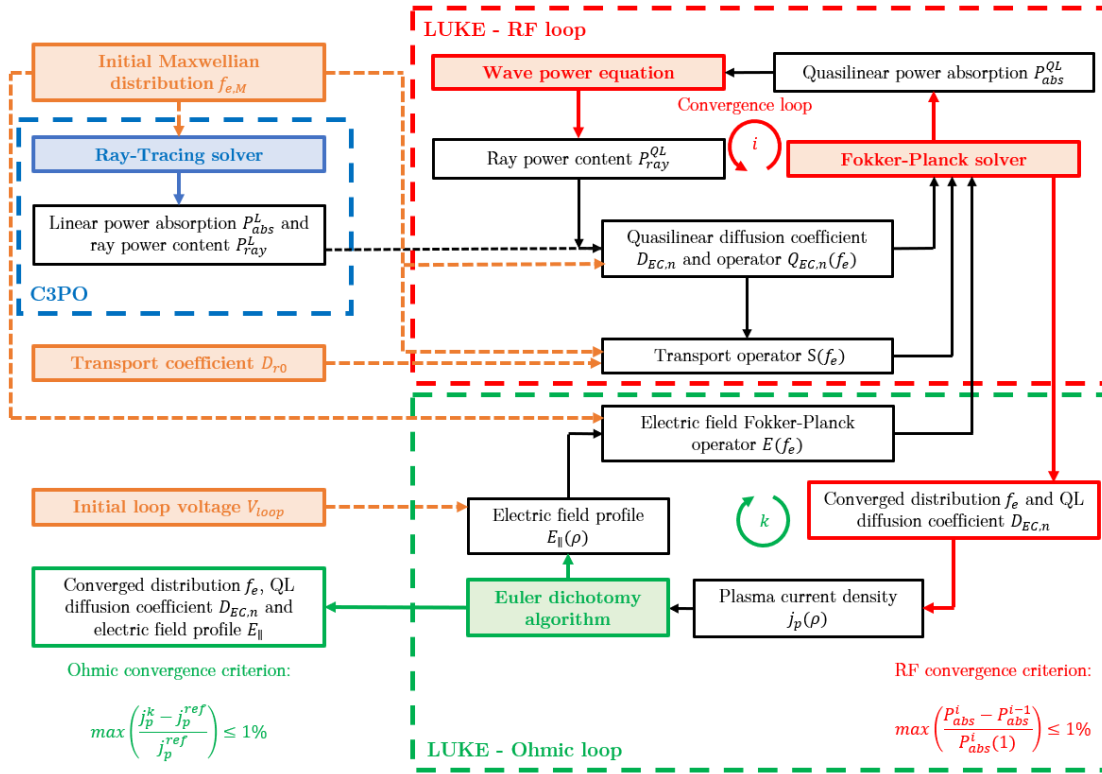


Figure 3.12: LUKE calculation and convergence scheme for the frozen current density mode. A first convergence loop over the wave power deposition calculation is performed [Peysson et al. 2011], included in a second convergence loop over the current density profile.

### 3.2.2 ORB5: the global flux-driven gyro-kinetic code

In LUKE, since the Fokker-Planck equation is linearized and bounce-averaged, non-linear turbulence cannot develop ab initio. Instead, turbulent transport is modeled using an ad-hoc radial transport term, used in forward simulation to match experimental data. To be able to study the wave-enhanced transport of fast electrons from first principles, inferred from the fact that an ad-hoc radial transport term is required in the drift-kinetic simulations of ECRH/ECCD experiments to recover the experimental results [Coda et al. 2003a; Nikkola et al. 2003; Choi et al. 2020a], other tools need to be developed. This state of affairs has motivated the development of a realistic EC source in the global flux-driven gyro-kinetic code ORB5, leading to two co-authored publications in *Plasma Physics and Controlled Fusion* [Donnel et al. 2021, 2022]. Parts of these papers, in particular the benchmark against LUKE, are adapted for this thesis, in the next subsections.

#### Principle

The global particle-in-cells flux-driven gyro-kinetic code ORB5 [Lanti et al. 2020] solves the Vlasov-Maxwell system of equations for both the ions and the electrons. Symbolically, the Vlasov part can be written as a system of non-linear Boltzmann equations (Vlasov equations in presence of collisions and other flux sources), averaged over the fast gyro-angle, reducing the 7D (6D + time) space to the 6D (5D + time) space  $(\mathbf{x}, p_{\parallel}, p_{\perp}, t)$

$$\frac{\partial f_e}{\partial t} + \{f_e, H_e\} = \sum_s \mathcal{C}(f_e, f_s) + \sum_{n=-\infty}^{+\infty} \mathcal{Q}_{EC,n} \quad (3.61)$$

$$\frac{\partial f_i}{\partial t} + \{f_i, H_i\} = \sum_s \mathcal{C}(f_i, f_s) \quad (3.62)$$

where  $f_e$  and  $f_i$  are the electron and ion distribution functions respectively, and the notations are similar to those of equation 3.37. To reduce the numerical cost of the gyro-kinetic simulations, the drift-kinetic approximation is made for the electrons and only the distribution of their guiding center is considered, while finite Larmor radius effects are kept for the ions. The Lagrangian particle-in-cells approach means that the Maxwell equations for the electric and magnetic fields are solved on a grid, while the particles are individually tracked in the 5D phase space, or, in the case of ORB5, markers sampling the phase space and representing the particles. The flux-driven approach signifies that the fluxes, such as defined in equations 3.47 and 3.48, are imposed in the simulations, and the profiles (temperature and density) evolves under their influence. This approach can be contrasted with the gradient-driven approach, where the profile gradients are imposed, so the fluxes evolve to match those gradients.

The Vlasov-Maxwell equation system is consistently coupled to the quasi-neutrality equation that involves the turbulent part of the electric potential  $\delta\phi_E = \phi_E - \langle\phi_E\rangle_{f_s}$ , where  $\phi_E$  is the local electric potential and  $\langle\cdot\rangle_{f_s}$  denotes the flux surface averaging. Different assumptions can be made about the distribution functions used in the estimation of the density entering in the

quasi-neutrality equation. The later reads

$$\sum_i \left( q_i \int f_i d\mathbf{p} \right) - e \int f_e d\mathbf{p} = -\nabla_{\perp} \cdot \left[ \sum_i \frac{m_i n_i}{B^2} \nabla_{\perp} (\phi_E) \right] \quad (3.63)$$

with  $q_i$  and  $m_i$  the charge and mass of ions of the species  $i$ , of density  $n_i = \int f_i d\mathbf{p}$ . In the present work, fully-kinetic ions are considered, meaning that the ion distribution function is the numerical solution of the Vlasov equation, while hybrid electrons are considered. The use of this hybrid electron model, described in [Idomura 2016], means that the trapped electrons are kinetically treated, similarly to the ions, while the passing electrons are assumed to have an adiabatic response, i.e.  $n_e^{pass} = n_{e,0}^{pass} \exp(\delta\phi_E / T_e)$ . The main consequences are that the physics of the ion-temperature-gradient modes and of the trapped-electron modes is captured by ORB5 simulations, but not the physics of the electron-temperature-gradient modes. Fully-kinetic electrons dramatically increases the numerical cost of ORB5 simulations, in particular when considered in conjunction with the quasilinear EC source. Turbulence arises naturally in ORB5 through the non-linear Poisson brackets terms  $\{f_s, H_s\}$ , the non-linear collision operator  $\mathcal{C}$  [Donnel et al. 2020] and the quasilinear diffusion operator  $\mathcal{Q}_{EC}$ , coupled to the quasi-neutrality equation.

#### The wave absorption model

The Fokker-Planck formalism is used to develop a model for the EC wave quasilinear absorption in ORB5, similarly to what is done in LUKE, even though the ORB5 code does not solve the Fokker-Planck equation per se. Indeed, the quasilinear diffusion induced by the wave is translated into stochastic velocity kicks to the markers. The model developed by Dr. Peter Donnel for ORB5 is able to treat pure ECRH [Donnel et al. 2021] as well as ECCD configurations [Donnel et al. 2022], for EC waves propagating on the plasma equatorial midplane.

The starting point for the derivation of the quasilinear operator  $\mathcal{Q}_{EC,n}$  in ORB5 is identical to the development detailed in section 3.2.1, and the diffusion tensor  $\mathbb{D}_{EC,n}$  is identical to equation 3.55. Proceeding to the integration over the volume in  $\mathbf{k}$  space in equation 3.55 is not trivial, in particular because of the resonant term represented by the  $\delta$  function. Assuming a cold plasma dispersion relation and a Gaussian wave electric field intensity of finite width  $w_0$  such that  $k_0 w_0 \ll 1$ , with  $k_0$  the average wavenumber, it is possible to perform this integration, yielding [Donnel et al. 2021]

$$D_{EC,n} \simeq \frac{\pi e^2 N(\langle\theta_0\rangle)}{2\omega} \frac{c}{|\nu_{\parallel}|} |\tilde{\mathbf{E}}|^2 \frac{\sin(\theta_{0,res}) \exp\left(-k_0^2 w_0^2 (\theta_{0,res} - \langle\theta_0\rangle)^2\right) N^2(\theta_{0,res})}{\int_0^{\pi} \sin(\theta_0) \exp\left(-k_0^2 w_0^2 (\theta_0 - \langle\theta_0\rangle)^2\right) N^2(\theta_0) d\theta_0} |\tilde{\Theta}_{k,res}^n|^2 \quad (3.64)$$

where  $\theta_0$  is the angle between the wavevector  $\mathbf{k}$  and the background magnetic field  $\bar{\mathbf{B}}$  such that  $\theta_0 = \pi/2$  is a pure ECRH configuration,  $\langle\theta_0\rangle$  is the mean angle, equivalent to the central ray position given by a ray-tracing code,  $N$  is the cold plasma refractive index; the resonant angle  $\theta_{0,res}$ , resulting from the integration of the  $\delta$  function, is found to fulfill the resonant

condition

$$N(\theta_{0,res}) \cos(\theta_{0,res}) = \left(1 - \frac{n\Omega_{c,e}}{\gamma\omega}\right) \frac{c}{v_{\parallel}} = \lambda_{res}(p_{\parallel}, p_{\perp}). \quad (3.65)$$

In equation 3.64, the electric field  $\tilde{\mathbf{E}}$  is the real electric field amplitude, which has replaced the Fourier transformed amplitude  $\tilde{\mathbf{E}}_{\mathbf{k}}$  using Parseval's theorem. The function  $\tilde{\Theta}_{k,res}^n$ , related to the electric field polarization and including finite Larmor radius effects, is given by

$$\tilde{\Theta}_{k,res}^n = \frac{[1 + C_1(\theta_{0,res})] J_{n+1}(\tilde{\rho}_{res}) + [1 - C_1(\theta_{0,res})] J_{n-1}(\tilde{\rho}_{res}) - 2C_2(\theta_{0,res}) \frac{v_{\parallel}}{v_{\perp}} J_n(\tilde{\rho}_{res})}{2\sqrt{1 + C_1^2(\theta_{0,res}) + C_2^2(\theta_{0,res})}} \quad (3.66)$$

where the argument of the Bessel functions of first kind  $J_n$  is the normalized Larmor radius  $\tilde{\rho}_{res} = \sin(\theta_{0,res}) N(\theta_{0,res}) \omega v_{\perp} \gamma / (\Omega_{c,e} c)$ . The functions  $C_1$  and  $C_2$  are defined by

$$\begin{aligned} C_1(\theta_0) &= \frac{D}{S - N^2(\theta_0)} \\ C_2(\theta_0) &= \frac{N^2(\theta_0) \cos(\theta_0) \sin(\theta_0)}{P - N^2(\theta_0) \sin^2(\theta_0)} \end{aligned} \quad (3.67)$$

with  $P$ ,  $D$  and  $S$  the Stix coefficients, as defined in equation 1.13. The cold plasma refractive index for O- and X-polarization reads

$$N_{O/X}^2(\theta_0) = \frac{(RL + SP) \tan^2(\theta_0) + 2SP \pm G_{\theta_0}}{2(S \tan^2(\theta_0) + P)} \quad (3.68)$$

with the function  $G_{\theta_0}$  defined by

$$G_{\theta_0} = \text{sign}(\omega - \Omega_{c,e}) \sqrt{(SP - RL)^2 \tan^4(\theta_0) + P^2 (L - R)^2 (\tan^2(\theta_0) + 1)} \quad (3.69)$$

where  $R$  and  $L$  are the right and left Stix coefficients defined by

$$R/L = \frac{P \mp \frac{\Omega_{c,e}}{\omega}}{1 \mp \frac{\Omega_{c,e}}{\omega}}. \quad (3.70)$$

Now that an explicit expression is given for the wave diffusion coefficient, it is important to proceed to its evaluation to characterize the EC power deposition and its impact on the electron distribution function. This evaluation process is illustrated in figure 3.13. The resonant condition has already been treated, assuming a finite EC beam width, and two important quantities remain to be evaluated to estimate the diffusion coefficient  $D_{EC,n}$ , namely the angle  $\langle\theta_0\rangle$ , which represents the EC beam propagation path, and the wave electric field amplitude  $\tilde{E}$ . This is done by a 2D ray-tracing algorithm and a power balance respectively [Donnel et al. 2022].

A simplified ray-tracing algorithm has been implemented in ORB5 to propagate the EC wave. In particular, the propagation of a central ray is performed, while the finite width of the beam is taken into account in the integration of the quasilinear diffusion coefficient and in the

### Chapter 3. Numerical tools

wave power damping calculation. This algorithm assumes a cold plasma propagation in the equatorial midplane of the plasma, neglecting the poloidal component of the magnetic field. In the Cartesian space  $(R, Z)$ , the equation to solve is then

$$N(\langle\theta_0\rangle)\cos(\langle\theta_0\rangle) = \frac{R_{in}}{R} N(\langle\theta_0\rangle_{in})\cos(\langle\theta_0\rangle_{in}) \quad (3.71)$$

where  $R_{in}$  is the position at which the beam enters the plasma last-closed flux surface and  $\langle\theta_0\rangle_{in}$  is the initial angle at which the beam enters the plasma. Depending if the wave is O- or X-polarized, the propagated central ray position is given by

$$\langle\theta_0\rangle^{O/X} = \begin{cases} \frac{1}{2} \cos^{-1} \left( x_{\mp} \left( \frac{R_{in}^2}{R^2} N^2(\langle\theta_0\rangle_{in}) \cos^2(\langle\theta_0\rangle_{in}) \right) \right) & \text{if: } \langle\theta_0\rangle_{in} \leq \frac{\pi}{2}, \\ \pi - \frac{1}{2} \cos^{-1} \left( x_{\mp} \left( \frac{R_{in}^2}{R^2} N^2(\langle\theta_0\rangle_{in}) \cos^2(\langle\theta_0\rangle_{in}) \right) \right) & \text{else,} \end{cases} \quad (3.72)$$

with  $x_{\mp}$  a function derived from the cold plasma refractive index, which reads

$$x_{\mp}(y) = \frac{P^2(2y-P) + \frac{\Omega_{c,e}^2}{\omega^2} (P(1-y)^2 - y^2) \mp \frac{\Omega_{c,e}}{\omega} (1-P)y \sqrt{\frac{\Omega_{c,e}^2}{\omega^2} (1-y)^2 + 4Py}}{P \left( P^2 - \frac{\Omega_{c,e}^2}{\omega^2} \right) + y \frac{\Omega_{c,e}^2}{\omega^2} (P-1)} \quad (3.73)$$

with  $P$  the Stix coefficient. From this equation, it is also possible to calculate an analytical solution for the resonant angle

$$\theta_{0,res}^{O/X} = \begin{cases} \frac{1}{2} \cos^{-1} (x_{\mp}(\lambda_{res}^2)) & \text{if: } \lambda_{res} \geq 0, \\ \pi - \frac{1}{2} \cos^{-1} (x_{\mp}(\lambda_{res}^2)) & \text{else,} \end{cases} \quad (3.74)$$

where the argument  $\lambda_{res}$  has been defined in equation 3.65.

The wave electric field intensity varies along the beam path due to the wave damping in the plasma. Indeed, in the  $(R, Z, \phi)$  Cartesian coordinate system, the EC power crossing a flux surface reads

$$P_{EC}(R) = \int_0^{2\pi} \int_{-\infty}^{+\infty} \frac{\varepsilon_0 |\tilde{\mathbf{E}}|^2}{2} \mathbf{v}_g \cdot \mathbf{e}_R R dZ d\phi \quad (3.75)$$

where  $\mathbf{v}_g$  is the group velocity associated with the EC wave and  $\varepsilon_0 |\tilde{\mathbf{E}}|^2/2$  is the energy stored in the electric field (in J/m<sup>3</sup>). Assuming that the deposited power is quickly spread toroidally, it is possible to simplify the integration over  $\phi$ , even though the EC beam itself has a finite toroidal extent. Considering a Gaussian beam electric field intensity of width  $w_0$  so that  $|\tilde{\mathbf{E}}|^2 = \tilde{E}_0^2 \exp(-Z^2/w_0^2)$ , it is possible to write

$$\tilde{E}_0^2 = \frac{P_{EC}(R)}{\pi^{3/2} R w_0 \varepsilon_0 |\nu_g| \sin^3(\langle\theta_0\rangle)}. \quad (3.76)$$

Thus, the wave electric field intensity is directly proportional to the wave power, which is damped when crossing the resonance layer in the plasma. The wave power radial evolution can be expressed as  $P_{EC}(R) = P_{EC,in} \exp(-\tau_A(R))$ , with  $\tau_A$  the plasma optical thickness. In ORB5, the wave absorption is estimated from first principles through the quasilinear operator

$\mathcal{Q}_{EC,n}$ . However, there is no feedback estimation of the wave power content  $P_{EC}$ , which can be problematic if the wave power is completely transferred to the plasma over a distance shorter than the resonance layer width. Moreover, the change in the wave power content also changes the diffusion coefficient estimation, and so the absorption properties. Implementing a feedback loop is in theory possible, but at the cost of increasing dramatically the numerical expense of the simulations. Instead, in ORB5, the Albajar quasi-exact analytical model for the optical thickness  $\tau_A$  is used, valid for an EC beam oblique propagation [Albajar et al. 2006]. This model is rather complicated, and is detailed in both [Albajar et al. 2006] and [Donnel et al. 2022]. The Albajar model evaluates the linear wave power damping and is a priori valid at low EC beam power, but ORB5 is still capable of capturing quasilinear effects as the effective transferred power is estimated through the quasilinear diffusion coefficient  $D_{EC,n}$ .

From the diffusion coefficient estimation, it is possible to explicitly express the quasilinear diffusion operator, which reads  $\mathcal{Q}_{EC,n} = \nabla_{\mathbf{p}} \cdot (\nabla_{\mathbf{p}} \cdot (\mathbb{D}_{EC,n} f_e) - \Gamma_{EC,n} f_e)$  with  $\Gamma_{EC,n} = \nabla_{\mathbf{p}} \cdot \mathbb{D}_{EC,n}$  the drag term. Under the small wavelength approximation  $\lambda_0 \ll w_0$ , it is possible to derive analytic expressions for the derivatives of the diffusion coefficient (see [Donnel et al. 2022] for details). This assumption is valid for high density and high magnetic field tokamaks, requiring the use of high-frequency gyrotrons. In the relatively low density, low magnetic field TCV plasma, the typical X2 gyrotron frequency is 82.7 GHz, meaning that  $\lambda_0 = 3.6$  mm, for a beam width  $w_0 = 18.8$  mm, so the short wavelength approximation is only marginally valid.

For low  $p_{\parallel}$ , the drag term diverges because of the width of the resonant area in the perpendicular direction going to zero, and a special treatment has to be applied to circumvent the issue. By considering that the low-velocity bulk plasma is locally close to a Maxwellian, it is possible to express the drag term as  $\Gamma_{EC,n} = \mathbb{D}_{EC,n} \cdot \mathbf{p} / p_{Te}^2$ , assuming a Maxwellian distribution function of electrons for markers with  $p_{\parallel} \leq 0.1 p_{Te}$ . This limit of  $0.1 p_{Te}$  has been set through numerical tests, but is not settled a priori.

As described in [Donnel et al. 2021], since ORB5 is a particle-in-cell code, it does not possess a velocity grid on which it is possible to easily project the quasilinear diffusion operator  $\mathcal{Q}_{EC,n}$ . Therefore, the chosen method to treat the EC wave quasilinear diffusion is to treat the underlying stochastic process using a Monte-Carlo approach. Indeed, the diffusion process in the Fokker-Planck equation can be equivalently seen as a series of random kicks in velocity applied to the particles, or to the markers in the ORB5 case. This stochastic process is found by applying Ito's lemma to the Fokker-Planck operator  $Q_{EC,n}$ , as further detailed in [Donnel et al. 2020] and the references therein for the collision operator, yielding its Langevin form which provides an expression for the kick in velocity  $\Delta \mathbf{v}$  applied to a given marker at a given position in the 5D phase space  $(\mathbf{x}, p_{\parallel}, p_{\perp})$

$$\Delta \mathbf{v} = \Gamma_{EC,n} \Delta t + \sqrt{2D_{EC,n} \Delta t} \mathbf{s}_n R^{\parallel} \quad (3.77)$$

with  $\Delta t$  the time increment and  $R^{\parallel}$  an independent random number distributed over a Gaussian of average zero and standard deviation one.



An analytic TCV-like equilibrium has been generated with the method explained in the appendix of [Görler et al. 2016], with minor radius  $a = 0.25$  m, major radius  $R_0 = 0.89$  m, magnetic field on axis  $B_0 = 1.4$  T, a parabolic safety factor profile  $q(r) = q_0 + (q_a - q_0)(r/a)^2$  (with  $q_0 = 1$ ,  $q_a = 3$  and  $r = R - R_0$ ), a constant density  $n_e^{ref}$  and a temperature profile corresponding to realistic temperature profiles obtained in TCV, as described in [Sauter et al. 2014]

$$\frac{T_e(\rho_{\psi_P})}{T_{e,edge}} = \begin{cases} \bar{T}_{axis} + \lambda_T \rho_{\psi_P}^2 & \text{if } \rho_{\psi_P} \leq \rho_{\psi_P,1} \\ \bar{T}_{ped} \exp[-\kappa_T(\rho_{\psi_P} - \rho_{\psi_P,2})] & \text{if } \rho_{\psi_P,1} \leq \rho_{\psi_P} \leq \rho_{\psi_P,2} \\ 1 - \mu_T(\rho_{\psi_P} - \rho_{\psi_P,3}) & \text{if } \rho_{\psi_P,2} \leq \rho_{\psi_P} \leq \rho_{\psi_P,3} \\ 1 & \text{if } \rho_{\psi_P} \geq \rho_{\psi_P,3} \end{cases} \quad (3.78)$$

where  $\rho_{\psi_P} = \sqrt{\psi_P/\psi_{Pa}}$ , with  $\psi_P$  is the poloidal magnetic flux,  $\rho_{\psi_P,1} = 0.27$ ,  $\rho_{\psi_P,2} = 0.72$ ,  $\rho_{\psi_P,3} = 0.90$  and

$$\begin{cases} \bar{T}_{axis} &= \bar{T}_{core} - \lambda_T \rho_{\psi_P,1}^2 \\ \bar{T}_{core} &= \bar{T}_{ped} \exp(-\kappa_T(\rho_{\psi_P,1} - \rho_{\psi_P,2})) \\ \bar{T}_{ped} &= 1 - \mu_T(\rho_{\psi_P,2} - \rho_{\psi_P,3}) \end{cases} \quad (3.79)$$

with  $\lambda_T = -\kappa_T \bar{T}_{core}/(2\rho_{\psi_P,1})$ ,  $\kappa_T = 3$ ,  $\mu_T = 12$  and  $T_{e,edge} = 140$  eV. A pure hydrogen plasma is assumed with  $n_e = n_i$  and  $T_e = T_i$ , and no Ohmic electric field is considered, as this option is not available in ORB5. In that case, the system is invariant by the change of coordinates  $v_{\parallel} \rightarrow -v_{\parallel}$  and  $\langle \theta_0 \rangle \rightarrow \pi - \langle \theta_0 \rangle$ . Then, for the energy absorption, there is no difference between  $\langle \theta_0 \rangle \leq \pi/2$  and  $\langle \theta_0 \rangle \geq \pi/2$ .

For all ORB5 simulations,  $2e8$  and  $1e10$  markers have been used for representing the ions and electrons respectively. With these resolutions, the results are converged with respect to the number of markers. In LUKE, the size of the phase space grid  $(p, \xi, \rho_{\psi_P})$  is  $151 \times 121 \times 30$ . The points in the spatial grid are not linearly spaced, they are concentrated around the power absorption location, guessed from the linear ray-tracing calculation.

As discussed in [Donnel et al. 2022], ORB5 simulations have been performed using two different proton-to-electron mass ratios: an artificially reduced mass ratio  $m_i/m_e = 100$  or a realistic mass ratio  $m_i/m_e = 1836$ . The advantage of using an artificially reduced mass ratio is to reduce the numerical cost of the gyro-kinetic simulations by increasing the time step of the simulation, which is inversely proportional to the ion-cyclotron frequency. Collision physics plays a major role in the balance between EC-induced acceleration of electrons and collisional relaxation. However, using an artificial mass ratio in ORB5 changes the collisionality, which has to be modified to keep the collision physics as close as possible between ORB5 and LUKE. The collision frequency of a species  $s_1$  of mass  $m_{s_1}$  on a species  $s_2$  of mass  $m_{s_2}$  reads [Donnel et al. 2020]

$$\nu_c^{s_1 s_2} = \frac{\ln \Lambda_{s_1 s_2}}{3\pi^{3/2} \epsilon_0^2} \frac{n_{s_2}}{T_{s_1}^{3/2}} \frac{q_{s_1}^2 q_{s_2}^2}{\sqrt{m_{s_1}}} \frac{\left(1 + \frac{m_{s_1}}{m_{s_2}}\right)}{\left[1 + \frac{m_{s_1} T_{s_2}}{m_{s_2} T_{s_1}}\right]^{3/2}} \quad (3.80)$$

with  $\ln \Lambda_{s_1 s_2}$  the Coulomb logarithm,  $q_{s_1}$  and  $q_{s_2}$  the charges of species  $s_1$  and  $s_2$ ,  $T_{s_1}$  and  $T_{s_2}$



their temperatures, and  $n_{s_2}$  the density of  $s_2$  particles. Considering that electrons are much lighter than ions, one can see that the electron-electron  $\nu_c^{ee}$  and electron-ion  $\nu_c^{ei}$  collision frequencies are proportional to  $m_e^{-1/2}$ . For simulations with heavy electrons of artificially increased mass  $m_{e,incr}$ , the correct ratio between the collision frequency of electrons and the electron-cyclotron frequency can be retrieved by multiplying the collision frequency of reference in ORB5 by  $\sqrt{m_{e,real}/m_{e,incr}}$ . This choice is made to retain the correct physics as much as possible when using an artificial mass ratio between protons and electrons. Note that, with this choice, the electron collisionality  $\nu_{c,e}^* = (\nu_c^{ee} + \nu_c^{ei}) qR/(\epsilon v_{Te})$  is lower than the real one. This choice therefore lowers the neoclassical transport of electrons. This hypothesis could also have an impact on trapped-electron-mode turbulence, which is sensitive to the electron collisionality.

The EC beam frequency is set to 75 GHz. The two angles of injection  $\langle\theta_0\rangle_{in}$  used in the benchmark are illustrated in figure 3.14, which shows poloidal and top views of C3PO ray tracing. Comparisons between ORB5 and LUKE/C3PO for the two angles of injection and for two different densities  $n_e^{ref} = 0.5e19 \text{ m}^{-3}$  and  $n_e^{ref} = 1.0e19 \text{ m}^{-3}$  are shown in figures 3.15, 3.16, 3.17 and 3.18. In each of these plots, the linear predictions of Albajar's model and C3PO are given as reference points. Error bars on LUKE absorbed power come from the relative gap on absorbed power density between the last iteration and the one before, which is basically less than 1% for completely converged simulations. In LUKE, error bars on the full-width at half maximum of the deposition profile and on the absorption location come from the spatial grid resolution. In ORB5, error bars on all quantities correspond to the standard deviation with respect to time.

At low power, an excellent agreement is found among all the predictions for the pure ECRH cases (see figures 3.15, 3.16). The agreement for the ECCD cases at low power is still good, but a mismatch of approximately 10% is found for the total absorbed power predicted by ORB5 compared with the other predictions (see figures 3.17, 3.18). As the total absorbed power is not constrained in the model implemented in ORB5, it is possible to estimate a total absorbed power above 100%. If this point becomes critical for later applications of the EC source term in ORB5, a convergence loop similar to what is implemented in LUKE (see figure 3.12) could be implemented too. As already discussed, this possibility has not been added in ORB5 yet, as it would significantly increase the numerical cost of the source term. The overall agreement at low power for all cases validates the implementation of the model in ORB5.

For high-power EC beams, quasilinear effects become important, especially for the total absorbed power. For the pure ECRH cases, quasilinear effects lead to a significant decrease of the total power deposited both in LUKE and ORB5. These quasilinear effects are stronger for LUKE than for ORB5. The quantitative difference between the results from the two codes can come from the fundamental differences between the two codes, i.e. 3D bounce-average for LUKE compared with 5D drift-kinetic for ORB5, but also from the difference between the collision operators, or the feedback loop on the power absorbed by the plasma and the power

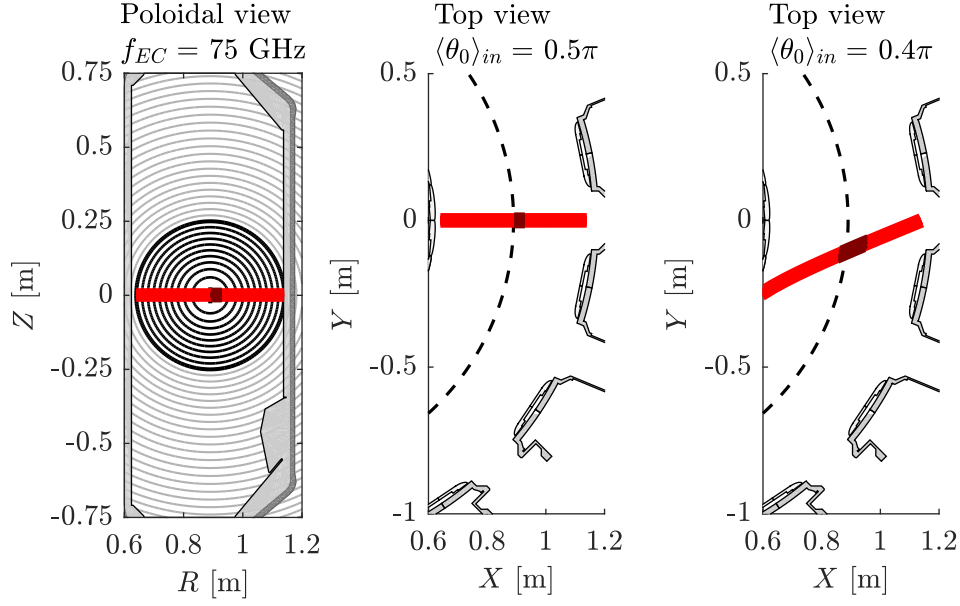


Figure 3.14: C3PO ray tracing for a 75-GHz EC beam propagating along the equatorial midplane, launched from the low-field side, for two angles  $\langle \theta_0 \rangle_{in}$  between the beam wave vector  $\mathbf{k}$  and the magnetic field  $\mathbf{B}$  at the beam entrance in the plasma:  $\langle \theta_0 \rangle_{in} = \pi/2$  (pure ECRH) and  $\langle \theta_0 \rangle_{in} = 0.4\pi$  (ECCD).

of the EC beam, which is included in LUKE but not in ORB5. It is also noteworthy that ORB5 simulations using the real mass ratio between electrons and protons display larger quasilinear effects than the one using heavy electrons. This difference is probably due to the difference in collisionality between the two versions of the code. It implies that simulations using the real electron mass have to be used to properly study the quasilinear effects. Simulations with a non-zero current-drive component display smaller quasilinear effects in both codes. Quasilinear dependencies at high injected power can be interpreted by writing the equation 3.60 for the deposited power density in the momentum-pitch-angle coordinates  $(p, \xi)$

$$\frac{\partial P_{EC,n}}{\partial V} = mc^2 \int_0^\infty dp (\gamma - 1) \int_{-1}^1 \left[ \frac{1}{p^2} \frac{\partial}{\partial p} (p^2 S_{EC,n,p}) - \frac{1}{p} \frac{\partial}{\partial \xi} \left( \sqrt{1 - \xi^2} S_{EC,n,\xi} \right) \right] d\xi \quad (3.81)$$

where the flux  $\mathbf{S}_{EC,n}$  in  $(p, \xi)$  is given by

$$\mathbf{S}_{EC,n} = -\mathbb{D}_{EC,n} \cdot \nabla_{\mathbf{p}} f_e = \begin{pmatrix} S_{EC,n,p} \\ S_{EC,n,\xi} \end{pmatrix} = \begin{pmatrix} -D_{EC,n}^{pp} \frac{\partial f_e}{\partial p} + \frac{\sqrt{1 - \xi^2}}{p} D_{EC,n}^{p\xi} \frac{\partial f_e}{\partial \xi} \\ -D_{EC,n}^{\xi p} \frac{\partial f_e}{\partial p} + \frac{\sqrt{1 - \xi^2}}{p} D_{EC,n}^{\xi\xi} \frac{\partial f_e}{\partial \xi} \end{pmatrix} \quad (3.82)$$

with  $D_{EC,n}^{pp}$ ,  $D_{EC,n}^{p\xi}$ ,  $D_{EC,n}^{\xi p}$  and  $D_{EC,n}^{\xi\xi}$  the components of the diffusion tensor  $\mathbb{D}_{EC,n}$  components in  $(p, \xi)$  coordinates. The dominant diffusion term is  $D_{EC,n}^{pp}$  (at least by an order of magnitude in all cases considered in this paper), so the quasilinear behavior can be partly understood by looking at the product  $D_{EC,n}^{pp} \partial f_e / \partial p$  at the absorption location in phase space. The quasilinear evolution of the total absorbed power results from a balance between the relative evolution of  $D_{EC,n}^{pp}$  with injected power due to the modification of the beam power along its path

(quasilinear effect due to the loop between the energy deposited on the plasma and the power carried by the beam, which is not included in ORB5) and the deviation of  $f_e$  from a Maxwellian distribution, resulting from the competition between the EC source, collisions and neoclassical effects (turbulence is not included in these simulations and neoclassical effects are reduced to the zeroth order in LUKE).

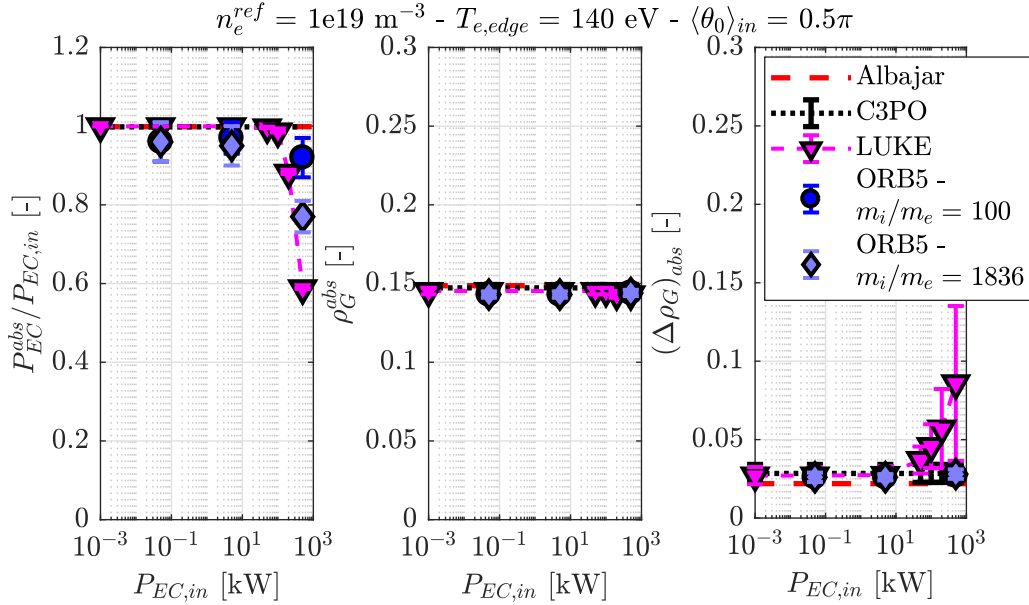


Figure 3.15: Scan in injected EC power  $P_{EC,in}$  for a pure ECRH case at high density, showing the absorbed power fraction  $P_{EC}^{abs} / P_{EC,in}$ , the absorption location  $\rho_G^{abs}$  and the full-width at half maximum of the power deposition profile  $(\Delta \rho_G)_{abs}$  for linear (Albajar's model, C3PO) and quasilinear (LUKE, ORB5) EC power deposition calculations. The normalized radius is  $\rho_G = (R - R_0) / a$ .

For the pure ECRH cases, the flattening of the distribution by the EC source, as shown in figure 3.19, is the dominant effect and leads to a drop of the fraction of absorbed power as seen in figures 3.15 and 3.16. The flattening of the distribution function increases with the absorbed power, explaining the dependence of quasilinear effects with respect to the injected power seen in figures 3.15 and 3.16. On the other hand, an increase of the collisionality, by increasing the density for instance, reduces the deviations of the electron distribution function from the Maxwellian distribution, and explains the difference of quasilinear effects between figures 3.15 and 3.16 at large power.

For ECCD cases, represented in figures 3.17 and 3.18, the combined effect of the source and the collision pitch-angle scattering can result in a large pitch-angle-dependent population of suprathermal electrons, as illustrated in figure 3.20, which shows the electron distribution in  $(p, \xi)$  space at the absorption location. The presence of a suprathermal population increases the absorbed power fraction. For ECCD cases, the two mechanisms described above, i.e. flattening of the distribution function by the source, which leads to a reduction of the absorbed

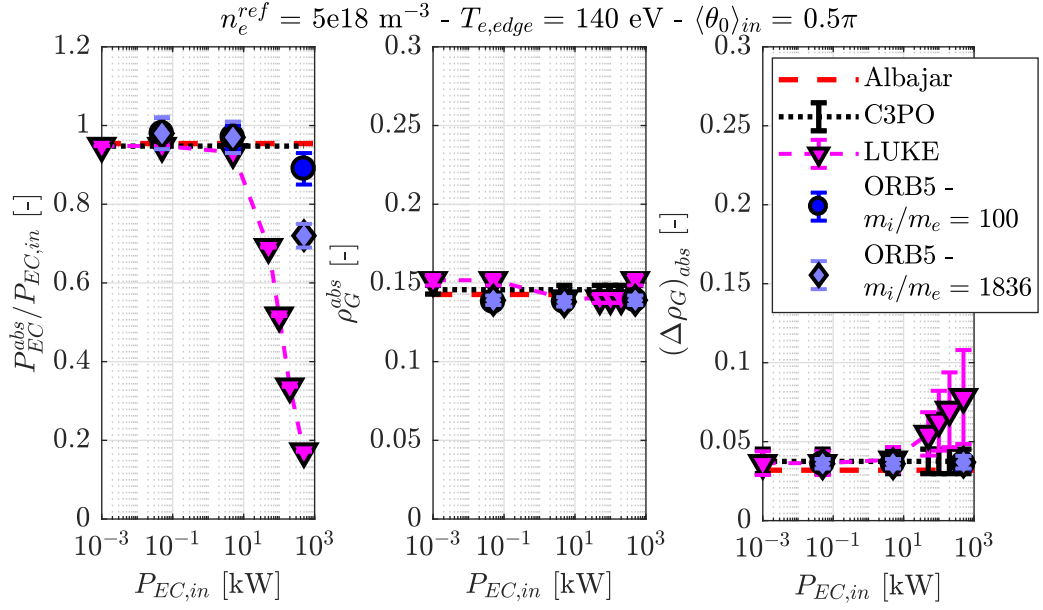


Figure 3.16: Scan in injected EC power  $P_{EC,in}$  for a pure ECRH case at low density, showing the absorbed power fraction  $P_{EC}^{abs}/P_{EC,in}$ , the absorption location  $\rho_G^{abs}$  and the full-width at half maximum of the power deposition profile  $(\Delta\rho_G)_{abs}$  for linear (Albajar's model, C3PO) and quasilinear (LUKE, ORB5) EC power deposition calculations. The normalized radius is  $\rho_G = (R - R_0)/a$ .

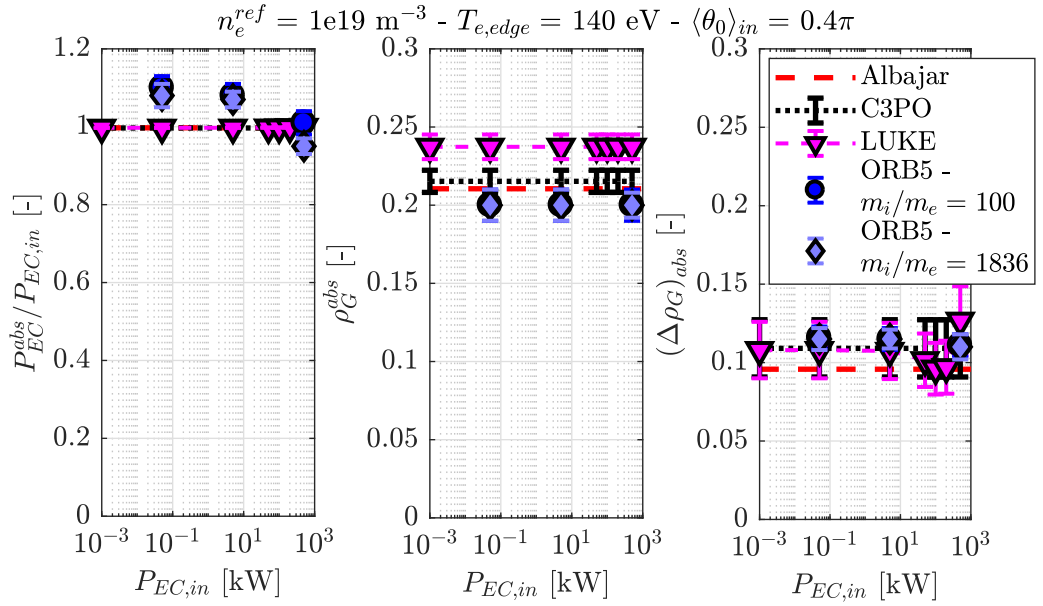


Figure 3.17: Scan in injected EC power  $P_{EC,in}$  for an ECCD case at high density, showing the absorbed power fraction  $P_{EC}^{abs}/P_{EC,in}$ , the absorption location  $\rho_G^{abs}$  and the full-width at half maximum of the power deposition profile  $(\Delta\rho_G)_{abs}$  for linear (Albajar's model, C3PO) and quasilinear (LUKE, ORB5) EC power deposition calculations. The normalized radius is  $\rho_G = (R - R_0)/a$ .

power fraction on one hand, and the increase of the suprathermal population by the combination of the source and collisions, leading to an increase of the absorbed power fraction, on the other hand, are in direct competition. The overall effect is therefore case dependent

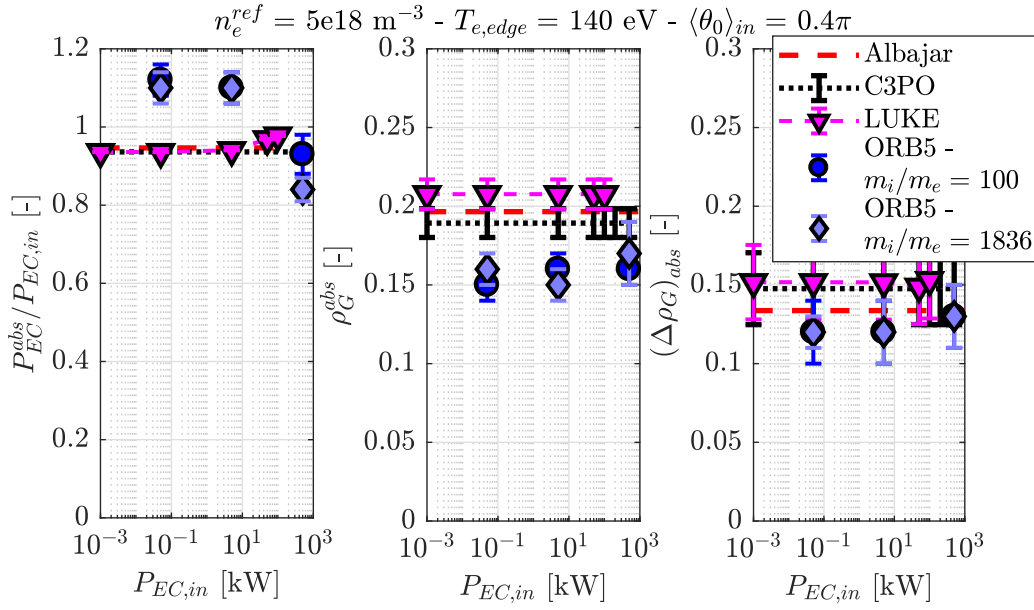


Figure 3.18: Scan in injected EC power  $P_{EC,in}$  for an ECCD case at low density, showing the absorbed power fraction  $P_{EC}^{abs} / P_{EC,in}$ , the absorption location  $\rho_G^{abs}$  and the full-width at half maximum of the power deposition profile  $(\Delta \rho_G)_{abs}$  for linear (Albajar's model, C3PO) and quasilinear (LUKE, ORB5) EC power deposition calculations. The normalized radius is  $\rho_G = (R - R_0) / a$ .

and sensitive to the collision operator. This explains the difference between ORB5, which predicts a decrease of the power in the ECCD case studied here, and LUKE, which predicts a small increase of the absorbed power, as shown in figures 3.17 and 3.18. It is important to note that, in ORB5, it is possible to observe a total absorbed power above 100%. This is due to the lack of consistency between the absorbed power, calculated using the quasilinear diffusion operator, and the damped wave electric field, calculated using an analytical model, which does not impose a constraint on the energy conservation. This can lead to a difference in the total absorbed power of the order of 10%. Solving this issue would require a consistent convergence looping over the calculated power (as it is done for LUKE) which, in turn, increases dramatically the numerical cost of the simulations.

The combination of low density, high temperature and high power leads to difficulty in convergence of the quasilinear power deposition in LUKE, as the collision frequency is low and the quasilinear diffusion is high. This translates the fact that the power density becomes high, leading to strong quasilinear distortions of the distribution, with fewer collisions to fill the hole the wave dug in the distribution. LUKE convergence is ensured in figures 3.15, 3.16 and 3.17, but it could not be reached for a launched EC power  $P_{EC,in} > 100 \text{ kW}$  in lower density plasma in ECCD ( $n_e^{ref} = 0.5e19 \text{ m}^{-3}$ , figure 3.18). The quantitative agreement between ORB5 and LUKE for low power deposition and the qualitative agreement at high power validates the derivation of the source term and its implementation in ORB5.

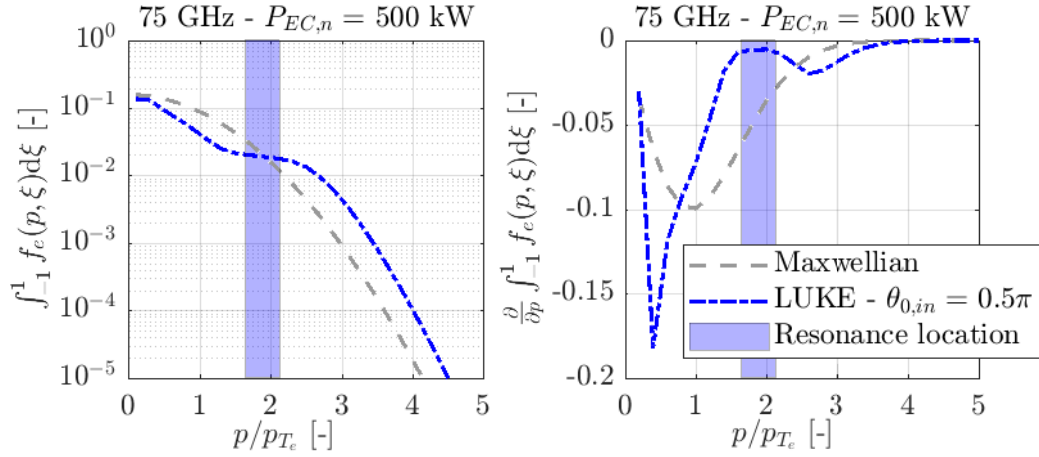


Figure 3.19: Pitch-angle integrated electron distribution function obtained with LUKE (*left*) and its derivative with respect to  $p$  (*right*), for the pure ECRH case, at the maximum of absorption location, compared with the initial Maxwellian distribution. The shaded area shows a rough approximation of the resonance location.

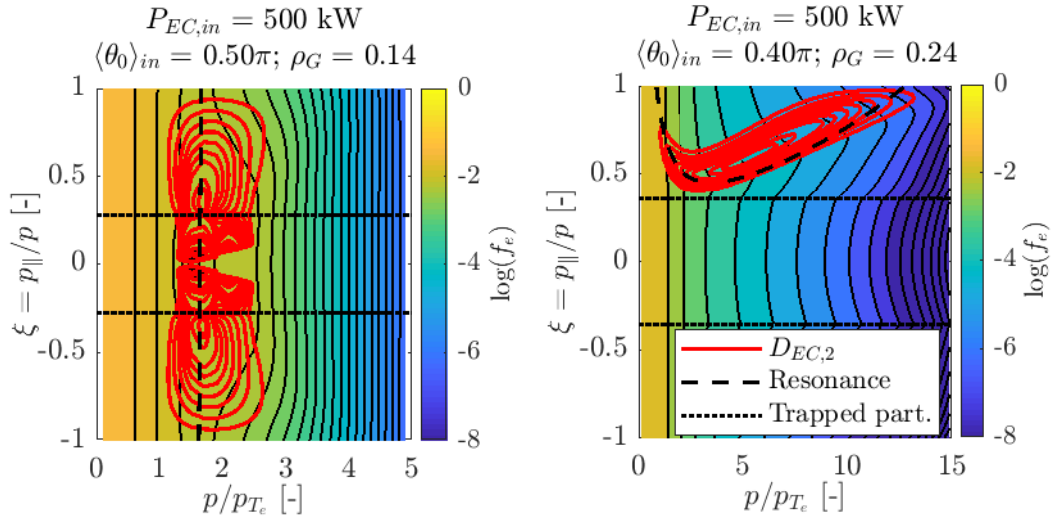


Figure 3.20: 2D electron distribution function obtained with LUKE for a pure ECRH (*left*) and an ECCD case (*right*), at the maximum of absorption location, for high injected power. The dominant term of the EC wave quasilinear bounce-averaged diffusion coefficient for the second harmonic  $D_{EC,2}^{pp}$  is overlaid in red, as well as a theoretical prediction for the resonance location (see [Prater 2004]). For the ECCD case, the Doppler-shifted resonance is pitch-angle dependent, leading to a wave interaction with particles at higher momentum.



## 4 Electron transport enhancement by Electron-Cyclotron waves

*Chaos is found in greatest abundance wherever order is being sought. It always defeats order, because it is better organized.*

---

Interesting Times: The Play,  
Terry Pratchett (1948-2015)

### 4.1 Introduction

As mentioned in section 1.4, externally launched Electron-Cyclotron (EC) waves are widely used in fusion devices to transfer energy to the plasma by resonant heating (ECRH) or current-drive (ECCD) [Prater 2004]. The ability of EC waves to drive current in a very narrow spatial region of the plasma, and the precise control of the power deposition via the launching angles, renders them the main foreseen tool for magnetohydrodynamic (MHD) mode control and mitigation (e.g. neoclassical tearing modes) in future large devices such as ITER, to be achieved by accurately driving current inside magnetic islands. Such a technique is being developed and already applied in practice [Kong et al. 2019]. However, to improve efficiency, one wants to avoid driving current outside the magnetic islands and an accurate understanding of the EC beam profile and power deposition in the plasma is required. Let's recall that an initial observation in TCV suggested that the inferred distribution of suprathermal electrons from hard X-ray (HXR) measurements was broader than what was expected from power deposition estimations made by ray-tracing and bounce-averaged drift-kinetic codes [Coda et al. 2003a]. The first explanation to this discrepancy is the broadening of the EC beam before its absorption by scattering through the edge turbulent refractive index, which is the object of chapter 5.

This chapter focuses on the second possible explanation to the observed discrepancy between codes and experiments, which is the radial transport of the suprathermal electrons indirectly generated by the wave through EC beam absorption. Indeed, to recover experimental data,



an ad-hoc radial transport of fast electrons has been added to bounce-averaged drift kinetic simulations of TCV [Nikkola et al. 2003; Choi et al. 2020a] and DIII-D [Harvey et al. 2002], while the potential effect of such a transport on current drive efficiency has been numerically studied for ITER [Bertelli and Westerhof 2009], showing that the maximum achievable current density decreases with the effective transport diffusion coefficient. One can further conjecture that this excess transport is caused by the wave absorption itself.

The present study proposes to investigate the nature of the EC-wave enhanced radial transport, using experimentally constrained forward modeling. The evolution of turbulent transport and turbulence properties is also investigated, both experimentally and numerically. The methodology is introduced in section 4.2 for the experimental setup and in section 4.3 for the numerical tools. Then, in section 4.4, the experimental data related to suprathermal electrons and ion-scale turbulence are analyzed and the enhancement of transport of suprathermal electron by EC waves is demonstrated, associated with increased turbulence level. In section 4.5, experimentally constrained drift-kinetic forward simulations are performed and radial transport coefficients are determined by matching experimental observations. Finally, before concluding, the particle transport analysis is completed in section 4.6 by global flux-driven gyro-kinetic simulations, with a newly developed realistic ECCD source [Donnel et al. 2021, 2022], testing the hypothesis of turbulent transport enhancement by EC waves from first principles for the first time in a global gyro-kinetic code.

This work has been published in the journal *Plasma Physics and Controlled Fusion*, under the special issue of the joint Varenna-Lausanne conference on the Theory of Fusion Plasma, held in Varenna (Italy) in September 2022, and is adapted here in this thesis [Cazabonne et al. 2023]. Preliminary results have been presented to the 48th edition of the conference on plasma physics of the European Physical Society [Cazabonne et al. 2022], and final results have been presented to the 49th edition of the same conference.

## 4.2 Experimental setup

### 4.2.1 Diagnostics

A set of different diagnostics has been used in TCV to study suprathermal electrons, turbulence and to build plasma equilibrium. The main tool to experimentally study the suprathermal electron population is the Hard X-Ray Spectrometer (HXRS) [Gnesin et al. 2008]. A detailed description of the spectrometer is provided in section 2.5. The line of sight span is displayed in figure 4.1. The thermal contribution to the X-ray signal is cut out by means of selectable filters, set to 0.15 mm of aluminum. To achieve a proper photon energy discrimination, it is important that the photoelectric effect dominates over Compton scattering in the cadmium telluride photodiodes, meaning that the HXRS energy range is limited to 20-300 keV (the typical central electron temperature in TCV is  $2 \leq T_{e0} \leq 5$  keV), with a resolution of  $\sim 8$  keV (from calibration at 59.54 keV using Am-241 X-ray source). The presence of very high energy electrons (runaway

electrons for instance) that can pollute the low energy HXR spectrum through Compton scattering is inferred using the blind detectors of each camera. The HXRS lines of sight cover a complete poloidal section of TCV, allowing for 2D tomographic reconstruction of the hard X-ray emissivity that can resolve poloidal asymmetries.

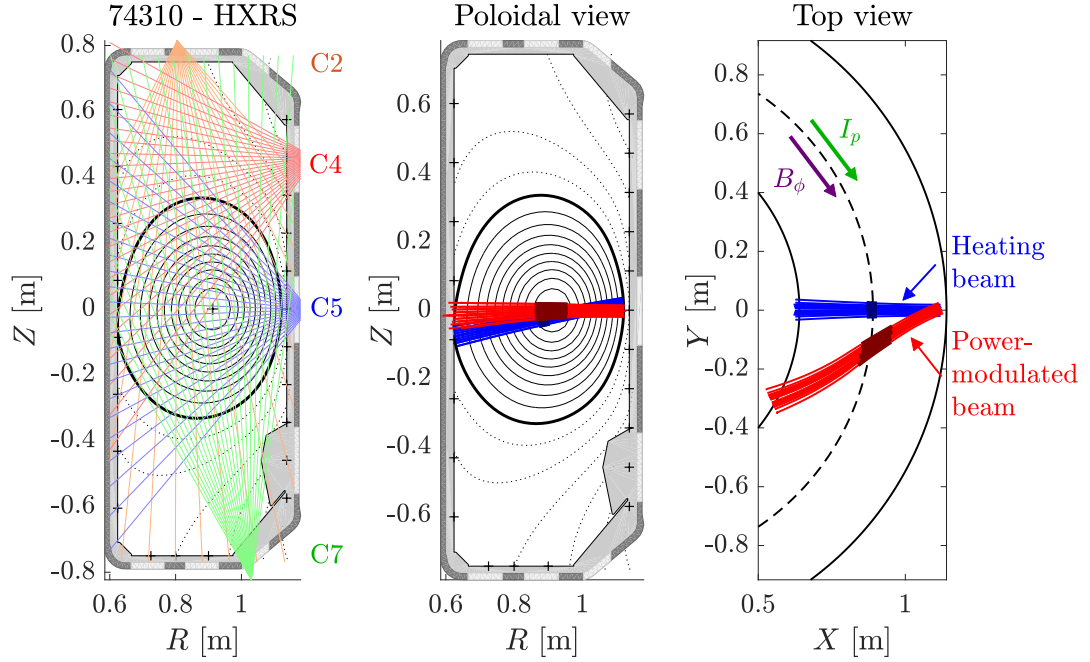


Figure 4.1: *Left*: HXRS lines of sight for the 4 cameras (C2, C4, C5 and C7). *Center*: Poloidal view of C3PO ray-tracing calculation for TCV shot #74310. *Right*: Top view of C3PO ray-tracing calculation for TCV shot #74310, with plasma current  $I_p$  and toroidal magnetic field  $B_\phi$  directions indicated. Shaded EC beam areas show maximum absorption. For the reference case #74304, only the red beam is used. These configurations are counter-ECCD.

Core and inner edge turbulence properties can be measured by Tangential Phase Contrast Imaging (TPCI) [Marinoni et al. 2006], while the Correlation Electron-Cyclotron Emission (CECE) diagnostic is a powerful tool to measure electron temperature fluctuations [Fontana et al. 2017]. Both diagnostics are already detailed in sections 2.4.2 and 2.4.3 respectively. The installed TPCI diagnostic is able to resolve ion scale turbulence (from 7.0 cm down to 0.1 cm), while the CECE diagnostic can estimate radial correlation length from 3.3 cm down to 0.9 cm in optimal conditions. The use of the CECE diagnostic is limited in the case of high power EC wave coupling to the plasma. Indeed, microwaves from the EC beam itself are in the same range of frequencies as microwaves from cyclotron emission of the plasma electrons, thus polluting the measured signal. An example of a TPCI configuration is shown in the left panel of figure 4.2. The CECE configuration used in this study is presented in the right-hand plot of figure 4.2.

The radial profiles of the electron temperature  $T_e$  and density  $n_e$  are measured by Thomson Scattering (TS) of vertically injected laser light by plasma electrons, with a good spatial res-

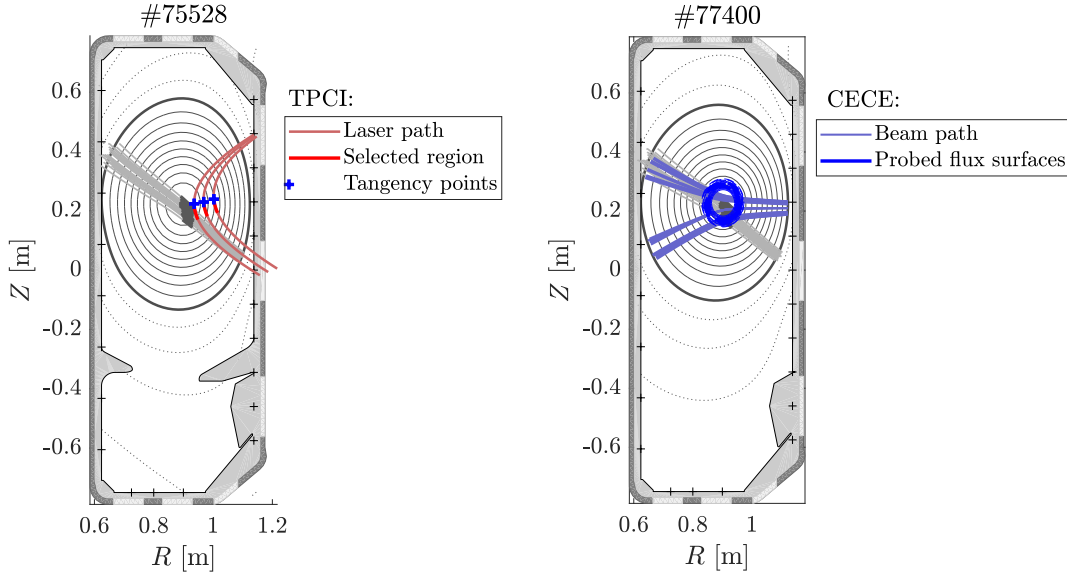


Figure 4.2: *Left*: TPCI configuration for TCV shot #75528 (similar to TCV shot #74304 but with  $Z_p = 23$  cm). *Right*: CECE configuration for TCV shot #77400 (similar to TCV shot #74304 but with  $Z_p = 23$  cm). Only the side and central rays are shown for clarity. The light gray lines show the power-modulated EC beam propagation and the dark gray area its absorption location.

olution but a rather low time resolution ( $\sim 60$  Hz, 3 pulsed lasers with 20 Hz repetition rate) [Blanchard et al. 2019]. On the other hand, soft X-ray measurements (XTe), using 4 vertically viewing diodes with different shielding properties for 6 different ratios, give approximate information on the central electron temperature  $T_{e0}$  with a high acquisition frequency (10 kHz), but can't resolve the profile. It has to be noticed that XTe assumes a Maxwellian model to infer  $T_{e0}$ , giving a good qualitative indication of its time evolution but not of its absolute value, for which TS is preferred (TS measurements are very weakly sensitive to the non-Maxwellian contribution of suprathermal electrons). The ion temperature  $T_i$  and density  $n_i$  are inferred from Charge eXchange Recombination Spectroscopy (CXRS), using the low-power neutral beam injector (DNBI), looking at  $C^{6+}$  impurities, assuming that the main ions and the impurity ions share the same temperature [Marini 2017]. It is also possible to derive an estimation of the effective charge  $Z_{eff}$  (lower bound as only one type of impurity is probed) from CXRS. This effective charge is a critical parameter for drift-kinetic simulations as it strongly influences the collisions between electrons and ions, and has a strong impact on the Ohmic current drive. This parameter will be discussed in more detail in section 4.5. Plasma current  $I_p$  and loop voltage  $V_{loop}$  are determined from magnetic measurements. Finally, the magnetic equilibrium (poloidal magnetic flux and flux surfaces, safety factor, etc) is reconstructed using magnetic probes, flux loops, and measurement of coil currents to feed the Grad-Shafranov reconstruction algorithm LIUQE [Moret et al. 2015]. These diagnostics are also described in section 2.3.

### 4.2.2 Electron-Cyclotron power modulation and conditional averaging

Dedicated plasma scenarios have been developed in TCV to study suprathermal electron dynamics [Coda et al. 2003b, 2006; Choi et al. 2020a]. In the present study, the scenario consists of limited, elongated L-mode plasmas into which the power-modulated EC beam is injected along the equatorial midplane in a current drive configuration (see center and right plots of figure 4.1). There are several constraints that need to be fulfilled by this scenario. First, the effects of the EC beam scattering on the power deposition profile has to be minimized, in order to distinguish these effects from local transport enhancement. This is achieved by the equatorial midplane EC wave injection (see central plot of figure 4.1), so that the beam propagates perpendicularly to poloidal projection of the field lines in the power deposition region: to first order, then, transverse broadening of the EC beam due to edge-localized density fluctuations will not change the wave power absorption profile location  $\rho_{\psi_p}^{abs}$  and width  $(\Delta\rho_{\psi_p})_{abs}$ . In particular, as shown in chapter 5, for field-aligned density fluctuations, the EC beam broadening due to diffraction occurs mainly in the poloidal direction.

MHD activity, such as the internal kink mode leading to sawtooth relaxations, must be avoided since it can enhance particle transport and may also accelerate core electrons through magnetic reconnection, generating spikes in the HXR signal that are difficult to distinguish from spikes from the EC power pulses. MHD minimization is achieved by injecting the EC wave in the counter-current drive direction (as shown in the right-hand plot of figure 4.1). Figure 4.3 shows an example of MHD spectrogram for a co-current drive and a counter-current drive configuration in a similar plasma equilibrium, highlighting the significant reduction of MHD activity in the counter-current drive configuration. Figure 4.4 shows the same thing in cases where an additional heating beam is used, steadily injecting power in the plasma. In that case, the reduction of the MHD activity is far from perfect. This is discussed later in section 4.5. On the other hand, no evident MHD activity is found when performing fast Fourier transform (FFT) of the central electron temperature: the frequency content of the central electron temperature measured with XTe is similar to the frequency content of the injected EC power, with the addition of a 50 Hz and a 1.275 kHz peaks (typical signatures of TCV power supplies) of small amplitude with respect to the power modulation frequencies (see figure 4.5). According to the equilibrium reconstruction, all shots used in the present study have a safety factor  $q$  above 1 everywhere, meaning that the  $m/n = 1$  internal kink mode, leading to sawtooth activity, can be excluded from the interpretation of the results.

Finally, EC power modulation techniques are used to increase the HXR statistics by performing 48 pulses per discharge, while keeping the plasma equilibrium (magnetic field, plasma current, plasma position) and electron density constant. The ion properties, measured with CXRS, are also kept constant (within the error bars). One EC pulse consists of a 1-ms power ramp-up, 2-ms high-power flat-top and 1-ms ramp-down, with 1 pulse every 11 ms, to ensure that the plasma has relaxed between each pulse. The high-power phase is short enough

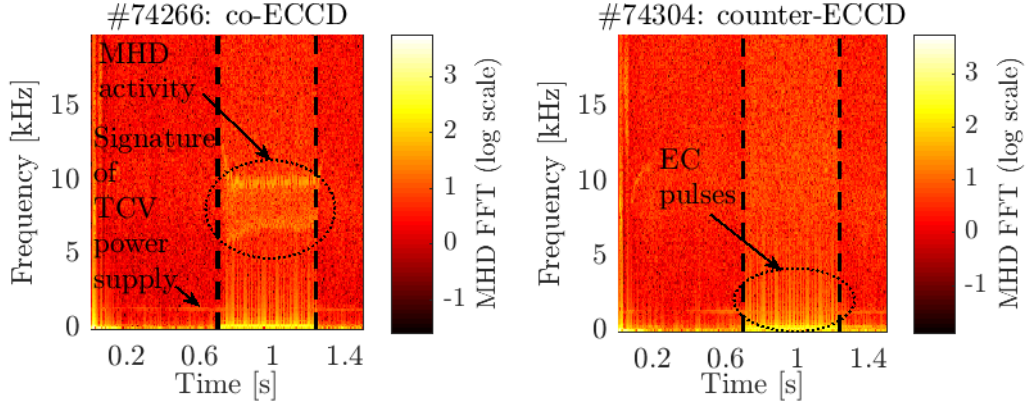


Figure 4.3: Fast Fourier Transform (FFT) of MHD probe signal (log scale) for TCV shots #74266 (co-current EC wave injection, with the angle between the EC beam wave-vector and the plasma magnetic field at absorption location  $\theta_0^{abs} = -57.1 \pm 0.4^\circ$ ) and #74304 (counter-current,  $\theta_0^{abs} = 57.4 \pm 0.6^\circ$ ). Both equilibria are similar.

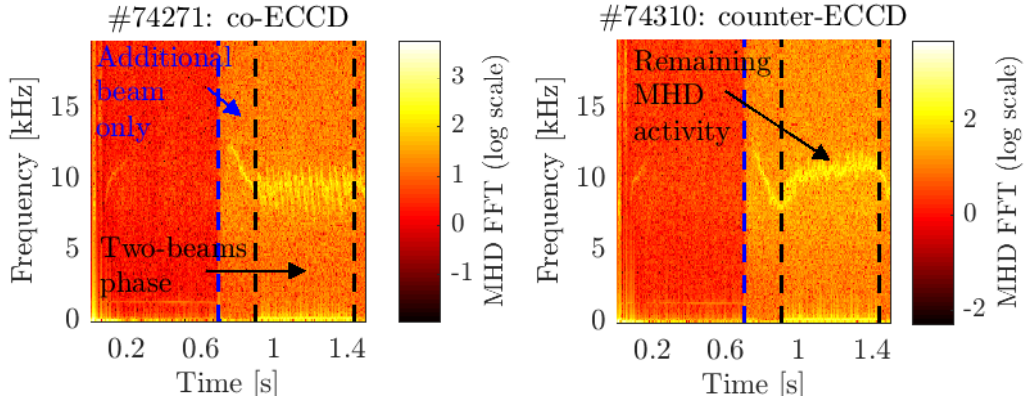


Figure 4.4: Fast Fourier Transform (FFT) of MHD probe signal (log scale) for TCV shots #74271 (similar to #74266 with an additional steady-power beam in ECRH firing 0.2s before the modulated-power beam) and #74310 (similar to #74271 in counter-ECCD).

to ensure that the wave-induced current density cannot diffuse appreciably because of the back-electromotive force that naturally compensates the current density modification over a short time scale [Choi et al. 2020a; Giruzzi et al. 1999]. The typical time scale for current diffusion  $\tau_{D_j}$  in the plasma is related to the resistive time scale  $\tau_\sigma = a^2 \mu_0 \sigma$ , where  $\sigma$  is the plasma conductivity taken at the absorption location  $\rho_{\psi_p}^{abs}$ ,  $a$  the plasma minor radius,  $\mu_0$  the vacuum permeability, by  $\tau_{D_j} = (\Delta \rho_{\psi_p})_{abs}^2 \tau_\sigma$  [Giruzzi et al. 1999]. For typical TCV shots used in this study, with the full-width at half-maximum of the power deposition profile  $(\Delta \rho_{\psi_p})_{abs} = 0.12 \pm 0.01$ , and using the Sauter-Angioni-Lin-Liu model for the neoclassical conductivity [Sauter et al. 1999, 2002], one finds  $23 \leq \tau_{D_j} \leq 135$  ms (note that higher EC power leads to longer  $\tau_{D_j}$  because of lower conductivity). EC power pulses are assumed to be physically identical, allowing for conditional averaging of experimental data over the pulses. This is illustrated for the main TCV discharges used in this study: #74304 the reference case in figure 4.6, using only one power-modulated EC beam, and #74310 in figure 4.7, similar to #74304 but using an additional EC beam in pure heating to generate a larger population of

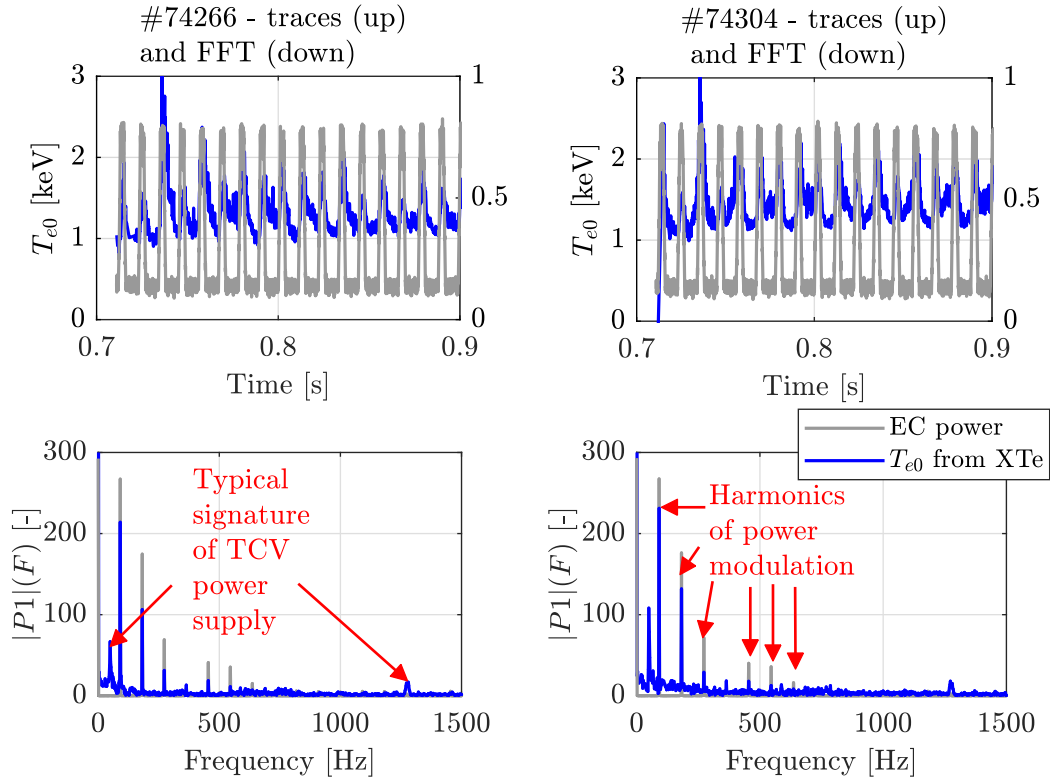


Figure 4.5: Time traces and Fast Fourier Transform (FFT) of XTe central temperature signal compared with EC power for TCV shots #74266 (co-current EC wave injection,  $\theta_0^{abs} = -57.1 \pm 0.4^\circ$ ) and #74304 (counter-current,  $\theta_0^{abs} = 57.4 \pm 0.6^\circ$ ). Both equilibria are similar.  $|P1|$  stands for the one-sided amplitude spectrum.

energetic electrons. This second beam is not power-modulated and starts injecting power 0.2 seconds earlier than the power-modulated EC beam to reach a steady-state background before starting the modulation study. Electron temperature and density profiles are also illustrated in figure 4.8 for both TCV shots #74304 and #74310. Other shots used in this work are: #74305 and #74309, similar to #74304 and #74310 respectively, but with a lower driven current through a larger angle between the EC wave-vector  $\mathbf{k}$  and the magnetic field  $\mathbf{B}$ , defined by  $\theta_0 = \tan^{-1}(k_\perp/k_\parallel)$ . A pure heating configuration corresponds to  $\theta_0 = \pi/2$ ,  $\theta_0 \leq 0$  is co-current drive ( $k_\parallel \leq 0$ ) and  $\theta_0 \geq 0$  is counter-current drive ( $k_\parallel \geq 0$ ). Finally, some shots have been repeated to benefit from TPCI and CECE measurements, with the plasma moved 23 cm upward to increase the depth of the probed area. Typically, #75528 and #77400 are replicas of #74304 at  $Z_p = 23$  cm, and #77401 is a replica of #74305 at  $Z_p = 23$  cm. The fast oscillations on the conditionally averaged loop voltage that can be seen on the right-hand panels of figures 4.6 and 4.7 are parasitic oscillations due to the machine power supply. These are the same that appear in figure 4.3 for the MHD probe spectrogram and figure 4.5 for the temperature FFT at around 1.275 kHz. Table 4.1 summarizes the properties of the TCV shots used in the present study.

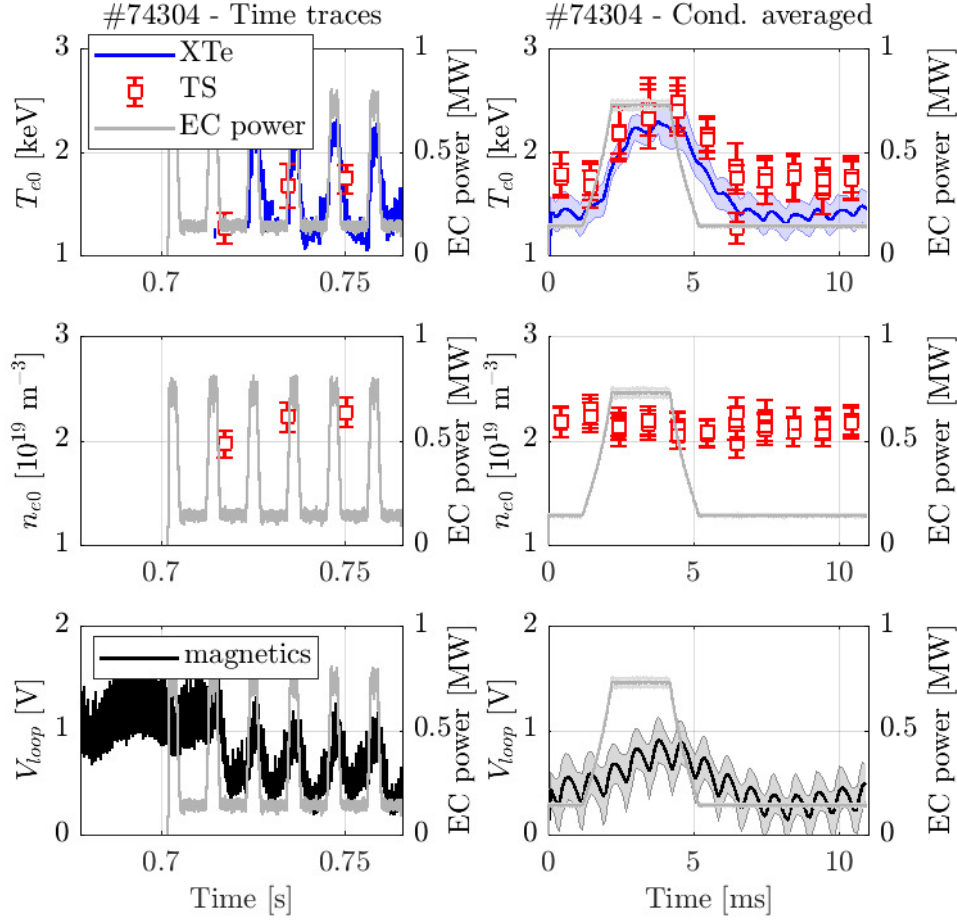


Figure 4.6: Time traces (*left*) and conditionally averaged time traces (*right*) of central electron temperature (XTe, TS), central electron density (TS) and loop voltage (flux loop) for TCV shot #74304. From C3PO ray-tracing:  $\theta_0^{abs} = 57.4 \pm 0.6^\circ$ .

Table 4.1: List of TCV shots used in the present study.

Shot #	Diagnostics	EC beam 1 <sup>a</sup>		Additional power <sup>b</sup> [MW]	Parameters	
		$\theta_0^{abs}$ [°]	$\rho_{\psi_p}^{abs}$ [-]		$Z_{eff}$ <sup>c</sup> [-]	$Z_p$ [cm]
74304	HXRS, CXRS	$57.4 \pm 0.6^\circ$	$0.21 \pm 0.03$	-	$2.0 \pm 0.4$	2.4
75528	HXRS, TPCI	$59.0 \pm 0.2^\circ$	$\sim 0.20$	-	-	23.0
77400	HXRS, CECE	$57.3 \pm 1.8^\circ$	$\sim 0.25$	-	-	23.0
74305	HXRS, CXRS	$65.7 \pm 0.4^\circ$	$0.18 \pm 0.03$	-	$1.9 \pm 0.3$	2.2
77401	HXRS, CECE	$69.5 \pm 0.3^\circ$	$\sim 0.19$	-	-	23.0
74310	HXRS, CXRS	$57.3 \pm 1.2^\circ$	$0.16 \pm 0.02$	0.794	$2.2 \pm 0.4$	-0.2
74309	HXRS, CXRS	$64.8 \pm 0.4^\circ$	$0.13 \pm 0.04$	0.794	$2.3 \pm 0.8$	0.0

<sup>a</sup>Power-modulated beam (maximum power 0.729 MW, minimum power 0.140 MW);

<sup>b</sup>Steady-state heating with additional EC beam;

<sup>c</sup>From CXRS estimations;



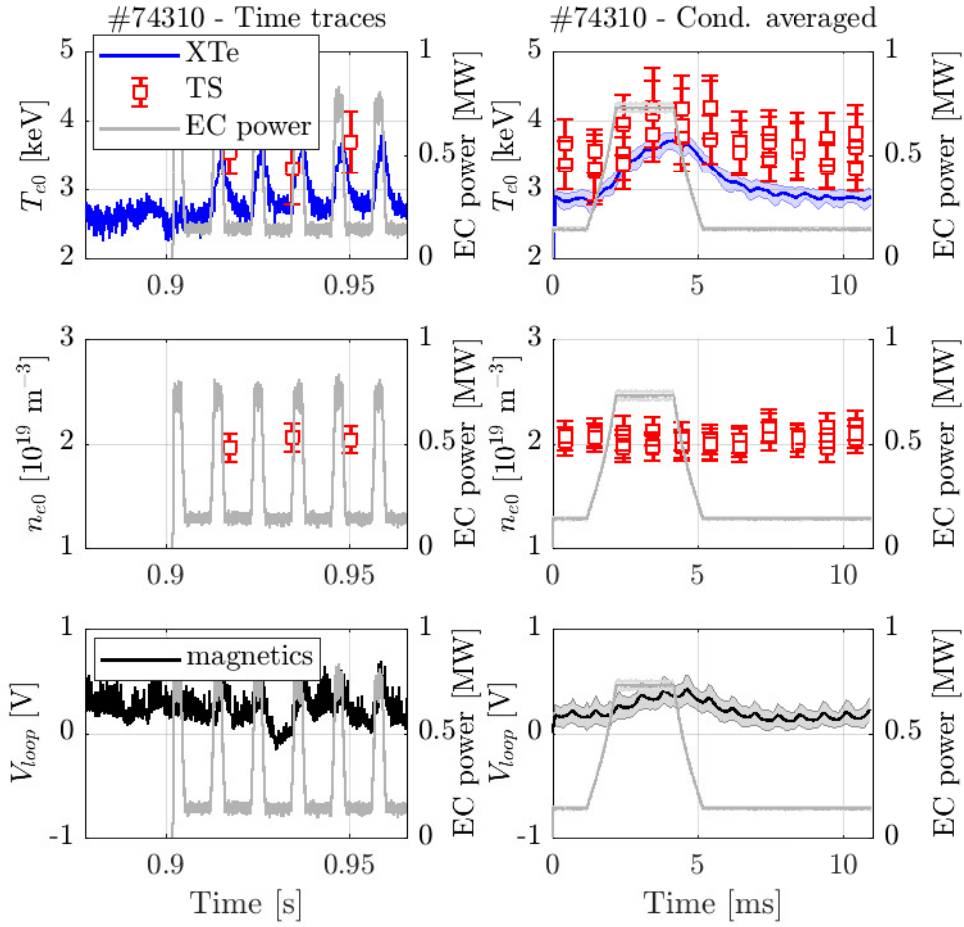


Figure 4.7: Time traces (*left*) and conditionally averaged time traces (*right*) of central electron temperature (XTe, TS), central electron density (TS) and loop voltage (flux loop) for TCV shot #74310. From C3PO ray-tracing:  $\theta_0^{abs} = 57.3 \pm 1.2^\circ$  for the power-modulated EC beam. The background heating EC beam power is not represented. Second beam parameters are  $P_{EC,0} = 0.794$  MW,  $\theta_0 = -89.37 \pm 0.05^\circ$ .

### 4.3 Numerical tools

Different numerical tools are used in this project. The first one is the bounce-averaged drift-kinetic Fokker-Planck solver (see section 3.2.1 for more details), coupled to the ray-tracing code C3PO (see section 3.1.2). Generally speaking, for electrons, the Fokker-Planck equation reads

$$\frac{\partial f_e}{\partial t} + \{f_e, H_e\} = \sum_s \mathcal{C}(f_e, f_s) + \sum_n \mathcal{Q}_{EC,n}(f_e) + \mathcal{E}(f_e) + \mathcal{S}(f_e) \quad (4.1)$$

where  $f_e$  is the electron distribution function,  $H_e$  the Hamiltonian for electrons and  $\{\cdot, \cdot\}$  the Poisson brackets. The collisions between electrons and species  $s$  are described by the collision operator  $\mathcal{C}(f_e, f_s)$ , the Ohmic electric field by the operator  $\mathcal{E}(f_e)$  and the EC plasma-wave interaction by the quasilinear (QL) diffusive operator  $\mathcal{Q}_{EC,n}$  for each harmonics  $n$ . This diffusive operator, detailed in section 3.2.1, can be written in the  $(\rho_{\psi_p}, p_{\parallel}, p_{\perp})$  phase space as



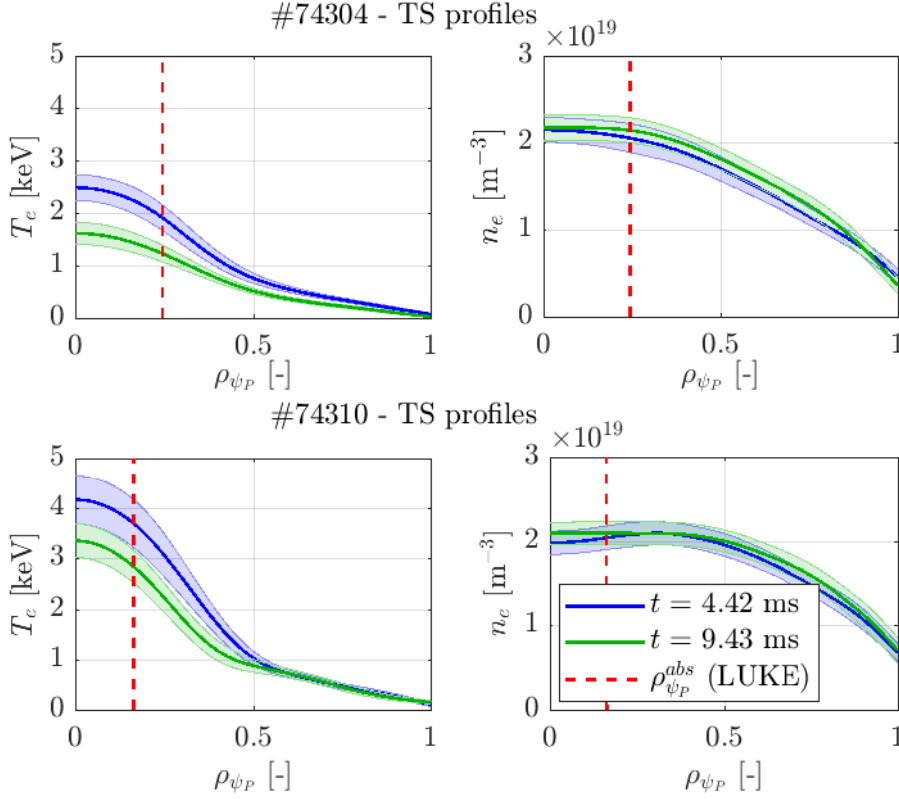


Figure 4.8: Electron temperature (*left*) and density (*right*) profiles measured with the Thomson Scattering diagnostic for TCV shot #74304 (*top*) and #74310 (*bottom*). Time  $t = 4.4$  ms is during the high power phase of the EC pulse, time  $t = 9.4$  ms corresponds to the low power phase.

follows

$$\mathcal{Q}_{EC,n} = \nabla_{\mathbf{p}} \cdot (\mathbb{D}_{EC,n} \cdot \nabla_{\mathbf{p}} f_e) \quad (4.2)$$

$$\mathbb{D}_{EC,n} = D_{EC,n}(\rho_{\psi_P}, p_{\parallel}, p_{\perp}) \begin{pmatrix} 0 & 0 & 0 \\ 0 & s_n^{\parallel\parallel} & s_n^{\parallel\perp} \\ 0 & s_n^{\perp\parallel} & s_n^{\perp\perp} \end{pmatrix} \quad (4.3)$$

where  $D_{EC,n}$  is the diffusion coefficient and  $s_n^{\perp\perp}$ ,  $s_n^{\perp\parallel}$ ,  $s_n^{\parallel\perp}$  and  $s_n^{\parallel\parallel}$  are the tensor elements for diffusion in phase space [Koch 2006; Donnel et al. 2021]. Zero orbit width has been assumed in LUKE, therefore, no neoclassical radial transport term is included in the EC wave diffusion matrix. As described in section 3.2.1, in LUKE, equation 4.1 is bounce-averaged and linearized (see equations 3.45 and 3.46), meaning that, by construction, turbulent transport cannot develop ab initio. Instead, turbulent transport is modeled using an ad-hoc radial transport model  $\mathcal{S}$  taking the form of a diffusive and convective operator

$$\mathcal{S}(f_e) = \nabla_{\rho_{\psi_P}} \cdot (\mathbb{D}_r \cdot \nabla_{\rho_{\psi_P}} f_e - \mathbf{V}_r f_e). \quad (4.4)$$

It has been shown in [Choi et al. 2020a] that a simple transport coefficient constant over time and homogeneous in phase space is not sufficient to correctly match the experimental data. Indeed, constant radial diffusion over time leads to an overestimated HXR decay rate after the

EC is turned off, implying that transport is at least time (or power) dependent (see figure 16 of [Choi et al. 2020a]). To recover the shape of the HXR emission profile over camera channels, a radial diffusion tensor  $\mathbb{D}_r$  proportional to the total EC power and to the EC diffusion in phase space was required (see figure 20 of [Choi et al. 2020a]). This radial transport operator takes the following form in  $(\rho_{\psi_p}, p_{\parallel}, p_{\perp})$  space (the pinch velocity is  $\mathbf{V}_r = (0, 0, 0)$ )

$$\mathbb{D}_r(\rho_{\psi_p}, p_{\parallel}, p_{\perp}, t) = D_r(\rho_{\psi_p}, p_{\parallel}, p_{\perp}, t) \begin{pmatrix} 1 & 0 & 0 \\ 0 & 0 & 0 \\ 0 & 0 & 0 \end{pmatrix} \quad (4.5)$$

where the radial diffusion coefficient  $D_r$  is defined by

$$D_r(\rho_{\psi_p}, p_{\parallel}, p_{\perp}, t) = D_{r0} \frac{P_{EC}(t)}{\max_t [P_{EC}]} \frac{D_{EC,n}(\rho_{\psi_p}, p_{\parallel}, p_{\perp}, t)}{\max_{\rho_{\psi_p}, p_{\parallel}, p_{\perp}} [D_{EC,n}]} \quad (4.6)$$

where  $P_{EC}$  is the EC power injected at a given time  $t$  and  $D_{r0}$  is the control parameter which is tuned to match experimental HXRS data. The time dependence of the wave diffusion coefficient  $D_{EC,n}$  arises from time variations in plasma equilibrium and EC parameters. LUKE normalizes this coefficient locally in time, so the actual EC power dependence has to be taken into account separately. It is important to note that the main characteristic of the suprathermal electron transport as developed in [Choi et al. 2020a] is the wave-power dependency rather than the phase-space dependency (see the difference between step-Dr and QL-Dr with respect to  $Dr = 1$  in figures 16 and 20 of [Choi et al. 2020a]).

As mentioned above, in EC power modulation experiments, the duty cycle is such that the high power phase is much shorter than the current density diffusion time, so it can be assumed that the plasma current remains frozen during modulation cycles [Choi et al. 2020a]. This assumption is made in LUKE calculations for the modulation experiments and the plasma current density profile  $j_p$  is constrained by adjusting the toroidal electric field profile  $E_{\parallel}$ . The LUKE frozen-current-density calculation scheme is presented in section 3.2.1, for a given time step. The first time step is initiated using a Maxwellian electron distribution function  $f_{e,M}$ , while the following time steps are initiated using the previous time step's distribution function. At a given time step, the bounce-averaged Fokker-Planck equation is solved, with prescribed temperature and density profiles, taken from the TS diagnostic measurement at the considered time. This means that the electron temperature profile at a given time is already affected by the EC waves. Therefore, the profiles are not self-consistently evolved, but remain as prescribed, and the prescription changes at each time step, according to the experimental data. To keep these profiles as initially defined, some dissipation is necessary. This dissipation is naturally introduced by the linearized relativistic electron-electron collision operator, which is, by construction, momentum conserving but not energy conserving [Braams and Karney 1989]. In fact, the temperature evolution is imposed in the kinetic equation through the field particle distribution in the e-e collision operator, accounting for the fact that this operator itself does not conserve energy. The approximation is valid as long as the temperature evolution is slower than the e-e collisional energy relaxation, reading  $(1/T_e) \times dT_e/dt \ll \nu_{ee}$  with  $\nu_{ee}$

the e-e collision frequency. Dynamical LUKE simulations are also described in [Peysson et al. 2011] and in [Decker et al. 2012], without the frozen current part.

The experiments aiming to study the dynamics of EC plasma-wave interaction also motivated the implementation of a new EC source [Donnel et al. 2021, 2022] in the global particle-in-cells flux-driven gyro-kinetic code ORB5 [Lanti et al. 2020] and represent the first opportunity for testing the hypothesis of turbulent transport enhancement of suprathermal electrons by EC waves from first principles. This second numerical tool is described in more details in section 3.2.2. Similarly to LUKE, ORB5 solves the equation 4.1 but for both ions and electrons and without the Ohmic electric field operator and the ad-hoc transport. This equation is consistently coupled to a quasi-neutrality equation. This set up allows one to compute consistently the evolution of the electron distribution function in presence of the EC source, of turbulence and of neoclassical transport. It is important to note that, in ORB5, the electron Larmor radius is neglected with respect to the ion Larmor radius, meaning that no neoclassical radial transport is included in the quasilinear plasma-wave interaction operator [Donnel et al. 2021]. The EC source is developed from a quasilinear plasma-wave interaction operator similar to the operator in LUKE [Donnel et al. 2021], and the process is detailed in section 3.2.2. Turbulent transport in ORB5 develops naturally from the non-linear terms included in the Poisson brackets  $\{f_e, H_e\}$  coupled to the quasi-neutrality equation, and potentially the quasilinear plasma-wave interaction operator.

### 4.4 Experimental suggestion of turbulent transport enhancement by EC waves

#### 4.4.1 Transport of fast electrons suggested by Hard X-Ray Spectrometer measurement

HXRS data have been sampled with a time binning of 0.2 ms. Conditional averaging over the 48 pulses per discharge then makes it possible to measure an HXR intensity  $I_{HXR}$  down to  $\sim 100$  counts-per-second (cps). The charge collection time in cadmium telluride sets an upper limit of  $\sim 5 \times 10^5$  cps (pile-up limit). To find the HXR emissivity  $\epsilon_{HXR}$ , 2D tomographic inversions of conditionally-averaged HXRS data are performed at each time step, using the Minimum Fisher Regularization inversion method, with a finite differences spatial discretization on a flux-based grid, i.e. in the poloidal cylindrical coordinates  $(\rho_{\psi_p}, \theta)$ . The principle of tomographic inversion is illustrated in figure 4.9, showing the selected HXRS channels covering the poloidal cross-section of the plasma, the spatial discretization of the plasma and the 2D reconstruction. Details on tomographic inversion methods used with the HXRS at TCV can be found in chapter 2.2 of [Choi 2020] and chapter 2.6 of [Kamleitner 2015]. From these tomographic inversions, it is possible to plot the conditionally-averaged HXR emissivity radial profile at a given poloidal angle  $\theta$ . Figure 4.10 shows the time evolution of this emissivity profile  $\epsilon_{HXR}(\rho_{\psi_p}, t)$  for photon energies  $20 \leq E_{HXR} \leq 30$  keV, taken at  $\theta = 0$ , which corresponds to the low-field side equatorial midplane. As expected, HXR emissivity is higher for configurations

with a stronger ECCD component, both with and without additional heating power (#74304  $\geq$  #74305 for no additional power and #74310  $\geq$  #74309 for 794 KW of additional ECRH), as well as for higher total EC power at a ECCD given angle (#74310  $\geq$  #74304 for  $\theta_0^{abs} \simeq 57^\circ$  and #74309  $\geq$  #74305 for  $\theta_0^{abs} \simeq 65^\circ$ ). The EC resonance condition is given by  $\omega - k_{\parallel} v_{\parallel} - n\Omega_{c,e}/\gamma$ , where  $\omega$  is the EC wave frequency,  $v_{\parallel}$  the parallel velocity of electrons and  $\Omega_{c,e}/\gamma$  the relativistic electron-cyclotron frequency [Prater 2004]. A stronger ECCD component means that electrons are accelerated at higher velocity due to the Doppler shift of the resonance (term in  $k_{\parallel} v_{\parallel}$ ), leading to an increase of the HXR signal. When background ECRH power is added, the initial distribution is already no longer Maxwellian: the bulk temperature increases and a plateau is formed in the distribution at the resonance location in phase space (this is illustrated in figure 9 of [Donnel et al. 2022]). This means that the initial energetic electron population is larger and so that there is a larger target for the power-modulated ECCD beam to be absorbed by. This is illustrated by the bottom plots of figure 4.10, which show a substantial amount of HXR during the low power phase, due to the background ECRH (contrary to the top plots of figure 4.10), and an enhanced emissivity is observed during the ECCD pulse.

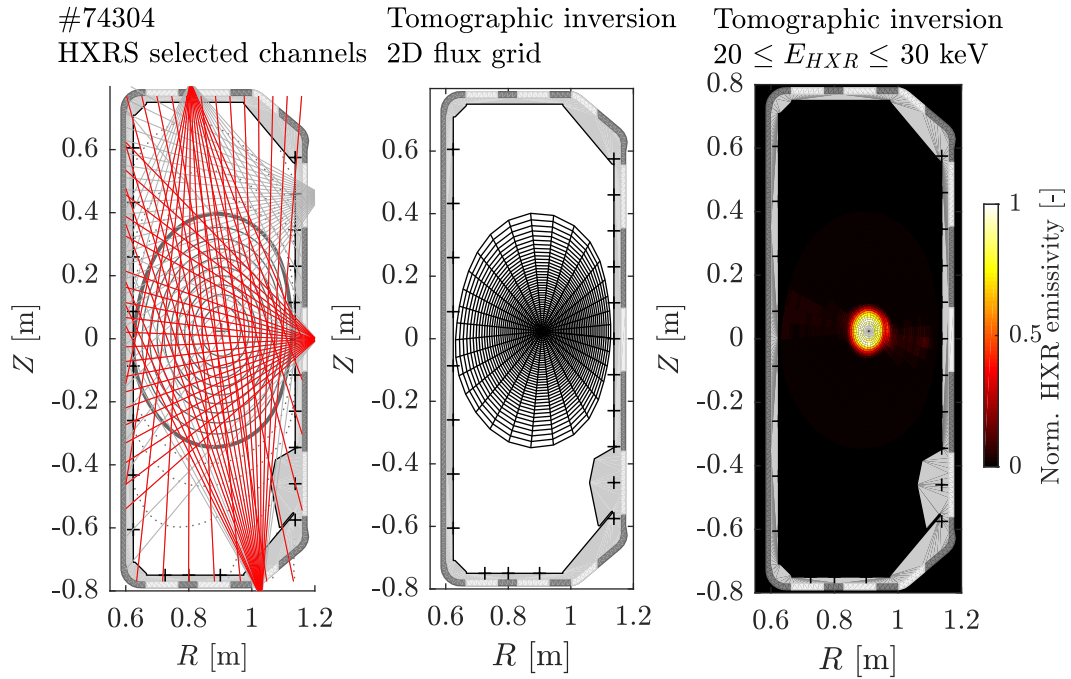


Figure 4.9: Selected HXR channels for tomographic inversion of experimental data (*left*), associated 2D flux-based grid (*center*) and results of the 2D inversion for shot #74304, for photon energies  $20 \leq E_{HXR} \leq 30$  keV, at time  $t = 4.4$  ms in the EC pulse frame (*right*), using the Minimum Fisher Regularization inversion method (target error  $\sigma_e = 0.07$ ).

The next step is to extract possible quantitative information about the transport of suprathermal electrons from these emissivity profiles. First, an estimation of the delay in the HXR rising front is proposed. Each time trace of the space and time emissivity data  $\epsilon_{HXR}(\rho_{\psi_P}, t)$  is

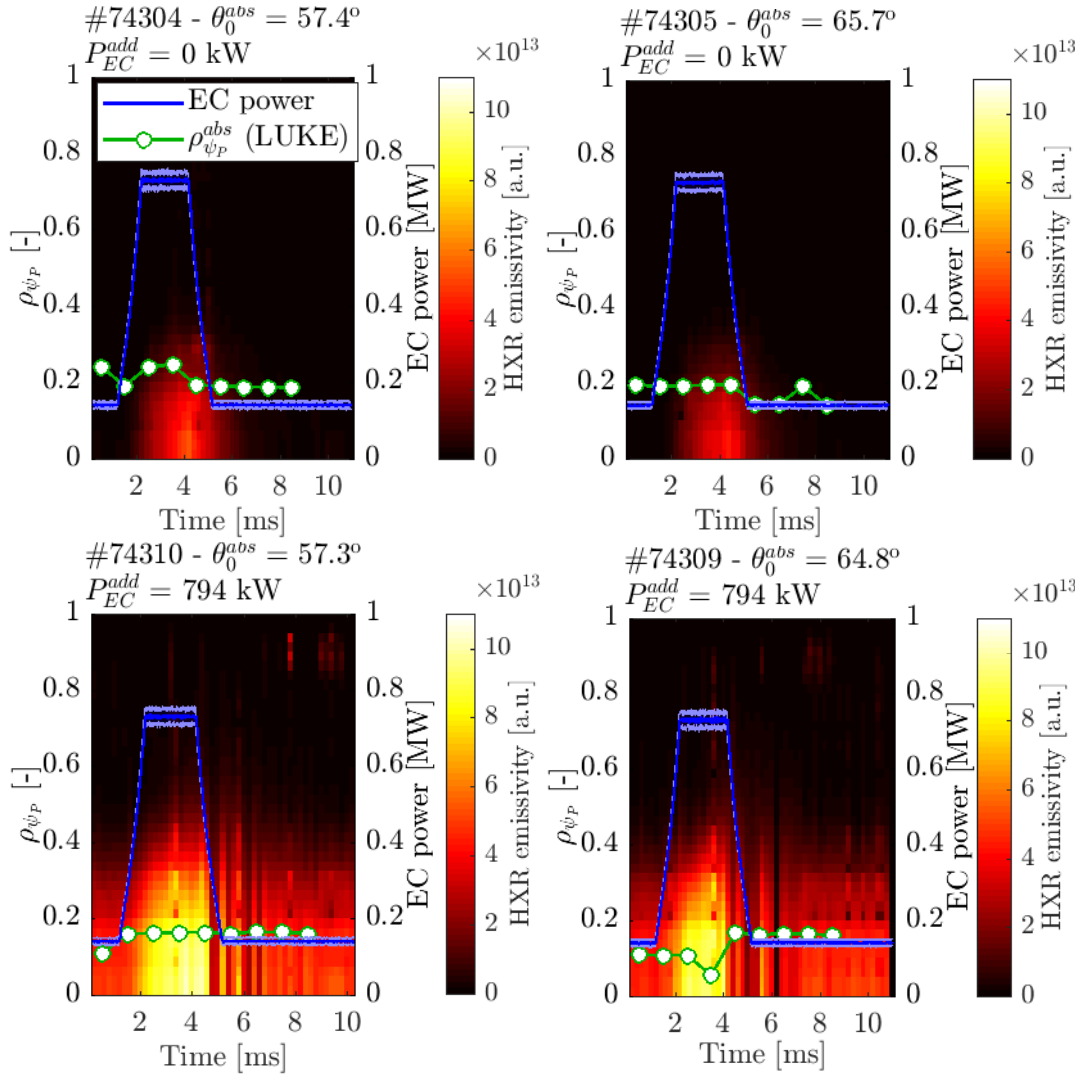


Figure 4.10: Evolution of radial hard X-ray emissivity profiles calculated from 2D tomographic inversion of conditionally-averaged HXRS experimental data for a set of TCV shots (see table 4.1), using the Minimum Fisher Regularization inversion method, and displayed as a radial function on the low-field side equatorial midplane (poloidal angle  $\theta = 0.03\pi$ ). The photon energy is  $20 \leq E_{HXR} \leq 30$  keV and the absorption location is computed with LUKE/C3PO.

normalized to its maximum at each radial location

$$\forall \rho_{\psi_P} \quad \bar{\epsilon}_{HXR}(\rho_{\psi_P}, t) = \frac{\epsilon_{HXR}(\rho_{\psi_P}, t)}{\max_t [\epsilon_{HXR}(\rho_{\psi_P}, t)]} \quad (4.7)$$

From this conditionally-averaged tomographically-inverted HXR signal, it is possible to estimate the aforementioned delay  $\tau_d$  between the HXR rising front at absorption location and the HXR rising front at other locations by computing the following cross-correlation function

$$c_{\times}(\rho_{\psi_P}, \tau_d) = \int_{-\infty}^{\infty} \bar{\epsilon}_{HXR}(\rho_{\psi_P}^{abs}, t) \bar{\epsilon}_{HXR}(\rho_{\psi_P}, t - \tau_d) dt. \quad (4.8)$$

In practice, the corresponding delay profile  $\tau_d(\rho_{\psi_p})$  can be obtained in two different ways: either by taking the local maximum of  $c_\times$  at each radial location

$$\forall \rho_{\psi_p} \quad c_\times(\rho_{\psi_p}, \tau_d^{max, c_\times}) = \max_{\tau_d} [c_\times(\rho_{\psi_p}, \tau_d)], \quad (4.9)$$

using smoothed normalized emissivity time traces to reduce the noise of the raw signal. A moving average method has been applied, using a five-samples wide window, to smooth the time traces. These cross-correlations (normalized with respect to their maximum value) and delays are represented in figure 4.11 and obtained from the tomographic data in figure 4.10, for photon energies  $20 \leq E_{HXR} \leq 30$  keV.

On average, for shots without additional background heating, a clear positive delay is observed, meaning that the signal is late compared to the reference signal at the absorption location. This positive delay increases with radius. This suggests that suprathermal electrons are transported away from the resonance radial location. When adding ECRH power, this delay remains positive but seems to be shorter, suggesting a higher level of transport with respect to shots without additional heating power. No clear differences are seen between the two different ECCD angles  $\theta_0^{abs} \simeq 57^\circ$  and  $\theta_0^{abs} \simeq 65^\circ$ . For shots with additional EC power, the safety factor is lower than for reference shots with only one EC beam, and the loss of correlation at  $\rho_{\psi_p} \sim 0.4$  seems to be correlated with the location of the  $q = 2$  surface. This loss of correlation may be due to some remaining MHD activity changing locally the shape of the HXR emissivity profile, by expelling particles for instance. Inside  $\rho_{\psi_p} \sim 0.4$ , the HXR emissivity time traces are consistent with ECRH/CD-dominated HXR generation, but for  $\rho_{\psi_p} \geq 0.4$ , the impact of MHD may not be completely excluded. It has to be noticed that, for radial locations  $\rho_{\psi_p} \geq 0.6$  (even  $\rho_{\psi_p} \geq 0.5$  for #74305, which shows the lowest HXR emissivity, due to its weaker ECCD component and its lack of additional heating power), the photon count rate becomes very low and the estimation of the delay becomes doubtful (this can be seen from the emissivity plotted in figure 4.10). Also, the time resolution of the processed HXR signal is 0.2 ms, for a typical observed delay  $\leq 1$  ms, meaning that it is difficult to extract solid quantitative information from this analysis (although it remains qualitatively valid). Imposing a higher time resolution on the HXRS would lead to a lower count rate statistics per time bin and 0.2 ms represents a good trade-off.

The power modulation of ECCD generates an electron temperature perturbation, but also a suprathermal electron density perturbation, which is reflected in the HXR emissivity. From the analysis of the hard-X ray emission, in particular of the delay in HXR emission from the wave absorption location, one can extract the radial phase velocity  $v_{\phi,d}$  of the hard X-ray perturbation and the associated exponential decay length of the perturbation  $\lambda_d$ , which are assumed to be proxies for the suprathermal electron density perturbation induced by the EC wave absorption. Assuming a purely diffusive radial transport, it is then possible to derive an estimation of the local effective radial diffusion coefficient through  $D_r^{exp} = \lambda_d v_{\phi,d} / 2$  [Cardozo 1995]. The diffusion coefficient obtained by such an analysis is then related to suprathermal electron particle transport. Studying the temperature perturbation should in principle enable

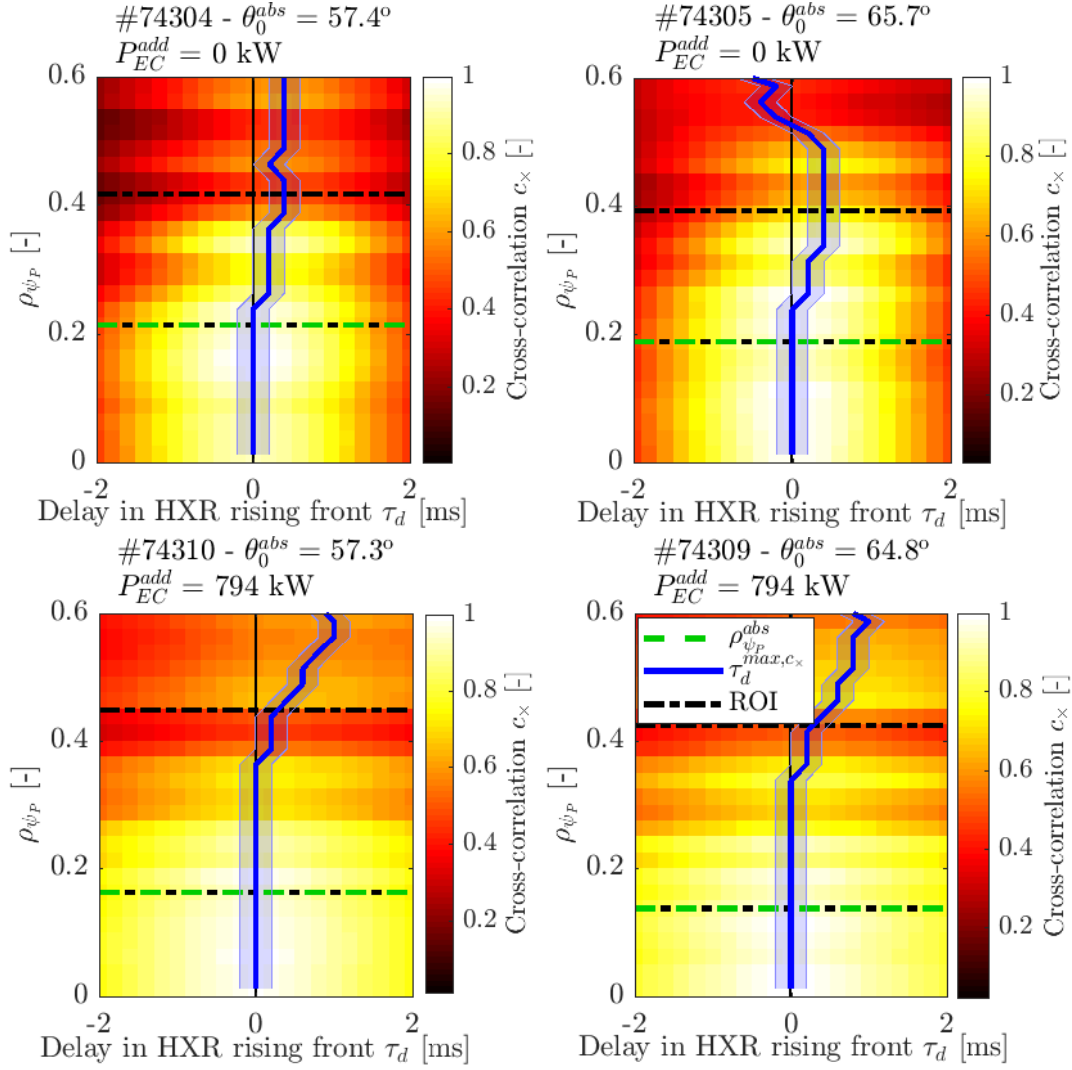


Figure 4.11: Estimation of the delay of the HXR rising front from cross-correlation  $c_x$  (equation 4.8) of tomographic data presented in figure 4.10. The delay is estimated from local maxima of the cross-correlation function. The absorption location is computed by LUKE/C3PO. The range of interest (ROI) of the fits to estimate the experimental radial diffusion coefficient is within the black dashed lines. The error bars on the delay correspond to the time resolution.

the study of electron heat transport [Ryter et al. 2010], but this is outside the scope of the present study. The estimation of the effective radial diffusion coefficient  $D_r^{exp}$  is achieved by taking the radial profile of the delay and the HXR emissivity amplitude corresponding to the measured delay at each radial location  $\epsilon_{HXR}(\tau_d^{max,c_x}(\rho_{\psi_P}))$  (similarly to a phase-amplitude diagram from Fourier transform), and applying linear fits in a region free of the perturbation source [Cardozo 1995; Ryter et al. 2010]. The linear fits read

$$\tau_d(r) = v_{\phi,d}^{-1} r + \tau_{d,0} \quad (4.10)$$

where  $r$  is the minor radius,  $v_{\phi,d}$  is the phase velocity of the perturbation, and

$$\ln[\epsilon_{HXR}(\tau_d(r))] = -\lambda_d^{-1}r + \ln[\epsilon_{HXR}]_0 \quad (4.11)$$

The estimation of  $D_r^{exp}$  has to be taken with care, as the convection has been neglected and the estimation of the delay is limited by the time resolution of the diagnostic. It has to be noted that convection affects mostly the amplitude profile, but not the phase profile, and the high modulation frequency of the perturbation reduces its impact [Ryter et al. 2010]. An example of fitting is shown in figure 4.12 for TCV shot #74304, with  $\theta_0^{abs} \simeq 57^\circ$  and no additional heating power.

Results for the experimental diffusion coefficient associated with suprathermal electron radial transport are shown in table 4.2. The fits are performed over four centimeters toward the plasma edge, starting from the EC wave absorption location, for shots without additional ECRH, and over five centimeters for shots with additional heating power. For shots with higher background power, the delay is much shorter than for shots without background heating and the validity of the fits may be questionable. In particular, it can be seen on figure 4.11 that the delay is shorter than the time resolution for  $\rho_{\psi_p} \leq 0.35$ . After this point, the delay consistently increases, suggesting that a positive average delay within the studied plasma layer is plausible, and extending this layer from four centimeters up to five helps to obtain a reasonable estimate for the phase velocity of the HXR perturbation (the expected order of magnitude is  $v_{\phi,d} \sim 250$  m/s for a time resolution of 0.2 ms and a width of 5 cm). In any case, these values should not be taken as accurate diffusion coefficient values, but are useful visual qualitative indicators of the increased transport of suprathermal electrons with increased EC power. On the other hand, no major differences can be identified for the different ECCD angles.

Table 4.2: Results of the transport analysis from HXRS measurements. For shots without additional background, the diffusion coefficient is estimated over 4 cm from  $\rho_{\psi_p}^{abs}$  and for shots with additional ECRH, it is estimated over 5 cm from  $\rho_{\psi_p}^{abs}$ .

Shot #	$\theta_0^{abs}$	$P_{EC}^{add}$	$v_{\phi,d}$ [m/s]	$\lambda_d$ [cm]	$D_r^{exp}$ [m <sup>2</sup> /s]
#74304	57°	-	110 ± 40	1.8 ± 0.4	0.9 ± 0.4
#74305	65°	-	80 ± 20	1.6 ± 0.2	0.6 ± 0.2
#74310	57°	794 kW	230 ± 140	4 ± 1	5 ± 3
#74309	65°	794 kW	230 ± 140	5 ± 2	6 ± 4

Finally, the decay rate of the HXR after the EC pulse is consistent with the collisional slowing-down of fast electrons on bulk electrons:  $\tau_{SL}^{ee} \sim 1$  ms for 20 keV electrons near the absorption location ( $\rho_{\psi_p} \leq 0.4$ ), while for fast electrons slowing down on bulk ions one gets  $\tau_{SL}^{ei} \sim 2\text{-}3\tau_{SL}^{ee}$ . The slowing-down times are estimated using the formulas in [Huba 2016].



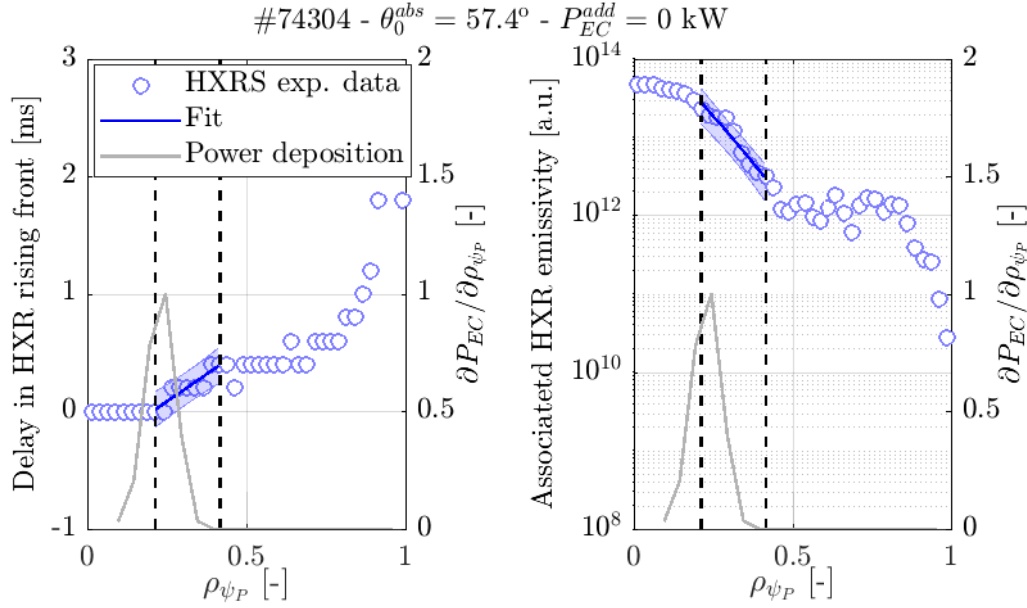


Figure 4.12: Phase  $\tau_d^{max, c_x}$  (left) and amplitude  $\epsilon(\tau_d^{max, c_x})$  (right) extracted from HXR emissivity analysis for TCV shot #74304. The linear fit and their associated coefficient of determination are also shown. The error bars give the 95% confidence of the fits.

#### 4.4.2 Increased turbulence during high-power Electron-Cyclotron phase from experimental measurements

As shown in [Happel et al. 2015; Navarro et al. 2015], changes in turbulent properties can be expected during the EC power pulses. Indeed, the turbulence level and frequency have been measured for different space scales using Doppler Back-Scattering diagnostic in ECRH experiments performed in ASDEX Upgrade [Happel et al. 2015] and compared with linear and non-linear gradient-driven gyro-kinetic simulations [Navarro et al. 2015], showing that high power ECRH (1.8 MW) leads to an increase of the ion-temperature-gradient (ITG)-dominated fluctuation level for large scale only, while small scales are not affected, with potentially increased probability of trapped electron mode (TEM) and ITG co-existence. These modes are briefly introduced in section 2.4.1.

These changes in turbulence properties can be due to the local changes in temperature profiles: both the electron temperature and the electron temperature gradient potentially increase when EC power increases. The normalized logarithmic gradient of temperature  $R/L_{T_e} = -R\nabla T_e/T_e$  (where  $R$  is the major radius) is a critical parameter that determines the stability of both electron and ion temperature gradient modes (ETG, ITG) or trapped electron modes (TEM), which are thought to be the main source of turbulent transport of heat and particles in tokamak plasmas (both being usually strongly correlated) [Garbet et al. 2004a; Happel et al. 2015]. On the other hand, in the case of stiff profiles,  $R/L_{T_e}$  is already at a critical value that cannot be exceeded much, and is maintained almost constant when locally depositing EC power by an increase in turbulent transport [Garbet et al. 2004a,b]. An analogy can be drawn with the critical slope of a pile of sand: when trying to build a pile of

sand with a steeper slope than a critical slope, the sand slides down due to gravity and the critical slope is maintained. The profile stiffness and the associated critical ion or electron temperature gradients as threshold for the destabilization of TEM, ITG or ETG have been demonstrated both experimentally and numerically for different devices [Ryter et al. 2001; Garbet et al. 2004a,b; Happel et al. 2015; DeBoo et al. 2012; Hillesheim et al. 2013]. For ITG, the ion temperature critical gradient is thought to depend on the density gradient and the ion-to-electron temperature ratio, while for TEM, the electron temperature critical gradient is expected to depend on the density gradient and the fraction of trapped electrons [Garbet et al. 2004a].

The normalized logarithmic gradient of electron temperature  $R/L_{T_e}$  are illustrated in figure 4.13 for the TCV shots used in this study. These gradients are derived from conditionally averaged electron temperature profiles, measured by the TS diagnostic. The measured profiles are automatically fitted after the shot acquisition, using cubic spline fits, providing the associated fitting and measurement errors. Propagating the errors through the gradient calculation lead to huge error bars, which renders the analysis more challenging (see figure 4.14). It is possible to reduce these error bars using dedicated kinetic equilibrium profile reconstruction. For the experimental scenarios presented here, the electron temperature gradient does not change significantly during the ECCD pulse (even considering the huge error bars), although a slight drop is observed after the pulse in the case of no additional background EC power. When adding the background ECRH,  $R/L_{T_e}$  increased a bit with respect to the reference case, but remains within the same range (between 15 and 20 around  $\rho_{\psi_p} = 0.4$  for shots without background ECRH power, and between 20 and 25 for shots with additional ECRH background power). It may be noticed that the normalized logarithmic gradient of electron density  $R/L_{n_e} = -R\nabla n_e/n_e$  also does not change significantly. However, as shown in figure 4.15, the temperature ratio  $T_{i0}/T_{e0}$  moves from 0.25 during the low-power phase to 0.10 during the high-power phase for shots using a single EC beam, and from 0.14 to 0.06 for shots with additional ECRH power. The decrease of  $T_{i0}/T_{e0}$  during ECRH has been associated with a strong increase in turbulence in tokamaks [Beurskens et al. 2021a] and stellarators [Beurskens et al. 2021b] in dominant electron-heated experiments, associated with the destabilization of ITG/TEM. The stiffness factor (ratio of perturbed heat diffusivity over background heat diffusivity during heating power modulation experiments) increases with increasing  $T_e$  [Ryter et al. 2001] and it is shown in [Garbet et al. 2004b] that a localized heat source moves the stiff-to-non-stiff limit toward the magnetic axis, while heating near the axis extends the range of the stiff region. These arguments are in favor of stiff profiles in the TCV experiments presented in this study, as the main EC beam is absorbed between  $\rho_{\psi_p} = 0.1$  and  $\rho_{\psi_p} = 0.2$ , for an absorption width estimated by LUKE of the order of  $(\Delta\rho_{\psi_p})_{abs} = 0.12$ . This means that increasing EC power is expected to locally increase turbulent transport rather than locally increase  $R/L_{T_e}$ .

In ASDEX Upgrade, JET, FTU and Tore Supra, dedicated experiments on electron stiffness found a critical logarithmic electron temperature gradient  $3 \leq (R/L_{T_e})_c \leq 8$ , consistent with ITG/TEM expectations from gyro-kinetic simulations [Garbet et al. 2004b]. Direct measurements of turbulence performed in DIII-D exhibit a critical electron temperature gradient

$4.1 \leq (R/L_{T_e})_c \leq 5.5$  (taking  $R = 1.7$  m for DIII-D) above which the electron temperature fluctuation level continuously increases; this has been associated with TEM, which are expected to be destabilized by increasing  $T_e$  or increasing  $R/L_{T_e}$  [Hillesheim et al. 2013; DeBoo et al. 2012]. Simplified analytic estimations of the critical gradients are available for ETG [Jenko et al. 2001; Horton et al. 2004] and TEM [Nordman et al. 1990], as well as for ITG (ion temperature critical gradient) [Horton et al. 2004]. These critical gradients read for TEM [Nordman et al. 1990]

$$(R/L_{T_e})_c^{TEM} = \left[ (1 - f_t) \frac{20}{9} \frac{T_i}{T_e} + \frac{1}{2(1 - f_t)} \frac{T_e}{T_i} \right] R/L_B \quad (4.12)$$

where  $f_t$  is the trapped particle fraction, computed from heated distribution functions obtained with LUKE, and  $R/L_B = -R\nabla B/B$  is the normalized magnetic field gradient, taken on the low-field side for this set of TCV shots (the wave is absorbed on the low-field side). For ETG, it reads [Jenko et al. 2001]

$$(R/L_{T_e})_c^{ETG} = \left( 1 + \frac{Z_{eff} T_e}{T_i} \right) \left( 1.33 + 1.91 \frac{r}{q^2} \frac{dq}{dr} \right) (1 - 1.5\epsilon_r) \left( 1 + 0.3\epsilon_r \frac{d\kappa}{d\epsilon_r} \right) \quad (4.13)$$

where  $\epsilon_r = r/R$  with  $r$  the minor radius and  $R$  the major radius,  $q$  the safety factor,  $Z_{eff}$  the effective charge and  $\kappa$  the plasma elongation. The actual critical electron temperature gradient is the maximum value between the results of equation 4.13 and  $0.8R/L_{ne}$ .

These typical critical gradients are overlaid on figure 4.13, showing that, for all TCV shots used in this study, the electron temperature profile is most probably stiff, at least outside  $\rho_{\psi_p} = 0.2$ . The analytic expression for the ETG critical electron temperature gradient  $(R/L_{T_e})_c^{ETG}$  [Jenko et al. 2001] suggests that ETG are probably unstable when  $T_i/T_e$  is large enough, i.e. during the low power phase of the reference shots, but are stabilized during the EC pulse peaks or for the shot with additional background ECRH. Here, the shaping term of  $(R/L_{T_e})_c^{ETG}$  has been neglected, meaning that the actual threshold for ETG is even higher. However, the analytic electron temperature gradient threshold associated with TEM  $(R/L_{T_e})_c^{TEM}$  indicates that these shots are most probably TEM-unstable, matching quite well expectations from [Garbet et al. 2004b] and [DeBoo et al. 2012].

Results from TPCI measurements, showing the root-mean-square (RMS) of the relative density fluctuation level  $[\delta n_e/\bar{n}_e]_{RMS}$  obtained from conditional averaging of the raw TPCI signal over different time steps of the EC power pulse, are presented in figure 4.16 for TCV shot #75528, which has no additional ECRH power for an ECCD angle  $\theta_0^{abs} \simeq 59^\circ$ . For this shot, the spatial covering of the 13 channels of the TPCI is  $0.2 \leq \rho_{\psi_p} \leq 0.6$ , which corresponds to the region with the maximum temperature gradient and is the deepest region accessible by the diagnostic in this configuration. The error bars consist of a quadratic sum of the measurement uncertainties and of the statistical error from the conditional time-averaging. Looking at the radially-averaged fluctuation level (left-hand plot of figure 4.16), a slight increase in turbulence level is seen with increased EC power. This increase may not look significant when considering

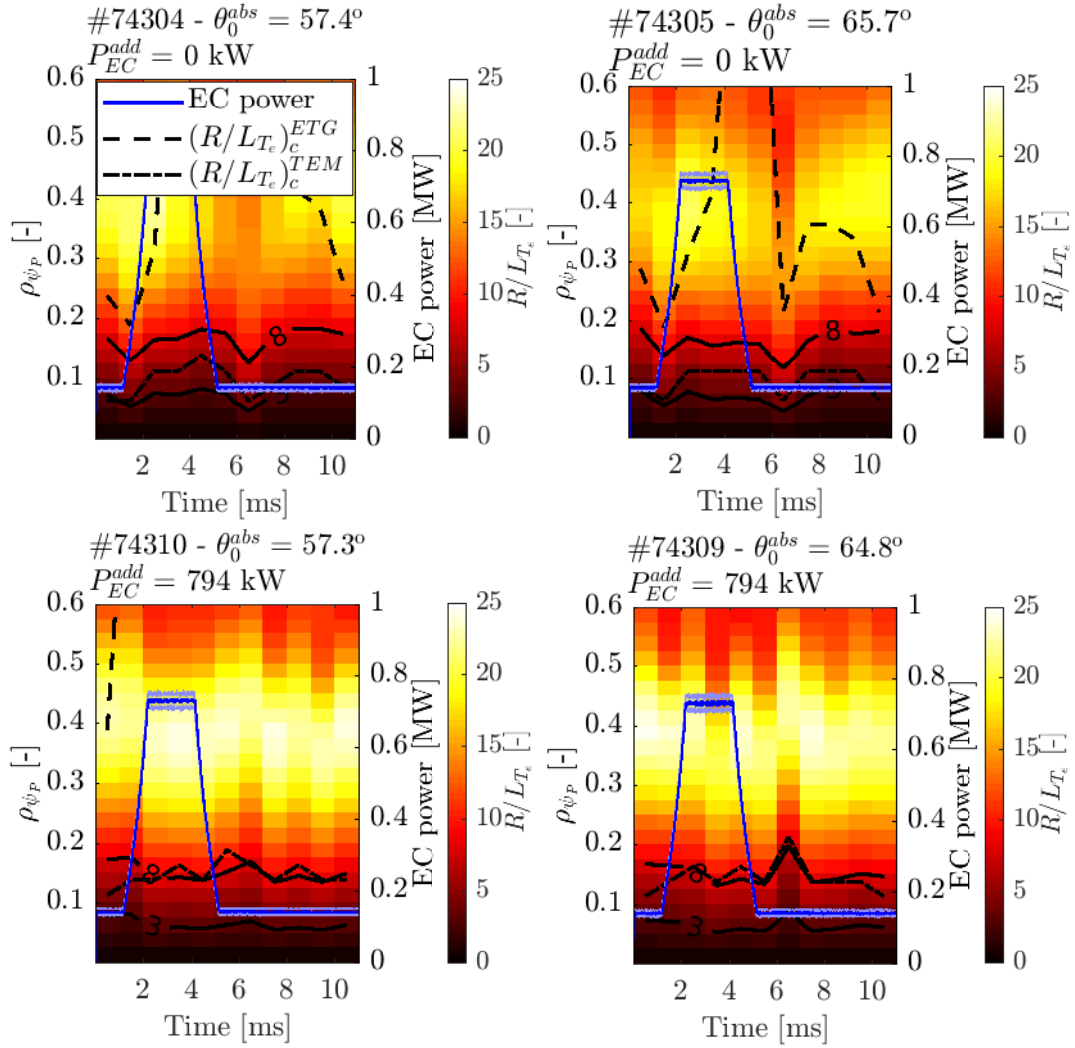


Figure 4.13: Normalized logarithmic gradient of electron temperature  $R/L_{T_e} = -RV_{T_e}/T_e$  for the same TCV shots as in figure 4.10, calculated from the electron temperature measured with the TS diagnostic. Solid black contours show the range of critical  $R/L_{T_e}$  found in [Garbet et al. 2004b]. Analytic formulas for  $(R/L_{T_e})_c^{ETG}$  and  $(R/L_{T_e})_c^{TEM}$  comes from [Jenko et al. 2001] and [Nordman et al. 1990] respectively. The respective contours show the  $\rho_{\psi_p}$  limits above which the  $R/L_{T_e}$  is over the critical values.

the error bars. However, looking at the non-averaged data (right-hand plot of figure 4.16), this slight increase is consistently observed for every TPCI channel (each channel corresponding to a different spatial location). The relative increase in fluctuation level  $(\delta n_e^{FT} - \delta n_e^{LP})/\delta n_e^{LP}$  ( $LP$  stands for low power and  $FT$  for flat-top) is shown for every TPCI channel in the bottom plot of figure 4.16. This consists of a channel-to-channel comparison, and the measurement location is the average between the two positions, while the error bars on the location have been propagated. One can see that, taking into account the error bars, the channel-to-channel increase is significant. Close to the absorption location ( $\rho_{\psi_p} \sim 0.2$ ), the relative increase of fluctuation from low power to high power is between 20% and 30%. This measured increase of turbulence is associated with the increase of  $T_e$  during the EC pulse, while the temperature

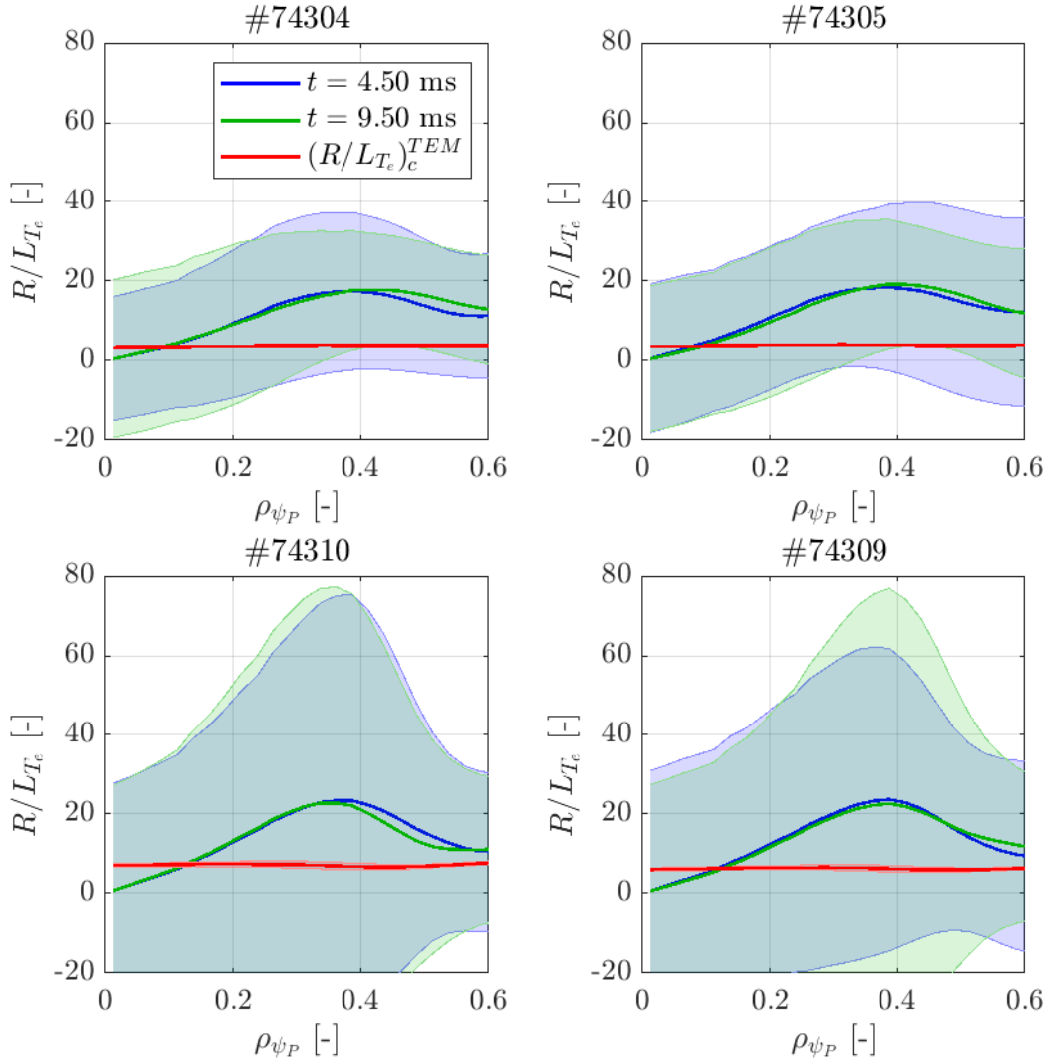


Figure 4.14: Normalized logarithmic gradient of electron temperature  $R/L_{T_e} = -R\nabla T_e/T_e$  for the same TCV shots as in figure 4.10, calculated from the electron temperature measured with the TS diagnostic. the critical TEM gradient  $(R/L_{T_e})_c^{TEM}$  estimated using the formula from [Nordman et al. 1990] is overlaid in red.

gradient  $R/L_{T_e}$  does not change significantly. This observation corroborates the hypothesis of stiff electron temperature profiles in those TCV shots.

Results from CECE measurements are presented in figure 4.17 for two ECCD angles: TCV shots #77400 with  $\theta_0^{abs} \simeq 57^\circ$  and #77401 with  $\theta_0^{abs} \simeq 70^\circ$ , both without additional ECRH power, showing the electron temperature fluctuation level  $\delta T_e/T_e$  for  $0.2 \leq \rho_{\psi_P} \leq 0.4$ . As for the TPCI, the raw CECE signal is first conditionally averaged over the different EC pulse phases (the high power flat-top and the low power phase). These data are produced by integrating the cross-correlation power spectrum of each channel with its closest neighbor (6 frequencies have been used from 78.9 GHz to 79.9 GHz, spaced in 0.2 GHz steps) between 10 kHz and 100 kHz to take the root-mean-square (RMS) of the signal. This RMS is related to the absolute

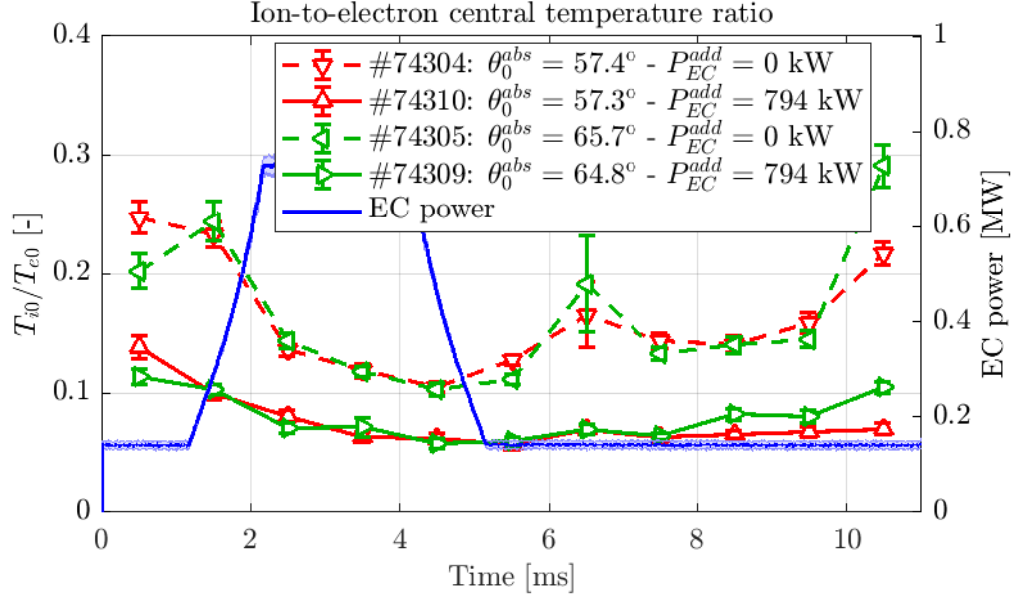


Figure 4.15: Ion-to-electron on-axis temperature ratio, estimated from conditionally-averaged measurements of CXRS and TS diagnostics, for TCV shots #74304, #74305, #74310 and #74309. For both diagnostics, data have been binned on the same local time basis. Error bars are taking into account a quadratic sum of the statistical errors from the conditional averaging and of the measurement errors of TS only.

electron temperature fluctuation level  $\delta T_e$  [Fontana et al. 2017]. The noise floor has been subtracted from the signal prior to its integration. For both ECCD angles, a relatively low level of electron temperature fluctuation  $\delta T_e / T_e$  is measured (between 1% and 6%), but this level consistently increases with higher EC power. From low to high EC power, an average channel-to-channel increase of  $35 \pm 24$  % of the relative electron temperature fluctuation level is measured for  $\theta_0^{abs} \simeq 70^\circ$  (excluding channel 1 for which the uncertainty at low power is higher than the measured level), and of  $49 \pm 37$  % for  $\theta_0^{abs} \simeq 57^\circ$  (excluding channels 1 and 4 for the same reason). It is significant that  $\delta T_e / T_e$  increases with increased EC power even though the absolute temperature increases too. This observation corroborates what has been deduced from TPCI measurements.

## 4.5 Transport studies with experimentally constrained LUKE simulations

LUKE simulations are performed in frozen current density mode, meaning that a reference current density has to be given to constraint the calculation. In LUKE, the bootstrap current  $I_{BS}$  is not calculated thus  $I_p - I_{BS}$  is used as a constraint, where  $I_p$  is the experimental plasma current. The bootstrap current is estimated using the Sauter-Angioni-Lin-Liu model [Sauter et al. 1999, 2002]. The plasma current density  $j_{p0}^{ref}$  is found by solving the steady-state Fokker-

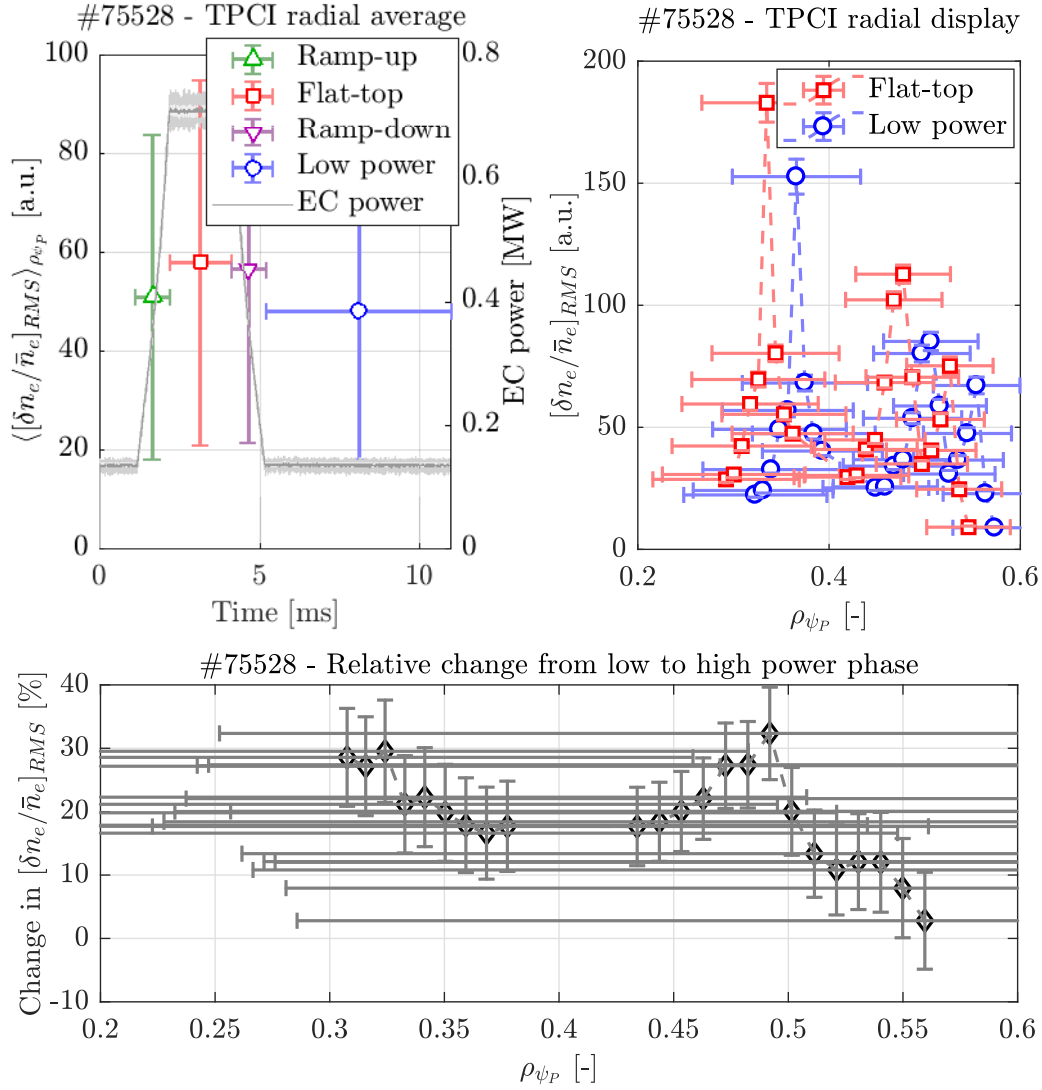


Figure 4.16: Estimation of the relative level of electron density fluctuations measured by the TPCI diagnostic for TCV shot #75528. Data are conditionally averaged over the different phases of the EC pulse. *Top-left*: Data averaged over all TPCI channels, showing turbulence level at different phases of the EC pulse. *Top-right*: Data for each channel, probing different radial locations (only data for the high-power plateau and the low-power phase are shown for clarity). *Bottom*: Relative gap in the density fluctuation level between the low power and the high power phase.

Planck equation (no more frozen current but asymptotic time limit, when the electric field fully diffuses) at the end of the low power phase of an EC pulse, adjusting the loop voltage within its error bar to match the plasma current  $I_p^{LUKE} = I_p - I_{BS_0}$ . Then, the constraint at each time step is given by  $j_p^{ref}(\rho, t) = j_{p_0}^{ref}(\rho) + j_{BS_0}(\rho) - j_{BS}(\rho, t)$ .

The estimation of the effective charge  $Z_{eff}$  is important for estimating the bootstrap current and accurately modeling the electron-ion collisions and thus the Ohmic contribution to the plasma current. In LUKE, only  $C^{6+}$  impurities are modeled, so the experimental values from CXRS can be used. However, the uncertainties on these measurements are non-negligible, in

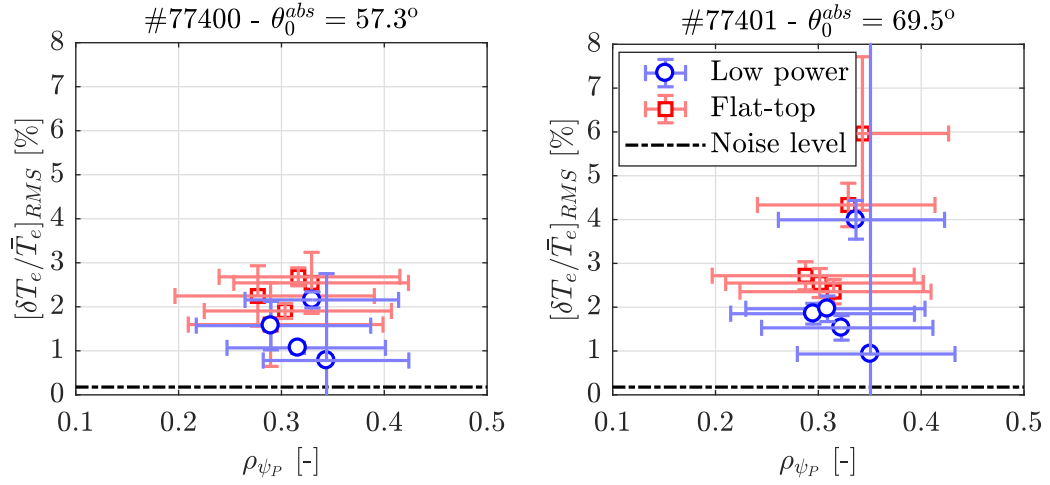


Figure 4.17: Estimation of the relative level of electron temperature fluctuations measured by the CECE for TCV shots #77400 (*left*) and #77401 (*right*). *Flat-top* corresponds to the conditional average over the high power phase of the EC pulses, while *low power* is the same for the low power phase.

particular in the low ion temperature experiments that have been performed ( $T_i \sim 0.2T_e$ ). It is safer to assume that  $Z_{eff}$  stays constant over the shot and to take an average value, rather than trying to determine its time dependency and profile. Indeed, these variations remains within expected error bars. The error bars on  $Z_{eff}$  have been used to add error bars to LUKE simulation results. It has to be noted that only the  $n = 2$  harmonic for the plasma-wave interaction is modeled in the present LUKE simulations to reduce the computational cost, and tests performed with all harmonics  $n = 0...3$  do not show any significant differences.

Another potential factor of uncertainty in LUKE results is the presence of plasma vertical oscillations that can lead to a broadening of the HXR distribution. For all TCV shots used in this study, the plasma vertical position was well controlled and its standard deviation is less than 4 mm. LUKE tests indicate that this change in plasma vertical position has an impact on simulated HXR profiles, but it is less significant than the impact of the effective charge, and could not explain the difference between experimental data and simulations without additional transport. To give an example, the variation of the plasma vertical position introduces a variation of  $\sim 8\%$  in the HXR intensity calculated by LUKE simulations for shot #74304 (considering camera C5, channels 9 to 13, which see the plasma), while the uncertainty in the effective charge introduces a variation of  $\sim 24\%$ . The impact of the plasma vertical oscillations on the EC power deposition width is also minimized by the EC launching configuration.

For the chosen transport model, the only free parameter remaining to match the experimental data is the transport coefficient  $D_{r0}$  (cf. equation 4.6), and the only remaining experimental data to be matched are HXRS data. As HXRS data span three dimensions (time, energy and space), the problem is greatly underdetermined and finding a good match is challenging. The matching process is heuristic and is illustrated in figures 4.18, 4.19 and 4.20 for shot #74304 and in figures 4.21, 4.22 and 4.23 for shot #74310. For shot #74304 with  $\theta_0^{abs} \simeq 57^\circ$



and no additional heating power, a reasonable agreement is found between experiment and simulation for  $D_{r0} = 2 \text{ m}^2/\text{s}$ . With the same procedure, it is found that  $D_{r0} = 2 \text{ m}^2/\text{s}$  for shot #74305 with  $\theta_0^{abs} \simeq 65^\circ$  and no additional heating power, and  $D_{r0} = 4 \text{ m}^2/\text{s}$  for shots #74309 and #74310 with additional heating power and  $\theta_0^{abs} \simeq 65^\circ$  and  $\theta_0^{abs} \simeq 57^\circ$  respectively. The optimum  $D_{r0}$  is similar for different ECCD angles at the same background power, suggesting that the amplitude of the radial transport is power dependent but is not specifically sensitive to the EC launching angles (in the scanned range). Since the effective charge introduces a significant variation in LUKE results, it has been chosen to reduce the granularity of the tested values of  $D_{r0}$  to unity and to not provide an error bar on this value, but to show error bars on the synthetic HXRS data instead. However, the typical uncertainty which can be associated to these  $D_{r0}$  values is of the order of  $1 \text{ m}^2/\text{s}$ .

It should be noted that for both TCV shots with additional ECRH power, the model is able to match well the experimental data for photon energies  $E_{HXR} \geq 30 \text{ keV}$ , but tends to overestimate the photon count rate for  $20 \leq E_{HXR} \leq 30 \text{ keV}$  (see figure 4.21 for instance). The computed HXR count rate is 2.5 to 3.6 times higher than the experimental one with matched transport, compared to 6.0 to 9.5 times higher without transport (for  $\theta_0^{abs} \simeq 57^\circ$  and  $\theta_0^{abs} \simeq 65^\circ$  respectively). This shows that, even though the model is able to reproduce the salient experimental results, it does not necessarily capture all the phenomena. In particular, it is possible that this lower energy range dynamics is still dominated by some remaining MHD activity. Indeed, as shown in figure 4.4, using background EC power, the plasma is not perfectly MHD-quiescent, although the counter-ECCD configuration reduces the MHD activity significantly, going from chirping-down structures to a constant frequency mode around 10 kHz. With the current settings, these modes are too fast to be identified on the HXRS signal (sampling frequency of 5 kHz), and very fast with respect to the beam modulation frequency ( $\sim 91 \text{ Hz}$ ).

The maximum radial transport of electrons in space and time is shown for two ECCD angles  $\theta_0^{abs}$  and two different levels of background ECRH power  $P_{EC}^{add}$  in figure 4.24. This electron transport  $D_r$  being directly proportional to the plasma-wave interaction diffusion coefficient (at the second cyclotron harmonic  $n = 2$ )  $D_{EC,2}$ , some properties of  $D_{EC,2}$  are also observed in  $D_r$ . One can notice that the radial extent of the diffusion coefficient is wider when the ECCD component is larger (lower  $\theta_0^{abs}$ ). This is explained by the fact that in this case the diffusion in real and velocity space is more extended, because of the stronger Doppler shift of the resonance and because the beam is absorbed along a slightly longer path. This is shown in figure 4.25, which displays the radial diffusion coefficient  $D_r$  (or equivalently  $D_{EC,2}$ ) in velocity space at the EC wave absorption location, at the maximum power of the modulation cycle (4 ms in the EC pulse time frame). The modulated EC beam in counter-ECCD is clearly visible and corresponds to the asymmetric trace in  $v_{||}$ , located in the  $v_{||} \geq 0$  half-plane. On the other hand, the additional heating EC beam draws a symmetric trace in  $v_{||}$ . One can

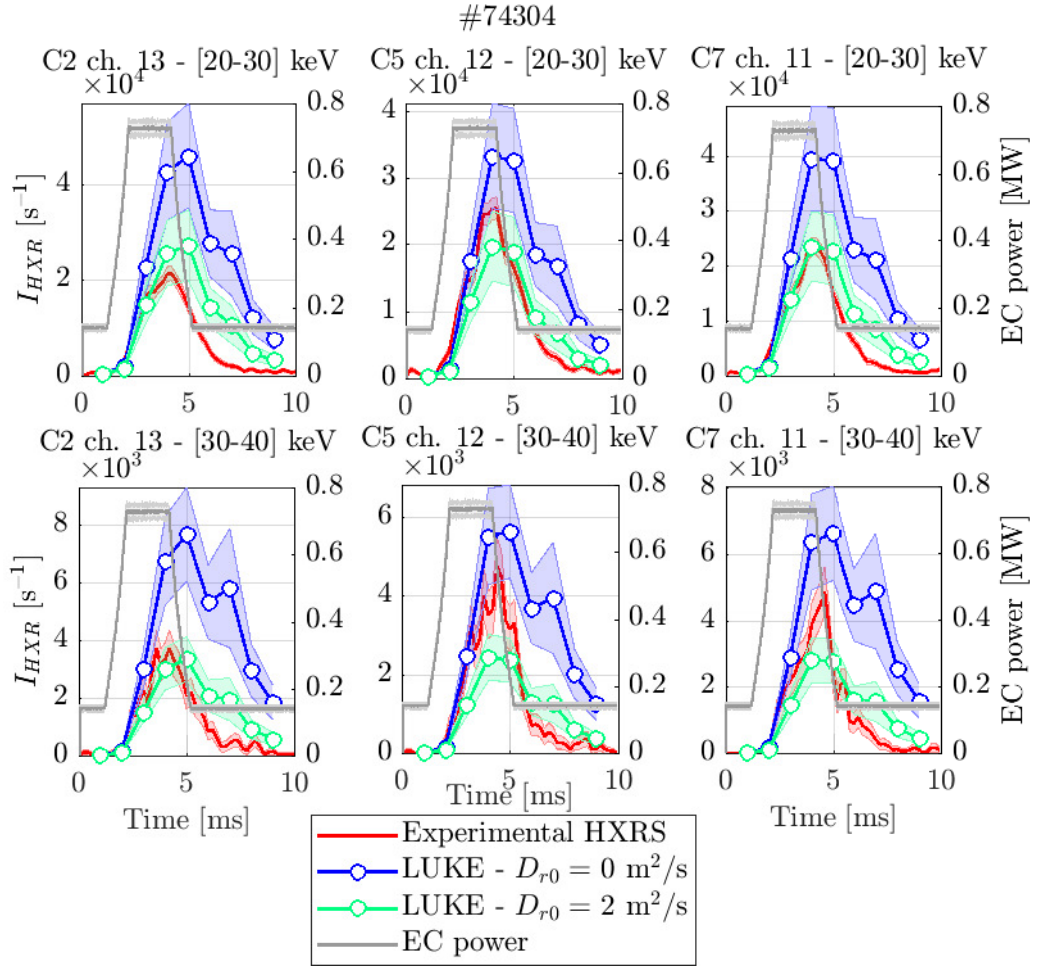


Figure 4.18: Time traces of HXR count rate measured with HXRS compared to LUKE simulations for different values of  $D_{r0}$ , for TCV shot #74304. The error bars on the simulations come from the uncertainties on the effective charge.

see that lower  $\theta_0^{abs}$  leads to an extended diffusion coefficient in absolute momentum (the normalized momentum  $p/p_{Te}$  is normalized with respect to the same temperature for each TCV shot). This is also consistent with the HXR emissivity shown in figure 4.10, as extended power deposition in momentum space means higher HXR count rate in a given energy bin (20-30 keV HXR corresponding to  $\sim 5 - 7.5 p_{Te}$  in figure 4.25). The results of these transport studies using experimentally constrained forward modeling are consistent with the experimental observations made with the HXRS: the experimental estimation of the delay in the HXR rising front from the radial absorption location suggests a faster transport at increased power, and no clear differences when changing the ECCD angle  $\theta_0$ . Both observations are recovered by LUKE simulations.

In principle, this increased radial transport with EC power could be due to the radial and cross momentum-radial or pitch-radial diffusion terms of the quasilinear EC wave operator, arising when considering finite electron Larmor radius effects, which are not included in LUKE. A

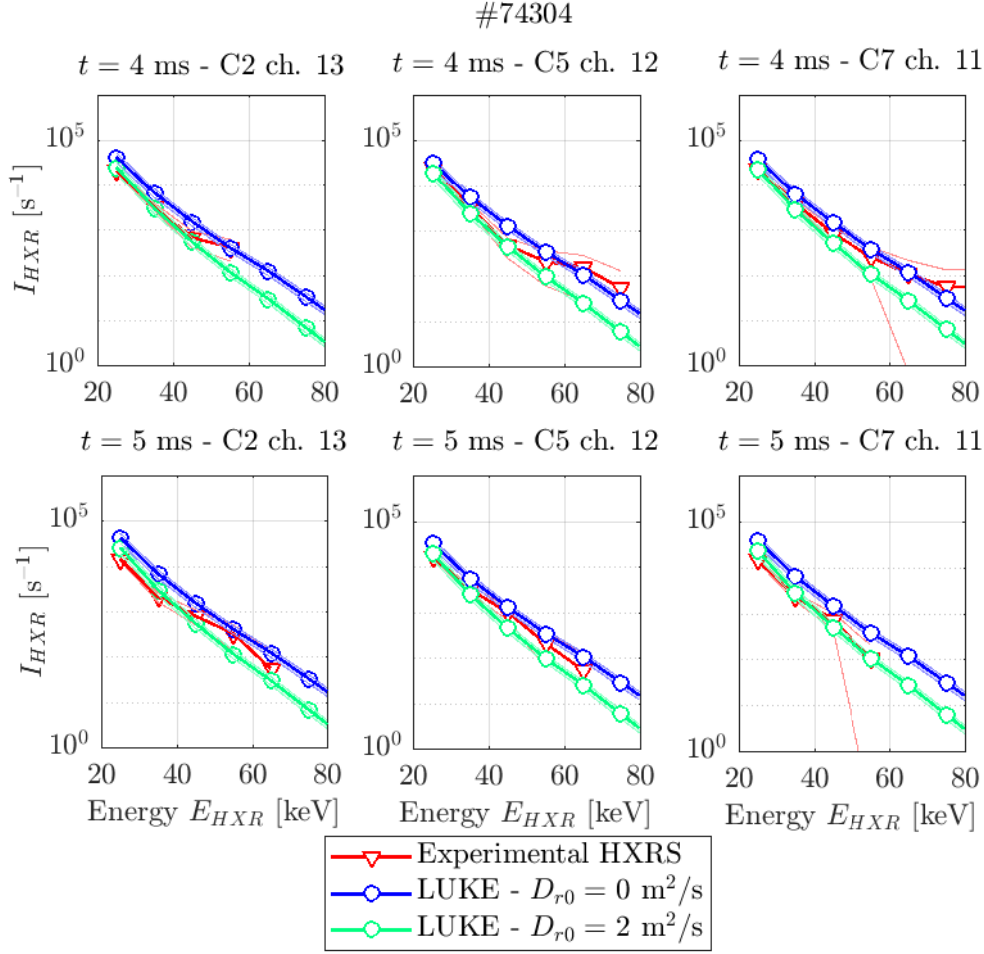


Figure 4.19: Energy spectra of HXR count rate measured with HXRS compared to LUKE simulations for different values of  $D_{r0}$ , for TCV shot #74304. The error bars on the simulations come from the uncertainties on the effective charge.

model for the complete neoclassical EC wave operator is given in [Petrov and Harvey 2016]. A rough estimate of the wave-induced neoclassical radial transport is obtained assuming

$$D_{EC,n}^{rr} \simeq 4w_b^2 \frac{\gamma^2 m_e^2}{p^2} \frac{1}{\xi^2} \left( 1 - \xi^2 - \frac{n\Omega_{c,e}}{\gamma\omega} \right)^2 D_{EC,n} \quad (4.14)$$

with  $p$  the relativistic momentum,  $\xi = p_{\parallel}/p$  and  $\gamma = (1 - v^2/c^2)^{-1/2}$  the Lorentz factor. The half-width of the banana orbit is given by  $w_b \simeq p_{\parallel}/(eB_p)$  with  $B_p$  the poloidal magnetic field [Westerhof and Peeters 1996]. It can be seen in figure 4.26 that the prescribed ad hoc radial transport reproduces the shape of the wave-induced neoclassical radial transport. However, this neoclassical transport appears to be one order of magnitude lower than the radial transport required to match experimental data. Complete neoclassical simulations are out of the scope of the present paper, but it could be worth investigating the role of the wave-induced neoclassical radial transport with adapted tools.

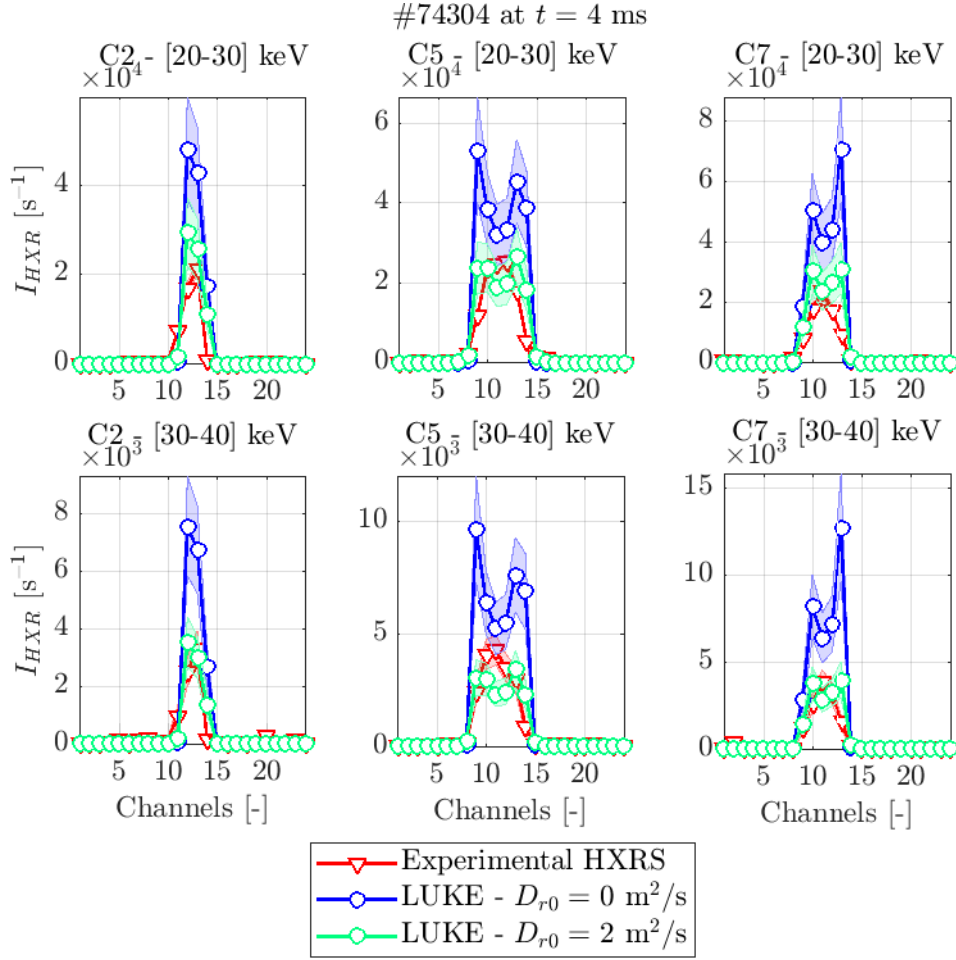


Figure 4.20: Channel display of HXR count rate measured with HXRS compared to LUKE simulations for different values of  $D_{r0}$ , for TCV shot #74304. The error bars on the simulations come from the uncertainties on the effective charge.

## 4.6 First principles transport analysis with ORB5

To attempt to explain the enhanced turbulent transport by the EC waves from first principles, global flux-driven gyro-kinetic simulations have been performed with ORB5, using a realistic quasilinear EC wave source [Donnel et al. 2021, 2022] with three different values of input power:  $P_{EC,0} = 140$  kW for the low-power case,  $P_{EC,0} = 730$  kW and  $P_{EC,0} = 2000$  kW for the high-power ones. The first two power cases correspond to the low and high power phases of the EC pulse in shots without additional power. The highest power case is closer to shots using constant additional power; however, in ORB5 only one launcher can be configured so the full power is injected with the same EC configuration in all cases. This is why two EC configurations have been tested, an ECCD case with launching angle  $\theta_0^{in} = 69.9^\circ$  corresponding to the modulation beam in experiments where  $\theta_0^{abs} \simeq 57^\circ$ , completed by a pure ECRH case, corresponding to the additional heating beam. Finally, a reference simulation without any EC source has been performed. Rather than simulating exactly the experiments, the aim of these ORB5 studies

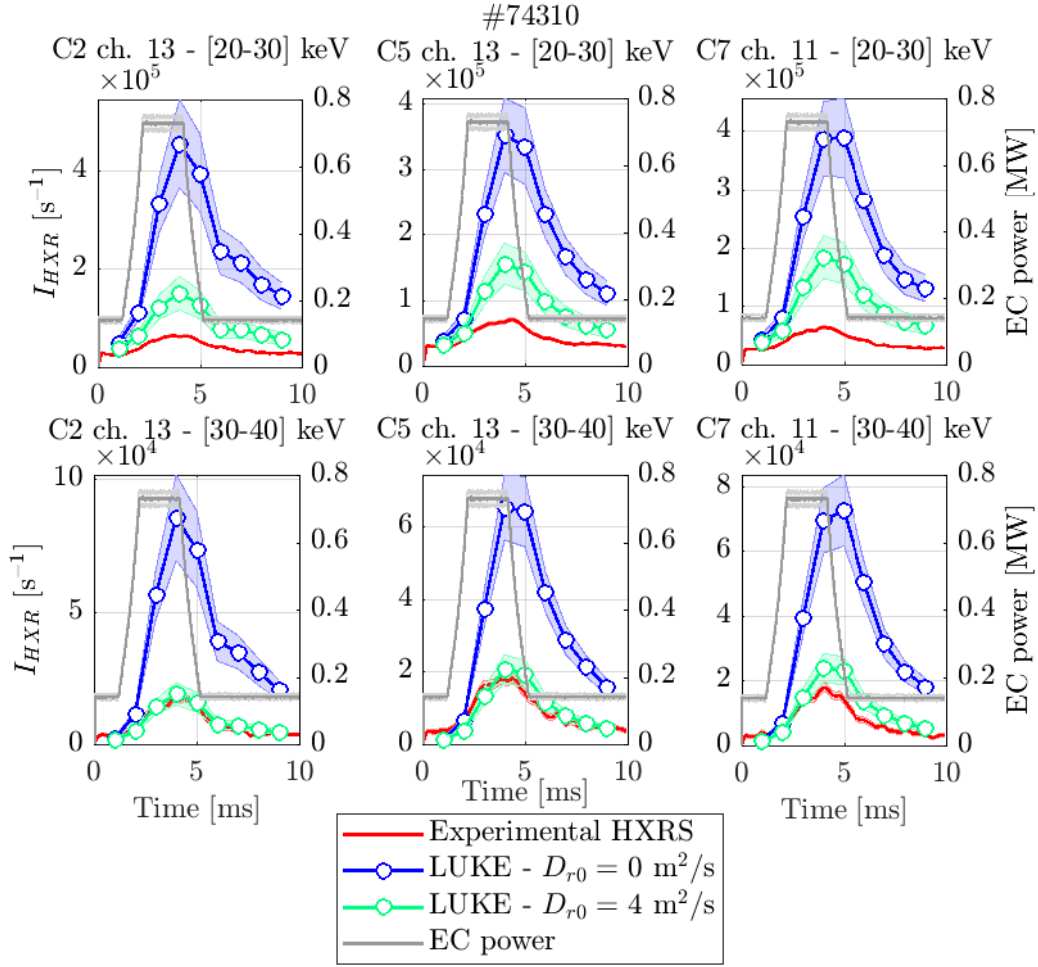


Figure 4.21: Time traces of HXR count rate measured with HXRS compared to LUKE simulations for different values of  $D_{r0}$ , for TCV shot #74310. The error bars on the simulations come from the uncertainties on the effective charge.

is to test the impact of the EC waves on fluctuations and transport, excluding as much as possible other additional effects (shaping, local profiles, MHD).

The ability of ORB5 to simulate experimental scenarios has been tested in ASDEX-Upgrade. For linear and non-linear studies of the up-chirping energetic-particle-driven geodesic acoustic modes, ORB5 is shown to be able to qualitatively reproduce the experimental time evolution of the mode [Novikau et al. 2020]. On the other hand, the global flux-driven gyro-kinetic code ORB5 have been benchmarked with the global version of the gradient-driven gyro-kinetic code GENE [Lapillonne et al. 2010]. In particular, in the tested conditions and using an ad-hoc external heating source, the two codes agreed within 10% on both the averaged heat diffusivity and the effective temperature gradient. In turn, global-GENE has been used to study negative triangularity TCV scenarios, matching the simulated heat fluxes with the experimental power balance [Merlo et al. 2021].

Some simplifications have to be made in order to render the ORB5 simulations numerically

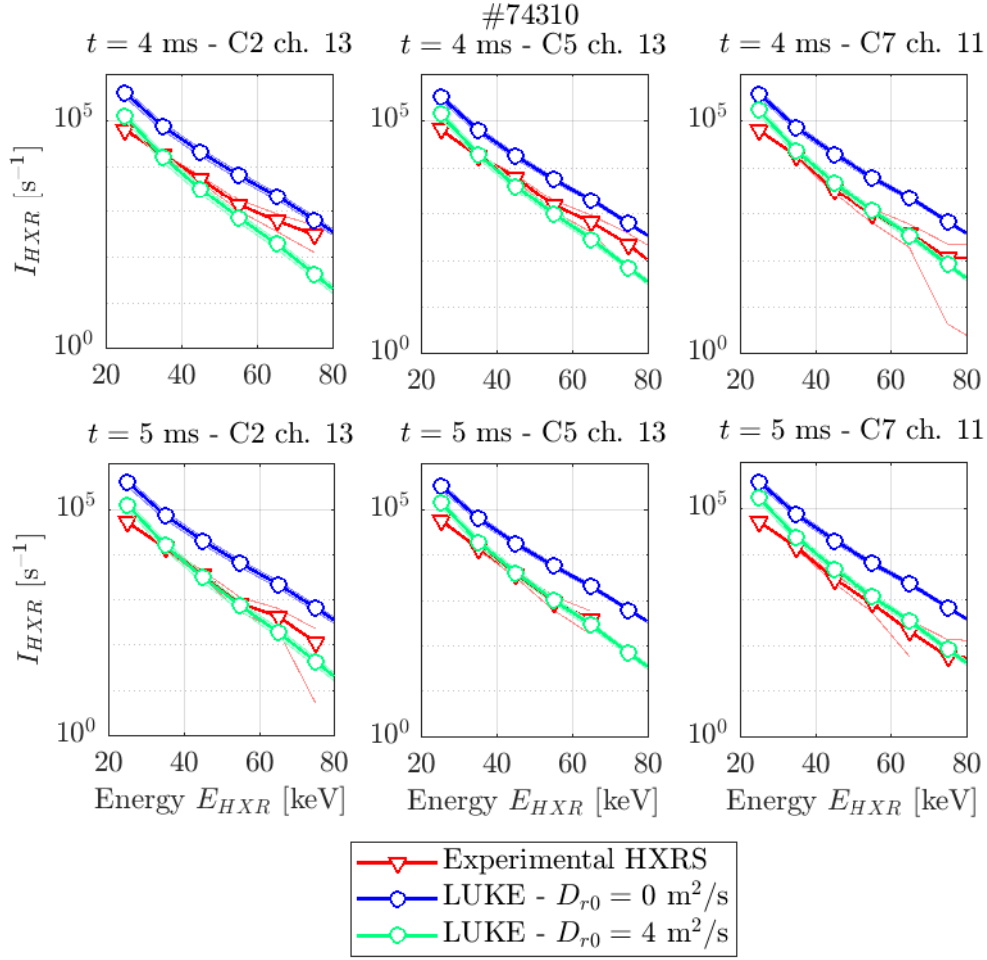


Figure 4.22: Energy spectra of HXR count rate measured with HXRS compared to LUKE simulations for different values of  $D_{r0}$ , for TCV shot #74310. The error bars on the simulations come from the uncertainties on the effective charge.

cheaper. First, an artificial mass ratio between ion and electrons is chosen  $m_i/m_e = 100$ . This allows increasing the numerical time step, saving computational resources. It has been shown in [Donnel et al. 2022] that a realistic mass ratio gives better quasilinear estimation of the deposited power, but the qualitative results remain acceptable using an artificial mass ratio. Moreover, the calculated wave absorption in such a configuration is above 90% in all ECCD cases, not showing any strong non-linear effects. This is expected in ECCD configurations where different non-linear effects are competing to explain the absorbed power [Donnel et al. 2022]. A similar behavior is observed with LUKE/C3PO. In pure ECRH, quasilinear effects on the absorbed power become noticeable, but the absorbed power remains above 70% in all cases. Since the absorption of the wave takes place near the magnetic axis, where the flux surfaces are almost circular, a circular equilibrium based on #74304 has been used. This simplifies the analysis by removing potential shaping effects. All simulations have been initiated with the same input profiles, shown in figure 4.27, to remove initial local effects from the analysis (e.g. an initially higher electron temperature). The electron density profile and the

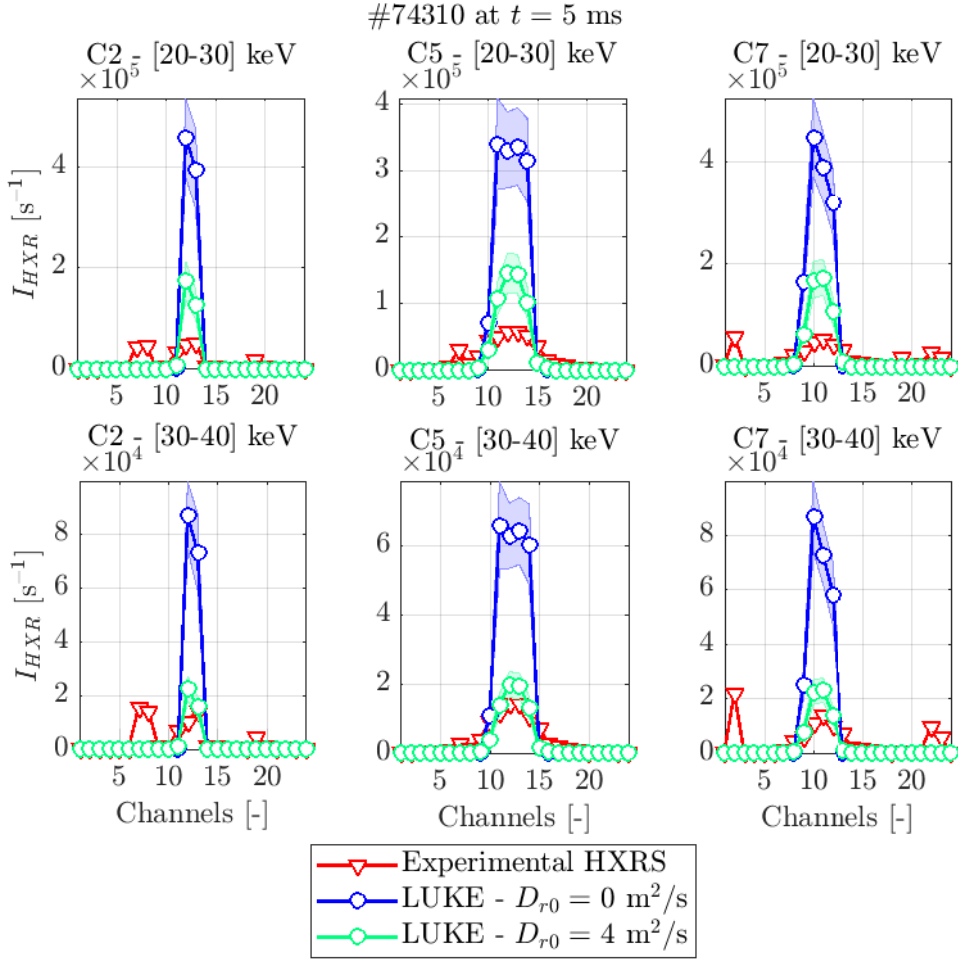


Figure 4.23: Channel display of HXR count rate measured with HXRS compared to LUKE simulations for different values of  $D_{r0}$ , for TCV shot #74310. The error bars on the simulations come from the uncertainties on the effective charge.

safety factor profile are close to that of experiments, while the electron temperature is lower in the core, with a lower gradient. This tends to reduce the turbulent transport with respect to experiments. Ion and electron temperatures are assumed to be equal  $T_e = T_i$  to lighten the simulations. Simulations using  $T_i = 0.5T_e$  have proven difficult to converge and substantial additional development appears necessary to understand the limitations and to perform such simulations. Assuming  $T_i = T_e$  changes the stability diagram of the ITG/TEM modes. According to [Garbet et al. 2004a], it is expected that the simulated cases are TEM and/or ITG unstable for  $\rho_V \gtrsim 0.2$  (see figure 4.28), which is close to what is expected experimentally (see figure 4.13). For each species (ions and electrons),  $6 \cdot 10^8$  markers are used in the simulations. The grid size used to solve the quasi-neutrality equation is ( $N_s = 256$ ,  $N_\chi = 512$ ,  $N_\phi = 256$ ).

As mentioned in section 3.2.2, the resolution of the quasi-neutrality equation in ORB5 provides the turbulent electric potential, enabling the study of the electrostatic turbulence. Estimating



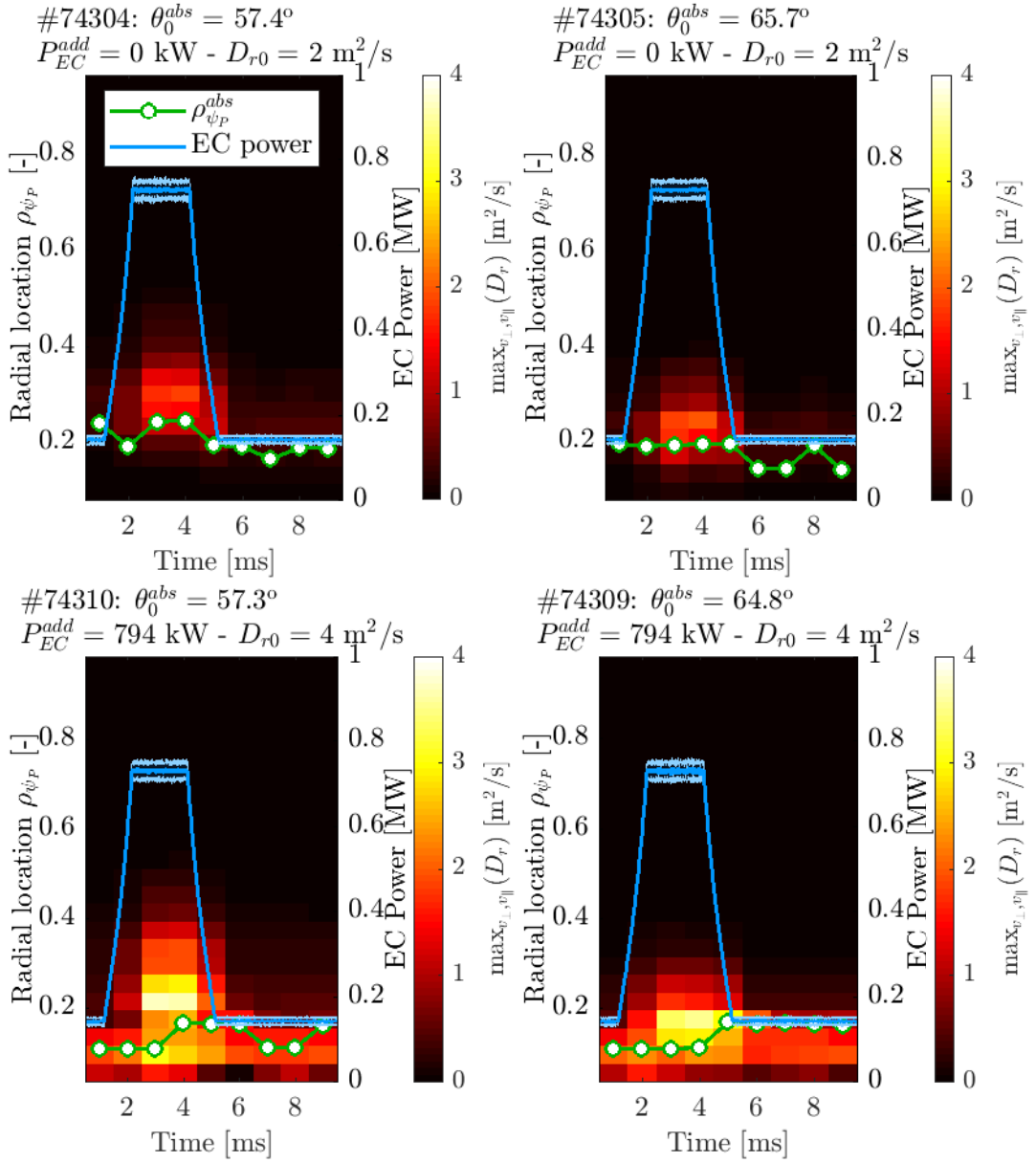


Figure 4.24: Local maximum of radial transport of electrons,  $\max_{\nu_{\perp}, \nu_{\parallel}}(D_r)$ , imposed by LUKE to match HXRS data for two ECCD angles  $\theta_0^{abs}$  and two levels of background ECRH power  $P_{EC}^{add}$ .

the ion and electron densities requires knowledge of their respective distribution. Kinetic ions are considered, meaning that the ion distribution is the direct result of the Fokker-Planck equation for the ions. A hybrid model is assumed for the electrons [Lanti et al. 2020; Idomura 2016]. The full electron distribution function is evolved in time via the Fokker-Planck equation and is therefore sensitive to the applied EC source. The subtlety appears when solving the quasi-neutrality equation, in which the trapped electrons are kinetically treated (similarly to the ions), while an adiabatic electron response is assumed for the passing electrons. This assumption is necessary to avoid the numerical cost of the simulations becoming prohibitive.



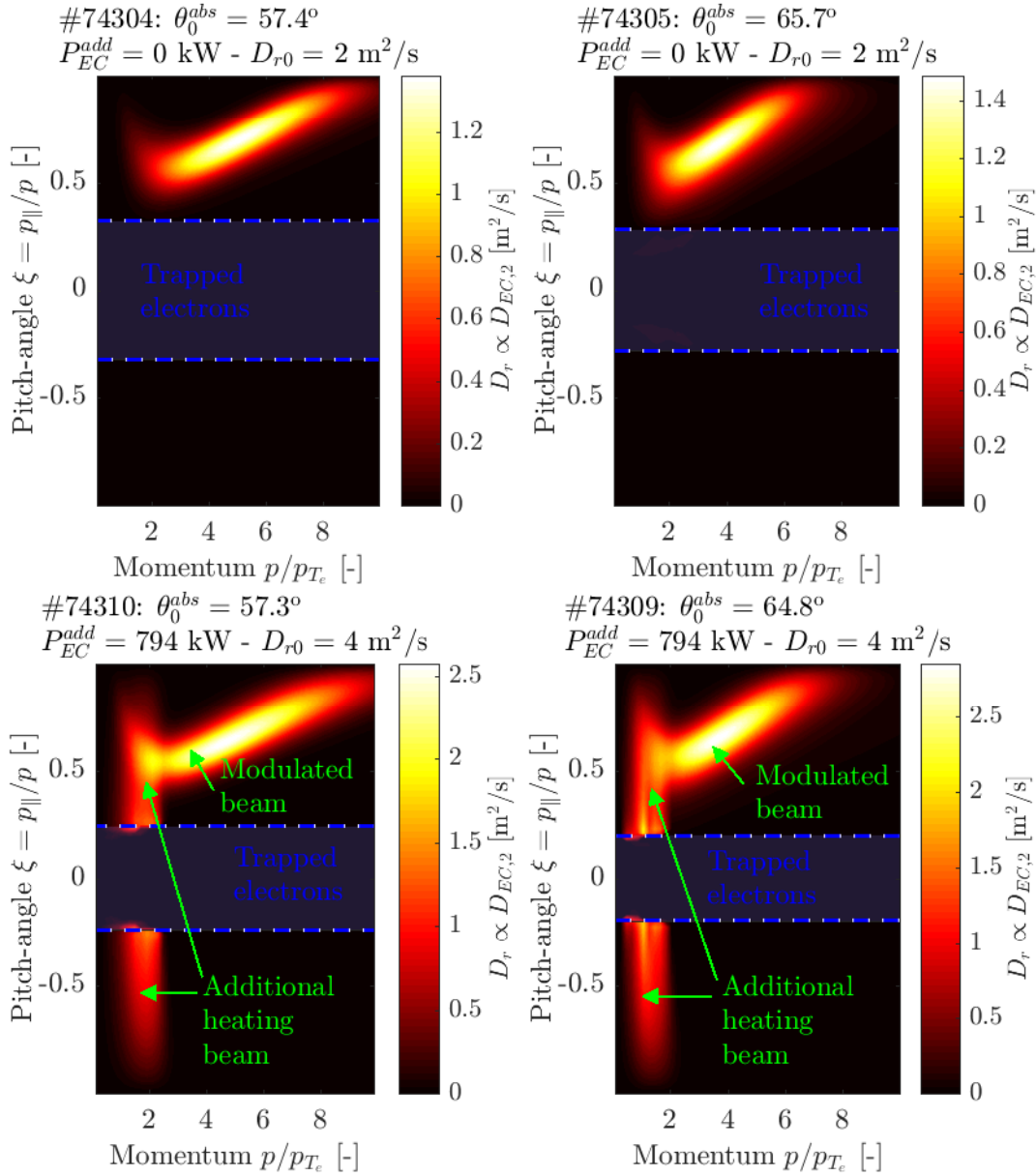


Figure 4.25: Radial electrons diffusion coefficient  $D_r$  in velocity space imposed by LUKE to match HXRS data for two ECCD angles  $\theta_0^{abs}$  and two levels of background ECRH power  $P_{EC}^{add}$ . The diffusion coefficient  $D_r$ , directly proportional to the plasma-wave interaction diffusion coefficient  $D_{EC,2}$ , is taken at the absorption location in each case, at the time  $t = 4$  ms in the EC pulse time frame. The momentum is normalized taking  $T_e^{ref} = 4.035$  keV.

The main consequence is that the physics of ITG and TEM is captured by ORB5 simulation, but not the physics of ETG. This is compatible with the experimental electron temperature analysis shown in figure 4.13, which tends to conclude that TEM are dominant over ETG in the studied TCV plasmas. Note that only one ion species is considered ( $Z_{eff} = 1$ ).

In these ORB5 simulations, suprathermal electrons up to 5 thermal velocities are simulated

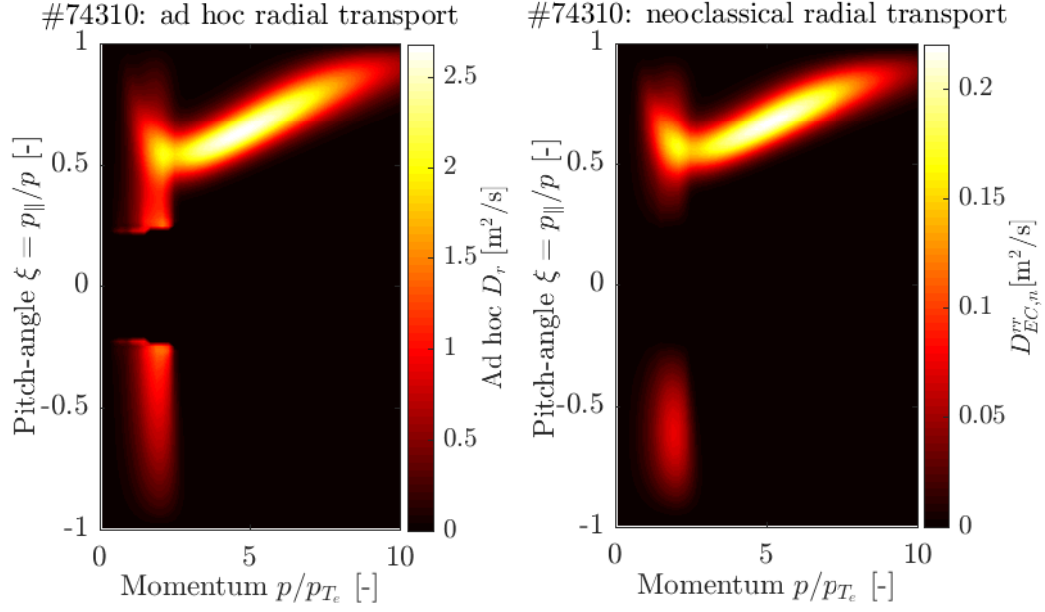


Figure 4.26: Radial electron diffusion coefficient  $D_r$  imposed by LUKE to match HXRS data (*left*) and neoclassical radial diffusion coefficient  $D_{EC,n}^{rr}$  estimated using equation 4.14 (*right*), for TCV shot #74310 ( $\theta_0^{abs} = 57.3^\circ$ ,  $P_{EC}^{add} = 794$  kW,  $D_{r0} = 4$  m<sup>2</sup>/s).

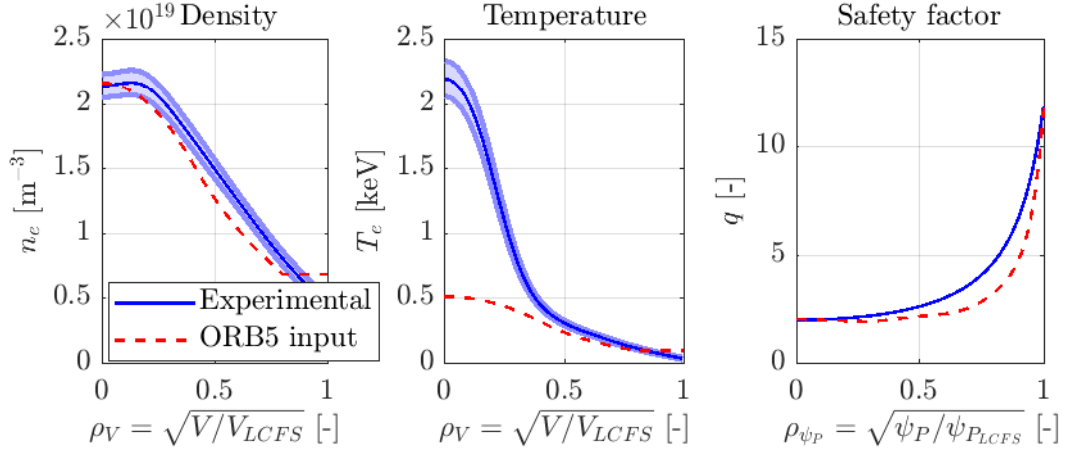


Figure 4.27: ORB5 input profiles compared with experimental profiles. In ORB5, the reference magnetic field is  $B_0 = 1.54$  T and the plasma minor axis is  $a = 0.25$  m.

(the numerical cost of the simulation being proportional to the square of the maximal simulated velocity), which is lower than the equivalent value for LUKE, but still enough to simulate significant effects of suprathermal electrons (see figure 4.25, the typical location in velocity space targeted by the wave is between 2 and 10 thermal velocities, peaking between 4 and 5 thermal velocities). All ORB5 simulations reach non-linear saturation of turbulence, and results are averaged over this non-linearly saturated period (between  $7000 \Omega_{c,i}^{-1}$  and  $9000 \Omega_{c,i}^{-1}$ ), corresponding to a simulated time of  $2000 \Omega_{c,i}^{-1} \approx 13 \mu\text{s}$ . The total simulated time  $9000 \Omega_{c,i}^{-1} \approx 59 \mu\text{s}$  is longer than the typical collisional slowing-down time of bulk electrons on bulk ions  $\tau_{SD}^{ei} \leq 50 \mu\text{s}$  [Huba 2016]. It is important to note that this time range is sufficient

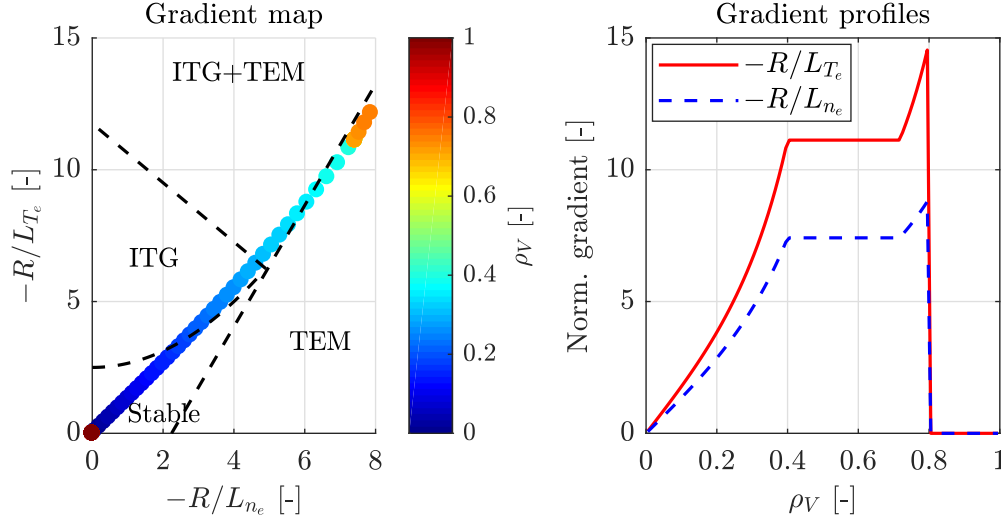


Figure 4.28: ORB5 input gradient profiles (*right*), and associated stability diagram from [Garbet et al. 2004a], assuming  $T_i = T_e$  (*left*).

to model the effect of the wave absorption on the electrons but not on the ions. Over this time range, the profiles (values and gradients) do not have time to evolve, meaning that the difference between the simulations (power scan and angle of injection) could not be retrieved with a flux tube approach using gradient-driven gyro-kinetic simulations. From exponential fits to XTe signals, the characteristic rising time of electron temperature ranges from 1.5 ms to 4.0 ms in the experiments. However, this simulated time window is too short to study the impact of the power deposition on quasi steady state profiles (density, temperature, etc), which is beyond of the scope of the present work. The aim of the study is to compare preliminary results that appear to point in the same direction as the experimental evidence. The present work thus describes the short term impact of the EC waves on the particle and heat fluxes. Over this short time window, the calculated heat fluxes reflect a mixture of the initial reorganization of the profiles and of the evolution due to the EC source. Therefore, the differences between cases at a given EC power and the reference case without the EC source are significant, but not the absolute value of the heat fluxes.

Results are shown in figure 4.29 for two EC configurations. The top-left plot of figure 4.29 shows the electron particle flux  $\Gamma_e$  while the top-right plot shows the electron heat flux  $Q_e$ , time-averaged over the non-linearly saturated period, for a launching angle  $\theta_0^{in} = 69.9^\circ$  such that  $\theta_0^{abs} \sim 58^\circ$  (82.7 GHz EC beam in X-mode polarization, resonating only at the second harmonic). The bottom plots show the same quantities averaged over the same time period, but for a pure ECRH case ( $\theta_0^{in} = 90^\circ$ ). The time averaging introduces non-negligible error bars, which are also shown in figure 4.29. It should be noted that, in all cases, the signal-to-noise ratio at the end of the simulation is above 50. In all cases, the fluxes vanishes at the plasma edge. This is due to the fact that both density and temperature gradients are zero at the edge (see figure 4.28) and that the boundary conditions are set to constrain this flux to remain zero (immersed boundary conditions). For these short simulations, it is expected that the

boundaries have a low impact on the results, as the power deposition profile is far from the edge. The non-linear saturation is illustrated for every cases in the time evolution of the total particle flux shown in figure 4.30. It can be seen that these fluxes saturate after a transport overshoot.

In ECCD, it can be seen that both the particle and heat transport increases with increasing EC power coupled to the plasma. In particular, going from 140 kW to 2 MW, both particle and heat transport is significantly increased, even considering the error bars coming from the time averaging.  $\Gamma_e$  increases by a factor between 2 and 3 (for  $\rho_V$  between 0.3 and 0.7), while  $Q_e$  increases by a factor between 2 and 3.5. It is less clear for the intermediate cases, going from 140 kW to 730 kW. An increased transport is visible on average between the two cases. Here,  $\Gamma_e$  increases by a factor around 2, while  $Q_e$  increases by a factor between 2 and 3. The fact that the simulated increase of transport between 140 kW and 730 kW is not sharp is compatible with the observation made with the TPCI of an increased density fluctuation level by only 20-30% for the same power jump. However, this apparent increase of transport between these two power cases has to be considered with caution, as it can be seen that the reference case without the EC power lies between them, which may contradict the initial observation of increased transport with increased EC power. Contrary to the 2 MW case, considering the error bars on the reference case and the 140 kW case (and even the 730 kW case), it is difficult to draw a solid conclusion on the decrease (or increase) of the transport with EC power. On the other hand, the increased particle transport with increased EC power observed at high power is compatible with LUKE forward modeling that requires a power-dependent (or equivalently time-dependent) radial transport model to recover experimental data. The increased transport being clearer at higher power is, again, compatible with LUKE forward modeling, which requires a significantly higher diffusion coefficient for TCV shots with an additional heating EC beam than for shots with a single EC beam (from 730 kW to 2 MW,  $\Gamma_e$  computed by ORB5 increases by a factor between 1 and 1.5). However, it is not possible to draw conclusions on the phase-space dependency of the electron radial transport, as the electron transport simulated by ORB5 encompasses both bulk and suprathermal electrons, and discriminating between the contributions of the two populations would require a prohibitive number of markers to increase the statistics for each energy bin.

In pure ECRH, both heat and particle transport seem initially slightly higher than in ECCD. The impact of the increased wave power shows a non-linear behavior. For power going from 140 kW to 730 kW, no difference is seen in both heat and particle fluxes (see bottom plots of figure 4.29). Going from 140 kW to 2 MW, both heat and particle transport increase noticeably (by a factor between 1.5 and 2), even though the error bars remain significant. This non-linear behavior of transport in ECRH coincides with the stronger non-linear behavior of plasma-wave interaction in pure ECRH with respect to ECCD previously observed [Donnel et al. 2022]. These simulations suggest that the impact of the background beam in pure ECRH configuration during the experiments may lead to a stronger enhancement of particle transport than a background beam in ECCD. Pure ECRH cases are difficult to study experimentally using HXRS, as, in pure ECRH, the plasma-wave interaction generates a plateau in the electron distribution

instead of pulling a tail of suprathermal electrons. Typically, in such a configuration, this plateau will be at  $\sim 2$  times the thermal momentum (see for instance the bottom plots of figure 4.25, showing the velocity-space diffusion associated with both a purely heating beam and a current-driving beam), meaning an electron energy below 10 keV, while the HXRS is sensitive to photons above 20 keV. The resulting measured HXRS signal will have a very low signal-to-noise ratio, making its statistical analysis challenging.

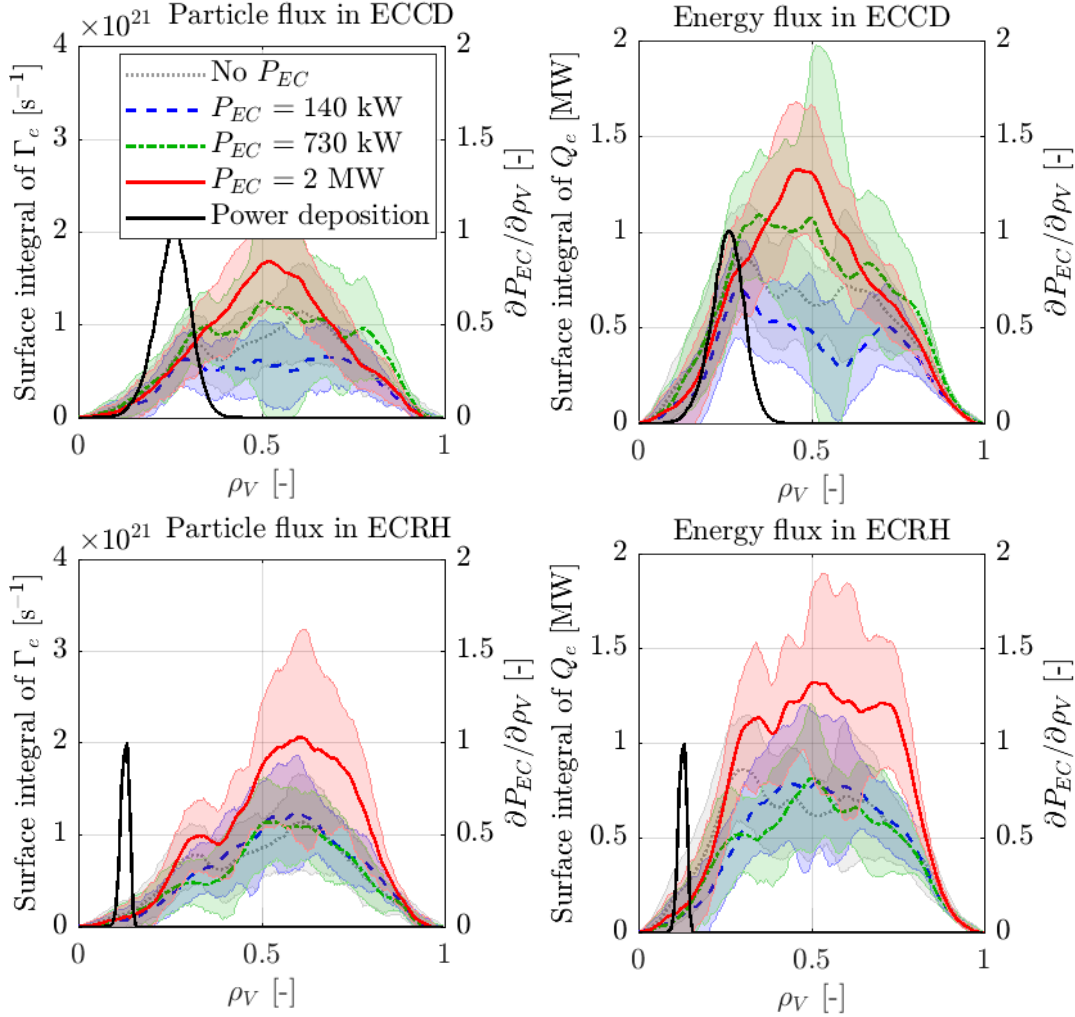


Figure 4.29: Results of ORB5 simulations for 3 different EC powers in a #74304-like equilibrium. *Left:* Electron particle flux integrated on surface *Right:* Electron energy flux integrated on surface. *Top* is an ECCD configuration close to TCV shot #74304, with  $\theta_0^{in} = 69.9^\circ$ . *Bottom* is a pure ECRH case, with  $\theta_0^{in} = 90^\circ$ . The error bars come from the time averaging.

A possible explanation for the non-local (i.e. not induced by changes in the profiles) increase of particle transport observed in ORB5 can be an avalanche effect: the turbulence is locally increased by the EC wave power deposition and cascades radially as the profiles are stiff and can't evolve over the considered time scale. This radial cascade results in increased particle transport, and is consistent with both analysis of experimental data (hard X-rays, electron

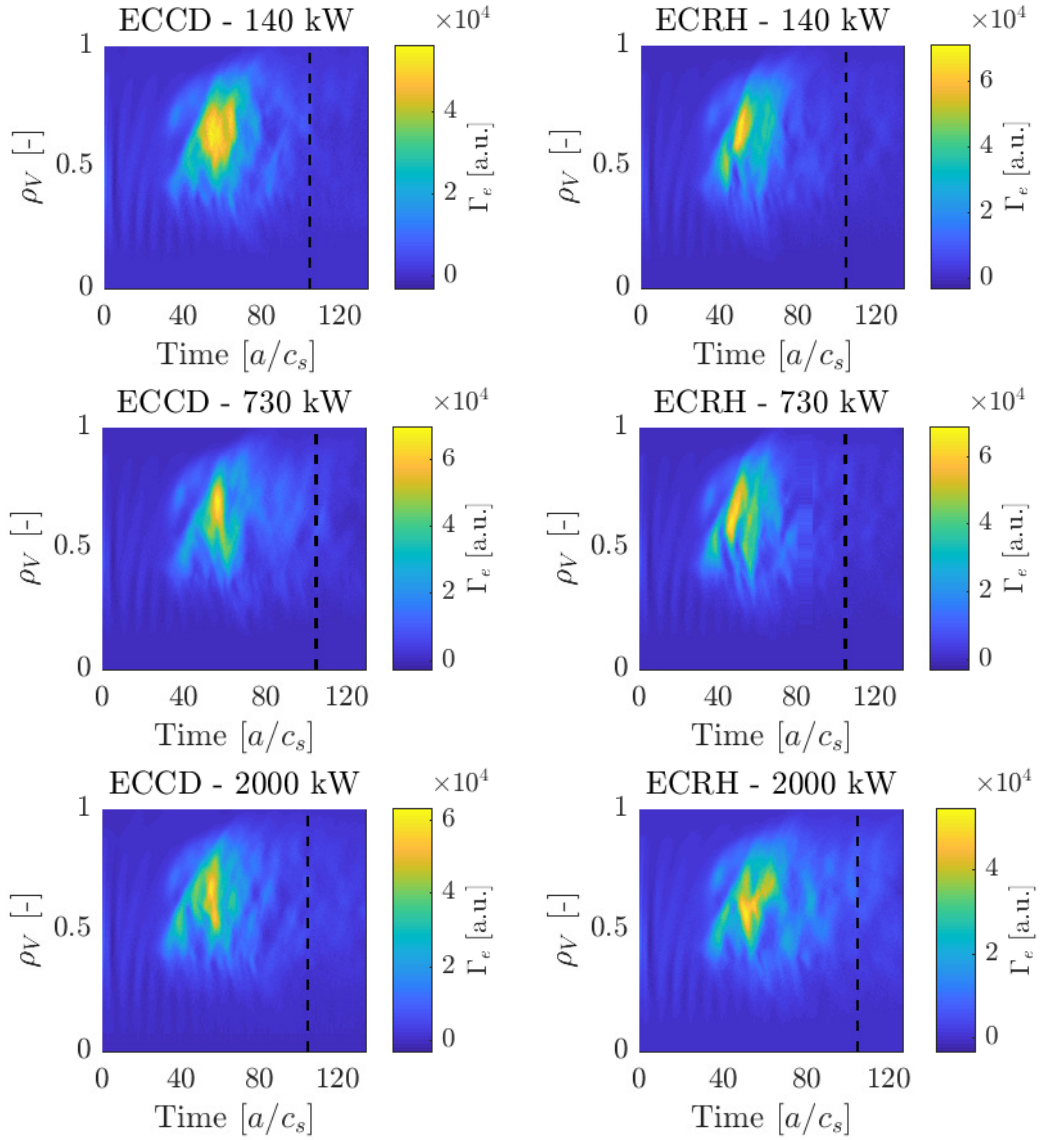


Figure 4.30: Time evolution of the total particle flux profile calculated by ORB5 for 3 different EC powers in a #74304-like equilibrium. *Left* is an ECCD configuration close to TCV shot #74304, with  $\theta_0^{in} = 69.9^\circ$ . *Right* is a pure ECRH case, with  $\theta_0^{in} = 90^\circ$ . The time-averaging is performed starting from time 105  $a/c_s$ .

temperature gradients and density fluctuation level) and forward drift-kinetic simulations. These potential avalanches can be seen in figure 4.31, which shows the time evolution of the  $\mathbf{E} \times \mathbf{B}$  flow shearing rate  $\omega_{E \times B}$ . For circular geometry, this can be written [Villard et al. 2002]

$$\omega_{E \times B} \simeq r \frac{\partial}{\partial r} \left( \frac{v_{E \times B}}{r} \right) \quad (4.15)$$

where  $v_{E \times B}$  is the  $\mathbf{E} \times \mathbf{B}$  drift velocity and  $r$  is the plasma minor radius. This shearing rate quantifies the shearing of the unstable modes by the  $\mathbf{E} \times \mathbf{B}$  flows, which leads to saturation of the turbulence. This parameter is therefore a good indicator of the plasma stability. On figure



4.31, for times below  $2500 \Omega_{c,i}^{-1}$ , Geodesic Acoustic Modes (GAM) can be seen in the form of very extended radial structures. This phase corresponds to the initial reorganization of the system, due to the fact that the initial distribution function is a local Maxwellian, which is not an exact solution of the system even in the absence of turbulence. After this period, the system enters the turbulent phase characterized by an overshoot, reached at around  $6000 \Omega_{c,i}^{-1}$ , followed by a long phase during which fluxes and kinetic profiles relax. During the relaxation/stabilization phase, coherent structures propagating outward can be seen for  $0.5 \leq \rho_V \leq 0.8$ , corresponding to the aforementioned avalanches. These avalanches may explain the enhanced radial particle and heat transports observed in figure 4.29, far from the power deposition area.

In the end, a qualitative agreement is found between experimental observations of turbulence and ORB5 simulations. Experimentally constrained LUKE forward modeling also suggests an increased electron transport with EC power, compatible with ORB5 simulations, even though the potential phase-space dependency cannot be tested in the gyro-kinetic simulations. Investigating such features in ORB5 would require extended computational resources, as well as further development, e.g. developing diagnostics to discriminate the contribution to transport from electrons in different energy groups or developing a fast electron Bremsstrahlung solver for ORB5 to enable direct comparison with experiments. Most importantly, it would also require very extensive computational resources to make the simulation last longer, ideally up to a millisecond ( $\sim 150000 \Omega_{c,i}^{-1}$ ), so that profiles and fluxes reach a relaxed state, in order to see if the avalanches persist in the system and determine the direct role the EC power source has on them.

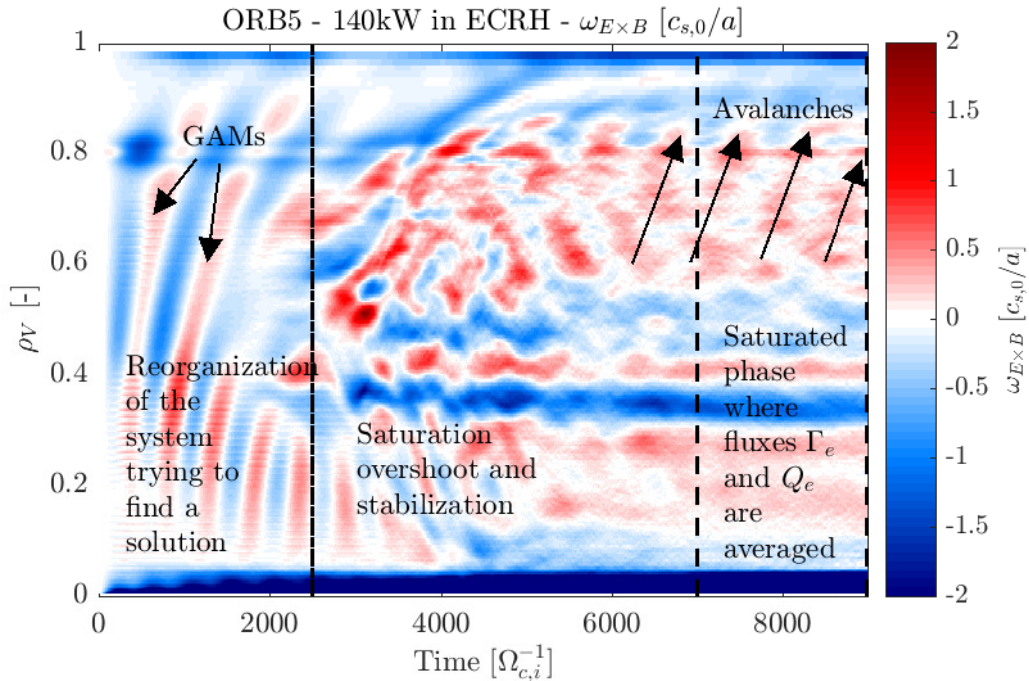


Figure 4.31: Time evolution of the  $E \times B$  flow shear rate profile  $\omega_{E \times B}$  for a given ORB5 simulation.

## 4.7 Conclusion

Experimental scenarios have been developed in TCV to study the dynamics of suprathermal electrons, based on power-modulated EC waves in current drive configuration generating a perturbed tail of fast electrons [Choi et al. 2020a].

The conditional averaging of experimental data allows analysis of hard X-rays and fluctuations with increased statistics. The analysis of inverted hard X-ray emissivity profiles suggests a transport of suprathermal electrons increasing with the EC power coupled to the plasma. The angle of EC wave injection has only a weak effect on the results. These observations are retrieved by forward LUKE modeling using a diffusion coefficient directly proportional to the phase space EC wave power deposition. Other phenomena that could have explained the broadening of the suprathermal electron distribution have been tested and excluded (plasma vertical oscillation, effective charge estimation) or minimized experimentally (MHD activity, EC beam scattering through density fluctuations).

The transport of fast electrons is associated with an increase of the relative fluctuation levels of density and temperature during the EC power pulse. The electron temperature profiles of TCV shots reported in this study are most probably stiff, in agreement with observations that the turbulence level and the corresponding transport increase with EC power. A simplified analytical formula for critical gradients tends to indicate that these shots are TEM unstable, driven by the increase of the electron temperature. First principles global flux-driven gyrokinetic simulations have been performed with ORB5 using a realistic EC source [Donnel et al. 2021, 2022]. They allow for the first time a first-principle simulation of the impact of EC power deposition on turbulent transport. Particle and heat transport of electrons, averaged over the non-linearly saturated phase, exhibits an increase with increased power that qualitatively agrees with observations of increased turbulence from TPCI and CECE.

Experimental observations and simulations point in the same direction: radial turbulent transport increases with EC power. ORB5 simulations suggest that this radial transport might be related to avalanches propagating outward, even though it is not clear if these avalanches will fade out with the rearrangement of the profiles, and near steady state studies have to be performed to confirm their role. These results are compatible with experimentally constrained LUKE forward modeling, which requires a diffusion coefficient proportional to the EC wave diffusion in phase space and to the total EC power to match the experimental data. The LUKE transport model best matching experimental data is also phase-space dependent. Further work could focus on checking the actual velocity-space dependency of the fast electron diffusion model, by developing new diagnostics in ORB5 (or another global flux-driven gyrokinetic code). However, reconstructing the distribution function and extracting velocity space information from ORB5 is not straightforward because of its particle-in-cells nature. Ultimately, steady-state fully converged ORB5 simulations could be used to determine a first principles transport model that can be used in LUKE. On the experimental side, turbulence properties will be determined from the upcoming additional or upgraded capabilities being



developed at TCV: short-pulse reflectometry and electron-scale turbulence probed by the phase contrast imaging for density fluctuations.

It is interesting to note that the wave-induced neoclassical radial transport exhibits a phase-space dependency similar to the ad-hoc radial transport used in LUKE to match experimental data. A rough estimation suggests that this neoclassical radial transport is one order of magnitude too low with respect to the required electron radial transport. However, further work can focus on checking the actual impact of neoclassical transport, using dedicated tools such as the neoclassical drift-kinetic code CQL3D [Petrov and Harvey 2016].

# 5 Electron-Cyclotron beam scattering by density fluctuations

## 5.1 Introduction

The present chapter explores the phenomenon of EC beam broadening and its impact on power deposition profile, both numerically and experimentally. In particular, we investigate whether beam broadening can explain the discrepancy between the hard X-ray measurements, from suprathermal electron Bremsstrahlung emission, and the results given by drift-kinetic Fokker-Planck simulations for TCV. The modeling and the density fluctuation measurement technique are introduced in section 5.2. Then, in section 5.3, the different numerical tools used in this work are quickly introduced. A purely numerical study is detailed in section 5.4, using TCV-like analytical equilibria and scanning the fluctuation parameters, with the aim of identifying the most probable beam broadening scenario in TCV, as well as a worst-case scenario. Finally, in section 5.5, experimental results are compared with simulations, using worst-case-scenario but realistic fluctuation parameters.

This work has been submitted to the *Nuclear Fusion* journal. The methodology and preliminary results of the numerical studies performed in section 5.4 have been presented to the 2019 joint annual meeting of the Swiss and of the Austrian Physical Societies, in Zürich, and to the 47th EPS conference on plasma physics, held remotely in 2021 [Cazabonne et al. 2021].

## 5.2 Density fluctuation measurement and modeling

In a turbulent plasma, the electron density can be written as  $n_e(\rho_{\psi_p}, \theta) = \bar{n}_e(\rho_{\psi_p}) + \delta n_e(\rho_{\psi_p}, \theta)$ , where  $\bar{n}_e$  is the averaged profile and  $\delta n_e$  the fluctuating part. In TCV, the profile of the root-mean-square (RMS) relative density fluctuation level  $[\delta n_e / \bar{n}_e]_{RMS}$  can be measured by Short-Pulse Reflectometry (SPR) [Molina Cabrera et al. 2019]. The SPR diagnostic is described in section 2.4. A poloidal view of the plasma area probed by the SPR for a relevant TCV shot used in this study is shown in figure 5.1.

Simulations are performed using random 2D fluctuating density profiles, generated by an

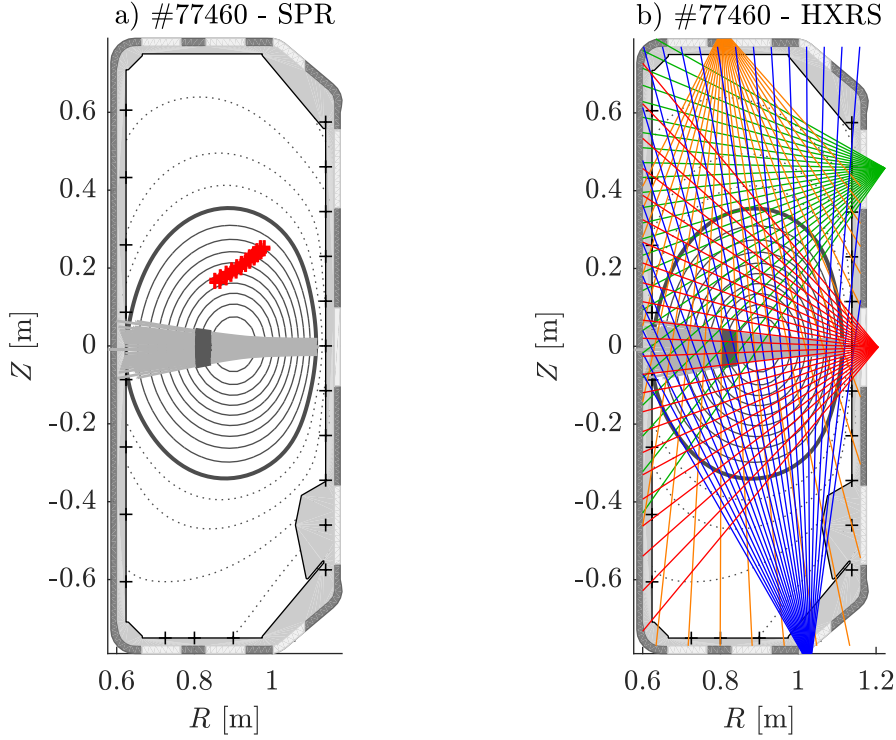


Figure 5.1: Poloidal view showing the plasma area (in red) probed by the Short Pulse Reflectometer (SPR) for TCV shot #77460 *a*) and lines of sight of the four cameras (C2, C4, C5 and C7) of the Hard X-Ray Spectrometer (HXRS) *b*).

analytical model, developed in a drift-wave theoretical framework [Peysson et al. 2011; Decker et al. 2012]. The beam propagation being much faster than the evolution of the turbulence, density fluctuations are assumed to be frozen with respect to beam propagation. The model consists of a truncated Fourier series of Gaussian modes, convoluted with a 1D spatial envelope  $F_{\Delta}(\rho_{\psi_p})$ . The turbulent density structures are assumed to be toroidally homogeneous (blob-like). In the poloidal coordinate system  $(\rho_{\psi_p}, \theta)$ , this model gives for each independent time step

$$\frac{\delta n_e}{\bar{n}_e}(\rho_{\psi_p}, \theta, t) = F_{\Delta}(\rho_{\psi_p}) \left[ 2\sigma_f \pi^{1/4} \sqrt{\frac{L_f}{L_c(\rho_{\psi_p})}} \times \sum_{p=1}^{p_{max}} \exp\left(-\frac{\pi^2}{2} \left(\frac{L_f}{L_c(\rho_{\psi_p})}\right)^2 p^2\right) \sin(\Phi_p(\rho_{\psi_p}, \theta, t)) \right] \quad (5.1)$$

where  $p$  is the mode number (note that the subscript  $P$  stands for poloidal),  $\sigma_f$  is a parameter controlling the RMS of the density fluctuation level  $[\delta n_e / \bar{n}_e]_{RMS}$ ,  $L_f$  is the characteristic size of the turbulent structures,  $\Phi_p$  is a random phase defined by

$$\Phi_p(\psi_p, \theta, t) = p\vartheta(\psi_p, \theta) + 2\pi\chi_p(t) \quad (5.2)$$

with  $\chi_p$  a random number ranging between 0 and 1 and  $\vartheta$  an angle describing the drift wave

poloidal structure, satisfying the relations  $\mathbf{B} \cdot \nabla \vartheta = 0$  and  $\nabla \psi_P \cdot \nabla \vartheta = 0$ . The characteristic length  $L_c$  is given by

$$L_c(\psi_P) = \frac{1}{q(\psi_P)} \int_0^{2\pi} r(\psi_P, \theta) \frac{B(\psi_P, \theta)}{B_\phi(\psi_P, \theta)} \frac{d\theta}{\cos(\alpha(\psi_P, \theta))} \quad (5.3)$$

where  $B$  and  $B_\phi$  are the total and toroidal magnetic fields respectively,  $r$  is the minor radius,  $q$  is the safety factor and  $\alpha$  the metric angle accounting for non-circular magnetic flux surfaces. Only dominant modes up to  $p_{max}$  are considered, with the limit set by

$$p_{max} = \frac{\sqrt{-2 \ln \beta} L_c(\psi_P)}{\pi L_f} \quad (5.4)$$

with  $\beta$  the minimum amplitude of the mode.

Different shapes can be assumed for the 1D spatial envelope  $F_\Delta$ , which is fitted to the SPR experimental data, parametrized by the Half-Width at Half Maximum (HWHM)  $\Delta$ , the RMS fluctuation level at the edge  $[\delta n_e / \bar{n}_e]_{RMS,1}$  and the background RMS fluctuation level  $[\delta n_e / \bar{n}_e]_{RMS,0}$ . In TCV, measurements with the SPR diagnostic are limited to  $\rho_{\psi_P} \leq 0.95$  for the studied scenarios, and it is very challenging to extrapolate data at the separatrix and in the outer edge, as the density fluctuation level is expected to sharply increase with radius. This behavior was already experimentally shown in the TEXT tokamak [Wootton et al. 1990] and later confirmed by experiments in TCV [Graves et al. 2005; Horacek et al. 2005] and in ASDEX Upgrade [Medvedeva et al. 2017], among others. This tendency is also observed in fluid simulations of the plasma edge, such as in TCV [Chellaï et al. 2021] or in DIII-D [Brookman et al. 2023]. In particular, it has been shown in TCV, using a fast reciprocating Langmuir probe on the plasma equatorial midplane, that the relative RMS level of density fluctuation sharply increases toward the edge, saturating in the SOL at  $[\delta n_e / \bar{n}_e]_{RMS,SOL} = 60 \pm 10\%$  for a wide range of plasma scenarios [Graves et al. 2005; Horacek et al. 2005]. Given the uncertainties on its determination, the parameter  $[\delta n_e / \bar{n}_e]_{RMS,1}$  has to be scanned over a realistic range to assess the potential impact of edge density fluctuations on the EC beam and power deposition broadening in actual experiments.

The expected typical size of turbulent structures is  $L_f \sim 5-10 \rho_{L,s}$ , with  $\rho_{L,s}$  the sonic Larmor radius defined by  $\rho_{L,s} = c_s / \Omega_{c,i}$  where the sound speed is  $c_s = \sqrt{k_B T_e / m_i}$  and the ion cyclotron frequency is  $\Omega_{c,i} = q_i B / m_i$ . It has been shown in DIII-D that, for L-mode plasmas, the edge density fluctuation correlation length scales as  $L_f \sim 5-10 \rho_{L,s}$ , by comparing experimental measurements from reflectometry and gyro-kinetic simulations of ITG modes [Rhodes et al. 2002]. In the linear magnetized plasma of the LAPD machine, density blob analysis using Langmuir probes shows that the typical blob size scales around  $10 \rho_{L,s}$  [Carter 2006]. Finally, fluid simulations of TCV L-mode discharges using the GBS code found a correlation length of  $7.4 \rho_{L,s}$  in the SOL [Nespoli et al. 2017].

Ultimately, the goal of this study is to test whether the EC beam scattering through the turbu-

lent plasma can explain the discrepancy between simulations and experiments, so the most interesting cases are the worst-case scenarios. This translates to ion-scale, high-amplitude density fluctuations. This will be discussed further in section 5.4.

### 5.3 Numerical tools for wave propagation and absorption, and for comparison with experiments

The different numerical tools have been described in details in chapter 3. The main tool used to propagate EC waves in turbulent plasmas is the full-wave COMSOL solver, described and tested in section 3.1.1. To estimate the EC wave power deposition, drift-kinetic calculations by LUKE are used.

In this chapter, LUKE calculations are performed either in time-asymptotic mode, meaning that the electric field is imposed by the measured loop voltage at the edge, assuming that the wave-induced electric field has completely diffused, or in frozen current density mode, meaning that the loop voltage profile is automatically adjusted to match a given plasma current density profile. These calculation modes are detailed in section 3.2.1.

LUKE calculations are interesting for the present study for two main reasons: the possibility of estimating the power deposition resulting from COMSOL full-wave propagation by using the custom beam width mode of C3PO detailed in section 3.1.2 (later referred to as COMSOL-LUKE simulations), and the ability to compare simulation results directly with TCV experimental data. Such comparisons are enabled by the R5-X2 module of the LUKE suite [Peysson and Decker 2008], which computes the fast electron Bremsstrahlung from the non-thermal electron distribution function, and is used as a synthetic diagnostic for the TCV Hard-X Ray Spectrometer (HXRS) [Gnesin et al. 2008], which is described in section 2.5. The HXRS consists of a set of four compact cameras, each possessing 24 cadmium telluride photodiodes, with a tungsten collimator defining the lines of sight, measuring the hard X-ray (HXR) count rate from suprathermal electron Bremsstrahlung (20-200 keV range, with 8 keV resolution). The count rate is sorted by energy bins using optimized digital pulse processing [Kamleitner et al. 2014]. The complete set covers a total poloidal section of the tokamak. The synthetic diagnostic uses an experiment-based model of the cadmium telluride response function to estimate the line-integrated hard X-ray count rate that can be directly compared to the HXRS data [Choi et al. 2020b]. A poloidal display of the HXRS lines of sight is shown in figure 5.1.

### 5.4 Full-Wave numerical studies and beam broadening regimes

To assess the possible impact of turbulent density on the EC beam broadening in the TCV configuration, a purely numerical study is performed for a wide range of turbulent parameters. Three analytic equilibria are generated, using the solution to the Grad-Shafranov equation provided in [Cerfon and Freidberg 2010] (see appendix B). The main parameters

for these equilibria are summarized in table 5.1. The fluctuation patterns are generated using Eq.5.1, enveloped by a 1D Gaussian centered around the last closed flux surface (LCFS)  $F_\Delta = \exp(-[(\rho_{\psi_p} - 1)/\Delta]^2)$ . The main parameters controlling the density fluctuations are the amplitude  $\sigma_f$ , the envelope HWHM  $\Delta$  and the characteristic size of the fluctuations  $L_f$ . The EC beam is a 82.7 GHz (3.625 mm vacuum wavelength) X-polarized beam, launched from the LFS in an ECRH configuration. In such a configuration, the beam is nearly fully-absorbed at the second harmonic resonance location (confirmed by C3PO ray-tracing calculation). To simulate a turbulent plasma, the EC beam is propagated through 100 individual and independent fluctuating density snapshots (assuming that the beam propagates much faster than the fluctuation correlation time), using the full-wave COMSOL model. The beam electric field is then averaged over the snapshots, yielding the average impact of edge-localized density fluctuation on its broadening. The number of snapshots is enough for the width and position of the averaged EC beam to converge (at least before the absorption location). The beam electric field profile transverse to its propagation direction is then fitted with both Gaussian and Lorentzian shapes, so that the best fit is used to build a custom beam width input for the COMSOL-LUKE simulations, which then calculates the quasilinear absorption. To illustrate the methodology, examples of an EC beam computed with COMSOL in a quiet plasma and in a turbulent plasma, both time-averaged and instantaneous, are shown in figure 5.2, together with the associated EC beam profiles taken just before the wave absorption location. The different scans in fluctuation parameters are summarized in table 5.2.

Table 5.1: Analytic equilibrium parameters generated using the method described in [Cerfon and Freidberg 2010]. All equilibria are up-down symmetric and share the minor radius  $a = 25$  cm, the major radius  $R_0 = 88$  cm, the on-axis magnetic field  $B_0 = 1.5$  T, the elongation  $\kappa = 1.3$ , the triangularity  $\delta = 0.1$ , the pressure gradient  $\partial p / \partial \psi_{p,n} = 1e4$  Pa (with  $\psi_{p,n} = \rho_{\psi_p}^2$  the normalized poloidal magnetic flux),  $T_e = T_i$  and  $Z_{eff} = 1$ . The density profile is proportional to  $(\rho_{\psi_p})^k$  with  $k = 4/3$ . The temperature profile is adjusted so that the requested pressure gradient is matched.

Analytic equilibrium #	AE#1	AE#2	AE#3
On-axis density $n_{e,0}$	$2.5e19 \text{ m}^{-3}$	$2.5e19 \text{ m}^{-3}$	$2.5e19 \text{ m}^{-3}$
Edge density $n_{e,1}$	$6.25e18 \text{ m}^{-3}$	$8.00e18 \text{ m}^{-3}$	$6.25e18 \text{ m}^{-3}$
Edge temperature $T_{e,1}$	599 eV	172 eV	172 eV
Edge Larmor radius $\rho_{L,s,1}$	3.0 mm	1.6 mm	1.6 mm

Table 5.2: Scanned fluctuation parameters for different analytic equilibria, using 1D Gaussian envelope  $F_\Delta = \exp(-(\rho_{\psi_p} - 1)^2 / \Delta^2)$  for the fluctuation model.

Scan #	Equilibrium	$\sigma_f$	$\Delta$	$L_f$
S#1.1	AE#1	0.4	0.10	$1-12 \rho_{L,s}$
S#1.2	AE#1	0.2-0.8	0.02, 0.10	$5 \rho_{L,s}$
S#2.1	AE#2	0.4	0.10, 0.15, 0.20	$1-10 \rho_{L,s}$
S#3.1	AE#3	0.4	0.10, 0.20	$1-10 \rho_{L,s}$

Beam scattering through a turbulent layer can be associated with different broadening regimes [Snicker et al. 2017a]. These regimes can be characterized within the framework of the wave-kinetic theory, considering the mode conversion of a wave by conservative momentum transfer

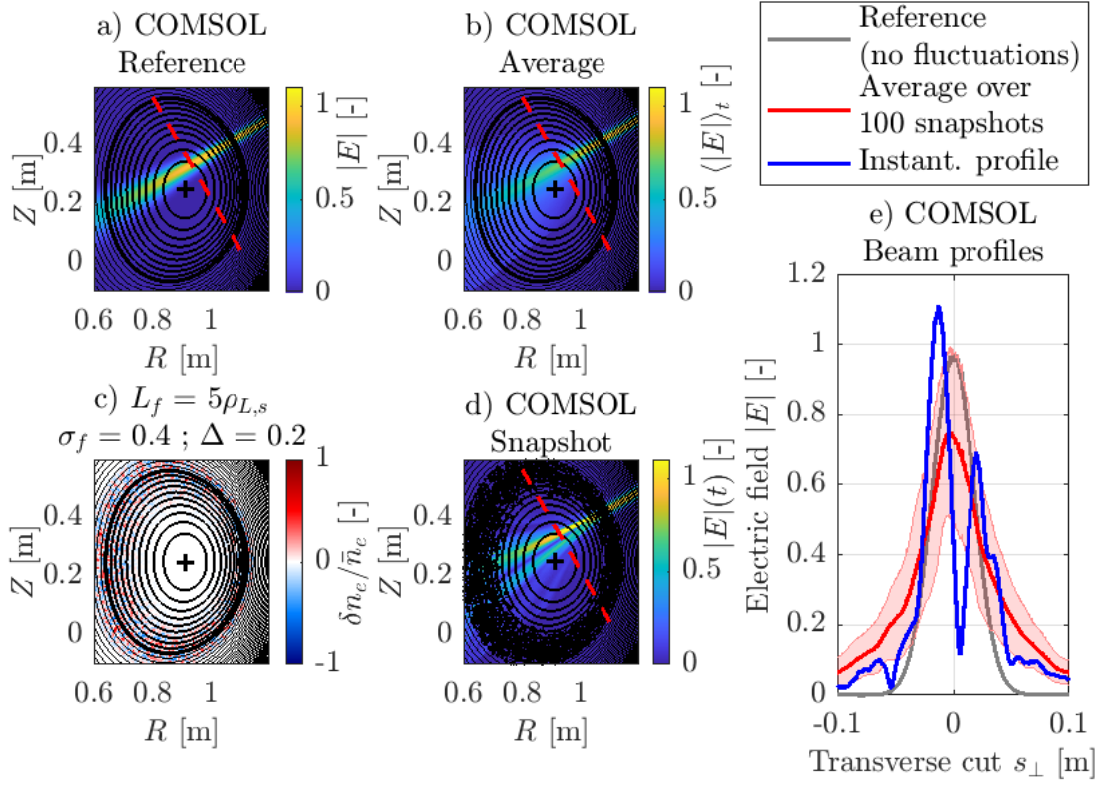


Figure 5.2: Poloidal view of *a)* the EC beam computed with COMSOL in a quiet plasma, *b)* the EC beam computed with COMSOL in a turbulent plasma, averaged over 100 fluctuation snapshots, *c)* an example of a fluctuation snapshot generated using equation 5.1 and *d)* the associated instantaneous EC beam electric field, computed with COMSOL. The red dashed line indicates the transverse cut along which the electric field is plotted in *e)*.

with fluctuations: it is a 3-wave coupling scenario involving the incident beam, the refracted beam and density fluctuations. Writing the 3-wave coupling equations yields a microscopic scattering cross-section, which is then integrated over the refractive index space and modes to give a macroscopic scattering cross-section. Finally, the number of scattering events  $\lambda_X$  is calculated by integrating this macroscopic cross-section along the beam path. For X-polarization, the simplified version can be written [Snicker et al. 2017a]

$$\lambda_X \approx \sqrt{\frac{\pi}{2}} \frac{1}{N_{\perp,X}} \left( \frac{\omega}{\omega + \Omega_{c,e}} \right)^2 \left[ \frac{\delta n_e}{n_c} \right]_{RMS}^2 k_0^2 L_f (\Delta s_{\parallel})_f \quad (5.5)$$

with  $N_{\perp,X}$  the perpendicular refractive index for X-polarization,  $n_c$  the cutoff density, defined by  $n_c = \bar{n}_e(\omega/\omega_{p,e})^2$ ,  $k_0$  the EC beam wave number in vacuum and  $(\Delta s_{\parallel})_f$  the width of the turbulent layer crossed by the beam. Figure 5.3 shows the EC beam broadening at the wave absorption location  $s_{\parallel}^{abs}$ , defined by  $\Gamma_b = \text{FWHM}[\langle |E| \rangle_{t,fluct}](s_{\parallel}^{abs}) / \text{FWHM}[|E|_{quiet}](s_{\parallel}^{abs}) - 1$ , and the associated power deposition profile broadening plotted against  $\log(\lambda_X)$  for all the simulated cases. Also shown is the difference between the coefficient of determination for a Gaussian fit  $R_G^2$  and a Lorentzian fit  $R_L^2$  of the transverse beam section at the absorption location. The particular effect of the fluctuation size on the beam broadening is shown in

figure 5.4. In pure ECRH, the power deposition profile is very peaked and the FWHM of this narrow peak is within the limits of the radial resolution in LUKE. However, the base of the peak is substantially larger and it is possible to clearly see the effect of the beam broadening on its width (see examples in figure 5.5). To estimate the broadening of the power deposition profile  $\Gamma_P$ , the base of the peak is fitted to a Gaussian, and the broadening estimated as the ratio of the FWHM of the fit for a case with fluctuation to the quiet case, minus 1. This is illustrated in figure 5.6. The obtained broadening  $\Gamma_P$  is thus a convenient parameter to qualitatively assess the relative impact of the beam broadening on the power deposition profile.

Three different beam broadening regimes can be described from these results. For  $\log(\lambda_X) \ll 0$ , the beam bulk is not very affected, and the transverse beam profile remains a nearly unmodified Gaussian, with a non-zero background electric field resulting from the beam scattering. This mode corresponds to the so-called superdiffusive regime described in [Snicker et al. 2017a]. On the other hand, for  $\log(\lambda_X) \geq 0$ , the beam clearly broadens and its transverse profile is either a broadened Gaussian or Lorentzian, as both Gaussian and Lorentzian fits quite well the transverse beam profile, with a small difference between the coefficients of determination of the respective fits. This corresponds to the diffusive regime described in [Snicker et al. 2017a]. An intermediate regime can also be identified for  $\log(\lambda_X) \leq 0$ , where the beam FWHM does not clearly increase, but the beam's transverse profile is distorted by scattering off the density blobs and becomes closer to a Lorentzian than a Gaussian, with non-negligible wings rising on the side of the bulk beam. This intermediate regime represents a smooth transition between the superdiffusive and the diffusive regime, with the sides of the beam profile being affected before the bulk. Such Lorentzian beam shapes have already been observed in other full-wave studies [Köhn et al. 2018]. These three regimes are illustrated in figure 5.5, which shows examples of transverse beam profiles for different fluctuation cases. As expected, the power deposition profile broadening increases with the beam broadening. However, a Lorentzian-shaped beam can also lead to power deposition profile broadening while having a beam FWHM close to the quiet case.

The worst case scenario, corresponding to a large power deposition profile broadening, is mainly the diffusive regime, although the intermediate regime can lead to a non-negligible power deposition profile broadening too (see figure 5.5). At a given EC beam frequency, the beam broadening is increased for high relative density fluctuation RMS  $[\delta n_e / \bar{n}_e]_{RMS}$  and high level of absolute background density  $\bar{n}_e$ , as well as for a large turbulent layer width  $(\Delta s_{\parallel})_f$ . As shown in figure 5.4, to maximize the beam broadening, the fluctuation size  $L_f$  must be close to the order of the beam width  $w_0$  or of the beam wavelength  $\lambda_0$  (in the cases presented here, the beam width is only 5 times higher than the beam wavelength  $\lambda_0$ ). If  $L_f \ll \lambda_0$ , the beam broadening is superdiffusive and the bulk of the beam is not affected. On the other hand, for very large fluctuation structures, typically  $L_f \gg w_0$ , the density fluctuations only impact the beam refraction, leading to almost no impact on beam width (see section 5.5.2 for



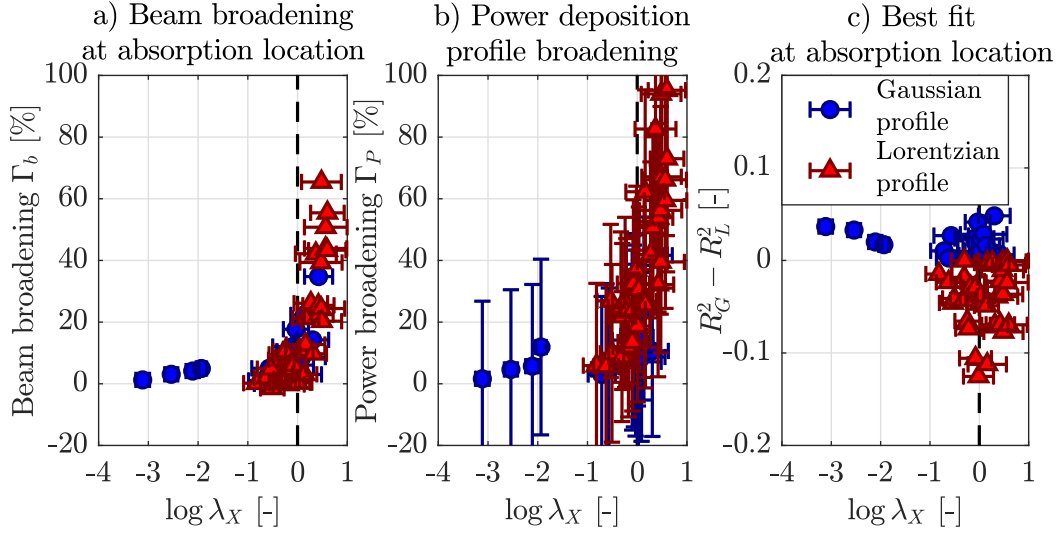


Figure 5.3: Broadening of the beam FWHM at the absorption location *a*), broadening of the base of the power deposition profile *b*) and difference in the coefficient of determination between a Gaussian and a Lorentzian fit of the transverse beam electric field profile from COMSOL simulations *c*) for the scans summarized in table 5.2, plotted against  $\log(\lambda_X)$  (see equation 5.5). Error bars on  $\lambda_X$  come from the variation of the profiles within the turbulent layer. Error bars on the power deposition broadening come from the 95% confidence interval of the Gaussian fits. All cases are ECRH cases.

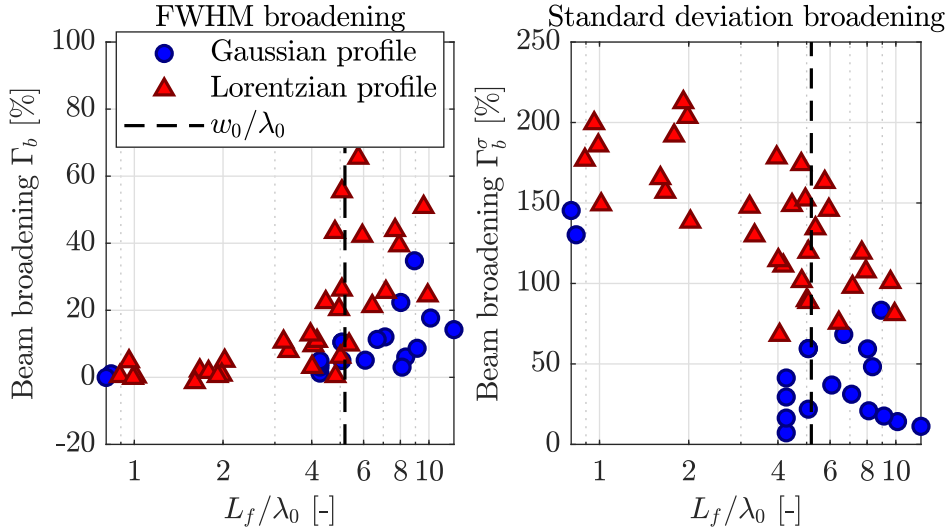


Figure 5.4: FWHM beam broadening estimated with COMSOL  $\Gamma_b$  (*left*) and broadening of the standard deviation of the beam profile  $\Gamma_b^\sigma$  (*right*), with respect to the fluctuation size.

an example). The present numerical study also highlights the fact that, in TCV, the X2 82.7 GHz beam broadening regime is most likely the intermediate beam broadening regime. The dependencies of the beam broadening on the different plasma and fluctuation parameters have been extensively studied in [Holland et al. 2023], using 2D full-wave simulations, yielding a semi-empirical formula to quickly estimate the FWHM broadening of the beam. This study focuses on parameters relevant for machines larger than TCV, such as DIII-D or ITER, and thus mainly on the diffusive broadening regime. It does not take into account the potential

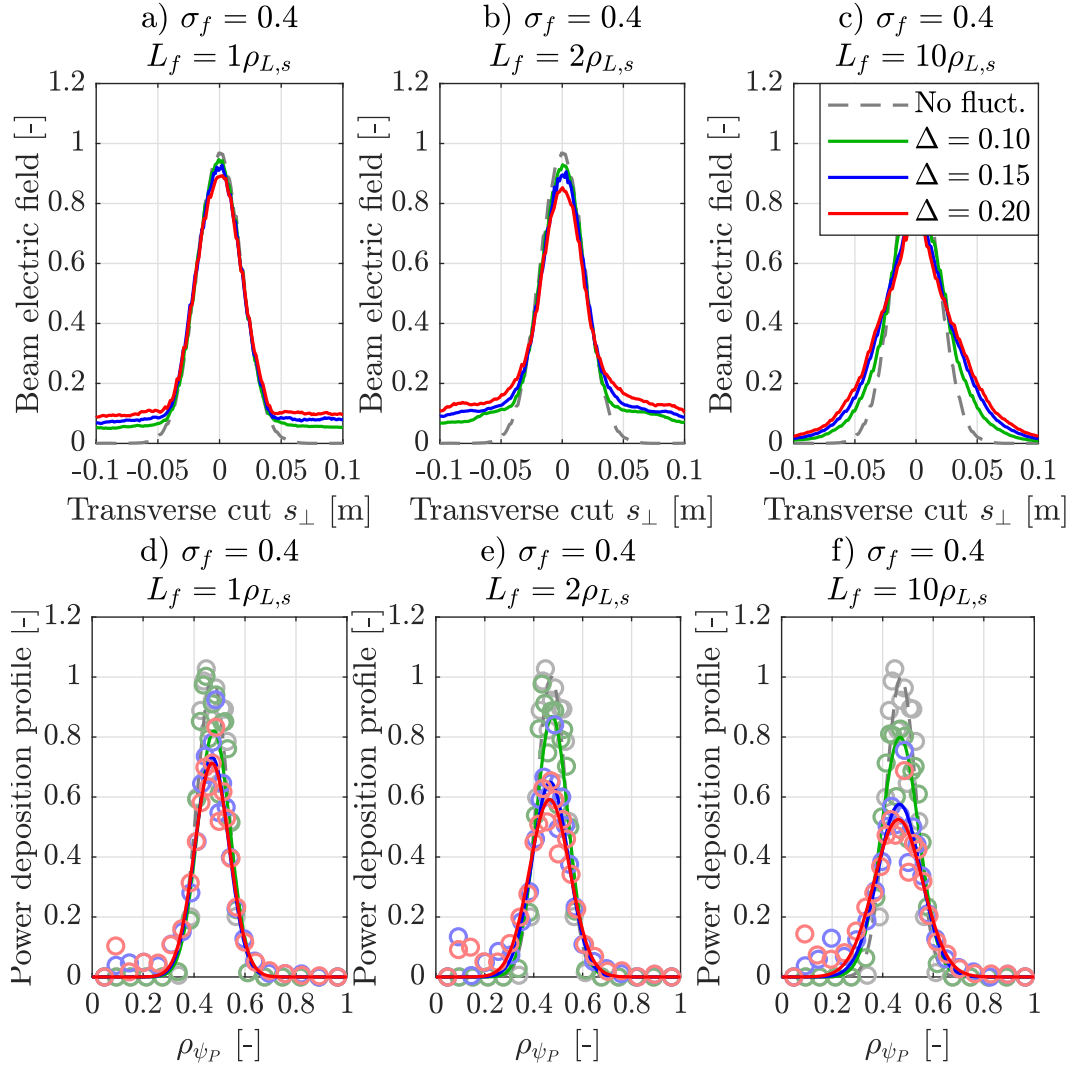


Figure 5.5: Transverse cut of the beam electric field averaged over 100 fluctuation snapshots, taken at the wave absorption location in equilibrium AE#2 (see table 5.1), computed by COMSOL and illustrating the superdiffusive regime *a)*, the intermediate regime *b)* and the diffusive regime *c)* of EC beam broadening. Associated Gaussian fits of the base of the power deposition profile (sharp, narrow peak has been removed) are shown in panels *d)*, *e)* and *f)* respectively. All cases are ECRH cases.

change in the shape of the beam, which can lead to a broader power deposition profile while the beam FWHM does not change much with respect to the quiet plasma case. As shown in figure 5.7, the semi-empirical model gives good estimates of beam broadening for the diffusive regime cases, but overestimates drastically the broadening for the intermediate regime cases, which are close to the limits of the fit parameters (and so to the validity domain of the fit). This discrepancy may also be due to the difference in the dependency of the beam broadening to the fluctuation size found between the two approaches. Indeed, the model presented in [Holland et al. 2023] predicts an increase of the FWHM broadening of the beam for a decreasing size of the turbulence (assuming both radial and poloidal fluctuation sizes are equal), contrary to what is shown in figure 5.4. It is possible that the Gaussian fit applied in

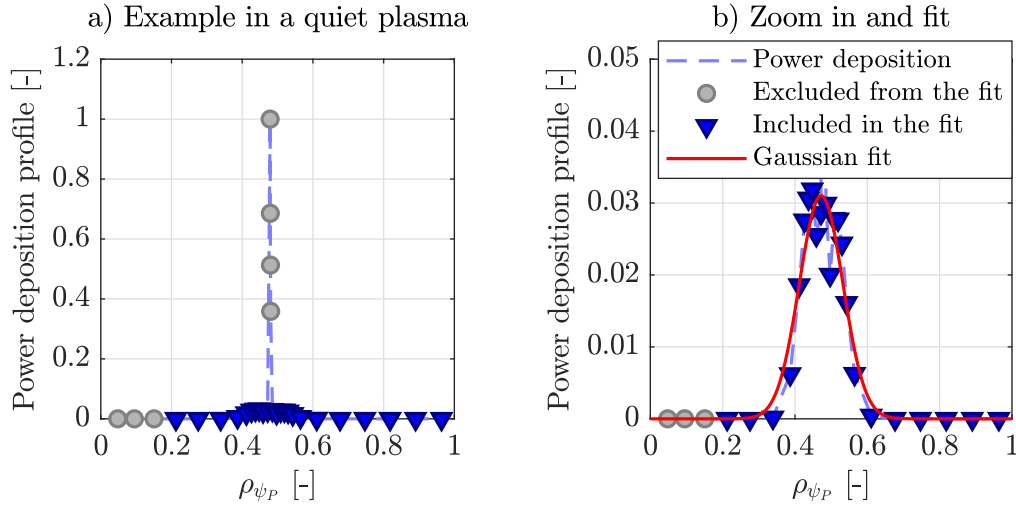


Figure 5.6: Example of fitting of the base of the power deposition profile, for a quiet plasma, using equilibrium AE#2 (see table 5.1). The beam is launched in ECRH configuration.

the semi-empirical model overestimates the FWHM of the beam in cases where a Lorentzian beam may be expected. This is illustrated in figure 5.4 which shows that the standard deviation of the beam profile does increase with decreasing fluctuation size, due to the wings rising on the side of the bulk of the beam (as seen in figure 5.5), while the FWHM broadening decreases. A wrong fit can therefore lead to a higher FWHM. Further investigating this difference would require additional simulations, varying the fluctuation size for different ratio of the beam width to the beam wavelength, which is out of the scope of the present study. The model values have been estimated using linear interpolation of data in table A1 of [Holland et al. 2023]. Analytical formulas derived from wave-kinetic theory are also available to estimate the broadened width of O-mode [Sysoeva et al. 2015] and X-mode [Tretinnikov et al. 2021] microwave beams propagating in 2D, but they are limited to Gaussian beam profiles in the low fluctuation level limit.

## 5.5 Experimental study: to assess the discrepancy between observations and simulations

### 5.5.1 Experimental setup

Two different experimental ECCD scenarios are proposed to study the impact of turbulence on beam scattering in TCV. Scenario A, illustrated in figure 5.8.a), minimizes the impact of beam broadening on the power deposition profile, as the power deposition is spread within a given flux surface. On the other hand, scenario B, illustrated in figure 5.8.b), maximizes this impact as the power is spread perpendicularly to the flux surfaces. In both scenarios, the 82.7 GHz X-polarized EC wave is steadily injected in the co-current direction, from 0.7 s to

## 5.5 Experimental study: to assess the discrepancy between observations and simulations

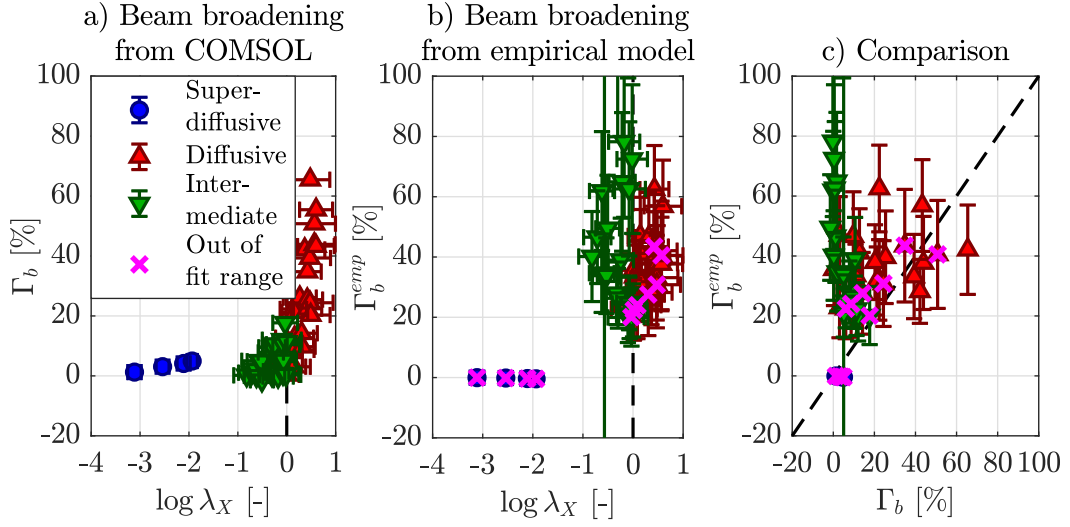


Figure 5.7: Comparison between the beam broadening estimated with COMSOL  $\Gamma_b$  and with the semi-empirical model  $\Gamma_b^{emp}$  developed in [Holland et al. 2023]. The magenta crosses represent points for which at least one parameter is out of the fit range.

2.5 s (the wave is absorbed at the second harmonic location in the plasma). Details on the X-polarization projection onto the Cartesian frame of COMSOL are given in appendix D. The equilibrium is averaged between 1.25 s and 1.55 s. At these times, the current induced by the wave absorption has had the time to diffuse completely. The profiles and time traces of the main plasma quantities are shown in figure 5.9 for the main TCV shots of the present study, namely TCV shots #74301 and #74302, as well as TCV shot #77460 which is a replica of #74301 used as a reference for SPR measurements.

As mentioned in section 5.2, information about the density fluctuation profile is obtained from SPR measurements. However, this experimental characterization is limited to  $\rho_{\psi_p} \leq 0.95$ ; therefore, the profile is extrapolated using a Lorentzian fit until the LCFS at  $\rho_{\psi_p} = 1$  and a constant value is assumed in the SOL, the free parameter being the RMS value at the LCFS  $[\delta n_e / \bar{n}_e]_{RMS,1}$  and measurements fixing the background fluctuation level  $[\delta n_e / \bar{n}_e]_{RMS,0}$ . Two values of edge density fluctuation level have been studied,  $[\delta n_e / \bar{n}_e]_{RMS,1} = 60\%$  and  $[\delta n_e / \bar{n}_e]_{RMS,1} = 80\%$ , the first one corresponding to what is expected in TCV [Graves et al. 2005] and the second to a more extreme case. The typical fluctuation correlation length is set to  $L_f = 10\rho_{L,s}$ . These profiles are illustrated in figure 5.10 for TCV shot #77460. As shown in figure 5.11, the expected beam broadening regime for these two values, and for both scenarios A and B, ranges between the superdiffusive and intermediate regimes, as described in section 5.4. A summary of the TCV shots used for this study is given in table 5.3.

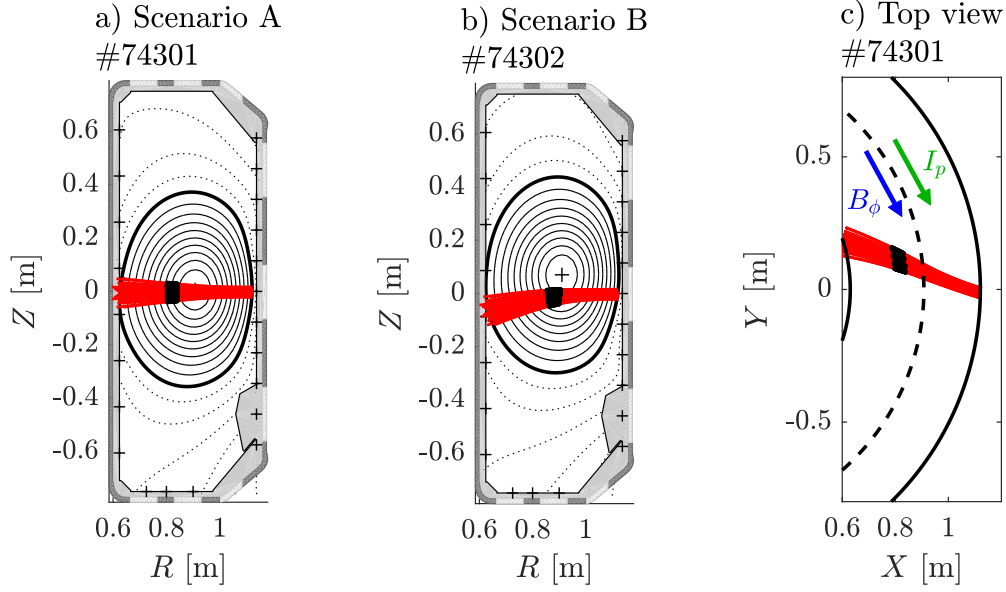


Figure 5.8: Results of C3PO ray tracing for the 3 different scenarios developed at TCV: a configuration minimizing the impact of density fluctuations on EC power deposition profile broadening *a)* and a configuration maximizing this impact *b)*. Top view of scenario A *c)*, showing the plasma current  $I_p$  and the toroidal magnetic field  $B_\phi$  directions. The configuration is co-ECCD.

Table 5.3: List of TCV shots used in the present study.

Shot #	Scenario <sup>a</sup>	Diagnostics	$\theta_0^{abs}$ [°] <sup>b</sup>	$\rho_{\psi_p}^{abs}$ [-] <sup>c</sup>	$Z_{eff}$ [-] <sup>d</sup>	$Z_p$ [cm]
74301	A	HXRS	$-64.2 \pm 1.7^\circ$	0.38	1.10	0.6
77460	A	SPR	$-63.1 \pm 1.5^\circ$	0.36	1.10	0.4
77458	A	SPR	$89.7 \pm 0.1^\circ$	0.41	1.10	0.8
74302	B	HXRS	$-63.7 \pm 1.3^\circ$	0.31	1.35	7.1
77456	B	SPR	$-89.0 \pm 0.1^\circ$	0.23	1.35	7.0

<sup>a</sup>EC power is 725 kW for shots #74301 and #74302, and 691 kW in all other cases;

<sup>b</sup> $\theta_0^{abs}$  is the angle between the wave vector and the magnetic field at absorption location (negative for co-ECCD);

<sup>c</sup> $\rho_{\psi_p}^{abs}$  is the absorption location in normalized poloidal flux coordinates;

<sup>d</sup>From LUKE estimations, matching  $I_p$  with experiments in ECRH;

### 5.5.2 Methodology for the ECCD cases and justification

The full-wave COMSOL simulations are limited to 2D configurations only, which makes it challenging to properly model the effect of edge density fluctuations on beam broadening in ECCD configurations. This means that the studied ECCD configuration must be constrained to cases in which the beam propagates in a plane. This is the case for the scenarios A and B (at least before the beam absorption, see figure 5.8), respectively minimizing and maximizing the effect of the beam broadening on the power deposition profile, for which a toroidal section can be considered instead of a poloidal section. Considering a toroidal section is useful to take into account the longer distance traveled by the beam in ECCD with respect to ECRH, as well as the additional thickness of the turbulent layer crossed by the beam due to its oblique propagation, without having to perform extra post-processing of the simulation results. The fluctuation model detailed in section 5.2 assumes field-aligned structures that are toroidally

## 5.5 Experimental study: to assess the discrepancy between observations and simulations

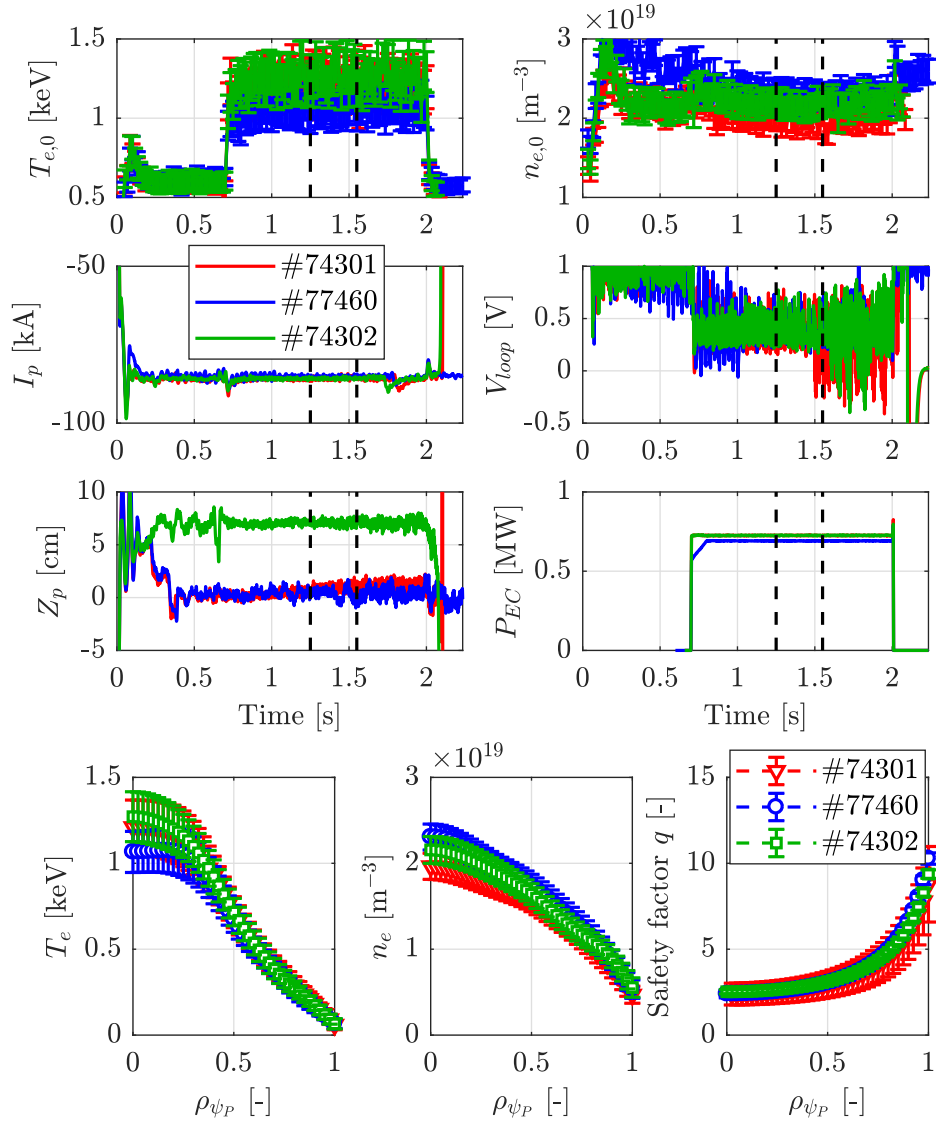


Figure 5.9: Time traces of central electron temperature and density, plasma current, loop voltage, plasma vertical position and EC injected power, as well as profiles of electron temperature and density and safety factor for TCV shots #74301 and #77460, corresponding to scenario A, and TCV shot #74302 corresponding to scenario B. The black dashed lines on time traces represent the time interval over which profiles are averaged.

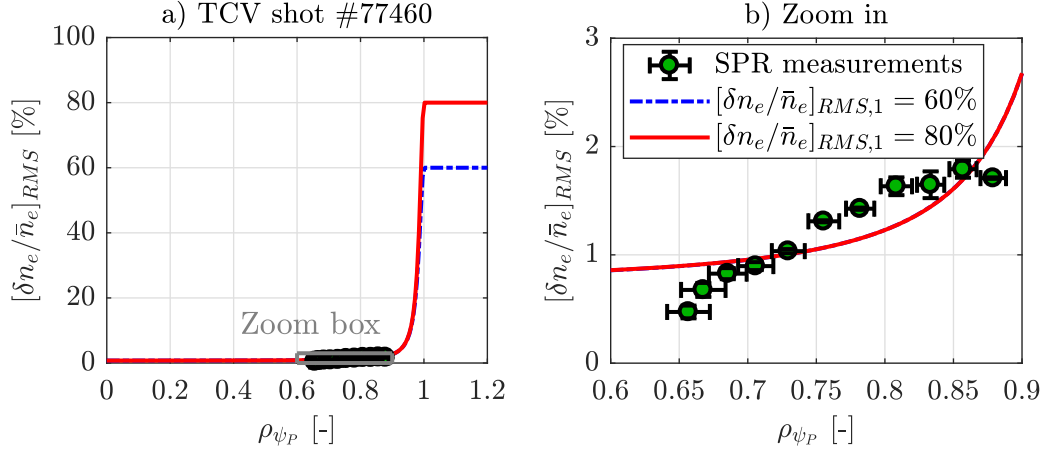


Figure 5.10: Short pulse reflectometry (SPR) data for TCV shot #77460 and associated Lorentzian models for two different values of density fluctuation RMS at the LCFS. The density fluctuation RMS is assumed constant in the SOL.

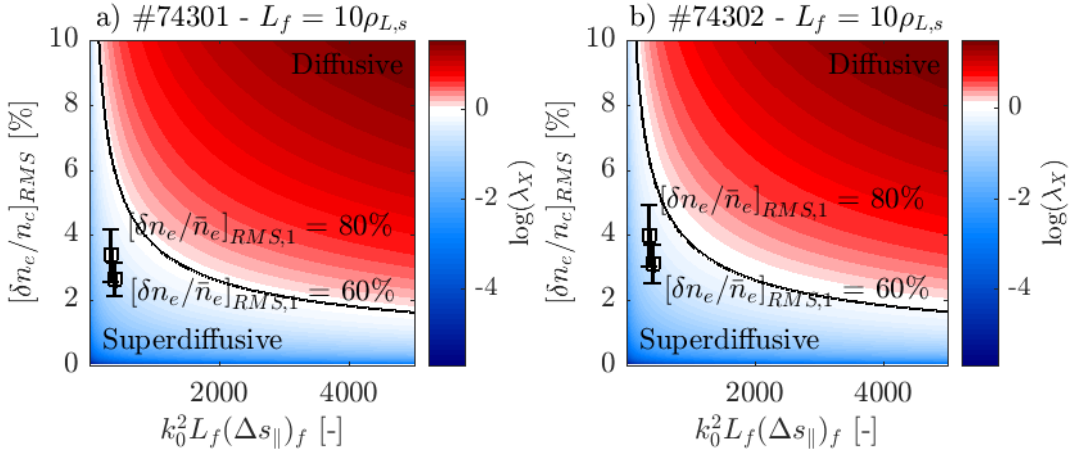


Figure 5.11: Expected beam broadening regime for scenario A) and scenario B), for the tested fluctuation parameters. The parameter  $\lambda_X$  is calculated using equation 5.5.

homogeneous. This is illustrated in figures 5.12.a) and 5.12.b).

A test case is used to assess the validity of using a toroidal section instead of a poloidal one to study the impact of turbulence on beam broadening. As shown in figure 5.12, an X-polarized beam in ECRH mode is propagated along the plasma equatorial midplane, and its broadening through an edge-localized fluctuation layer is studied in three different 2D configurations: a standard poloidal section (figure 5.12.a)), the corresponding toroidal section (5.12.b)) and a modified toroidal section, using an artificial fluctuation pattern imitating the poloidal structure (characteristic eddy size) in the toroidal direction (figure 5.12.c)). It can be seen in figure 5.12.d) that, on average, the beam FWHM does not change much between the different cases. However, for the poloidal and modified toroidal cases, the beam profile is distorted and evolves from a Gaussian to a Lorentzian profile along the propagation direction. This is illustrated in figure 5.12.e), which shows the beam electric field transverse to the beam

## 5.5 Experimental study: to assess the discrepancy between observations and simulations

propagation at the wave absorption location. Here, it is clear that the standard toroidal case does not reproduce the broadening observed in the standard poloidal case, while the modified toroidal case matches the poloidal one well.

Two main consequences arise from this test. First, the beam broadening in the presence of field-aligned structures, assuming a poloidal correlation length of the same order (or smaller) as the beam width, is anisotropic, and the beam mainly broadens in the poloidal direction. The second consequence is that, to model the beam propagation in a turbulent plasma for a 2D ECCD configuration, it is preferable to use the modified toroidal fluctuation pattern, which reproduces the poloidal beam broadening, as the coupling between COMSOL and LUKE assumes an EC beam with an azimuthally symmetric transverse cross-section. This limit maximizes the overall broadening with respect to a case with a realistic 3D fluctuation pattern. For the present study, we are interested in a worst case scenario to be compared with experimental data, but if one wants to improve the prediction capabilities of the numerical tools, the use of a 3D wave propagation solver is required, at least to treat ECCD configurations.

### 5.5.3 COMSOL-LUKE simulations of experimental cases

COMSOL-LUKE simulations have been performed for TCV shots. LUKE simulations require an estimation of the effective charge  $Z_{eff}$ . For the ECCD cases (TCV shots #74301 and #74302 for scenarios A and B respectively), the effective charge is obtained, assuming a constant profile, by matching the plasma current from LUKE simulations  $I_p^{LUKE}$  in pure ECRH cases (TCV shots #77458 and #77456 for scenario A and B respectively) with the experimental plasma current  $I_p$  from which the bootstrap current  $I_{BS}$  has been removed (the bootstrap current is not simulated in LUKE), so that  $I_p^{LUKE} = I_p - I_{BS}$ . Indeed, for pure ECRH cases, the current driven by the EC waves is negligible and the effective charge can be used as a free parameter to match the experimental current. This gives the  $Z_{eff}$  values indicated in table 5.3.

LUKE simulations have been performed in time-asymptotic mode, which is the most relevant mode for the present experiments as the typical characteristic time for the wave-induced electric field diffusion is of the order of 0.01 to 0.1 seconds in limited L-mode TCV plasmas [Choi et al. 2020a]. However, the frozen current density mode has also been used to get a lower boundary for the HXR emission. In this mode, the plasma current density to match is taken from the ECRH cases, as the total plasma current is the same between the ECRH and the ECCD cases (in TCV, the plasma current is controlled by feedback on the Ohmic transformer primary, and driving current with ECCD will affect the loop voltage, but not the total current). This mode corresponds to the limit in which the inductive electric field generated by the locally noninductively driven current does not diffuse at all. This tends to reduce the Ohmic electric field, and thus to lower the HXR count rate from the synthetic diagnostic by reducing the synergy between the Ohmic and the EC current drive.

Results from COMSOL simulations, showing the beam width and beam transverse section



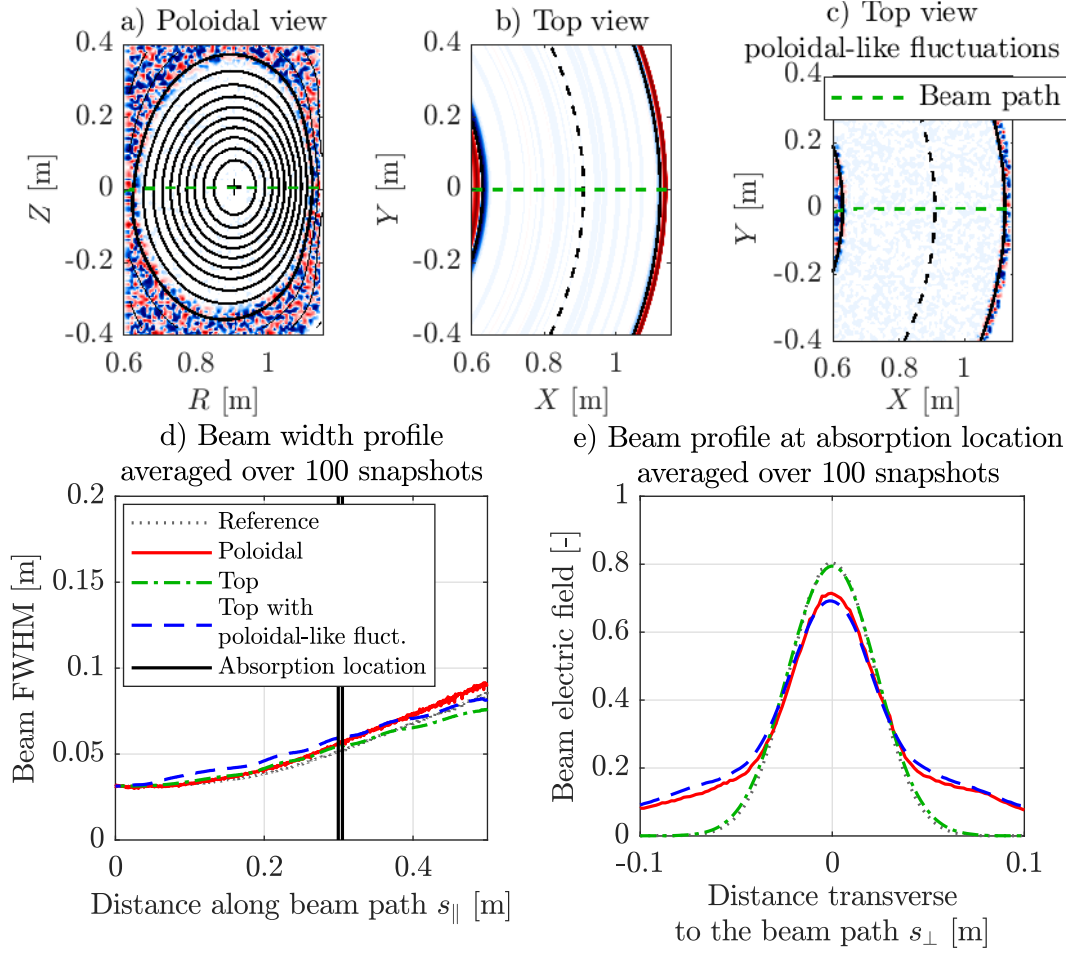


Figure 5.12: Results of 2D COMSOL simulations showing the beam FWHM along the beam path *d*) and the associated beam transverse section at the absorption location *e*) for configurations *a*) (poloidal section), *b*) (toroidal section) and *c*) (toroidal section, but using poloidal-like density fluctuations). The blue-and-red color map in plots *a*), *b*) and *c*) shows the fluctuation level  $\delta n_e / \bar{n}_e$  (red is positive and blue is negative).

at the absorption location for the two scenarios, are given in figure 5.13. The beam FWHM increases slightly, but does not change much with increasing RMS of the density fluctuations. However, the beam profile is distorted from a Gaussian to a Lorentzian shape. These features are characteristic of the intermediate beam broadening regime, described in section 5.4, matching the expectations obtained using equation 5.5 (see figure 5.11). Finally, one can notice that the beam scattering leads to an asymmetric beam profile, and this asymmetry increases with the density fluctuation RMS. The average beam refraction is negligible. In the worst case, at the absorption location, the beam is shifted by 1 mm with respect to the reference case. In both scenarios, a comparable beam broadening is observed for the different fluctuation patterns that have been tested, in spite of the fact that the beam travels over a slightly longer distance before being absorbed in scenario A. The resulting absorbed EC power profile is shown in figure 5.14. It can be clearly seen that, for scenario A, the impact of edge density fluctuations on the power deposition profile is almost negligible, while the power

## 5.5 Experimental study: to assess the discrepancy between observations and simulations

deposition profile significantly broadens for scenario B, even though the beam broadening is similar in both cases. This confirms that the impact of beam broadening on the actual power deposition profile is also dependent on the beam launching configuration, and that scenario A minimizes this impact.

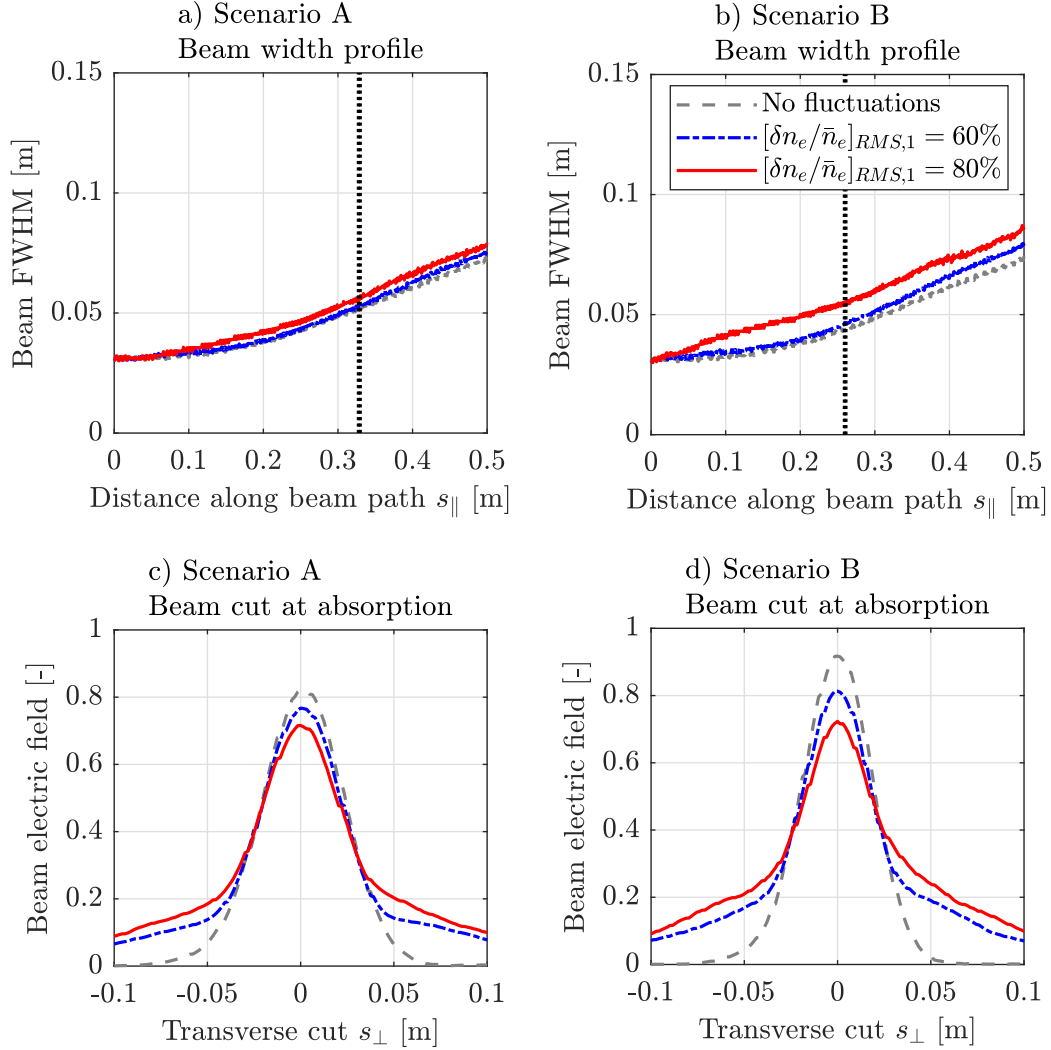


Figure 5.13: Beam width profile for scenario A (TCV shot #74301) *a)* and scenario B (TCV shot #74302) *b)*, as well as beam transverse profile at beam absorption location for scenario A *c)* and scenario B *d)*, computed using COMSOL and poloidal-like top fluctuations, as shown in figure 5.12.c). Black lines show the absorption location along the beam path.

Results from COMSOL-LUKE simulations are compared to experimental HXRS data in figure 5.15 for scenario A (TCV shot #74301) and in figure 5.16 for scenario B (TCV shot #74302). The first important observation is that, in both cases, the measured HXR count rate is around one order of magnitude lower than what is estimated using time-asymptotic COMSOL-LUKE simulations. Even frozen current density COMSOL-LUKE simulations still overestimate the

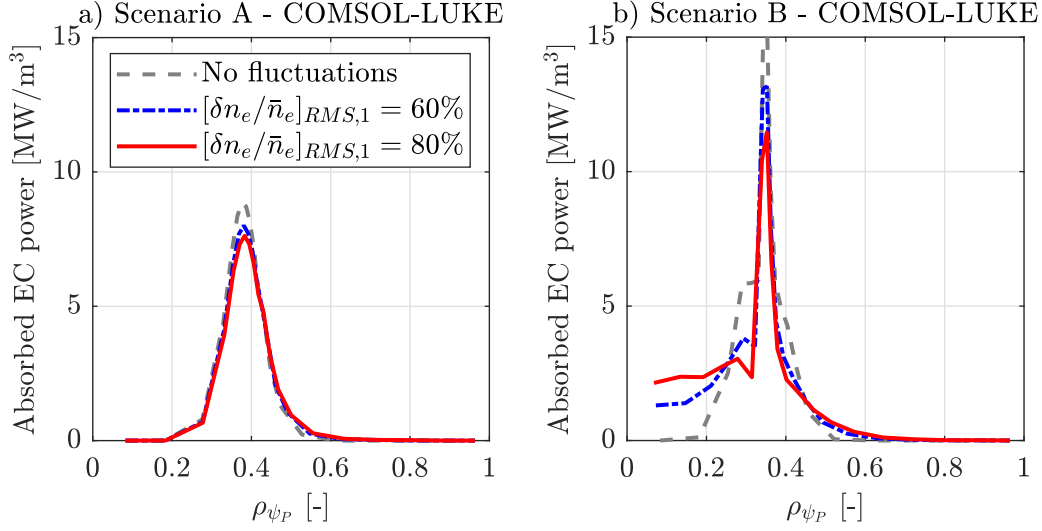


Figure 5.14: Power deposition calculation performed using COMSOL-LUKE in time-asymptotic mode for scenario A (TCV shot #74301) *a)* and scenario B (TCV shot #74302) *b)*.

HXR count rate by a factor 2 to 5 for scenario B, somewhat less for scenario A - which is due to the frozen current model itself and not to the beam broadening. It has to be recalled that the frozen current mode gives only a lower bound for the HXR emission, but is less realistic than the time asymptotic mode for such experimental scenarios. The other main observation is that the impact of density fluctuations on the simulated HXR count rate is almost negligible for scenario A. On the other hand, the impact of density fluctuations is clearly visible in scenario B, where the increase of the density fluctuation RMS induces a flattening of the HXR distribution. However, this flattening is still not sufficient to explain the discrepancy between the measurement and the simulations, even though the studied beam broadening has been maximized (highest realistic level of density fluctuation RMS, isotropic beam broadening). It means that another mechanism plays a dominant role in explaining the broadening of the suprathermal electron distribution observed in these TCV configurations. The proposed mechanism is a wave-enhanced radial transport of the fast electrons, which has been first inferred in [Choi et al. 2020a] where an ad-hoc radial transport proportional to the phase-space-localized EC wave diffusion and to the total absorbed EC power was used to match experimental data. This electron transport has then been associated to an increase of turbulent transport with the EC wave power in chapter 4. This does not mean that, for other machine conditions, the EC beam broadening cannot be the dominant mechanism. In particular, the effect of density fluctuations is expected to have an important impact in the case of long beam path before wave absorption far in the diffusive beam broadening regime (e.g. for high density fluctuation RMS with respect to the EC cutoff density, or for turbulent layer width much larger than the EC wavelength), as can happen in bigger machines like ASDEX-Upgrade [Snicker et al. 2017a] and potentially in future large devices like ITER [Decker et al. 2012; Snicker et al. 2017a].

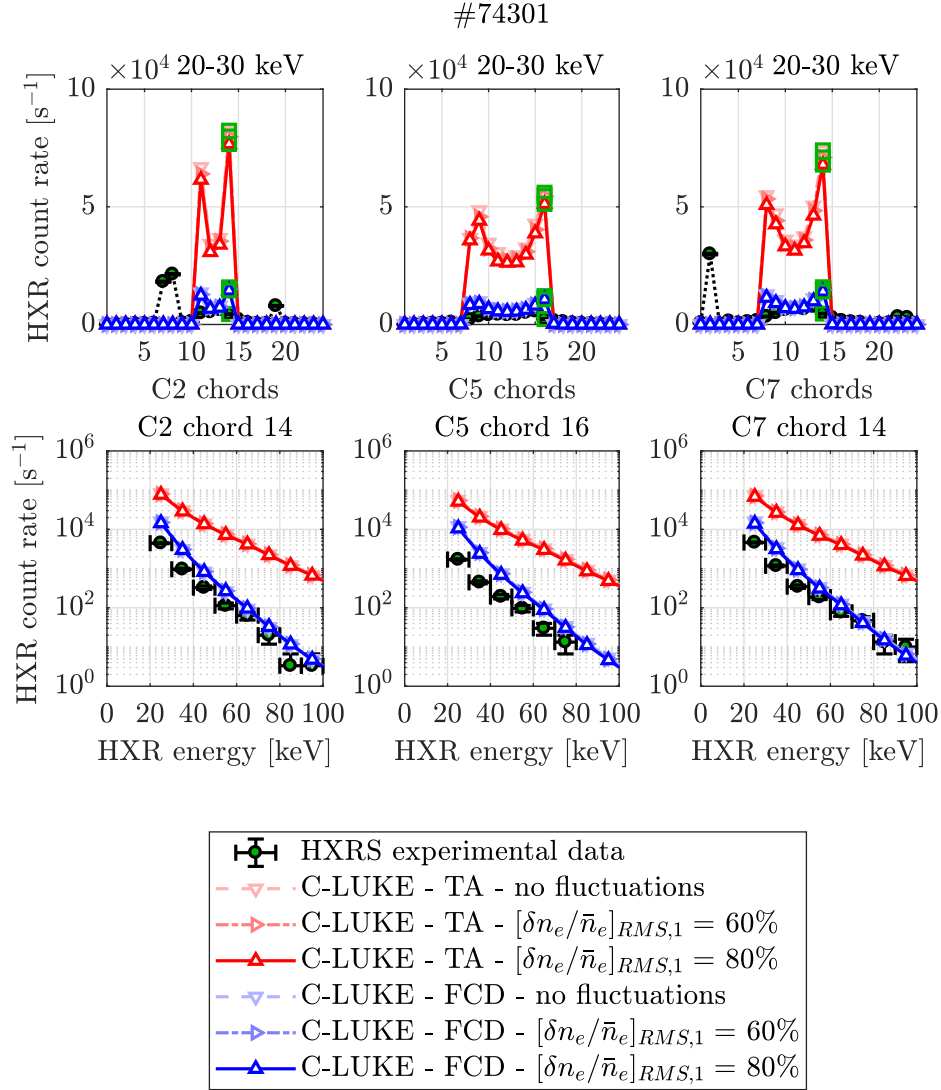


Figure 5.15: Hard X-ray (HXR) count rate measured by the HXRS and estimated from COMSOL-LUKE simulations (C-LUKE), using both the time-asymptotic (TA) and the frozen current density (FCD) modes, for different density fluctuation conditions, for TCV shot #74301 (scenario A). The green squares on the top panels indicate the selected chords for which the HXR spectrum is plotted in the bottom panels. Note that the three types of symbols for each color (blue and red) are almost exactly superimposed and thus not all visible.

## 5.6 Conclusions

The impact of EC beam broadening, caused by the beam scattering off the turbulent density structures, on the power deposition profile has been numerically and experimentally studied in TCV. Contrary to previous experimental studies performed in TCV [Chellaï et al. 2018a; Chellaï et al. 2021], the present study focuses on an EC beam launched from the low-field side,

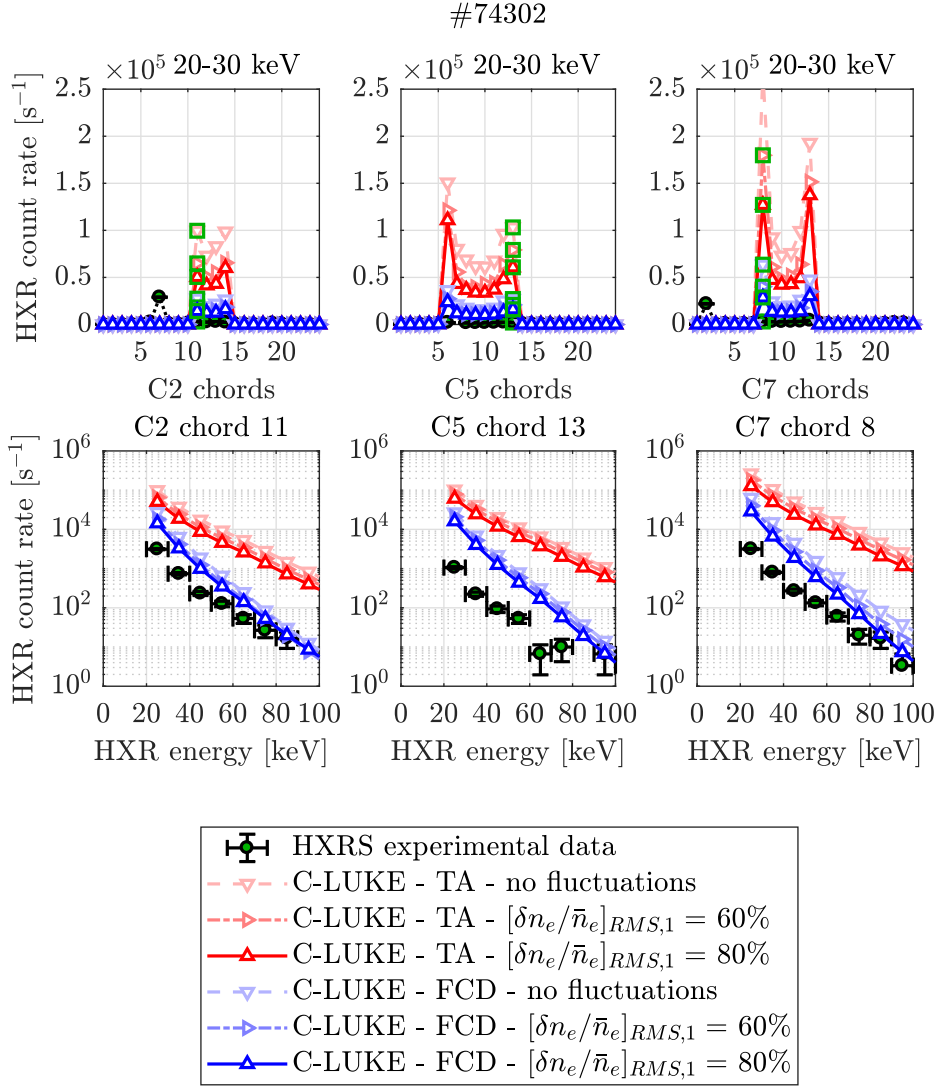


Figure 5.16: Hard X-ray (HXR) count rate measured by the HXRS and estimated from COMSOL-LUKE simulations (C-LUKE), using both the time-asymptotic (TA) and the frozen current density (FCD) modes, for different density fluctuation conditions, for TCV shot #74302 (scenario B). The green squares on the top panels indicate the selected chords for which the HXR spectrum is plotted in the bottom panels.

which is fully absorbed at the second harmonic resonant location.

First, a full-wave numerical study performed in a TCV-like configuration allows the identification of different beam broadening regimes, recovering results from previous numerical studies [Snicker et al. 2017a]. It is shown that, in TCV, the most probable beam broadening regime is an intermediate regime between diffusive and superdiffusive regimes, in which the beam is distorted from a Gaussian into a Lorentzian shape, but the beam FWHM is not increased

significantly with respect to the quiet plasma case. The numerical tools have been adapted to treat the absorption of such Lorentzian beams, coupling the full-wave COMSOL model to the drift-kinetic bounce-averaged Fokker-Planck solver LUKE.

Experimental scenarios have been developed in TCV to investigate the possibility that beam broadening could explain the unresolved discrepancy between the measured hard X-rays, emitted from suprathermal electron Bremsstrahlung, and the synthetic diagnostic results from LUKE/R5-X2 [Coda et al. 2003a; Nikkola et al. 2003]. Relative density fluctuations are measured within the plasma edge by short pulse reflectometry, and profiles are extrapolated based on previous reciprocating Langmuir probe measurements [Graves et al. 2005]. Multiple conclusions can be drawn from the comparison between experimental results and worst-case-scenario simulations. First, the launching configuration plays a very important role in the impact of the beam broadening on the power deposition profile broadening: this impact is minimized for a beam propagating along the plasma equatorial midplane. In any event, in all tested TCV configurations, the impact of the beam broadening is not sufficient to explain the aforementioned discrepancy. It is possible that, for such configurations, the enhanced turbulent transport by the EC wave absorption is the dominant mechanism that flattens the hard X-ray distribution (see [Choi et al. 2020a] and chapter 4). Both effects do not exclude each other, and it is possible that, in other configurations (e.g. far in the diffusive beam broadening regime), beam broadening could indeed become the dominant mechanism.

To better assess the beam broadening occurring in TCV and other devices, a better characterization of turbulence is necessary. In particular, one should focus on measuring the relative density fluctuation level around the separatrix, from inner edge to SOL, as it plays a major role in scattering the beam before it reaches its absorption location. Another key parameter to determine is the turbulent correlation length and, as shown in [Tretinnikov et al. 2021] and [Holland et al. 2023], both radial and poloidal correlation lengths are important as they play different roles in the beam broadening. In TCV, different fluctuations diagnostics are being upgraded, such as the tangential phase contrast imaging system [Marinoni et al. 2006], and the ability to characterize turbulence will thus significantly improve in the near future.

On the simulation side, one of the main difficulties is to obtain a good estimate of the actual plasma current density in the presence of EC waves. This is mainly due to the uncertainties on the effective charge and, more importantly, on the loop voltage profile. This forces one to choose between two extreme models of current density profile in LUKE: time-asymptotic and frozen current density. This could be improved by solving the electric field diffusion equation from first principles, allowing for the reconstruction of the actual Ohmic electric field profile. This feature has been implemented very recently in LUKE and could be used in a future work. Finally, to improve the coupling between LUKE/C3PO and other wave propagation solvers, a fully 2D ray spreading can be implemented to take into account non-isotropic beam broadening.



## 6 Conclusion and outlook

*Imprimer la forme à une durée,  
c'est l'exigence de la beauté mais  
aussi celle de la mémoire. Car ce  
qui est informe est insaisissable,  
immémorable. [...] Il y a un lien  
secret entre la lenteur et la mémoire,  
entre la vitesse et l'oubli.*

---

La Lenteur,  
Milan Kundera (1929-2023)

### 6.1 Conclusions

This thesis work focuses on investigating the underlying mechanisms that could explain the discrepancy between experimental data and synthetic data calculated by quasilinear bounce-averaged drift-kinetic simulations, for Electron-Cyclotron heating and current drive scenarios. The work achieved for this thesis has significantly advanced the modeling of EC wave propagation and absorption, enabling a better understanding of the interplay between EC waves, plasma turbulence and suprathermal electrons.

Considerable efforts have been placed in developing a software toolkit dedicated to the study of EC beam broadening by plasma density fluctuations, and of the turbulent transport enhancement by EC wave interaction with the plasma. In particular, the capabilities of the ray-tracing code C3PO have been extended to treat Gaussian beam propagation in a dielectric medium with varying refractive index, enabling more realistic calculations of EC wave power deposition in a quiet plasma. To calculate the EC power deposition in a turbulent plasma, a custom beam width option has been added to C3PO, with the possibility of using a Gaussian or a Lorentzian beam profile. This feature enables the coupling of the ray-tracing code C3PO with the full-wave COMSOL model, which can treat EC beam broadening in 2D configura-



tions. On the other hand, the work performed for this thesis has spurred the development of a new ECRH/ECCD source for the gyro-kinetic code ORB5. The model itself, based on a quasilinear approach, has been developed and implemented by Dr. Peter Donnel, while tests and benchmarks against drift-kinetic models have been performed in collaboration. This new tool enables the study of turbulent transport enhancement by EC waves from first principles for the first time.

The study of suprathermal electron dynamics, based on an experimental scenario developed by Dr. Dahye Choi, has pushed forward the analysis of HXRS data, by estimating a radial diffusion coefficient from tomographically inverted data. Such analyses suggest that the radial diffusion of suprathermal electrons increases with the absorbed EC power, which is consistent with experimentally-constrained dynamical drift-kinetic simulations performed with LUKE, using an ad-hoc radial transport model. This increased transport with EC power is associated with an increase of the electron density and temperature fluctuation level with EC power, measured for ion-scale turbulence. This phenomenon could be explained by a destabilization of TEM/ITG turbulence in a stiff gradient configuration. These observations are compatible with first principles ORB5 simulations, showing an increased turbulent transport with EC power. These preliminary results tend to indicate that another mechanism is at play to explain the observed power deposition profile broadening than the commonly invoked beam scattering in a turbulent medium.

This is further evidenced by the study of beam scattering through the turbulent plasma edge, which has been performed in TCV. Full-wave numerical studies have confirmed previous observations of different regimes of beam broadening, depending on beam and fluctuation parameters. It appears that TCV scenarios are most likely to lie in the intermediate regime, for which the beam becomes a slightly broadened Lorentzian beam. In this context, it has been shown that the scattering-induced beam broadening is not sufficient to explain the discrepancy between experimental and synthetic HXRS data, meaning that another mechanism is necessary to reproduce the experimental data, at least for the tested TCV configurations.

This thesis work paves the way for a better understanding of the EC power deposition broadening mechanisms, and in particular of the potential wave-enhanced turbulent transport, rendered possible by newly developed tools. Both broadening mechanisms are not excluding each other, and it is important to further study the suggested wave-enhanced turbulent transport, performing comprehensive parameter scans, in particular to assess which mechanism dominates and what are the implications for future larger fusion devices, such as ITER and DEMO. Further suggestions of improvement and of future research paths are detailed in the next section.

### 6.2 Outlook and future works

Generally speaking, both the study of turbulent transport and beam scattering could benefit from better experimental characterization of the turbulence. In particular, studies can be

completed by extending the scanned range of parameters such as injected EC power, EC power deposition location and ECCD angle, together with systematic measurement of turbulence, with the aim of characterizing both scattering and transport enhancement effects for various plasma scenarios and EC configurations. Clearly separating the two effects requires the accurate modeling of beam scattering effects, and thus a solid estimation of the density fluctuation level, as well as the fluctuation correlation lengths (both radial and poloidal), from the core to the scrape-off layer. This will be partly possible thanks to the planned improvement of fluctuation diagnostics on TCV, in particular of the SPR and of the TPCI diagnostics. Missing information could be retrieved using experimentally-constrained local gradient-driven gyro-kinetic simulations, providing that an accurate measurement of the ion temperature and of the effective charge is available.

With better experimental characterization of the turbulence comes the improvement of the modeling of the beam scattering effects. The coupling between the full-wave code and the drift-kinetic Fokker-Planck solver LUKE could be further developed by introducing two different beam widths, a poloidal and a toroidal one, to take into account the anisotropy in beam broadening. Another tool that can be included in the workflow is WKBeam, which, unfortunately, could not be used for the work performed in this thesis, but has been specifically designed to treat beam scattering through a turbulent refractive index. Coupling WKBeam to the synthetic diagnostic capabilities of LUKE and to complete and accurate measurements of turbulence should, in principle, enable consistent modeling of the EC beam broadening. The remaining transport necessary to explain the experimental and synthetic HXRS data could then be estimated using the LUKE forward modeling approach with ad-hoc transport models.

However, a source of uncertainty in LUKE modeling is the current density profile estimation, which, in TCV, relies on a noisy loop voltage estimation. This difficulty could be overcome by using the recently developed induction equation solver, now implemented in LUKE by Dr. Joan Decker and Dr. Mathias Hoppe. It would be therefore possible to redo LUKE simulations for TCV shots used in both chapters 4 and 5, to assess the validity of the different applied methodologies, in the form of the frozen current density and of the time-asymptotic modes.

Over the long term, the ad-hoc transport model could be replaced by first principles transport models calculated by global flux-driven gyro-kinetic simulations. This would require some substantial, and non-straightforward, improvements: extend the simulated time duration to reach steady-state equilibrium and consistently scan over a wide range of beam and plasma parameters. Moreover, to test the potential phase-space dependency of the wave-enhanced transport, new diagnostics should be built in ORB5 to discretize the phase-space distribution of electrons, which will require a higher number of markers to obtain sufficient statistics, rendering the steady state more numerically expensive to reach. Another solution could be to use a global flux-driven gyro-kinetic code not based on a particle-in-cell approach, to attain easier access to the phase-space-dependent electron distribution function.

Finally, interesting insights could be gained on wave-enhanced transport by calculating the

## Chapter 6. Conclusion and outlook

---

wave-induced neoclassical transport, using dedicated tools such as CQL3D, and performing a systematic benchmark with LUKE.

The interplay between waves, turbulence and suprathermal electrons has been studied throughout this thesis, minimizing and neglecting MHD activity. However, it is important to note that MHD activity, in particular via magnetic reconnection, is also a source of electron acceleration and transport, and that the interplay between MHD, suprathermal electrons and EC waves could also be an interesting research path, as it can impact the ECCD efficiency for instance.

# A The TCV X2 launcher geometry

## A.1 Definitions of the different frames

### A.1.1 TCV Cartesian frame

The TCV Cartesian frame  $(X, Y, Z)$  is defined as follows

- $\mathbf{e}_X$  is the direction of the West-East axis,
- $\mathbf{e}_Y$  is the direction of the South-North axis,
- $\mathbf{e}_Z$  is the direction of the vertical axis (upward), so the basis is direct.

### A.1.2 TCV cylindrical frame

The TCV cylindrical frame  $(R, \phi, Z)$  is defined as follows

- $\mathbf{e}_R$  is the the radial direction of the tokamak, pointing outward of the machine,
- $\mathbf{e}_\phi$  is the toroidal direction, going anti-clockwise looking from the top,
- $\mathbf{e}_Z$  is the direction of the vertical axis (upward), so the basis is direct.

### A.1.3 Launcher cylindrical frame

The launcher cylindrical frame  $(x, \phi_L, z)$  is defined as follows

- $\mathbf{e}_x$  is along the launcher axis of rotation,
- $\mathbf{e}_{\phi_L}$  is the direction of the rotation of the launcher around its axis at  $Z = l_{axis}$ ,
- $\mathbf{e}_z$  is perpendicular to  $\mathbf{e}_x$  and  $\mathbf{e}_{\phi_L}$  such that the basis is direct (when  $\phi_L = 0$ ,  $\mathbf{e}_z = \mathbf{e}_Z$  and  $\mathbf{e}_x = \mathbf{e}_R$ ).

### A.2 Definitions

#### A.2.1 Definitions of launcher angles

In TCV, there are different types of EC wave launchers. The X2 launchers are located on the low-field side, either in equatorial or in upper low-field side ports. It is possible to change the EC beam direction by tuning two angles: the tilt angle of the last movable mirror of the launcher, labeled mirror 4 (the other launcher mirrors are fixed), and the rotation angle of the whole launcher on itself. In the frame of the launcher  $(x, \phi_L, z)$ , the angle between the horizontal  $x$ -axis and the beam direction from mirror 4 is called the poloidal launching angle, or beam angle,  $\theta_L$ . The angle of rotation of the whole launcher on itself is called the toroidal launcher angle  $\phi_L$ .

#### A.2.2 Definition of launcher's geometrical parameters

Launchers L1 and L4 are equatorial, while launchers L2 and L5 are upper low-field side. The calculation of the beam position and of its direction of propagation from mirror 4 is done in the launcher frame first, or equivalently in the TCV Cartesian frame assuming  $\phi_L = 0$ , the  $\phi_L$  rotation being applied afterwards. The launcher geometry is illustrated in figure A.1. First, different points need to be defined:

- $p_3$  the beam center on mirror 3 (fixed) ;
- $p_4$  the beam center on mirror 4. The first value  $p_{4_0}$  is given knowing the trajectory of the beam from mirror 3, but the actual position will be re-evaluated later ;
- $p_p$  the poloidal rotation axis of mirror 4 (fixed) ;
- $r_p = 1$  cm the distance between mirror 4 surface and its rotation axis (mirror thickness, fixed) ;
- $l_{axis}$  the vertical coordinate of the launcher port (and so of its toroidal rotation axis) ;
- $d_{w_3} = 27.55$  cm the distance from beam waist to mirror 3 (fixed).

The coordinates of these different points are given in the  $(X, Y, Z)$  frame in tables A.1 and A.2.

Table A.1: Points coordinates for L1 and L4.

Point	X	Y	Z	Units
$p_3$	130.723	0	-5.865	cm
$p_{4_0}$	121.8869	0	5.45	cm
$p_p$	119.056	0	6.45	cm
$l_{axis}$	0	0	-0.25	cm

Table A.2: Points coordinates for L2 and L5.

Point	X	Y	Z	Units
$p_3$	130.723	0	39.885	cm
$p_{4_0}$	121.8869	0	51.2	cm
$p_p$	119.056	0	52.2	cm
$l_{axis}$	0	0	45.5	cm

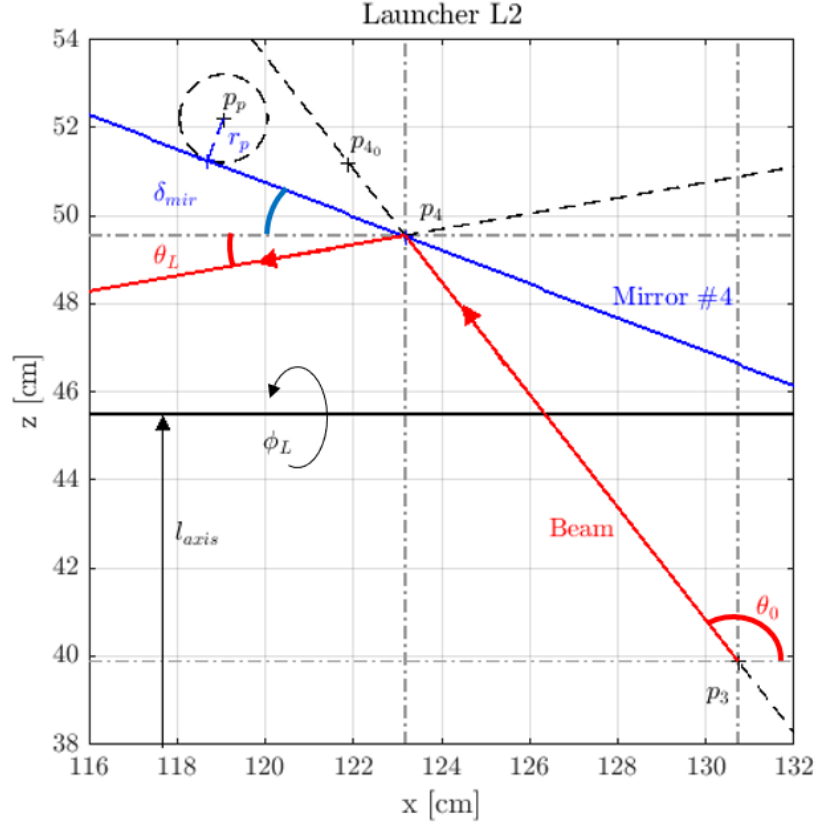


Figure A.1: Example of TCV X2 launcher geometry, in the launcher frame  $(x, \phi_L, z)$ . Here,  $\theta_L = 10^\circ$ .

### A.3 Ray initial position and direction on mirror 4

In the launcher frame, the angle between the horizontal  $x$ -axis and the direction of the beam from mirror 3 before it intersect the mirror 4 is given by

$$\tan \theta_0 = \frac{z_{p_4} - z_{p_3}}{x_{p_4} - x_{p_3}}. \quad (\text{A.1})$$

The tilt angle of mirror 4 with respect to the horizontal is then

$$\delta_{mir} = -\frac{\pi - \theta_0 - \theta_L}{2}. \quad (\text{A.2})$$

## Appendix A. The TCV X2 launcher geometry

---

From this point, it is necessary to express the coordinates of the beam center on mirror 4. Defining the notations

$$\xi_{p_p} = x_{p_p} - x_{p_3}, \quad (\text{A.3})$$

$$\zeta_{p_p} = z_{p_p} - z_{p_3}, \quad (\text{A.4})$$

leads to

$$\zeta_{p_4} = \frac{\zeta_{p_p} - r_p \cos(\delta_{mir}) - \tan(\delta_{mir}) [\xi_{p_p} + r_p \sin(\delta_{mir})]}{1 + \tan(\delta_{mir}) \cot(\pi - \theta_0)}, \quad (\text{A.5})$$

$$\xi_{p_4} = -\zeta_{p_4} \cot(\pi - \theta_0). \quad (\text{A.6})$$

Applying the rotation by  $\phi_L$  of the launcher yields in TCV Cartesian frame  $(X, Y, Z)$

$$X_{p_4} = \xi_{p_4} + x_{p_3}, \quad (\text{A.7})$$

$$Y_{p_4} = (\zeta_{p_4} + z_{p_3} - l_{axis}) \sin(\phi_L), \quad (\text{A.8})$$

$$Z_{p_4} = (\zeta_{p_4} + z_{p_3} - l_{axis}) \cos(\phi_L) + l_{axis}. \quad (\text{A.9})$$

This translates in TCV cylindrical frame  $(R, \phi, Z)$  into

$$R_{p_4} = \sqrt{X_{p_4}^2 + Y_{p_4}^2}, \quad (\text{A.10})$$

$$\phi_{p_4} = -\tan^{-1}\left(\frac{Y_{p_4}}{X_{p_4}}\right), \quad (\text{A.11})$$

$$Z_{p_4} = Z_{p_4}. \quad (\text{A.12})$$

This method is the one used in C3PO, which gives equal results to the method developed by Dr. S. Coda in the MATLAB® function `launch_point_on_mirror_16.m`, where the intersection is found between the direction of the beam from mirror 3 and the mirror 4, computing the position of the point on the mirror 4 the closest to its poloidal rotation axis as an intermediate step.

### A.4 Conversion from launcher angles to TORAY/C3PO angles

To convert launcher angles  $(\theta_L, \phi_L)$  into TORAY/C3PO angles, we need to project the 3D beam onto the  $(X, Y)$ -plane to get the toroidal angle  $\phi_T$ , and onto the  $(X, Z)$ -plane to get the poloidal angle  $\theta_T$ . Indeed, the poloidal angle in TORAY/C3PO is defined as the angle between the vertical  $Z$ -axis and the beam trajectory ( $\theta_T \in [0; \pi]$ ), in the  $(R, Z)$ -plane and the toroidal angle is defined as the angle between the horizontal  $R$ -axis and the beam trajectory in the  $(X, Y)$ -plane, such that pure-ECRH corresponds to  $\phi_T = \pi$  ( $\phi_T \in [-\pi; \pi]$ ). In the standard TCV

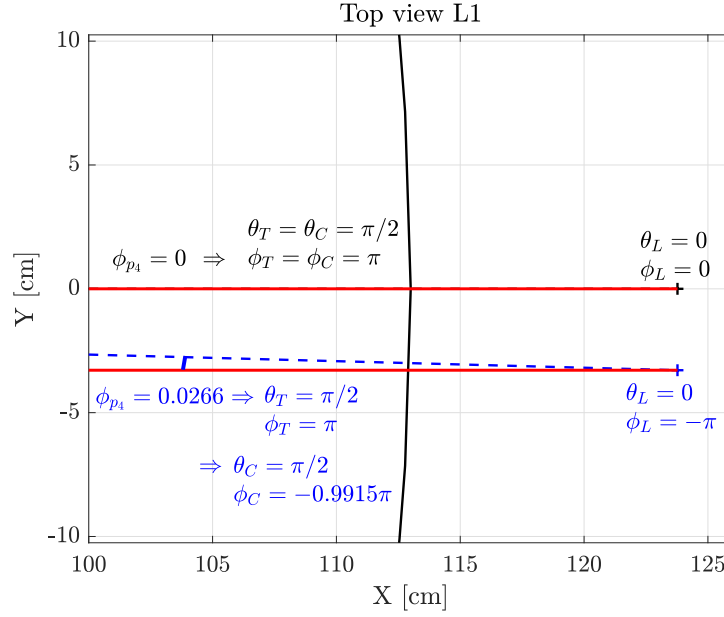


Figure A.2: Example of TCV X2 launcher geometry, in the TCV Cartesian frame  $(X, Y, Z)$ , illustrating the difference of launcher-to-ray angles conversion between TORAY and C3PO.

configuration, co-current injection corresponds to  $\phi_T \geq 0$ . Both angles are defined as

$$\theta_T = \cos^{-1}(-\sin(\theta_L) \cos(\phi_L)), \quad (\text{A.13})$$

$$\phi_T = \tan^{-1}(\tan(\theta_L) \cos(\phi_L)). \quad (\text{A.14})$$

To compute properly  $\phi_T$  in MATLAB®, one should use the `atan2` function (tangent defined on the four-quadrants trigonometric circle) with the following arguments

$$\phi_T = \text{atan2}(-\sin(\theta_L) \cos(\phi_L), -\cos(\theta_L)). \quad (\text{A.15})$$

Angles in TORAY and C3PO are equivalent. In C3PO, the reference horizontal axis is shifted to the  $R$ -axis passing by the beam launching point. The toroidal ray angle therefore needs to be corrected by the angle  $\phi_{p_4}$ . Indeed, this angle takes into account the fact that the movement of the launcher induces a tilt of the beam angle with respect to the line perpendicular to the plasma (the  $R$ -axis is tilted by  $\phi_{p_4}$ ). The C3PO angles  $(\theta_C, \phi_C)$  with respect to the TORAY angles  $(\theta_T, \phi_T)$  are then given by

$$\theta_C = \theta_T, \quad (\text{A.16})$$

$$\phi_C = \phi_T + \phi_{p_4}. \quad (\text{A.17})$$

This difference is small, as the maximum angle  $\phi_{p_4}$  is roughly around  $1.5^\circ$  for  $\phi_L = -90^\circ$ . This difference is illustrated in figure A.2. In practice, the  $\theta_L$  range is mechanically limited, roughly from  $9^\circ$  to  $40^\circ$ .





## B Analytic equilibrium generation

There are many advantages associated with generating an analytic equilibrium to perform purely numerical studies and code benchmark. The generated equilibrium is simplified and parametrized, allowing for an easier analysis of the results and a better control of the magnetic configuration. However, choosing a specific magnetic configuration adds some constraints on the pressure and current functions, since the Grad-Shafranov equation needs to be satisfied. Still, analytic equilibrium generation remains a flexible, tunable, and simple tool that helps to understand complex physics. It also renders results more easily reproducible.

There are many different ways of producing an analytic equilibrium solution of the Grad-Shafranov equation [Takeda and Tokuda 1991]. The most famous and most used is the Solov'ev family of solutions, characterized by profiles of pressure  $p(\psi_P)$  and current function  $F^2(\psi_P)$  linear in poloidal magnetic flux  $\psi_P$  [Solov'ev 1968; Cerfon and Freidberg 2010; Aydemir et al. 2019]. Other types of families of solutions exist, such as solutions based on polynomial expansion and hypergeometric functions [Atanasiu et al. 2004; Guazzotto and Freidberg 2007]. Such solutions allow for more freedom and more possibilities in the choice of pressure and current function profiles, but are more complicated to set up properly. The method presented in [Guazzotto and Freidberg 2007] for instance does not prescribe completely the plasma shape, which depends upon some free parameters that are not obvious to choose.

The method presented in [Cerfon and Freidberg 2010] has been chosen as the base root of the equilibrium generator detailed hereafter. In that case, the shape of the plasma is prescribed by three control points, assuming up-down symmetry of the plasma equilibrium. In the original paper, the option of adding a fourth control point with additional boundary conditions to break the up-down symmetry and generating diverted plasmas is also detailed. This method has been generalized for a chosen set of control points in [Aydemir et al. 2019].

## B.1 Poloidal magnetic flux calculation

The calculation procedure for the poloidal magnetic flux  $\psi_P$  is directly taken from [Cerfon and Freidberg 2010] and summarized here. The calculation is done in the cylindrical system of coordinates  $(R, Z, \phi)$ . In a tokamak, axysymmetry is assumed, so that the 3D problem reduces to a 2D problem in  $(R, Z)$  space. The poloidal flux is normalized, as well as the spatial coordinates

$$\psi = \psi_P / \psi_{P0} \quad (\text{B.1})$$

$$x = R / R_0 \quad (\text{B.2})$$

$$y = Z / R_0 \quad (\text{B.3})$$

where  $R_0$  is the major radius of the device, and  $\psi_{P0}$  is the flux normalization constant in Weber. In this configuration, the normalized flux  $\psi$  is defined such that  $\psi = 0$  on the last-closed flux surface, and becomes more and more negative toward the magnetic axis, until a given value  $\psi_{ax} < 0$ . The Grad-Shafranov equation for the pressure  $p$  in Pa and the current function  $F = RB_\phi$  in T·m can now be written as

$$x \frac{\partial}{\partial x} \left( \frac{1}{x} \frac{\partial \psi}{\partial x} \right) + \frac{\partial^2 \psi}{\partial y^2} = -\mu_0 \frac{R_0^4}{\psi_{P0}^2} x^2 \frac{dp}{d\psi} - \frac{R_0^2}{\psi_{P0}^2} F \frac{dF}{d\psi} = (1 - A)x^2 + A \quad (\text{B.4})$$

where  $B_\phi$  is the toroidal magnetic field, and  $A$  a free constant, adjusting the balance between current and pressure contribution to the equilibrium. This constant defines the Solov'ev profiles

$$-\mu_0 \frac{R_0^4}{\psi_{P0}^2} \frac{dp}{d\psi} = 1 - A, \quad (\text{B.5})$$

$$-\frac{R_0^2}{\psi_{P0}^2} F \frac{dF}{d\psi} = A. \quad (\text{B.6})$$

The solution to this form of the Grad-Shafranov equation is the sum of a particular solution, which depends on  $A$ , and of a homogeneous solution, which depends on boundary conditions

$$\psi(x, y) = \frac{x^4}{8} + A \left( \frac{1}{2} x^2 \ln(x) - \frac{x^4}{8} \right) + \sum_{i=1}^7 c_i \psi_i(x, y) \quad (\text{B.7})$$

where the  $c_i$  coefficients are constants deduced from the boundary conditions set by the prescribed shape, and the  $\psi_i$  are the following polynomials

$$\psi_1 = 1 \quad (\text{B.8})$$

$$\psi_2 = x^2 \quad (\text{B.9})$$

$$\psi_3 = y^2 - x^2 \ln(x) \quad (\text{B.10})$$

$$\psi_4 = x^4 - 4y^2 x^2 \quad (\text{B.11})$$

$$\psi_5 = 2y^4 - 9y^2 x^2 + 3x^4 \ln(x) - 12y^2 x^2 \ln(x) \quad (\text{B.12})$$

$$\psi_6 = x^6 - 12y^2 x^4 + 8y^4 x^2 \quad (\text{B.13})$$

$$\begin{aligned} \psi_7 = & 8y^6 - 140y^4 x^2 + 75y^2 x^4 - 15x^6 \ln(x) + 180y^2 x^4 \ln(x) \\ & - 120y^4 x^2 \ln(x) \end{aligned} \quad (\text{B.14})$$

Boundary conditions are given by a prescribed shape for the last-closed flux surface (LCFS). This shape is parametrized by (see figure B.1)

$$x(\theta) = 1 + \varepsilon \cos(\theta + \delta \sin \theta) \quad (\text{B.15})$$

$$y(\theta) = \varepsilon \kappa \sin \theta \quad (\text{B.16})$$

where the shaping parameters are the inverse aspect ratio  $\varepsilon = a/R_0$ , the elongation  $\kappa$  and the triangularity  $\delta$ . Three control points are used to constrain the shape, assuming an up-down symmetry: a first point on the low field side of the equatorial plane located at  $(1 + \varepsilon, 0)$ , a second point on the high field side located at  $(1 - \varepsilon, 0)$  and a third point at the maximum of elongation located at  $(1 - \delta\varepsilon, \kappa\varepsilon)$ . Six conditions are given by fixing the value and the curvature of  $\psi$  at these three points. A seventh condition is added by ensuring that the third point is the maximum height. These conditions are respectively given by

$$\psi(1 + \varepsilon, 0) = 0 \quad (\text{B.17})$$

$$\psi(1 - \varepsilon, 0) = 0 \quad (\text{B.18})$$

$$\psi(1 - \delta\varepsilon, \kappa\varepsilon) = 0 \quad (\text{B.19})$$

$$\frac{\partial^2 \psi}{\partial y^2}(1 + \varepsilon, 0) = - \left[ \frac{\partial^2 x}{\partial y^2} \right]_{\theta=0} \frac{\partial \psi}{\partial x}(1 + \varepsilon, 0) \quad (\text{B.20})$$

$$\frac{\partial^2 \psi}{\partial y^2}(1 - \varepsilon, 0) = - \left[ \frac{\partial^2 x}{\partial y^2} \right]_{\theta=\pi} \frac{\partial \psi}{\partial x}(1 - \varepsilon, 0) \quad (\text{B.21})$$

$$\frac{\partial^2 \psi}{\partial x^2}(1 - \delta\varepsilon, \kappa\varepsilon) = - \left[ \frac{\partial^2 y}{\partial x^2} \right]_{\theta=\pi/2} \frac{\partial \psi}{\partial x}(1 - \delta\varepsilon, \kappa\varepsilon) \quad (\text{B.22})$$

$$\frac{\partial \psi}{\partial x}(1 - \delta\varepsilon, \kappa\varepsilon) = 0 \quad (\text{B.23})$$

with

$$\left[ \frac{\partial^2 x}{\partial y^2} \right]_{\theta=0} = -\frac{(1+\delta)^2}{\epsilon \kappa^2} \quad (\text{B.24})$$

$$\left[ \frac{\partial^2 x}{\partial y^2} \right]_{\theta=\pi} = \frac{(1-\delta)^2}{\epsilon \kappa^2} \quad (\text{B.25})$$

$$\left[ \frac{\partial^2 y}{\partial x^2} \right]_{\theta=\pi/2} = -\frac{\kappa}{\epsilon \cos^2(\delta)} \quad (\text{B.26})$$

Thus, a 7x7 system of unknowns/equations is built. The system is simply implemented in MATLAB® (version R2017b) using the symbolic functions (syms function). Then, the native solver of MATLAB® is used to solve the system (solve function).

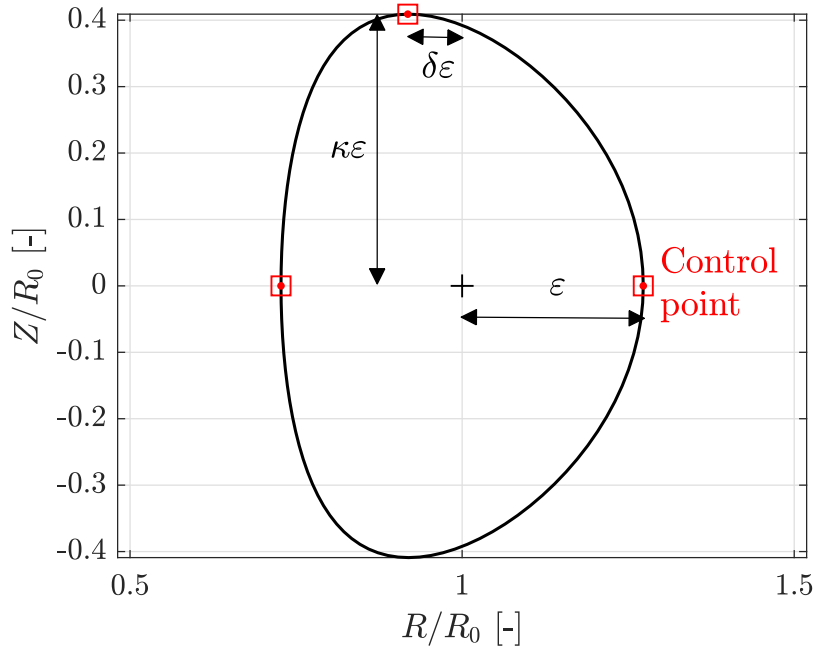


Figure B.1: Plasma boundary geometry and control points, showing elongation  $\kappa$  and triangularity  $\delta$

## B.2 Magnetic field and pressure calculations

Once the magnetic flux is calculated, it is possible to compute the magnetic field and the pressure profile from the imposed Solov'ev profiles. The toroidal magnetic field (in Tesla) and

the total pressure (in Pascal) are given by

$$B_\phi(x, y) = \frac{R_0}{R} \sqrt{B_0^2 - 2 \frac{\psi_{P0}^2}{R_0^4} A \psi(x, y)}, \quad (\text{B.27})$$

$$p(x, y) = -\frac{\psi_{P0}^2}{\mu_0 R_0^4} (1 - A) \psi(x, y) + p_{edge}. \quad (\text{B.28})$$

The parameters  $A$ ,  $R_0$  (in meter) and  $B_0$  (in Tesla) are given as input in the equilibrium generation routine. The other parameter that is given in input is the pressure gradient (in Pascal, considering  $\psi_{P,n} = \psi/\psi_{ax}$  going from 1 to 0)

$$\frac{dp}{d\psi_{P,n}} = \psi_{ax} \frac{dp}{d\psi} = p_{ax} - p_{edge} = -\psi_{ax} \frac{\psi_{P0}^2}{\mu_0 R_0^4} (1 - A) \quad (\text{B.29})$$

so that the flux normalization in Weber is

$$\psi_{P0} = \sqrt{-\frac{\mu_0 R_0^4}{(1 - A) \psi_{ax}} \frac{dp}{d\psi_{P,n}}} \quad (\text{B.30})$$

The poloidal components of the magnetic field (in Tesla) are then given by

$$B_R(x, y) = -\frac{\psi_{P0}}{R_0^2 x} \frac{\partial \psi}{\partial y} \quad (\text{B.31})$$

$$B_Z(x, y) = \frac{\psi_{P0}}{R_0^2 x} \frac{\partial \psi}{\partial x} \quad (\text{B.32})$$

$$B_P(x, y) = \sqrt{B_R^2(x, y) + B_Z^2(x, y)} \quad (\text{B.33})$$

### B.3 Gradient-controlled profiles

The equilibrium generator has been developed in such a way that the density and temperature gradients can be controlled. The ratio of logarithmic gradients is an input of the equilibrium generator, defined by

$$R_\nabla = \frac{\nabla_\psi(\ln n)}{\nabla_\psi(\ln T)} \quad (\text{B.34})$$

where  $n$  is the density and  $T$  the temperature. This ratio sets the shape of the density and temperature profiles. In this model, a deuterium plasma without impurities is assumed, so  $n_e = n_i = n$  to ensure electroneutrality. However, it is possible to tune the ratio of ion versus electron temperature, also set as an input for the equilibrium generator, and defined by

$$R_T = \frac{T_i}{T_e}. \quad (\text{B.35})$$

## Appendix B. Analytic equilibrium generation

---

The last input that can be set to prescribe the profiles is the ratio of edge to axis temperature and density :

$$R_{ed-ax} = \frac{n_{edge}}{n_{ax}} = \frac{T_{edge}}{T_{ax}} \quad (B.36)$$

The computation of the profiles is based on the total plasma pressure, satisfying the Grad-Shafranov equation

$$p = \frac{1}{2} en T_e (1 + R_T) \quad (B.37)$$

where  $e$  is the elementary charge,  $n$  the density (in  $m^{-3}$ ) and  $T_e$  is the electron temperature (in eV). The boundaries of the profiles (axis and edge values) are given by

$$n_{ax} \quad \text{INPUT} \quad (B.38)$$

$$n_{edge} = R_{ed-ax} n_{ax} \quad (B.39)$$

$$p_{ax} = \frac{1}{1 - (R_{ed-ax})^2} \frac{dp}{d\psi_{P,n}} \quad (B.40)$$

$$p_{edge} = (R_{ed-ax})^2 p_{ax} \quad (B.41)$$

$$T_{e,ax} = \frac{2p_{ax}}{en_{ax}(1 + R_T)} \quad (B.42)$$

$$T_{e,edge} = R_{ed-ax} T_{e,ax} \quad (B.43)$$

The power dependency in  $\psi$  of the profiles is determined by the ratio of the logarithmic gradients

$$k = \frac{R_{\nabla}}{1 + R_{\nabla}}, \quad (B.44)$$

which leads to

$$p(\psi) = -\frac{\psi_{P0}^2}{\mu_0 R_0^4} (1 - A) \psi + p_{edge} \quad (B.45)$$

$$n(\psi) = (n_{ax} - n_{edge}) \left( \frac{\psi}{\psi_{ax}} \right)^k + n_{edge} \quad (B.46)$$

$$T_e(\psi) = (T_{e,ax} - T_{e,edge}) \left( \frac{\psi}{\psi_{ax}} \right)^{1-k} + T_{e,edge} \quad (B.47)$$

$$T_i(\psi) = R_T T_e(\psi) \quad (B.48)$$

These profiles are only valid for  $R_{ed-ax} = 0$ . For  $R_{ed-ax} \neq 0$ , a correction is applied to recover the total pressure when multiplying the density and the temperature

$$T_e(\psi) = \frac{2p(\psi)}{en(\psi)(1 + R_T)} \quad \text{if: } R_{\nabla} \geq 1 \quad (B.49)$$

$$n(\psi) = \frac{2p(\psi)}{eT_e(\psi)(1 + R_T)} \quad \text{else} \quad (B.50)$$

This correction depends on a condition on  $R_{\nabla}$  to avoid a positive gradient at the edge, due to the constrained values of  $n_{edge}$  and  $T_{e,edge}$ . This means that the value of  $R_{\nabla}$  is locally changed, especially at the edge, and is different from the input value.

## B.4 Surface- and volume-averaged quantities

Some important physical quantities are computed by averaging over the plasma volume or over the last closed flux surface. The `contourc` function of MATLAB® is used to obtain the equation of half (up-down symmetry) of the last-closed flux surface  $y_{edge}(x_{edge})$ , in a form of an array of  $N + 1$  points (see figure B.2). The plasma volume (in cubic meters) is computed as follow

$$V = 2\pi \oint_{edge} R_0^2 y(x) x dx = 2 \times 2\pi R_0^3 \sum_{j=1}^N y_{edge,j} x_{edge,j} \Delta x_{edge,j} \quad (B.51)$$

with  $\Delta x_{edge,j} = x_{edge,i+1} - x_{edge,i}$ . The volume-averaged pressure is given by

$$\langle p \rangle_V = 2\pi R_0^3 \frac{\int \int p(x, y) x dx dy}{V} = \frac{2\pi R_0^3}{V} \sum_{l=1}^{N_y-1} \sum_{m=1}^{N_x-1} p(x_m, y_l) x_m \Delta x_m \Delta y_l \quad (B.52)$$

where the  $x_m$  and the  $y_l$  values are local values of  $x$  and  $y$ , and  $\Delta x_m = x_{j+1} - x_j$ ,  $\Delta y_l = y_{i+1} - y_i$ . The normalized circumference of the plasma last closed flux surface is given by

$$C_p = \oint_{edge} \frac{dl}{R_0} = 2 \sum_{j=1}^N \Delta C_{p,j} = 2 \sum_{j=1}^N \sqrt{(\Delta x_{edge,j})^2 + (\Delta y_{edge,j})^2} \quad (B.53)$$

where  $dl$  is an element of the last-closed flux surface contour and  $\Delta y_{edge,j} = y_{edge,i+1} - y_{edge,i}$ . The poloidal magnetic field (in Tesla), averaged over the last closed flux surface can be computed as follows

$$\bar{B}_p = \frac{\oint_{edge} B_{p,edge} dl}{\oint_{edge} dl} = \frac{2R_0 \sum_{j=1}^N B_{p,edge,j} \Delta C_{p,j}}{R_0 C_p} \quad (B.54)$$

where  $B_{p,edge} = B_p(x_{edge}, y_{edge})$ . It is possible to obtain some equilibrium and MHD parameters from all these quantities, such as plasma total  $\beta$ , toroidal  $\beta_T$  and poloidal  $\beta_P$

$$\beta = \frac{2\mu_0}{B_0^2 + \bar{B}_p^2} \langle p \rangle \quad (B.55)$$

$$\beta_T = \frac{2\mu_0}{B_0^2} \langle p \rangle \quad (B.56)$$

$$\beta_P = \frac{2\mu_0}{\bar{B}_p^2} \langle p \rangle \quad (B.57)$$



## Appendix B. Analytic equilibrium generation

The parallel component of the plasma current  $I_p$  (in Amp) is given by

$$I_p = \frac{R_0 C_p \bar{B}_P}{\mu_0}. \quad (\text{B.58})$$

Finally, one can evaluate the edge safety factor

$$q_{edge} = \frac{1}{2\pi} \oint_{edge} \frac{B_\phi}{RB_P} dl = \frac{1}{\pi} \sum_{j=1}^N \frac{B_{\phi,edge,j}}{R_0 x_{edge,j} B_{P,edge,j}} R_0 \Delta C_{p,j} \quad (\text{B.59})$$

where  $B_{\phi,edge} = B_\phi(x_{edge}, y_{edge})$ . It is possible to compute the complete safety factor profile by activating an option in the equilibrium generator. However, the recursive call to `contourc` considerably increases the computation time (at least by a factor 10). A last parameter can be computed, the so-called kink safety factor, given by [Cerfon and Freidberg 2010]

$$q_* = \varepsilon \frac{B_0}{\bar{B}_P} \quad (\text{B.60})$$

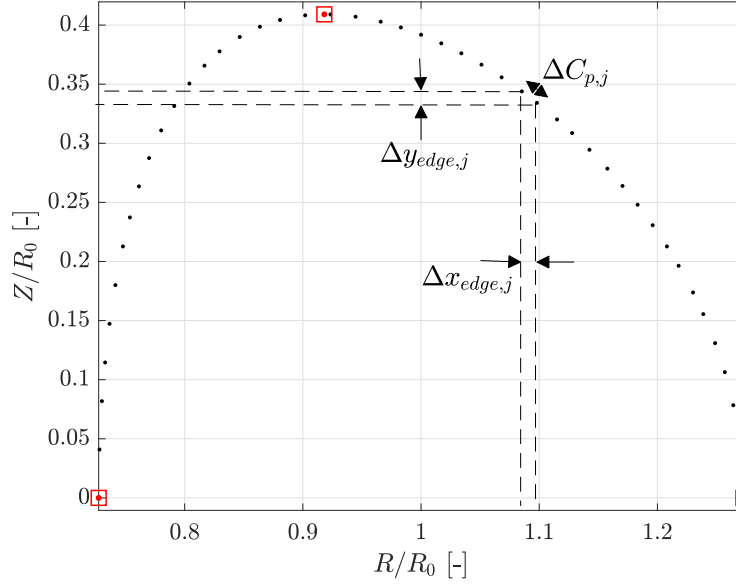


Figure B.2: Discrete contour of the plasma last closed flux surface used for volume and surface integration

## B.5 Verification with an ITER configuration

The code has been checked using an ITER-like equilibrium, as described in [Cerfon and Freidberg 2010]. The following inputs have been used

$$\begin{aligned}
 R_0 &= 6.20 \text{ [m]} \\
 a &= 1.98 \text{ [m]} \\
 \kappa &= 1.70 \text{ [-]} \\
 \delta &= 0.33 \text{ [-]} \\
 B_0 &= 5.30 \text{ [T]} \\
 \frac{dp}{d\psi_{P,n}} &= 1.1528\text{e6 [Pa]} \\
 R_T &= 1.00 \text{ [-]} \\
 R_\nabla &= 1.00 \text{ [-]} \\
 R_{ed-ax} &= 0 \text{ [-]} \\
 n_{axis} &= 5\text{e20 [m}^{-3}\text{]} \\
 A &= -0.155 \text{ [-]}
 \end{aligned} \tag{B.61}$$

Results and comparisons are summarized in table B.1. A constraint has been set on  $\beta_T$  to find a good pressure gradient, which is instead an input in our model instead of the plasma current, which is an input in [Cerfon and Freidberg 2010]. In the end, a very good agreement is shown, with a relative difference less than 2% on the different parameters. This small difference may be due to the multiple numerical integration estimations that have been performed on a finite mesh in our local implementation of the equilibrium generator.

Table B.1: Comparison of outputs/inputs between the equilibrium generator and [Cerfon and Freidberg 2010]

Parameters	Local code	Cerfon	Relative gap
$\beta_T$ [-]	0.05	0.05	0.0 %
$C_p$ [-]	2.76	2.79	-1.1 %
$V_n$ [-]	0.52	0.53	-1.9 %
$I_p$ [MA]	14.87	15.00	-0.9 %
$q_*$ [-]	1.55	1.57	-1.3 %
$\bar{B}_p$ [T]	1.09	1.08	0.9 %

## B.6 LUKE equilibrium reconstruction

The analytic equilibrium has been generated in the  $(R, Z)$  coordinate system. It has to be turned into the  $(\psi, \theta)$  coordinate system in order to be used for LUKE/C3PO drift-kinetic Fokker-Planck simulations. Some definitions are slightly different in LUKE, in particular for  $x$ ,

## Appendix B. Analytic equilibrium generation

$y$  and  $\psi$ , leading to

$$x_{LUKE} = xR_0 - R_p \quad (B.62)$$

$$y_{LUKE} = yR_0 - Z_p \quad (B.63)$$

$$\psi_{P,n}^{LUKE} = \frac{\psi_{ax} - \psi}{\psi_{ax}} \quad (B.64)$$

where  $R_p$  and  $Z_p$  are the coordinates of the magnetic axis ( $R_p \neq R_0$ ). The conversion to  $(\psi, \theta)$  is made by an adaptation of the MATLAB® routine `rz2pt_jd.m` embedded in the LUKE suite. It uses  $x_{LUKE}(R, Z)$ ,  $y_{LUKE}(R, Z)$  and  $\psi_P^{LUKE}(R, Z)$  as inputs and gives  $(\psi_{P,n}, \theta)$ ,  $x_{LUKE}(\psi_{P,n}, \theta)$ ,  $y_{LUKE}(\psi_{P,n}, \theta)$ ,  $d\psi_{P,n}/dx(\psi_{P,n}, \theta)$  and  $d\psi_{P,n}/dy(\psi_{P,n}, \theta)$  as outputs. In LUKE, the normalization of the magnetic flux in Weber is given by  $\psi_a^{LUKE} = -\psi_{ax}\psi_{P,0}$ . The poloidal magnetic field components (in Tesla) are thus given by

$$B_R(\psi_{P,n}, \theta) = -\frac{\psi_a^{LUKE}}{x_{LUKE} + R_p} \frac{d\psi_{P,n}}{dy}, \quad (B.65)$$

$$B_Z(\psi_{P,n}, \theta) = \frac{\psi_a^{LUKE}}{x_{LUKE} + R_p} \frac{d\psi_{P,n}}{dx}. \quad (B.66)$$

The toroidal magnetic field, the pressure and the density and temperature profiles are computed exactly in the same way as for the equilibrium in  $(R, Z)$ . The only difference is the safety factor calculation

$$\begin{aligned} q(\psi) &= \int_{\theta=0}^{\theta=2\pi} \frac{r(\psi, \theta)}{R(\psi, \theta)} \frac{B_\phi(\psi, \theta)}{B_P(\psi, \theta)} \frac{d\theta}{2\pi \cos(\alpha)} \\ &= \sum_j \frac{r(\psi, \theta_j)}{x(\psi, \theta_j) + R_p} \frac{B_\phi(\psi, \theta_j)}{B_P(\psi, \theta_j)} \frac{\Delta\theta_j}{2\pi \cos(\alpha)} \end{aligned} \quad (B.67)$$

where  $r = \sqrt{x_{LUKE}^2 + y_{LUKE}^2}$  is the local minor radius,  $\Delta\theta_j = \theta_{i+1} - \theta_i$  and  $\alpha$  is the metric angle due to the non-circularity of the poloidal magnetic flux contours. This angle can be evaluated by

$$\tan \alpha = -\frac{1}{r} \frac{dr}{d\theta} \quad (B.68)$$

### B.7 Alternative inputs convenient for density fluctuation generation

Another version of the code has been developed in which the edge parameters can be tuned, so that it is possible to control the edge fluctuation parameters. In that case, plasma geometry is still an input ( $R_0$ ,  $a$ ,  $\kappa$  and  $\delta$ ). Other similar inputs are the magnetic field on axis  $B_0$ , pressure gradient  $dp/d\psi_{P,n}$ , the temperature ratio  $R_T$ , the logarithmic gradient ratio  $R_\nabla$ , the density on axis  $n_{axis}$  and the force-balance free parameter  $A$ . The new parameters to set are the edge pressure  $p_{edge}$ , the edge density  $n_{edge}$  and the power dependency in  $\psi$  of the density profile  $k$ . This fixes the pressure and density profiles, and the temperature profile is deduced from them.

# C Coordinate systems for describing phase space

## C.1 Description of the configuration space

In tokamaks, the configuration space can be described using many different coordinate systems. These systems are illustrated in figure C.1a), and described in details in [Decker and Peysson 2004]. LUKE conventions have been used in the following definitions.

A first coordinate system is the cylindrical coordinate system  $(R, Z, \phi)$ , where  $R$  is the tokamak major radius, or horizontal axis,  $Z$  is the vertical axis and  $\phi$  is the toroidal angle, such that the basis is direct. The position of the magnetic axis (in axisymmetric devices such as tokamaks) is given by  $(R_p, Z_p)$ . From this basis, it is possible to build a toroidal coordinate system  $(r, \theta, \phi)$

$$r = \sqrt{(R - R_p)^2 + (Z - Z_p)^2} \quad (\text{C.1})$$

$$\tan \theta = \frac{Z - Z_p}{R - R_p} \quad (\text{C.2})$$

with the minor radius  $r \in [0; +\infty[$  and the poloidal angle  $\theta \in [0; 2\pi]$ . It is interesting to note that the choice of  $\theta$  is just a convention, and that, in the equilibrium reconstruction code LIUQE,  $\theta^{LIUQE}$  is defined in the opposite direction than in LUKE (see figure C.1). In most of the cases, flux surfaces are not circular and  $r = r(\theta)$ . It is therefore convenient to define flux coordinates  $(\psi, s_\theta, \phi)$ , where  $s_\theta$  is the coordinate along the flux surface of flux  $\psi$ , and  $\mathbf{e}_\psi \cdot \mathbf{e}_{s_\theta} = 0$ . The  $(\mathbf{e}_\psi, \mathbf{e}_{s_\theta})$  set then corresponds to the  $(\mathbf{e}_r, \mathbf{e}_\theta)$  set locally tilted by an angle  $\alpha$ , the so-called metric angle. This metric angle is a function of both  $r$  and  $\theta$ , and can be defined as

$$\tan(\alpha) = -\frac{1}{r} \frac{\partial r}{\partial \theta} \quad (\text{C.3})$$

thus yielding

$$\begin{pmatrix} \mathbf{e}_\psi \\ \mathbf{e}_{s_\theta} \end{pmatrix} = \begin{pmatrix} \cos \alpha & -\sin \alpha \\ \sin \alpha & \cos \alpha \end{pmatrix} \cdot \begin{pmatrix} \mathbf{e}_r \\ \mathbf{e}_\theta \end{pmatrix}. \quad (\text{C.4})$$

It is common to use a hybrid system of coordinates  $(\psi, \theta, \phi)$ . To make shot-to-shot or even

## Appendix C. Coordinate systems for describing phase space

machine-to-machine comparison, the radial coordinate is often normalized. Here are some of the main definitions

$$\rho_{\psi_P} = \sqrt{\psi_P / \psi_P^{LCFS}} \quad (C.5)$$

$$\rho_{\psi_T} = \sqrt{\psi_T / \psi_T^{LCFS}} \quad (C.6)$$

$$\rho_V = \sqrt{V / V^{LCFS}} \quad (C.7)$$

$$\rho_G = r / r^{LCFS} \quad (C.8)$$

with  $\psi_P$  the poloidal magnetic flux,  $\psi_T$  the toroidal magnetic flux,  $V$  the plasma volume enclosed within a given flux surface and *LCFS* standing for last-closed flux surface.

### C.2 Description of the velocity space

Charged particles perform a helical movement along the magnetic field lines. In a Cartesian framework, the particle momentum can be written  $(p_x, p_y, p_z)$ . Assuming that the magnetic field is in the  $z$  direction, it is convenient to express the total momentum  $p = \sqrt{p_{\parallel}^2 + p_{\perp}^2}$ , with  $p_{\parallel} = p_z$  and  $p_{\perp} = \sqrt{p_x^2 + p_y^2}$ . This is described in figure C.1b). To complete the description of the particle momentum, one can specify the gyro-angle  $\varphi$ , defined by  $\tan \varphi = p_y / p_x$ . Thus, the basis  $(p_{\parallel}, p_{\perp}, \varphi)$  can be built with  $p_{\parallel} \in ]-\infty; +\infty[$ ,  $p_{\perp} \in [0; +\infty[$  and  $\varphi \in [0; 2\pi]$ . This system is perfectly adapted to treat the particle helical motion. An alternative system consists of expressing the pitch-angle cosine as  $\xi = p_{\parallel} / p$  to use the  $(p, \xi, \varphi)$  system, with  $p \in [0; +\infty[$  and  $\xi \in [-1; 1]$ .

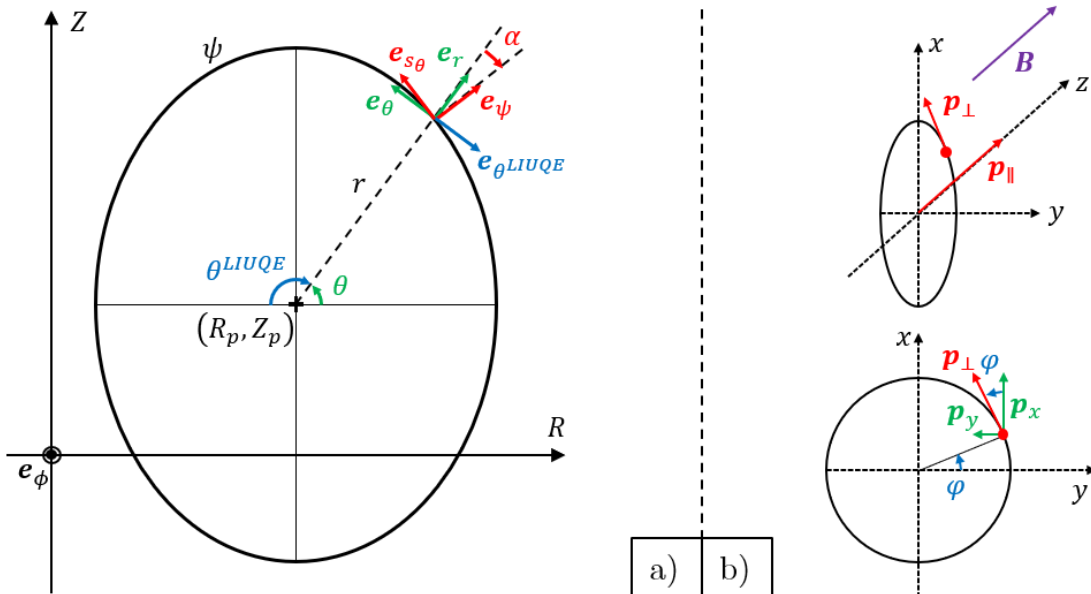


Figure C.1: Description of the different coordinate systems for describing configuration space a) and velocity space b).

## D Polarization for 2D ECCD configurations in COMSOL

In ECCD, the Electron-Cyclotron wave polarization is no longer linear but elliptic in the plane perpendicular to the wave propagation direction. This elliptic polarization is illustrated in figure D.1, in the Cartesian frame  $(x_p, y_p, z_p)$  attached to the wavevector  $\mathbf{k}$ , which points in the  $z_p$ -direction. The wave electric field is decomposed in a major-axis  $\mathbf{E}_M$  and a minor-axis  $\mathbf{E}_m$  components, which are  $90^\circ$  out of phase:  $\mathbf{E} = \mathbf{E}_M + \mathbf{E}_m$  [Prater 2004]. The ellipticity is given by the angle  $\beta_p$ , leading to  $|E_m| = |\tan(\beta_p)| |E_M|$  or, by taking into account the phase shift, to  $E_m = |\tan(\beta_p)| E_M \exp(i\pi/2)$ , where  $E_M$  and  $E_m$  are the complex components of the Gaussian electric field (amplitude and phase). For  $\beta_p = 0$ , the polarization is linear, while for  $\beta_p = \pi/4$  the polarization is circular. The major-axis electric field relates to the norm of the total electric field  $E$  as

$$|E_M| = \sqrt{\frac{|E|^2}{|\tan(\beta_p)|^2 + 1}}. \quad (\text{D.1})$$

The ellipse can be tilted by an angle  $-\pi/2 \leq \alpha_p \leq \pi/2$  with respect to the initial frame  $(x_p, y_p, z_p)$ . Therefore, the electric field projected on  $(x_p, y_p)$  gives

$$\begin{aligned} E_{x_p} &= -E_m \sin(|\alpha_p|) - E_M \cos(|\alpha_p|), \\ E_{y_p} &= -E_m \cos(|\alpha_p|) + E_M \sin(|\alpha_p|). \end{aligned} \quad (\text{D.2})$$

The angles  $\alpha_p$  and  $\beta_p$  are computed at the launcher entrance by the MATLAB® routine `pol3d.m`, called by the `ox_fraction.m` program.

To perform COMSOL simulations of 2D ECCD cases, as is done in chapter 5, it is necessary to project the electric field at the launcher mirror onto the COMSOL Cartesian frame  $(X, Y, Z)$ . This frame is illustrated in figure D.2. It is assumed that the beam propagates in the  $(X, Y)$  plane. The vertical axis  $Z$  coincides with the axis  $y_p$  and the axis  $x_p$  is in the  $(X, Y)$ -plane. The wave launching point position  $(X_M, Y_M)$  is known. The ECCD angle  $\theta_0$ , which is the angle between the wavevector  $\mathbf{k}$  and the plasma magnetic field  $\mathbf{B}$ , can be extracted from C3PO/LUKE simulations, or roughly estimated as  $\theta_0 = \pi/2 - \alpha - \beta$ , by neglecting the poloidal component magnetic field. The projection angle for the wave electric field is  $\vartheta = \theta_0 + \beta = \pi/2 - \alpha$ , assuming

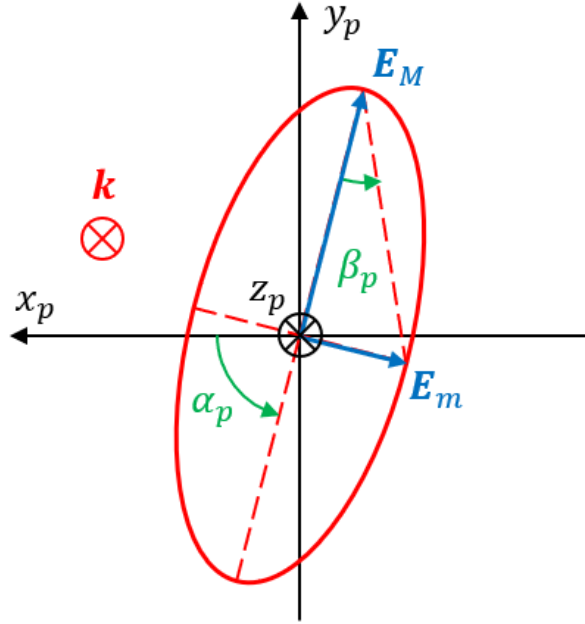


Figure D.1: Electron-Cyclotron wave polarization in the case of oblique propagation with respect to the magnetic field. The wave electric field is perpendicular to the propagation direction. Here the situation corresponds to negative  $\alpha_p$  and  $\beta_p$ .

the wave propagates in a straight line before it reaches the last closed flux surface (LCFS), which is true in vacuum. For the cases studies in chapter 5, it is also assumed that the wave polarization does not change from the launcher entrance to the plasma entrance, as, until there, the wave propagates in the horizontal  $(X, Y)$  plane. The electric field component  $E_Z$  is directly equal to  $E_{y_p}$ , while  $E_{x_p}$  needs to be projected in  $(X, Y)$ . For the case depicted in figure D.1, this leads to

$$\begin{aligned} E_X &= \frac{|E_M|}{E_0} E \left[ |\tan(\beta_p)| \sin(|\alpha_p|) \exp\left(i\frac{\pi}{2}\right) + \cos(|\alpha_p|) \right] \cos(\vartheta), \\ E_Y &= \frac{|E_M|}{E_0} E \left[ |\tan(\beta_p)| \sin(|\alpha_p|) \exp\left(i\frac{\pi}{2}\right) + \cos(|\alpha_p|) \right] \sin(\vartheta), \\ E_Z &= \frac{|E_M|}{E_0} E \left[ -|\tan(\beta_p)| \cos(|\alpha_p|) \exp\left(i\frac{\pi}{2}\right) + \sin(|\alpha_p|) \right], \end{aligned} \quad (\text{D.3})$$

since  $\mathbf{e}_{x_p} = -\cos(\vartheta)\mathbf{e}_X - \sin(\vartheta)\mathbf{e}_Y$ . Here,  $E$  is the complex Gaussian beam electric field, as described by equation 3.5.

Finally, it is also possible to determine the position of the beam at the plasma LCFS  $(X_0, Y_0)$ , as well as the angle  $\beta$ . The propagation from the mirror position  $(X_M, Y_M)$  to the plasma LCFS  $(X_0, Y_0)$  is parametrized by a straight line

$$Y = aX + b = -|\tan^{-1}(\alpha)|X + (Y_M + |\tan^{-1}(\alpha)|X_M). \quad (\text{D.4})$$

The position of the beam at the LCFS is therefore given by solving the system of equation

$$\begin{cases} X_0^2 + Y_0^2 = R_{LCFS}^2 \\ Y_0 = aX_0 + b \end{cases} \quad (D.5)$$

which yields  $\beta = \sin^{-1}(Y_0/R_{LCFS})$ .

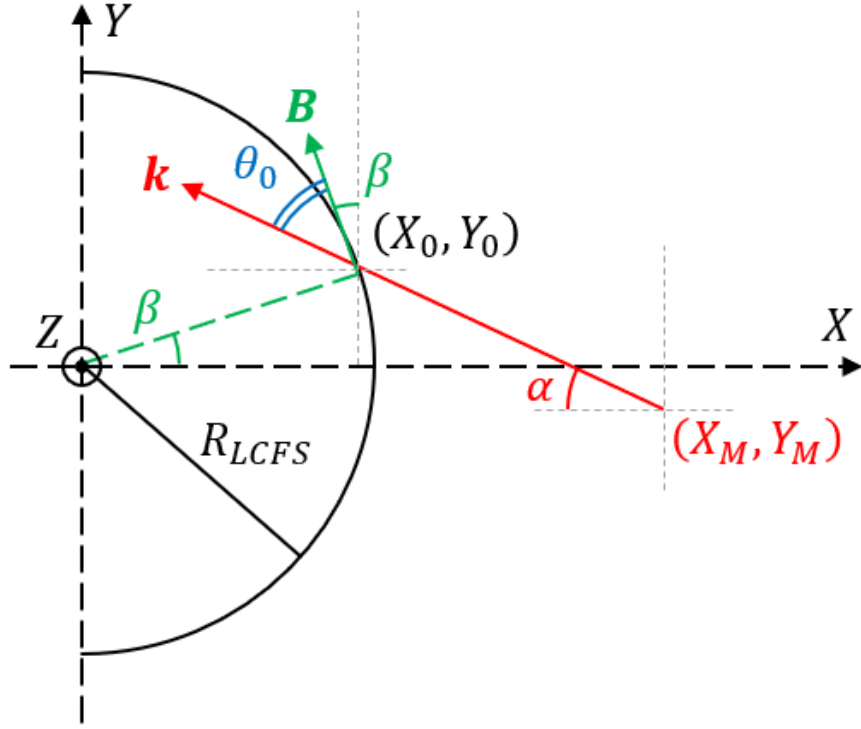


Figure D.2: Top view of TCV in COMSOL Cartesian frame  $(X, Y, Z)$ .





## Bibliography

- [COMSOL] COMSOL RF Module User's Guide, version 5.4. – URL <https://doc.comsol.com/5.4/doc/com.comsol.help.rf/RFModuleUsersGuide.pdf>
- [Albajar et al. 2006] ALBAJAR, F ; BERTELLI, N ; BORNATICI, M ; ENGELMANN, F: Electron-cyclotron absorption in high-temperature plasmas: quasi-exact analytical evaluation and comparative numerical analysis. In: *Plasma Physics and Controlled Fusion* 49 (2006), nov, 1, 15–29. – URL <https://doi.org/10.1088/0741-3335/49/1/002>
- [Alberti et al. 2017] ALBERTI, S. ; GENOUD, J. ; GOODMAN, T. ; HOGGE, J.-P. ; PORTE, L. ; SILVA, M. ; TRAN, T.-M. ; TRAN, M.-Q. ; AVRAMIDIS, K. ; PAGONAKIS, I. ; JIN, J. ; ILLY, S. ; GANTENBEIN, G. ; JELONNEK, J. ; THUMM, M. ; BIN, W. ; BRUSCHI, A. ; GARAVAGLIA, S. ; MORO, A. ; KASPAREK, W. ; LEGRAND, F. ; PERIAL, E. ; ROZIER, Y. ; CISMONTI, F. ; DOELMAN, N.: Recent progress in the upgrade of the TCV EC-system with two 1MW/2s dual-frequency (84/126GHz) gyrotrons. In: *EPJ Web Conf.* 157 (2017), 03001. – URL <https://doi.org/10.1051/epjconf/201715703001>
- [Anton et al. 1996] ANTON, M ; WEISEN, H ; DUTCH, M J. ; LINDEN, W von der ; BUHLMANN, F ; CHAVAN, R ; MARLETAZ, B ; MARMILLOD, P ; PARIS, P: X-ray tomography on the TCV tokamak. In: *Plasma Physics and Controlled Fusion* 38 (1996), 11, 1849–1878. – URL <https://doi.org/10.1088/0741-3335/38/11/1849>
- [Arnichand et al. 2019] ARNICHAND, H. ; ANDREBE, Y. ; BLANCHARD, P. ; ANTONIONI, S. ; COUTURIER, S. ; DECKER, J. ; DUVAL, B.P. ; FELICI, F. ; GALPERTI, C. ; ISOZ, P.-E. ; LAVANCHY, P. ; LLOBET, X. ; MARLÉTAZ, B. ; MARMILLOD, P. ; MASUR, J.: New capabilities of the incoherent Thomson scattering diagnostics in the TCV tokamak: divertor and real-time measurements. In: *Journal of Instrumentation* 14 (2019), sep, 09, C09013. – URL <https://dx.doi.org/10.1088/1748-0221/14/09/C09013>
- [Atanasiu et al. 2004] ATANASIU, C. V. ; GÜNTER, S. ; LACKNER, K. ; MIRON, I. G.: Analytical solutions to the Grad–Shafranov equation. In: *Physics of Plasmas* 11 (2004), 7, 3510–3518. – URL <https://doi.org/10.1063/1.1756167>
- [Aydemir et al. 2019] AYDEMIR, A. Y. ; PARK, B. H. ; HAN, K. S.: Exact Solov'ev equilibrium with an arbitrary boundary. In: *Physics of Plasmas* 26 (2019), 11, 112503. – URL <https://doi.org/10.1063/1.5124138>

## Bibliography

---

- [Barbui et al. 2021] BARBUI, T. ; DELGADO-APARICIO, L. F. ; PABLANT, N. ; DISCH, C. ; LUETHI, B. ; PILET, N. ; STRATTON, B. ; VANMETER, P.: Multi-energy calibration of a PILATUS3 CdTe detector for hard x-ray measurements of magnetically confined fusion plasmas. In: *Review of Scientific Instruments* 92 (2021), 2, 023105. – URL <https://doi.org/10.1063/5.0040571>
- [Berenger 1996] BERENGER, J. ...: Perfectly matched layer for the FDTD solution of wave-structure interaction problems. In: *IEEE Transactions on Antennas and Propagation* 44 (1996), 1, 110–117
- [Bertelli et al. 2010] BERTELLI, N. ; BALAKIN, A. A. ; WESTERHOF, E. ; GARCIA, O. E. ; NIELSEN, A. H. ; NAULIN, V.: The influence of the edge density fluctuations on electron cyclotron wave beam propagation in tokamaks. In: *Journal of Physics: Conference Series* 26 (2010), 012002. – URL <https://doi.org/10.1088%2F1742-6596%2F260%2F1%2F012002>
- [Bertelli and Westerhof 2009] BERTELLI, N. ; WESTERHOF, E.: Consequences of finite transport on the effectiveness of ECCD for neoclassical tearing mode stabilization in ITER. In: *Nuclear Fusion* 49 (2009), 9, 095018. – URL <https://doi.org/10.1088%2F0029-5515%2F49%2F9%2F095018>
- [Beurskens et al. 2021a] BEURSKENS, M.N.A. ; ANGIONI, C. ; BOZHENKOV, S. A. ; FORD, O. ; KIEFER, C. ; XANTHOPOULOS, P. ; TURKIN, Y. ; ALCUSÓN, J.A. ; BAEHNER, J.P. ; BEIDLER, C. ; BIRKENMEIER, G. ; FABLE, E. ; FUCHERT, G. ; GEIGER, B. ; GRULKE, O. ; HIRSCH, M. ; JAKUBOWSKI, M. ; LAQUA, H.P. ; LANGENBERG, A. ; LAZERSON, S. ; PABLANT, N. ; REISNER, M. ; SCHNEIDER, P. ; SCOTT, E.R. ; STANGE, T. ; STECHOW, A. von ; STOBER, J. ; STROTH, U. ; WEGNER, Th. ; WEIR, G. ; ZHANG, D. ; ZOCCO, A. ; WOLF, R.C. ; ZOHM, H. ; W7-X TEAM the ; ASDEX UPGRADE TEAM the ; EUROFUSION MST1 TEAM the: Confinement in electron heated plasmas in Wendelstein 7-X and ASDEX Upgrade; the necessity to control turbulent transport. In: *Nuclear Fusion* 62 (2021), dec, 1, 016015. – URL <https://dx.doi.org/10.1088/1741-4326/ac36f1>
- [Beurskens et al. 2021b] BEURSKENS, M.N.A. ; BOZHENKOV, S.A. ; FORD, O. ; XANTHOPOULOS, P. ; ZOCCO, A. ; TURKIN, Y. ; ALONSO, A. ; BEIDLER, C. ; CALVO, I. ; CARRALERO, D. ; ESTRADA, T. ; FUCHERT, G. ; GRULKE, O. ; HIRSCH, M. ; IDA, K. ; JAKUBOWSKI, M. ; KILLER, C. ; KRYCHOWIAK, M. ; KWAK, S. ; LAZERSON, S. ; LANGENBERG, A. ; LUNSFORD, R. ; PABLANT, N. ; PASCH, E. ; PAVONE, A. ; REIMOLD, F. ; ROMBA, Th. ; STECHOW, A. von ; SMITH, H.M. ; WINDISCH, T. ; YOSHINUMA, M. ; ZHANG, D. ; WOLF, R.C. ; W7-X TEAM the: Ion temperature clamping in Wendelstein 7-X electron cyclotron heated plasmas. In: *Nuclear Fusion* 61 (2021), oct, 11, 116072. – URL <https://doi.org/10.1088/1741-4326/ac1653>
- [Bigot 2022] BIGOT, B.: Preparation for assembly and commissioning of ITER. In: *Nuclear Fusion* 62 (2022), jan, 4, 042001. – URL <https://dx.doi.org/10.1088/1741-4326/ac168f>
- [Blanchard et al. 2019] BLANCHARD, P. ; ANDREBE, Y. ; ARNICHAND, H. ; AGNELLO, R. ; ANTONIONI, S. ; COUTURIER, S. ; DECKER, J. ; D`EXAERDE, T. De K. ; DUVAL, B.P. ; FURNO, I. ; ISOZ,

- P.-F. ; LAVANCHY, P. ; LLOBET, X. ; MARLÉTAZ, B. ; MASUR, J.: Thomson scattering measurements in the divertor region of the TCV Tokamak plasmas. In: *Journal of Instrumentation* 14 (2019), oct, 10, C10038–C10038. – URL <https://doi.org/10.1088/1748-0221/14/10/c10038>
- [Bornatici et al. 1983] BORNATICI, M. ; CANO, R. ; BARBIERI, O. D. ; ENGELMANN, F.: Electron cyclotron emission and absorption in fusion plasmas. In: *Nuclear Fusion* 23 (1983), 9, 1153–1257. – URL <https://doi.org/10.1088/0029-5515%2F23%2F9%2F005>
- [Braams and Karney 1989] BRAAMS, Bastiaan J. ; KARNEY, Charles F. E.: Conductivity of a relativistic plasma. In: *Physics of Fluids B: Plasma Physics* 1 (1989), 7, 1355–1368. – URL <https://doi.org/10.1063/1.858966>
- [Brookman et al. 2017] BROOKMAN, M. W. ; AUSTIN, M. E. ; GENTLE, K. W. ; PETTY, C. C. ; ERNST, D. E. ; PEYSSON, Y. ; DECKER, J. ; BARADA, K.: Experimental Measurement of ECH Deposition Broadening: Beyond Anomalous Transport. In: *EPJ Web Conf.* 147 (2017), 03001. – URL <https://doi.org/10.1051/epjconf/201714703001>
- [Brookman et al. 2021] BROOKMAN, M. W. ; AUSTIN, M. E. ; PETTY, C. C. ; LA HAYE, R. J. ; BARADA, K. ; RHODES, T. L. ; YAN, Z. ; KÖHN, A. ; THOMAS, M. B. ; LEDDY, J. ; VANN, R. G. L.: Resolving ECRH deposition broadening due to edge turbulence in DIII-D. In: *Physics of Plasmas* 28 (2021), 4, 042507. – URL <https://doi.org/10.1063/1.5140992>
- [Brookman et al. 2023] BROOKMAN, Michael ; HOLLAND, Lou ; THOMAS, Matthew B. ; AUSTIN, Max E. ; BARADA, Kshitish K. ; GENTLE, Kenneth W. ; LA HAYE, Robert J. ; LEDDY, Jarrod ; PETTY, Craig ; RHODES, Terry L. ; YAN, Z. ; VANN, Roddy G. L. ; KÖHN-SEEMANN, Alf: Broadening of microwave heating beams in the DIII-D tokamak by edge turbulence. In: *Nuclear Fusion* (2023). – URL <http://iopscience.iop.org/article/10.1088/1741-4326/acbb8e>
- [Cao et al. 2020] CAO, Hong-Rui ; WANG, Hai-Xiang ; ZHENG, Ying-Ying ; LIU, Shi-Xing ; ZHAO, Jin-Long ; ZHANG, Ji-Zong ; LIN, Shi-Yao ; HU, Li-Qun: Development of Digital Multi-channel and Time-division Pulse Height Analyzer Based on PXIE Bus for Hard X-ray Diagnostic in East. In: *Instruments and Experimental Techniques* 63 (2020), Oktober, 4, 453–460. – URL <https://doi.org/10.1134/S002044122004003X>. – ISSN 1608-3180
- [Cardinali et al. 2007] CARDINALI, A. ; MORINI, L. ; CASTALDO, C. ; CESARIO, R. ; ZONCA, E.: Analysis of the validity of the asymptotic techniques in the lower hybrid wave equation solution for reactor applications. In: *Physics of Plasmas* 14 (2007), 11, 11. – URL <https://doi.org/10.1063/1.2805435>. – 112506. – ISSN 1070-664X
- [Cardozo 1995] CARDOZO, N J L.: Perturbative transport studies in fusion plasmas. In: *Plasma Physics and Controlled Fusion* 37 (1995), 8, 799–852. – URL <https://doi.org/10.1088/0029-5515%2F37%2F8%2F001>
- [Carter 2006] CARTER, T. A.: Intermittent turbulence and turbulent structures in a linear magnetized plasma. In: *Physics of Plasmas* 13 (2006), 1, 010701. – URL <https://doi.org/10.1063/1.2158929>

## Bibliography

---

- [Cazabonne et al. 2021] CAZABONNE, J. ; CODA, S. ; DECKER, J. ; PEYSSON, Y.: Scattering of electron-cyclotron waves by plasma density fluctuations in tokamaks. In: *Proceedings of the 47th Conference on Plasma Physics (EPS), Stiges (Spain)* (2021). – URL <http://ocs.ciemat.es/eps2021pap/pdf/P1.1061.pdf>
- [Cazabonne et al. 2022] CAZABONNE, J. ; CODA, S. ; DECKER, J. ; PEYSSON, Y.: Investigation of suprathermal electron transport induced by Electron-Cyclotron waves in tokamak plasmas. In: *Proceedings of the 48th Conference on Plasma Physics (EPS), Maastricht (Netherlands)* (2022). – URL [https://indico.fusenet.eu/event/28/contributions/289/attachments/303/760/Paper\\_EPS\\_2022\\_JCazabonne.pdf](https://indico.fusenet.eu/event/28/contributions/289/attachments/303/760/Paper_EPS_2022_JCazabonne.pdf)
- [Cazabonne et al. 2023] CAZABONNE, J. ; DONNEL, P. ; CODA, S. ; DECKER, J. ; GIANNATALE, G. D. ; IANTCHENKO, A. ; KUMAR, U. ; PEYSSON, Y. ; PORTE, L. ; RIENÄCKER, S. ; TEMA-BIWOLE, A. ; VILLARD, L. ; TCV TEAM the: Experimental and numerical investigations of electron transport enhancement by electron-cyclotron plasma-wave interaction in tokamaks. In: *Plasma Physics and Controlled Fusion* 65 (2023), sep, 10, 104001. – URL <https://dx.doi.org/10.1088/1361-6587/acf39c>
- [Cerfon and Freidberg 2010] CERFON, Antoine J. ; FREIDBERG, Jeffrey P.: “One size fits all” analytic solutions to the Grad–Shafranov equation. In: *Physics of Plasmas* 17 (2010), 3, 032502. – URL <https://doi.org/10.1063/1.3328818>
- [Chellaï 2019] CHELLAÏ, O.: *Millimeter-Wave Beam Scattering by Edge Turbulence in Magnetically-Confined Plasmas*, École Polytechnique Fédérale de Lausanne, Dissertation, 2019
- [Chellaï et al. 2018a] CHELLAÏ, O. ; ALBERTI, S. ; BAQUERO-RUIZ, M. ; FURNO, I. ; GOODMAN, T. ; LABIT, B. ; MAJ, O. ; RICCI, P. ; RIVA, F. ; GUIDI, L. ; POLI, E.: Millimeter-wave beam scattering by edge-plasma density fluctuations in TCV. In: *Plasma Physics and Controlled Fusion* 61 (2018), 1, 014001. – URL <https://doi.org/10.1088%2F1361-6587%2Faae7bf>
- [Chellaï et al. 2018b] CHELLAÏ, O. ; ALBERTI, S. ; BAQUERO-RUIZ, M. ; FURNO, I. ; GOODMAN, T. ; MANKE, F. ; PLYUSHCHEV, G. ; GUIDI, L. ; KOEHN, A. ; MAJ, O. ; POLI, E. ; HIZANIDIS, K. ; FIGINI, L. ; RICCI, D.: Millimeter-Wave Beam Scattering by Field-Aligned Blobs in Simple Magnetized Toroidal Plasmas. In: *Phys. Rev. Lett.* 120 (2018), 105001. – URL <https://link.aps.org/doi/10.1103/PhysRevLett.120.105001>
- [Chellaï et al. 2021] CHELLAÏ, O. ; ALBERTI, S. ; FURNO, I. ; GOODMAN, T. ; MAJ, O. ; MERLO, G. ; POLI, E. ; RICCI, P. ; RIVA, F. ; WEBER, H.: Millimeter-wave beam scattering and induced broadening by plasma turbulence in the TCV tokamak. In: *Nuclear Fusion* 61 (2021), apr, 6, 066011. – URL <https://doi.org/10.1088/1741-4326/abf43f>
- [Choi 2020] CHOI, D.: *Experimental analysis of suprathermal electrons generated by electron-cyclotron waves in tokamak plasmas*, École Polytechnique Fédérale de Lausanne, Dissertation, 2020

- [Choi et al. 2020a] CHOI, D ; CODA, S ; DECKER, J ; CAZABONNE, J A. ; PEYSSON, Y: Study of suprathermal electron dynamics during electron cyclotron current drive using hard x-ray measurements in the TCV tokamak. In: *Plasma Physics and Controlled Fusion* 62 (2020), sep, 11, 115012. – URL <https://doi.org/10.1088/1361-6587/abb0d3>
- [Choi et al. 2020b] CHOI, D. ; CODA, S. ; DECKER, J. ; PEYSSON, Y.: Modeling of the response function of CdTe detectors for a hard X-ray synthetic diagnostic. In: *Fusion Engineering and Design* 159 (2020), 111733. – URL <http://www.sciencedirect.com/science/article/pii/S0920379620302817>. – ISSN 0920-3796
- [Choi et al. 2019] CHOI, D. ; MERLE, A. ; CODA, S. ; DECKER, J. ; GRAVES, J. P. ; BIWOLE, A. S. T. ; PORTE, L. ; PEYSSON, Y.: Suprathermal electron driven fishbone instability in the TCV tokamak. In: *Plasma Physics and Controlled Fusion* 62 (2019), 2, 025006. – URL <https://doi.org/10.1088%2F1361-6587%2Fab5147>
- [Choudhary and Felsen 1973] CHOUDHARY, S. ; FELSEN, L.: Asymptotic theory for inhomogeneous waves. In: *IEEE Transactions on Antennas and Propagation* 21 (1973), 6, 827–842
- [Coda et al. 2019] CODA, S. et al.: Physics research on the TCV tokamak facility: from conventional to alternative scenarios and beyond. In: *Nuclear Fusion* 59 (2019), 11, 112023. – URL <https://doi.org/10.1088%2F1741-4326%2Fab25cb>
- [Coda et al. 2003a] CODA, S. ; ALBERTI, S. ; BLANCHARD, P. ; GOODMAN, T. P. ; HENDERSON, M. A. ; NIKKOLA, P. ; PEYSSON, Y. ; SAUTER, O.: Electron cyclotron current drive and suprathermal electron dynamics in the TCV tokamak. In: *Nuclear Fusion* 43 (2003), 11, 1361–1370. – URL <https://doi.org/10.1088%2F0029-5515%2F43%2F11%2F008>
- [Coda et al. 2003b] CODA, S. ; ALBERTI, S. ; BLANCHARD, P. ; KLIMANOV, I. ; MORET, J.-M. ; WEBER, P.: Dynamical studies of suprathermal electron relaxation by modulated ECCD. In: *30th EPS Conf. on Controlled Fusion and Plasma Physics (St. Petersburg, Russia)* 27A (ECA) (2003), P–3.134
- [Coda et al. 2006] CODA, S. ; KLIMANOV, I. ; ALBERTI, S. ; ARNOUX, G. ; BLANCHARD, P. ; FASOLI, A. ; TCV TEAM the: The effect of ECRH on the electron velocity distribution function. In: *Plasma Physics and Controlled Fusion* 48 (2006), 12B, B359–B369. – URL <https://doi.org/10.1088%2F0741-3335%2F48%2F12b%2Fs33>
- [Cox et al. 1993] COX, M ; DELIYANAKIS, N ; HUGILL, J ; ROBINSON, D.C ; ASHRAF, M ; FIELDING, S.J ; LEAN, H.W ; MANTICA, P ; MILLAR, W ; O'BRIEN, M.R ; PARHAM, B.J ; PITTS, R.A ; SIMONETTO, A ; VAYAKIS, G: Thermal wave studies of electron transport using modulated ECRH. In: *Nuclear Fusion* 33 (1993), nov, 11, 1657–1676. – URL <https://doi.org/10.1088/0029-5515/33/11/i07>
- [Dal Molin et al. 2021] DAL MOLIN, A. ; FUMAGALLI, L. ; NOCENTE, M. ; RIGAMONTI, D. ; TARDOCCHI, M. ; GIACOMELLI, L. ; PANONTIN, E. ; LVOVSKIY, A. ; PAZ-SOLDAN, C. ; EDIETIS,

## Bibliography

---

- N. W. ; GORINI, G.: Novel compact hard x-ray spectrometer with MCps counting rate capabilities for runaway electron measurements on DIII-D. In: *Review of Scientific Instruments* 92 (2021), 4, 043517. – URL <https://doi.org/10.1063/5.0043762>
- [DeBoo et al. 2012] DEBOO, J. C. ; PETTY, C. C. ; WHITE, A. E. ; BURRELL, K. H. ; DOYLE, E. J. ; HILLESHEIM, J. C. ; HOLLAND, C. ; MCKEE, G. R. ; RHODES, T. L. ; SCHMITZ, L. ; SMITH, S. P. ; WANG, G. ; ZENG, L.: Electron profile stiffness and critical gradient studies. In: *Physics of Plasmas* 19 (2012), 8, 082518. – URL <https://doi.org/10.1063/1.4750061>
- [Decker and Peysson 2004] DECKER, J. ; PEYSSON, Y.: DKE: a fast numerical solver for the 3-D relativistic bounce-averaged electron Drift Kinetic Equation / Rep. EUR-CEA-FC-1736. 2004. – Forschungsbericht
- [Decker et al. 2012] DECKER, J. ; PEYSSON, Y. ; CODA, S.: Effect of density fluctuations on ECCD in ITER and TCV. In: *EPJ Web of Conferences* 32 (2012), 01016
- [Donnel et al. 2021] DONNEL, P. ; CAZABONNE, J. ; VILLARD, L. ; BRUNNER, S. ; CODA, S. ; DECKER, J. ; MURUGAPPAN, M. ; SADR, M.: Quasilinear treatment of wave–particle interactions in the electron cyclotron range and its implementation in a gyrokinetic code. In: *Plasma Physics and Controlled Fusion* 63 (2021), apr, 6, 064001. – URL <https://doi.org/10.1088/1361-6587/abf53f>
- [Donnel et al. 2022] DONNEL, P. ; FONTANA, J-B. ; CAZABONNE, J. ; VILLARD, L. ; BRUNNER, S. ; CODA, S. ; DECKER, J. ; PEYSSON, Y.: Electron-cyclotron resonance heating and current drive source for flux-driven gyrokinetic simulations of tokamaks. In: *Plasma Physics and Controlled Fusion* 64 (2022), jul, 9, 095008. – URL <https://doi.org/10.1088/1361-6587/ac7974>
- [Donnel et al. 2020] DONNEL, P. ; GHELLER, C. ; BRUNNER, S. ; VILLARD, L. ; LANTI, E. ; OHANA, N. ; MURUGAPPAN, M.: Moment approach of the multi-species non-linear Coulomb collision operator adapted to particle-in-cell codes. In: *Plasma Physics and Controlled Fusion* 63 (2020), dec, 2, 025006. – URL <https://dx.doi.org/10.1088/1361-6587/abc92b>
- [Eyring et al. 2021] EYRING, V. ; GILLETT, N.P. ; RAO, K.M. A. ; BARIMALALA, R. ; PARRILLO, M. B. ; BELLOUIN, N. ; CASSOU, C. ; DURACK, P.J. ; KOSAKA, Y. ; MCGREGOR, S. ; MIN, S. ; MORGENSTERN, O. ; ; SUN, Y.: *Climate Change 2021: The Physical Science Basis. Contribution of Working Group I to the Sixth Assessment Report of the Intergovernmental Panel on Climate Change*. Kap. 2021: Human Influence on the Climate System, 423–552, Cambridge University Press, 2021
- [Farina 2007] FARINA, Daniela: A Quasi-Optical Beam-Tracing Code for Electron Cyclotron Absorption and Current Drive: GRAY. In: *Fusion Science and Technology* 52 (2007), 2, 154–160. – URL <https://doi.org/10.13182/FST07-A1494>
- [Federici et al. 2014] FEDERICI, G. ; KEMP, R. ; WARD, D. ; BACHMANN, C. ; FRANKE, T. ; GONZALEZ, S. ; LOWRY, C. ; GADOMSKA, M. ; HARMAN, J. ; MESZAROS, B. ; MORLOCK, C. ; ROMANELLI, F. ; WENNINGER, R.: Overview of EU DEMO design and R&D

- activities. In: *Fusion Engineering and Design* 89 (2014), 7, 882–889. – URL <https://www.sciencedirect.com/science/article/pii/S0920379614000714>. – Proceedings of the 11th International Symposium on Fusion Nuclear Technology-11 (ISFNT-11) Barcelona, Spain, 15-20 September, 2013. – ISSN 0920-3796
- [Figini et al. 2012] FIGINI, L ; DECKER, J ; FARINA, D ; MARUSHCHENKO, N B. ; PEYSSON, Y ; POLI, E ; WESTERHOF, E ; CONTRIBUTORS, ITM-TF: Benchmarking of electron cyclotron heating and current drive codes on ITER scenarios within the European Integrated Tokamak Modelling framework. In: *EPJ Web of Conferences* 32 (2012), 01011. – URL <https://doi.org/10.1051/epjconf/20123201011>
- [Fontana et al. 2017] FONTANA, M. ; PORTE, L. ; MOLINA CABRERA, P.: Correlation electron cyclotron emission diagnostic in TCV. In: *Review of Scientific Instruments* 88 (2017), 8, 083506. – URL <https://doi.org/10.1063/1.4997075>
- [Frei 2015] FREI, W.: *Using perfectly matched layers and scattering boundary conditions for wave electromagnetics problems*. January 2015
- [Gambier et al. 1990] GAMBIER, D.J. ; EVRARD, M.P. ; ADAM, J. ; BECOULET, A. ; CORTI, S. ; HENNEQUIN, P. ; JACQUINOT, J. ; START, D.E.H. ; THOMSEN, K. ; TUBBING, B.J.D. ; ZANZA, V.: ICRF power deposition profile and determination of the electron thermal diffusivity by modulation experiments in JET. In: *Nuclear Fusion* 30 (1990), jan, 1, 23–34. – URL <https://doi.org/10.1088/0029-5515/30/1/003>
- [Gamov and Critchfield 1949] GAMOV, G. ; CRITCHFIELD, C. L.: *Theory of the atomic nucleus and nuclear energy source*. Oxford University Press, 1949
- [Garbet et al. 2004a] GARBET, X ; MANTICA, P ; ANGIONI, C ; ASP, E ; BARANOV, Y ; BOURDELLE, C ; BUDNY, R ; CRISANTI, F ; CORDEY, G ; GARZOTTI, L ; KIRNEVA, N ; HOGWEIJ, D ; HOANG, T ; IMBEAUX, F ; JOFFRIN, E ; LITAUDON, X ; MANINI, A ; McDONALD, D C. ; NORDMAN, H ; PARAIL, V ; PEETERS, A ; RYTER, F ; SOZZI, C ; VALOVIC, M ; TALA, T ; THYAGARAJA, A ; VOITSEKHOVITCH, I ; WEILAND, J ; WEISEN, H ; ZABOLOTSKY, A ; JET EFDA CONTRIBUTORS the: Physics of transport in tokamaks. In: *Plasma Physics and Controlled Fusion* 46 (2004), nov, 12B, B557–B574. – URL <https://doi.org/10.1088/0741-3335/46/9/002>
- [Garbet et al. 2004b] GARBET, X ; MANTICA, P ; RYTER, F ; CORDEY, G ; IMBEAUX, F ; SOZZI, C ; MANINI, A ; ASP, E ; PARAIL, V ; WOLF, R ; JET EFDA CONTRIBUTORS the: Profile stiffness and global confinement. In: *Plasma Physics and Controlled Fusion* 46 (2004), jul, 9, 1351. – URL <https://dx.doi.org/10.1088/0741-3335/46/9/002>
- [Gier and Bock 2023] GIER, T. ; BOCK, L.: Chapter 3 of the Working Group I Contribution to the IPCC Sixth Assessment Report - data for Figure 3.31 (v20211203). In: *NERC EDS Centre for Environmental Data Analysis* (2023)
- [Giruzzi et al. 1999] GIRUZZI, G ; ZABIÉGO, M ; GIANAKON, T.A ; GARBET, X ; CARDINALI, A ; BERNABEI, S: Dynamical modelling of tearing mode stabilization by RF current drive. In:



## Bibliography

---

- Nuclear Fusion* 39 (1999), jan, 1, 107–125. – URL <https://doi.org/10.1088/0029-5515/39/1/307>
- [Gnesin 2011] GNESIN, S.: *Electron-cyclotron heating and suprathermal electron dynamics in the TCV tokamak*, École Polytechnique Fédérale de Lausanne, Dissertation, 2011
- [Gnesin et al. 2008] GNESIN, S. ; CODA, S. ; DECKER, J. ; PEYSSON, Y.: Suprathermal electron studies in the TCV tokamak: Design of a tomographic hard-x-ray spectrometer. In: *Review of Scientific Instruments* 79 (2008), 10, 10F504. – URL <https://doi.org/10.1063/1.2957843>
- [Goldsmith 1998] GOLDSMITH, P. F. ; ANDERSON, J. B. (Hrsg.): *Quasioptical systems: Gaussian beam propagation and applications*. IEEE Press/Chapman & Hall Publishers series on microwave technology and techniques, 1998
- [Graves et al. 2005] GRAVES, J. P. ; HORACEK, J. ; PITTS, R. A. ; HOPCRAFT, K. I.: Self-similar density turbulence in the TCV tokamak scrape-off layer. In: *Plasma Physics and Controlled Fusion* 47 (2005), feb, 3, L1. – URL <https://dx.doi.org/10.1088/0741-3335/47/3/L01>
- [Greenwald 2002] GREENWALD, Martin: Density limits in toroidal plasmas. In: *Plasma Physics and Controlled Fusion* 44 (2002), jul, 8, R27. – URL <https://dx.doi.org/10.1088/0741-3335/44/8/201>
- [Guazzotto and Freidberg 2007] GUAZZOTTO, L. ; FREIDBERG, J. P.: A family of analytic equilibrium solutions for the Grad–Shafranov equation. In: *Physics of Plasmas* 14 (2007), 11, 112508. – URL <https://doi.org/10.1063/1.2803759>
- [Görler et al. 2016] GÖRLER, T. ; TRONKO, N. ; HORNSBY, W. A. ; BOTTINO, A. ; KLEIBER, R. ; NORSCINI, C. ; GRANDGIRARD, V. ; JENKO, F. ; SONNENDRÜCKER, E.: Intercode comparison of gyrokinetic global electromagnetic modes. In: *Physics of Plasmas* 23 (2016), 7, 072503. – URL <https://doi.org/10.1063/1.4954915>
- [Happel et al. 2015] HAPPEL, T. ; NAVARRO, A. B. ; CONWAY, G. D. ; ANGIONI, C. ; BERNERT, M. ; DUNNE, M. ; FABLE, E. ; GEIGER, B. ; GÖRLER, T. ; JENKO, F. ; McDERMOTT, R. M. ; RYTER, F. ; STROTH, U.: Core turbulence behavior moving from ion-temperature-gradient regime towards trapped-electron-mode regime in the ASDEX Upgrade tokamak and comparison with gyrokinetic simulation. In: *Physics of Plasmas* 22 (2015), 3, 032503. – URL <https://doi.org/10.1063/1.4914153>
- [Hartfuss et al. 1986] HARTFUSS, H. J. ; MAASSBERG, H. ; TUTTER, M. ; AND: Evaluation of the local heat conductivity coefficient by power-modulated electron cyclotron heating in the Wendelstein VII-A Stellarator. In: *Nuclear Fusion* 26 (1986), may, 5, 678–684. – URL <https://doi.org/10.1088/0029-5515/26/5/014>
- [Harvey et al. 2002] HARVEY, R. W. ; SAUTER, O. ; PRATER, R. ; NIKKOLA, P.: Radial Transport and Electron-Cyclotron-Current Drive in the TCV and DIII-D Tokamaks. In: *Phys. Rev. Lett.* 88 (2002), 205001. – URL <https://link.aps.org/doi/10.1103/PhysRevLett.88.205001>

- [Haye 2006] HAYE, R. J. L.: Neoclassical tearing modes and their control. In: *Physics of Plasmas* 13 (2006), 5, 055501
- [Heidbrink and Sadler 1994] HEIDBRINK, W.W. ; SADLER, G.J.: The behaviour of fast ions in tokamak experiments. In: *Nuclear Fusion* 34 (1994), apr, 4, 535. – URL <https://dx.doi.org/10.1088/0029-5515/34/4/107>
- [Heidbrink and Sadler 1995] HEIDBRINK, W.W. ; SADLER, G.J.: The behaviour of fast ions in tokamak experiments. In: *Nuclear Fusion* 35 (1995), feb, 2, 243. – URL <https://dx.doi.org/10.1088/0029-5515/35/2/514>
- [Helander et al. 2012] HELANDER, P. ; BEIDLER, C D. ; BIRD, T M. ; DREVLAK, M. ; FENG, Y. ; HATZKY, R. ; JENKO, F. ; KLEIBER, R. ; PROLL, J H E. ; TURKIN, Yu. ; XANTHOPOULOS, P.: Stellarator and tokamak plasmas: a comparison. In: *Plasma Physics and Controlled Fusion* 54 (2012), nov, 12, 124009. – URL <https://dx.doi.org/10.1088/0741-3335/54/12/124009>
- [Hillesheim et al. 2013] HILLESHEIM, J. C. ; DEBOO, J. C. ; PEEBLES, W. A. ; CARTER, T. A. ; WANG, G. ; RHODES, T. L. ; SCHMITZ, L. ; MCKEE, G. R. ; YAN, Z. ; STAEBLER, G. M. ; BURRELL, K. H. ; DOYLE, E. J. ; HOLLAND, C. ; PETTY, C. C. ; SMITH, S. P. ; WHITE, A. E. ; ZENG, L.: Observation of a Critical Gradient Threshold for Electron Temperature Fluctuations in the DIII-D Tokamak. In: *Phys. Rev. Lett.* 110 (2013), Jan, 045003. – URL <https://link.aps.org/doi/10.1103/PhysRevLett.110.045003>
- [Hizanidis et al. 2010] HIZANIDIS, K. ; RAM, A. K. ; KOMINIS, Y. ; TSIRONIS, C.: Fokker–Planck description of the scattering of radio frequency waves at the plasma edge. In: *Physics of Plasmas* 17 (2010), 2, 022505
- [Hofmann et al. 1994] HOFMANN, F. ; LISTER, J B. ; ANTON, W. ; BARRY, S. ; BEHN, R. ; BERNEL, S. ; BESSON, G. ; BUHLMANN, F. ; CHAVAN, R. ; CORBOZ, M. ; DUTCH, M J. ; DUVAL, B P. ; FASEL, D. ; FAVRE, A. ; FRANKE, S. ; HEYM, A. ; HIRT, A. ; HOLLENSTEIN, C. ; ISOZ, P. ; JOYE, B. ; LLOBET, X. ; MAGNIN, J C. ; MARLETAZ, B. ; MARMILLOD, P. ; MARTIN, Y. ; MAYOR, J M. ; MORET, J M. ; NIESWAND, C. ; PARIS, P J. ; PEREZ, A. ; PIETRZYK, Z A. ; PITTS, R A. ; POCHELON, A. ; RAGE, R. ; SAUTER, O. ; TONETTI, G. ; TRAN, M Q. ; TROYON, F. ; WARD, D J. ; WEISEN, H.: Creation and control of variably shaped plasmas in TCV. In: *Plasma Physics and Controlled Fusion* 36 (1994), dec, 12B, B277. – URL <https://dx.doi.org/10.1088/0741-3335/36/12B/023>
- [Hogge et al. 2020] HOGGE, J.-P. ; ALBERTI, S. ; AVRAMIDIS, K. A. ; BRUSCHI, A. ; BIN, W. ; CAU, F. ; CISMONDI, F. ; DUBRAY, J. ; FASEL, D. ; GANTENBEIN, G. ; GARAVAGLIA, S. ; GENOUD, J. ; GOODMAN, T. P. ; ILLY, S. ; JIN, J. ; LEGRAND, F. ; MARCHESIN, R. ; MARLÉTAZ, B. ; MASUR, J. ; MORO, A. ; MOURA, C. ; PAGONAKIS, I. G. ; PÉRIAL, E. ; SAVOLDI, L. ; SCHERER, T. ; SIRAVO, U. ; THUMM, M. ; TOUSSAINT, M. ; TRAN, M.-Q.: Megawatt power generation of the dual-frequency gyrotron for TCV at 84 and 126 GHz, in long pulses. In: *AIP Conference Proceedings* 2254 (2020), 09, 1, 090006. – URL <https://doi.org/10.1063/5.0014343>. – ISSN 0094-243X

## Bibliography

---

- [Holland et al. 2023] HOLLAND, Lou ; KÖHN-SEEMANN, Alf ; VANN, Roddy G L.: Parametric dependence of microwave beam broadening by plasma density turbulence. In: *Nuclear Fusion* (2023). – URL <http://iopscience.iop.org/article/10.1088/1741-4326/acc25e>
- [Horacek et al. 2005] HORACEK, J. ; PITTS, R. A. ; GRAVES, J. P.: Overview of edge electrostatic turbulence experiments on TCV. In: *Czechoslovak Journal of Physics* 55 (2005), März, 3, 271–283. – URL <https://doi.org/10.1007/s10582-005-0040-z>. – ISSN 1572-9486
- [Horton 1999] HORTON, W.: Drift waves and transport. In: *Rev. Mod. Phys.* 71 (1999), 735–778. – URL <https://link.aps.org/doi/10.1103/RevModPhys.71.735>
- [Horton et al. 2004] HORTON, W. ; HOANG, G. T. ; BOURDELLE, C. ; GARBET, X. ; OTTAVIANI, M. ; COLAS, L.: Electron transport and the critical temperature gradient. In: *Physics of Plasmas* 11 (2004), 5, 2600–2606. – URL <https://doi.org/10.1063/1.1690761>
- [Huba 2016] HUBA, J.D.: *NRL Plasma Formulary*. 2016
- [Hubbell et al. 1975] HUBBELL, J. H. ; VEIGELE, Wm. J. ; BRIGGS, E. A. ; BROWN, R. T. ; CROMER, D. T. ; HOWERTON, R. J.: Atomic form factors, incoherent scattering functions, and photon scattering cross sections. In: *Journal of Physical and Chemical Reference Data* 4 (1975), 3, 471–538. – URL <https://doi.org/10.1063/1.555523>
- [Hutchinson 1987] HUTCHINSON, I. H.: *Principles of plasma diagnostics*. Cambridge University Press, 1987
- [Idomura 2016] IDOMURA, Y.: A new hybrid kinetic electron model for full-f gyrokinetic simulations. In: *Journal of Computational Physics* 313 (2016), 511–531. – URL <https://www.sciencedirect.com/science/article/pii/S0021999116001297>. – ISSN 0021-9991
- [Intergovernmental Panel on Climate Change (IPCC) 2023a] INTERGOVERNMENTAL PANEL ON CLIMATE CHANGE (IPCC): *Climate Change 2021 – The Physical Science Basis: Working Group I Contribution to the Sixth Assessment Report of the Intergovernmental Panel on Climate Change*. Cambridge University Press, 2023
- [Intergovernmental Panel on Climate Change (IPCC) 2023b] INTERGOVERNMENTAL PANEL ON CLIMATE CHANGE (IPCC): *Climate Change 2022 - Mitigation of Climate Change: Working Group III Contribution to the Sixth Assessment Report of the Intergovernmental Panel on Climate Change*. Cambridge University Press, 2023
- [Intergovernmental Panel on Climate Change (IPCC) 2023c] INTERGOVERNMENTAL PANEL ON CLIMATE CHANGE (IPCC): *Climate Change 2022 – Impacts, Adaptation and Vulnerability: Working Group II Contribution to the Sixth Assessment Report of the Intergovernmental Panel on Climate Change*. Cambridge University Press, 2023
- [Intergovernmental Panel on Climate Change (IPCC) 2023d] INTERGOVERNMENTAL PANEL ON CLIMATE CHANGE (IPCC): *Summary for Policymakers*. 3–32. In: *Climate Change 2021 – The Physical Science Basis: Working Group I Contribution to the Sixth Assessment Report of the Intergovernmental Panel on Climate Change*, Cambridge University Press, 2023

- [International Energy Agency 2021] INTERNATIONAL ENERGY AGENCY: Key World Energy Statistics / International Energy Agency. URL <https://www.iea.org/reports/key-world-energy-statistics-2021>, 2021. – Forschungsbericht
- [Ioannidis et al. 2017] IOANNIDIS, Zisis C. ; RAM, Abhay K. ; HIZANIDIS, Kyriakos ; TIGELIS, Ioannis G.: Computational studies on scattering of radio frequency waves by density filaments in fusion plasmas. In: *Physics of Plasmas* 24 (2017), 10, 102115. – URL <https://doi.org/10.1063/1.4992032>
- [ITER Organization 2018] ITER ORGANIZATION: ITER Research Plan within the Staged Approach (Level III - Provisional Version) / ITER Organization. 2018 (ITR-18-003). – techreport
- [ITER Physics Expert Group on Confinement and Transport et al. 1999] ITER PHYSICS EXPERT GROUP ON CONFINEMENT AND TRANSPORT ; ITER PHYSICS EXPERT GROUP ON CONFINEMENT MODELLING AND DATABASE ; ITER PHYSICS BASIS EDITORS: Chapter 2: Plasma confinement and transport. In: *Nuclear Fusion* 39 (1999), dec, 12, 2175. – URL <https://dx.doi.org/10.1088/0029-5515/39/12/302>
- [Jahns et al. 1986] JAHNS, G.L. ; WONG, S.K. ; PRATER, R. ; LIN, S.H. ; EJIMA, S.: Measurement of thermal transport by synchronous detection of modulated electron cyclotron heating in the Doublet III tokamak. In: *Nuclear Fusion* 26 (1986), feb, 2, 226–231. – URL <https://doi.org/10.1088/0029-5515/26/2/011>
- [James et al. 2010] JAMES, A. N. ; HOLLMANN, E. M. ; TYNAN, G. R.: Spatially distributed scintillator arrays for diagnosing runaway electron transport and energy behavior in tokamaks. In: *Review of Scientific Instruments* 81 (2010), 10, 10E306. – URL <https://doi.org/10.1063/1.3475710>
- [James et al. 2011] JAMES, A.N. ; AUSTIN, M.E. ; COMMAUX, N. ; EIDIETIS, N.W. ; EVANS, T.E. ; HOLLMANN, E.M. ; HUMPHREYS, D.A. ; HYATT, A.W. ; IZZO, V.A. ; JERNIGAN, T.C. ; HAYE, R.J. L. ; PARKS, P.B. ; STRAIT, E.J. ; TYNAN, G.R. ; WESLEY, J.C. ; YU, J.H.: Measurements of hard x-ray emission from runaway electrons in DIII-D. In: *Nuclear Fusion* 52 (2011), 1, 013007. – URL <https://doi.org/10.1088/0029-5515/52/1/013007>
- [Jenko et al. 2001] JENKO, F. ; DORLAND, W. ; HAMMETT, G. W.: Critical gradient formula for toroidal electron temperature gradient modes. In: *Physics of Plasmas* 8 (2001), 9, 4096–4104. – URL <https://doi.org/10.1063/1.1391261>
- [Joye et al. 1988] JOYE, B. ; LISTER, J. B. ; MORET, J. M. ; POCHOLON, A. ; SIMM, C. W.: Dynamical plasma response to additional heating. In: *Plasma Physics and Controlled Fusion* 30 (1988), jun, 6, 743–762. – URL <https://doi.org/10.1088/0741-3335/30/6/007>
- [Kamleitner 2015] KAMLEITNER, J.: *Suprathermal electron studies in tokamak plasmas by means of diagnostic measurements and modeling*, École Polytechnique Fédérale de Lausanne, Dissertation, 2015

## Bibliography

---

- [Kamleitner et al. 2015] KAMLEITNER, J. ; CODA, S. ; DECKER, J. ; GRAVES, J. P.: Suprathermal electron dynamics and MHD instabilities in a tokamak. In: *Plasma Physics and Controlled Fusion* 57 (2015), 10, 104009. – URL <https://doi.org/10.1088%2F0741-3335%2F57%2F10%2F104009>
- [Kamleitner et al. 2014] KAMLEITNER, J. ; CODA, S. ; GNESIN, S. ; MARMILLOD, P.: Comparative analysis of digital pulse processing methods at high count rates. In: *Nuclear Instruments and Methods in Physics Research Section A: Accelerators, Spectrometers, Detectors and Associated Equipment* 736 (2014), 88 – 98. – URL <http://www.sciencedirect.com/science/article/pii/S0168900213013697>. – ISSN 0168-9002
- [Karney 1986] KARNEY, Charles F.: Fokker-Planck and quasilinear codes. In: *Computer Physics Reports* 4 (1986), 3, 183 – 244. – URL <http://www.sciencedirect.com/science/article/pii/0167797786900298>. – ISSN 0167-7977
- [Karpushov et al. 2023] KARPUSHOV, Alexander N. ; BAGNATO, Filippo ; BAQUERO-RUIZ, Marcelo ; CODA, Stefano ; COLANDREA, Claudia ; DOLIZY, Frédéric ; DUBRAY, Jérémie ; DUVAL, Basil P. ; FASEL, Damien ; FASOLI, Ambrogio ; JACQUIER, Rémy ; LAVANCHY, Pierre ; MARLÉTAZ, Blaise ; MARTIN, Yves ; MARTINELLI, Lorenzo ; MYKYTCHUK, Dmytry ; PEDRINI, Marta M. ; POLEY, Jesús ; REIMERDES, Holger ; SHEIKH, Umar ; SIRAVO, Ugo ; TOUSSAINT, Matthieu ; VALLAR, Matteo: Upgrade of the neutral beam heating system on the TCV tokamak – second high energy neutral beam. In: *Fusion Engineering and Design* 187 (2023), 113384. – URL <https://www.sciencedirect.com/science/article/pii/S092037962200374X>. – ISSN 0920-3796
- [Kennel and Engelmann 1966] KENNEL, C. F. ; ENGELMANN, E.: Velocity Space Diffusion from Weak Plasma Turbulence in a Magnetic Field. In: *The Physics of Fluids* 9 (1966), 12, 2377–2388. – URL <https://aip.scitation.org/doi/abs/10.1063/1.1761629>
- [Knoll 2000] KNOLL, G.E.: *Radiation Detection and Measurement*. Wiley, 2000. – URL <https://books.google.ch/books?id=HKBVAAAAMAAJ>. – ISBN 9780471073383
- [Koch 2006] KOCH, R.: Wave-particle interactions in plasmas. In: *Plasma Physics and Controlled Fusion* 48 (2006), nov, 12B, B329–B345. – URL <https://doi.org/10.1088%2F0741-3335%2F48%2F12b%2Fs31>
- [Köhn et al. 2018] KÖHN, A. ; GUIDI, L. ; HOLZHAUER, E. ; MAJ, O. ; POLI, E. ; SNICKER, A. ; WEBER, H.: Microwave beam broadening due to turbulent plasma density fluctuations within the limit of the Born approximation and beyond. In: *Plasma Physics and Controlled Fusion* 60 (2018), 7, 075006. – URL <https://doi.org/10.1088%2F1361-6587%2Faac000>
- [Kong et al. 2019] KONG, M. ; BLANKEN, T.C. ; FELICI, F. ; GALPERTI, C. ; MALJAARS, E. ; SAUTER, O. ; VU, T. ; CARPANESE, F. ; MERLE, A. ; MORET, J.-M. ; PESAMOSCA, F. ; POLI, E. ; REICH, M. ; TEPLUKHINA, A.A. ; AND: Control of neoclassical tearing modes and integrated multi-actuator plasma control on TCV. In: *Nuclear Fusion* 59 (2019), jun, 7, 076035. – URL <https://doi.org/10.1088/1741-4326/able1e>

- [Krutkin et al. 2023] KRUTKIN, O. ; BRUNNER, S. ; CODA, S.: A method for density fluctuation measurements using pulse reflectometry. In: *Nuclear Fusion* 63 (2023), may, 7, 076012. – URL <https://dx.doi.org/10.1088/1741-4326/acd5e0>
- [Köhn et al. 2008] KÖHN, A. ; CAPPA, Á. ; HOLZHAUER, E. ; CASTEJÓN, F. ; FERNÁNDEZ, Á. ; STROTH, U.: Full-wave calculation of the O–X–B mode conversion of Gaussian beams in a cylindrical plasma. In: *Plasma Physics and Controlled Fusion* 50 (2008), jun, 8, 085018. – URL <https://dx.doi.org/10.1088/0741-3335/50/8/085018>
- [Lanti et al. 2020] LANTI, E. ; OHANA, N. ; TRONKO, N. ; HAYWARD-SCHNEIDER, T. ; BOTTINO, A. ; McMILLAN, B.F. ; MISHCHENKO, A. ; SCHEINBERG, A. ; BIANCALANI, A. ; ANGELINO, P. ; BRUNNER, S. ; DOMINSKI, J. ; DONNEL, P. ; GHELLER, C. ; HATZKY, R. ; JOCKSCH, A. ; JOLLIET, S. ; LU, Z.X. ; MARTIN COLLAR, J.P. ; NOVIKAU, I. ; SONNENDRÜCKER, E. ; VERNAY, T. ; VILLARD, L.: Orb5: A global electromagnetic gyrokinetic code using the PIC approach in toroidal geometry. In: *Computer Physics Communications* 251 (2020), 107072. – URL <http://www.sciencedirect.com/science/article/pii/S0010465519303911>. – ISSN 0010-4655
- [Lapillonne et al. 2010] LAPILLONNE, X. ; McMILLAN, B. F. ; GÖRLER, T. ; BRUNNER, S. ; DANNERT, T. ; JENKO, F. ; MERZ, F. ; VILLARD, L.: Nonlinear quasisteady state benchmark of global gyrokinetic codes. In: *Physics of Plasmas* 17 (2010), 11, 11. – URL <https://doi.org/10.1063/1.3518118>. – ISSN 1070-664X
- [Lawson 1957] LAWSON, J.D.: Some Criteria for a Power Producing Thermonuclear Reactor. In: *Proceedings of the Physical Society. Section B* 70 (1957), jan, 1, 6. – URL <https://dx.doi.org/10.1088/0370-1301/70/1/303>
- [Lax et al. 1975] LAX, Melvin ; LOUISELL, William H. ; MCKNIGHT, William B.: From Maxwell to paraxial wave optics. In: *Phys. Rev. A* 11 (1975), Apr, 1365–1370. – URL <https://link.aps.org/doi/10.1103/PhysRevA.11.1365>
- [Lerche 1968] LERCHE, I.: Quasilinear Theory of Resonant Diffusion in a Magneto-Active, Relativistic Plasma. In: *The Physics of Fluids* 11 (1968), 8, 1720–1727. – URL <https://aip.scitation.org/doi/abs/10.1063/1.1692186>
- [Ma et al. 2017] MA, T.K. ; CHEN, Z.Y. ; HUANG, D.W. ; TONG, R.H. ; YAN, W. ; WANG, S.Y. ; DAI, A.J. ; WANG, X.L.: Development of hard X-ray spectrometer with high time resolution on the J-TEXT tokamak. In: *Nuclear Instruments and Methods in Physics Research Section A: Accelerators, Spectrometers, Detectors and Associated Equipment* 856 (2017), 81–85. – URL <https://www.sciencedirect.com/science/article/pii/S0168900217303121>. – ISSN 0168-9002
- [Marini 2017] MARINI, C.: *Poloidal CX visible light plasma rotation diagnostics in TCV*, École Polytechnique Fédérale de Lausanne, Dissertation, 2017
- [Marinoni et al. 2006] MARINONI, A. ; CODA, S. ; CHAVAN, R. ; POCHON, G.: Design of a tangential phase contrast imaging diagnostic for the TCV tokamak. In: *Review of Scientific Instruments* 77 (2006), 10, 10E929. – URL <https://doi.org/10.1063/1.2222333>

## Bibliography

---

- [McDonald 1991] MCDONALD, S.W.: Wave kinetic equation in a fluctuating medium. In: *Phys. Rev. A* 43 (1991), Apr, 4484–4499. – URL <https://link.aps.org/doi/10.1103/PhysRevA.43.4484>
- [Medvedeva et al. 2017] MEDVEDEVA, A ; BOTTEREAU, C ; CLAIRET, F ; HENNEQUIN, P ; STROTH, U ; BIRKENMEIER, G ; CAVEDON, M ; CONWAY, G D. ; HAPPEL, T ; HEURAUX, S ; MOLINA, D ; SILVA, A ; AND, M W.: Density profile and turbulence evolution during L-H transition studied with the ultra-fast swept reflectometer on ASDEX Upgrade. In: *Plasma Physics and Controlled Fusion* 59 (2017), 12, 125014. – URL <https://doi.org/10.1088/1361-6587/2Faa9251>
- [Merlo 2016] MERLO, G.: *Flux-tube and global grid-based gyrokinetic simulation of plasma microturbulence and comparisons with experimental TCV measurements*, École Polytechnique Fédérale de Lausanne, Dissertation, 2016
- [Merlo et al. 2021] MERLO, G ; HUANG, Z ; MARINI, C ; BRUNNER, S ; CODA, S ; HATCH, D ; JAREMA, D ; JENKO, F ; SAUTER, O ; VILLARD, L: Nonlocal effects in negative triangularity TCV plasmas. In: *Plasma Physics and Controlled Fusion* 63 (2021), mar, 4, 044001. – URL <https://dx.doi.org/10.1088/1361-6587/abe39d>
- [Molina Cabrera et al. 2019] MOLINA CABRERA, P ; CODA, S. ; PORTE, L. ; SMOLDERS, A.: V-band nanosecond-scale pulse reflectometer diagnostic in the TCV tokamak. In: *Review of Scientific Instruments* 90 (2019), 12, 123501. – URL <https://doi.org/10.1063/1.5094850>
- [Moret et al. 2015] MORET, J.-M. ; DUVAL, B. P. ; LE, H. B. ; CODA, S. ; FELICI, F. ; REIMERDES, H.: Tokamak equilibrium reconstruction code LIUQE and its real time implementation. In: *Fusion Engineering and Design* 91 (2015), 1 – 15. – URL <http://www.sciencedirect.com/science/article/pii/S0920379614005973>. – ISSN 0920-3796
- [Murakami et al. 2000] MURAKAMI, S ; GASPARINO, U ; IDEI, H ; KUBO, S ; MAASSBERG, H ; MARUSHCHENKO, N ; NAKAJIMA, N ; ROMÉ, M ; OKAMOTO, M: 5-D simulation study of suprathermal electron transport in non-axisymmetric plasmas. In: *Nuclear Fusion* 40 (2000), mar, 3Y, 693–700. – URL <https://doi.org/10.1088/0029-5515/40/3y/333>
- [Navarro et al. 2015] NAVARRO, A. B. ; HAPPEL, T. ; GÖRLER, T. ; JENKO, F. ; ABITEBOUL, J. ; BUSTOS, A. ; DOERK, H. ; TOLD, D.: Gyrokinetic studies of core turbulence features in ASDEX Upgrade H-mode plasmas. In: *Physics of Plasmas* 22 (2015), 4, 042513. – URL <https://doi.org/10.1063/1.4919022>
- [Nespoli et al. 2017] NESPOLI, F ; FURNO, I ; LABIT, B ; RICCI, P ; AVINO, F ; HALPERN, F D. ; MUSIL, F ; RIVA, F: Blob properties in full-turbulence simulations of the TCV scrape-off layer. In: *Plasma Physics and Controlled Fusion* 59 (2017), mar, 5, 055009. – URL <https://dx.doi.org/10.1088/1361-6587/aa6276>
- [Nikkola et al. 2003] NIKKOLA, P. ; SAUTER, O. ; BEHN, R. ; CODA, S. ; CONDREA, I. ; GOODMAN, T. P. ; HENDERSON, M. A. ; HARVEY, R. W. ; TCV TEAM the: Modelling of the electron cyclotron

- current drive experiments in the TCV tokamak. In: *Nuclear Fusion* 43 (2003), 11, 1343–1352. – URL <https://doi.org/10.1088%2F0029-5515%2F43%2F11%2F006>
- [Nocente et al. 2018] NOCENTE, M. ; SHEVELEV, A. ; GIACOMELLI, L. ; PAUTASSO, G. ; TARDOCHI, M. ; GIN, D. ; GOBBIN, M. ; GORINI, G. ; FERNANDES, A. ; HERRMANN, A. ; KHILKEVITCH, E. ; PANONTIN, E. ; PAPP, G. ; PEREIRA, R. C. ; SALEWSKI, M. ; TARDINI, G. ; VALISA, M.: High resolution gamma-ray spectrometer with MHz capabilities for runaway electron studies at ASDEX Upgrade. In: *Review of Scientific Instruments* 89 (2018), 10, 10124. – URL <https://doi.org/10.1063/1.5036658>
- [Nordman et al. 1990] NORDMAN, H. ; WEILAND, J. ; JARMÉN, A.: Simulation of toroidal drift mode turbulence driven by temperature gradients and electron trapping. In: *Nuclear Fusion* 30 (1990), jun, 6, 983. – URL <https://dx.doi.org/10.1088/0029-5515/30/6/001>
- [Novikau et al. 2020] NOVIKAU, I. ; BIANCALANI, A. ; BOTTINO, A. ; LAUBER, Ph. ; POLI, E. ; MANZ, P. ; CONWAY, G. D. ; DI SIENA, A. ; OHANA, N. ; LANTI, E. ; VILLARD, L. ; TEAM, ASDEX U.: Nonlinear dynamics of energetic-particle driven geodesic acoustic modes in ASDEX Upgrade. In: *Physics of Plasmas* 27 (2020), 04, 4. – URL <https://doi.org/10.1063/1.5142802>. – 042512. – ISSN 1070-664X
- [Petrov and Harvey 2016] PETROV, Yu V. ; HARVEY, R W.: A fully-neoclassical finite-orbit-width version of the CQL3D Fokker–Planck code. In: *Plasma Physics and Controlled Fusion* 58 (2016), sep, 11, 115001. – URL <https://dx.doi.org/10.1088/0741-3335/58/11/115001>
- [Peysson et al. 2001] PEYSSON, Y. ; CODA, S. ; IMBEAUX, E.: Hard X-ray CdTe tomography of tokamak fusion plasmas. In: *Nuclear Instruments and Methods in Physics Research Section A: Accelerators, Spectrometers, Detectors and Associated Equipment* 458 (2001), 1, 269–274. – URL <https://www.sciencedirect.com/science/article/pii/S0168900200008706>. – Proc. 11th Inbt. Workshop on Room Temperature Semiconductor X- and Gamma-Ray Detectors and Associated Electronics. – ISSN 0168-9002
- [Peysson and Decker 2008] PEYSSON, Y. ; DECKER, J.: Fast electron bremsstrahlung in axisymmetric magnetic configuration. In: *Physics of Plasmas* 15 (2008), 9, 092509. – URL <https://doi.org/10.1063/1.2981391>
- [Peysson and Decker 2014] PEYSSON, Y. ; DECKER, J.: Numerical Simulations of the Radio-Frequency-driven Toroidal Current in Tokamaks. In: *Fusion Science and Technology* 65 (2014), 1, 22–42. – URL <https://doi.org/10.13182/FST13-643>
- [Peysson et al. 2012] PEYSSON, Y. ; DECKER, J. ; MORINI, L.: A versatile ray-tracing code for studying rf wave propagation in toroidal magnetized plasmas. In: *Plasma Physics and Controlled Fusion* 54 (2012), 4, 045003. – URL <https://doi.org/10.1088%2F0741-3335%2F54%2F4%2F045003>
- [Peysson et al. 2011] PEYSSON, Y. ; DECKER, J. ; MORINI, L. ; CODA, S.: RF current drive and plasma fluctuations. In: *Plasma Physics and Controlled Fusion* 53 (2011), 12, 124028. – URL <https://doi.org/10.1088%2F0741-3335%2F53%2F12%2F124028>



## Bibliography

---

- [Peysson and Imbeaux 1999] PEYSSON, Yves ; IMBEAUX, Frédéric: Tomography of the fast electron bremsstrahlung emission during lower hybrid current drive on TORE SUPRA. In: *Review of Scientific Instruments* 70 (1999), 10, 3987–4007. – URL <https://doi.org/10.1063/1.1150025>
- [Plyusnin et al. 2019] PLYUSNIN, V.V. ; KIPTILY, V.G. ; SHEVELEV, A.E. ; KHILKEVITCH, E.M. ; GERASIMOV, S. ; MLYNAR, J.: Hard X-ray Bremsstrahlung of relativistic Runaway Electrons in JET. In: *Journal of Instrumentation* 14 (2019), sep, 09, C09042–C09042. – URL <https://doi.org/10.1088/1748-0221/14/09/c09042>
- [Poli et al. 2018] POLI, E. ; BOCK, A. ; LOCHBRUNNER, M. ; MAJ, O. ; REICH, M. ; SNICKER, A. ; STEGMEIR, A. ; VOLPE, F. ; BERTELLI, N. ; BILATO, R. ; CONWAY, G.D. ; FARINA, D. ; FELICI, F. ; FIGINI, L. ; FISCHER, R. ; GALPERTI, C. ; HAPPEL, T. ; LIN-LIU, Y.R. ; MARUSHCHENKO, N.B. ; MSZANOWSKI, U. ; POLI, F.M. ; STOBER, J. ; WESTERHOF, E. ; ZILLE, R. ; PEETERS, A.G. ; PEREVERZEV, G.V.: TORBEAM 2.0, a paraxial beam tracing code for electron-cyclotron beams in fusion plasmas for extended physics applications. In: *Computer Physics Communications* 225 (2018), 36–46. – URL <https://www.sciencedirect.com/science/article/pii/S001046551730423X>. – ISSN 0010-4655
- [Poli et al. 2001] POLI, E. ; PEETERS, A.G. ; PEREVERZEV, G.V.: TORBEAM, a beam tracing code for electron-cyclotron waves in tokamak plasmas. In: *Computer Physics Communications* 136 (2001), 1, 90–104. – URL <https://www.sciencedirect.com/science/article/pii/S0010465501001461>. – ISSN 0010-4655
- [Prater 2004] PRATER, R.: Heating and current drive by electron cyclotron waves. In: *Physics of Plasmas* 11 (2004), 5, 2349–2376
- [Prater et al. 2008] PRATER, R. ; FARINA, D. ; GRIBOV, Yu. ; HARVEY, R.W. ; RAM, A.K. ; LIN-LIU, Y.-R. ; POLI, E. ; SMIRNOV, A.P. ; VOLPE, F. ; WESTERHOF, E. ; AND, A. Z.: Benchmarking of codes for electron cyclotron heating and electron cyclotron current drive under ITER conditions. In: *Nuclear Fusion* 48 (2008), 3, 035006. – URL <https://doi.org/10.1088/0029-5515/48/3/035006>
- [Purohit et al. 2020] PUROHIT, S. ; CHOWDHURI, M.B. ; JOISA, Y.S. ; GUPTA, M.K. ; RAVAL, J.V. ; NAGORA, U.C. ; ATREY, P.K. ; PATHAK, S.K. ; JADEJA, K.A. ; BHATT, S.B. ; GUPTA, C.N. ; TANNA, R.L. ; GHOSH, J.: Lanthanum Bromide (LaBr<sub>3</sub>(Ce)) based hard X-ray spectroscopic diagnostic for the study of runaway electrons at Aditya Tokamak. In: *Journal of Instrumentation* 15 (2020), aug, 08, P08015–P08015. – URL <https://doi.org/10.1088/1748-0221/15/8/P08015>
- [Ram et al. 2013] RAM, A. K. ; HIZANIDIS, K. ; KOMINIS, Y.: Scattering of radio frequency waves by blobs in tokamak plasmas. In: *Physics of Plasmas* 20 (2013), 5, 056110. – URL <https://doi.org/10.1063/1.4803898>
- [Reimerdes et al. 2022] REIMERDES, H. ; AGOSTINI, M. ; ALESSI, E. ; ALBERTI, S. ; ANDREBE, Y. ; ARNICHAND, H. ; BALBIN, J. ; BAGNATO, F. ; BAQUERO-RUIZ, M. ; BERNERT, M. ; BIN, W. ;

- BLANCHARD, P. ; BLANKEN, T.C. ; BOEDO, J.A. ; BRIDA, D. ; BRUNNER, S. ; BOGAR, C. ; BOGAR, O. ; BOLZONELLA, T. ; BOMBARDA, F. ; BOUQUEY, F. ; BOWMAN, C. ; BRUNETTI, D. ; BUERMANS, J. ; BUFFERAND, H. ; CALACCI, L. ; CAMENEN, Y. ; CARLI, S. ; CARNEVALE, D. ; CARPANESE, F. ; CAUSA, F. ; CAVALIER, J. ; CAVEDON, M. ; CAZABONNE, J.A. ; CEROVSKY, J. ; CHANDRA, R. ; JAYALEKSHMI, A. C. ; CHELLAI, O. ; CHMIELEWSKI, P. ; CHOI, D. ; CIRAOLO, G. ; CLASSEN, I.G.J. ; CODA, S. ; COLANDREA, C. ; MOLIN, A. D. ; DAVID, P. ; BAAR, M.R. de ; DECKER, J. ; DEKEYSER, W. ; OLIVEIRA, H. de ; DOUAL, D. ; DREVAL, M. ; DUNNE, M.G. ; DUVAL, B.P. ; ELMORE, S. ; EMBREUS, O. ; ERIKSSON, F. ; FAITSCH, M. ; FALCHETTO, G. ; FARNIK, M. ; FASOLI, A. ; FEDORCZAK, N. ; FELICI, F. ; FÉVRIER, O. ; FICKER, O. ; FIL, A. ; FONTANA, M. ; FRANSSON, E. ; FRASSINETTI, L. ; FURNO, I. ; GAHLE, D.S. ; GALASSI, D. ; GALAZKA, K. ; GALPERTI, C. ; GARAVAGLIA, S. ; GARCIA-MUNOZ, M. ; GEIGER, B. ; GIACOMIN, M. ; GIRUZZI, G. ; GOBBIN, M. ; GOLFINOPOULOS, T. ; GOODMAN, T. ; GORNO, S. ; GRANUCCI, G. ; GRAVES, J.P. ; GRIENER, M. ; GRUCA, M. ; GYERGYEK, T. ; HAEFTERMAN, R. ; HAKOLA, A. ; HAN, W. ; HAPPEL, T. ; HARRER, G. ; HARRISON, J.R. ; HENDERSON, S. ; HOGEWELJ, G.M.D. ; HOGGE, J.-P. ; HOPPE, M. ; HORACEK, J. ; HUANG, Z. ; IANTCHENKO, A. ; INNOCENTE, P. ; BJÖRK, K. I. ; IONITA-SCHRITTWEISER, C. ; ISLIKER, H. ; JARDIN, A. ; JASPERS, R.J.E. ; KARIMOV, R. ; KARPUSHOV, A.N. ; KAZAKOV, Y. ; KOMM, M. ; KONG, M. ; KOVACIC, J. ; KRUTKIN, O. ; KUDLACEK, O. ; KUMAR, U. ; KWIATKOWSKI, R. ; LABIT, B. ; LAGUARDIA, L. ; LAMMERS, J.T. ; LARIBI, E. ; LASZYNSKA, E. ; LAZAROS, A. ; LINDER, O. ; LINEHAN, B. ; LIPSCHULTZ, B. ; LLOBET, X. ; LOIZU, J. ; LUNT, T. ; MACUSOVA, E. ; MARANDET, Y. ; MARASCHEK, M. ; MARCECA, G. ; MARCHETTO, C. ; MARCHIONI, S. ; MARMAR, E.S. ; MARTIN, Y. ; MARTINELLI, L. ; MATOS, F. ; MAURIZIO, R. ; MAYORAL, M.-L. ; MAZON, D. ; MENKOVSKI, V. ; MERLE, A. ; MERLO, G. ; MEYER, H. ; MIKSZUTA-MICHALIK, K. ; CABRERA, P.A. M. ; MORALES, J. ; MORET, J.-M. ; MORO, A. ; MOULTON, D. ; MUHAMMED, H. ; MYATRA, O. ; MYKYTCHUK, D. ; NAPOLI, F. ; NEM, R.D. ; NIELSEN, A.H. ; NOCENTE, M. ; NOWAK, S. ; OFFEDDU, N. ; OLSEN, J. ; ORSITTO, F.P. ; PAN, O. ; PAPP, G. ; PAU, A. ; PEREK, A. ; PESAMOSCA, F. ; PEYSSON, Y. ; PIGATTO, L. ; PIRON, C. ; PORADZINSKI, M. ; PORTE, L. ; PÜTTERICH, T. ; RABINSKI, M. ; RAJ, H. ; RASMUSSEN, J.J. ; RATTÁ, G.A. ; RAVENSBERGEN, T. ; RICCI, D. ; RICCI, P. ; RISPOLI, N. ; RIVA, F. ; RIVERO-RODRIGUEZ, J.F. ; SALEWSKI, M. ; SAUTER, O. ; SCHMIDT, B.S. ; SCHRITTWEISER, R. ; SHARAPOV, S. ; SHEIKH, U.A. ; SIEGLIN, B. ; SILVA, M. ; SMOLDERS, A. ; SNICKER, A. ; SOZZI, C. ; SPOLAORE, M. ; STAGNI, A. ; STIPANI, L. ; SUN, G. ; TALA, T. ; TAMAIN, P. ; TANAKA, K. ; BIWOLE, A. T. ; TERRANOVA, D. ; TERRY, J.L. ; TESTA, D. ; THEILER, C. ; THORNTON, A. ; THRYSDØE, A. ; TORREBLANCA, H. ; TSUI, C.K. ; VACCARO, D. ; VALLAR, M. ; BERKEL, M. van ; EESTER, D. V. ; KAMPEN, R.J.R. van ; MULDER, S. V. ; VERHAEGH, K. ; VERHAEGHE, T. ; VIANELLO, N. ; VILLONE, F. ; VIEZZER, E. ; VINCENT, B. ; VOITSEKHOVITCH, I. ; VU, N.M.T. ; WALKDEN, N. ; WAUTERS, T. ; WEISEN, H. ; WENDLER, N. ; WENSING, M. ; WIDMER, F. ; WIESEN, S. ; WISCHMEIER, M. ; WIJAMP, T.A. ; WÜNDERLICH, D. ; WÜTHRICH, C. ; YANOVSKIY, V. ; ZEBROWSKI, J. ; EUROFUSION MST1 TEAM the: Overview of the TCV tokamak experimental programme. In: *Nuclear Fusion* 62 (2022), mar, 4, 042018. – URL <https://dx.doi.org/10.1088/1741-4326/ac369b>
- [Reimerdes et al. 2017] REIMERDES, H. ; ALBERTI, S. ; BLANCHARD, P. ; BRUZZONE, P. ; CHAVAN, R. ; CODA, S. ; DUVAL, B.P. ; FASOLI, A. ; LABIT, B. ; LIPSCHULTZ, B. ; LUNT, T. ; MARTIN, Y. ; MORET, J.-M. ; SHEIKH, U. ; SUDKI, B. ; TESTA, D. ; THEILER, C. ; TOUSSAINT,

- M. ; UGLIETTI, D. ; VIANELLO, N. ; WISCHMEIER, M.: TCV divertor upgrade for alternative magnetic configurations. In: *Nuclear Materials and Energy* 12 (2017), 1106–1111. – URL <https://www.sciencedirect.com/science/article/pii/S2352179116301727>. – Proceedings of the 22nd International Conference on Plasma Surface Interactions 2016, 22nd PSI. – ISSN 2352-1791
- [Reimerdes et al. 2021] REIMERDES, H. ; DUVAL, B.P ; ELAIAN, H. ; FASOLI, A. ; FÉVRIER, O. ; THEILER, C. ; BAGNATO, F. ; BAQUERO-RUIZ, M. ; BLANCHARD, P. ; BRIDA, D. ; COLANDREA, C. ; OLIVEIRA, H. D. ; GALASSI, D. ; GORNO, S. ; HENDERSON, S. ; KOMM, M. ; LINEHAN, B. ; MARTINELLI, L. ; MAURIZIO, R. ; MORET, J.-M. ; PEREK, A. ; RAJ, H. ; SHEIKH, U. ; TESTA, D. ; TOUSSAINT, M. ; TSUI, C.K. ; WENSING, M. ; TCV TEAM the ; EUROFUSION MST1 TEAM the: Initial TCV operation with a baffled divertor. In: *Nuclear Fusion* 61 (2021), jan, 2, 024002. – URL <https://dx.doi.org/10.1088/1741-4326/abd196>
- [Rhodes et al. 2002] RHODES, T. L. ; LEBOEUF, J.-N. ; SYDORA, R. D. ; GROEBNER, R. J. ; DOYLE, E. J. ; MCKEE, G. R. ; PEEBLES, W. A. ; RETTIG, C. L. ; ZENG, L. ; WANG, G.: Comparison of turbulence measurements from DIII-D low-mode and high-performance plasmas to turbulence simulations and models. In: *Physics of Plasmas* 9 (2002), 5, 2141–2148. – URL <https://doi.org/10.1063/1.1464544>
- [Rigamonti et al. 2018] RIGAMONTI, D. ; BROSLAWSKI, A. ; FERNANDES, A. ; FIGUEIREDO, J. ; GIACOMELLI, L. ; GORINI, G. ; GOSK, M. ; KAVENEY, G. ; KIPTILY, V. ; KOROLCZUK, S. ; MURARI, A. ; NOCENTE, M. ; PEREIRA, R. C. ; POPOVICHEV, S. ; SANTOS, B. ; URBAN, A. ; ZYCHOR, I. ; TARDOCCI, M.: The upgraded JET gamma-ray cameras based on high resolution/high count rate compact spectrometers. In: *Review of Scientific Instruments* 89 (2018), 10, 10I116. – URL <https://doi.org/10.1063/1.5038839>
- [Ryter et al. 2001] RYTER, F. ; ANGIONI, C. ; BEURSKENS, M. ; CIRANT, S. ; HOANG, G. T. ; HOGWEIJ, G. M. D. ; IMBEAUX, F. ; JACCHIA, A. ; MANTICA, P. ; SUTTROP, W. ; TARDINI, G.: Experimental studies of electron transport. In: *Plasma Physics and Controlled Fusion* 43 (2001), 12A, A323–A338. – URL <https://doi.org/10.1088/0741-3335/43/12/A323>
- [Ryter et al. 2010] RYTER, F. ; DUX, R. ; MANTICA, P. ; TALA, T.: Perturbative studies of transport phenomena in fusion devices. In: *Plasma Physics and Controlled Fusion* 52 (2010), nov, 12, 124043. – URL <https://dx.doi.org/10.1088/0741-3335/52/12/124043>
- [Sauter et al. 1999] SAUTER, O. ; ANGIONI, C. ; LIN-LIU, Y. R.: Neoclassical conductivity and bootstrap current formulas for general axisymmetric equilibria and arbitrary collisionality regime. In: *Physics of Plasmas* 6 (1999), 7, 2834–2839. – URL <https://doi.org/10.1063/1.873240>
- [Sauter et al. 2002] SAUTER, O. ; ANGIONI, C. ; LIN-LIU, Y. R.: Erratum: “Neoclassical conductivity and bootstrap current formulas for general axisymmetric equilibria and arbitrary collisionality regime” [Phys. Plasmas 6, 2834 (1999)]. In: *Physics of Plasmas* 9 (2002), 12, 5140–5140. – URL <https://doi.org/10.1063/1.1517052>

- [Sauter et al. 2014] SAUTER, O. ; BRUNNER, S. ; KIM, D. ; MERLO, G. ; BEHN, R. ; CAMENEN, Y. ; CODA, S. ; DUVAL, B. P. ; FEDERSPIEL, L. ; GOODMAN, T. P. ; KARPUSHOV, A. ; MERLE, A. ; TEAM, TCV: On the non-stiffness of edge transport in L-mode tokamak plasmas. In: *Physics of Plasmas* 21 (2014), 5, 055906. – URL <https://doi.org/10.1063/1.4876612>
- [Scofield 1973] SCOFIELD, J. H.: Theoretical photoionization cross sections from 1 to 1500 keV / Lawrence Livermore Laboratory. 1973 (UCRL-51326). – resreport
- [Shafranov 1980] SHAFRANOV, V.D.: Stellarators. In: *Nuclear Fusion* 20 (1980), sep, 9, 1075. – URL <https://dx.doi.org/10.1088/0029-5515/20/9/005>
- [Shevelev et al. 2016] SHEVELEV, A.E. ; KHILKEVITCH, E.M. ; LASHKUL, S.I. ; ROZHDESTVENSKY, V.V. ; ALTUKHOV, A.B. ; CHUGUNOV, I.N. ; DOINIKOV, D.N. ; ESIPOV, L.A. ; GIN, D.B. ; ILIASOVA, M.V. ; NAIDENOV, V.O. ; NERSESYAN, N.S. ; POLUNOVSKY, I.A. ; SIDOROV, A.V. ; KIPTILY, V.G.: High performance gamma-ray spectrometer for runaway electron studies on the FT-2 tokamak. In: *Nuclear Instruments and Methods in Physics Research Section A: Accelerators, Spectrometers, Detectors and Associated Equipment* 830 (2016), 102–108. – URL <https://www.sciencedirect.com/science/article/pii/S0168900216304685>. – ISSN 0168-9002
- [Slief et al. 2023] SLIEF, J.H. ; KAMPEN, R.J.R. van ; BROOKMAN, M.W. ; DIJK, J. van ; WESTERHOF, E. ; BERKEL, M. van: Quantifying electron cyclotron power deposition broadening in DIII-D and the potential consequences for the ITER EC system. In: *Nuclear Fusion* 63 (2023), jan, 2, 026029. – URL <https://dx.doi.org/10.1088/1741-4326/acaedc>
- [Smirnov 2009] SMIRNOV, V.P.: Tokamak foundation in USSR/Russia 1950–1990. In: *Nuclear Fusion* 50 (2009), dec, 1, 014003. – URL <https://dx.doi.org/10.1088/0029-5515/50/1/014003>
- [Snicker et al. 2017a] SNICKER, A. ; POLI, E. ; MAJ, O. ; GUIDI, L. ; KÖHN, A. ; WEBER, H. ; CONWAY, G. ; HENDERSON, M. ; SAIBENE, G.: The effect of density fluctuations on electron cyclotron beam broadening and implications for ITER. In: *Nuclear Fusion* 58 (2017), 1, 016002. – URL <https://doi.org/10.1088%2F1741-4326%2Faa8d07>
- [Snicker et al. 2017b] SNICKER, A. ; POLI, E. ; MAJ, O. ; GUIDI, L. ; KÖHN, A. ; WEBER, H. ; CONWAY, G. D. ; HENDERSON, M. ; SAIBENE, G.: Interaction of the electron density fluctuations with electron cyclotron waves from the equatorial launcher in ITER. In: *Plasma Physics and Controlled Fusion* 60 (2017), nov, 1, 014020. – URL <https://doi.org/10.1088%2F1361-6587%2Faa8f1a>
- [Solov'ev 1968] SOLOV'EV, L.S.: THE THEORY OF HYDROMAGNETIC STABILITY OF TOROIDAL PLASMA CONFIGURATIONS. In: *Soviet Physics JETP* 26 (1968), 2
- [Stix 1992] STIX, T. H.: *Waves in plasmas*. American Institute of Physics, 1992
- [Strauss 1977] STRAUSS, A. J.: The physical properties of cadmium telluride. In: *Revue de Physique Appliquée (Paris)* 12 (1977), 2

## Bibliography

---

- [Stroth et al. 2020] STROTH, U. ; FUCHERT, G. ; BEURSKENS, M.N.A. ; BIRKENMEIER, G. ; SCHNEIDER, P.A. ; SCOTT, E.R. ; BRUNNER, K.J. ; GÜNZKOFER, F. ; HACKER, P. ; KARDAUN, O. ; KNAUER, J.P. ; RAHBARNIA, K. ; ZHANG, D. ; TEAM, MST1: Stellarator-tokamak energy confinement comparison based on ASDEX Upgrade and Wendelstein 7-X hydrogen plasmas. In: *Nuclear Fusion* 61 (2020), nov, 1, 016003. – URL <https://dx.doi.org/10.1088/1741-4326/abbc4a>
- [Sysoeva et al. 2015] SYSOEVA, E.V. ; SILVA, F. da ; GUSAKOV, E.Z. ; HEURAU, S. ; POPOV, A.Yu.: Electron cyclotron resonance heating beam broadening in the edge turbulent plasma of fusion machines. In: *Nuclear Fusion* 55 (2015), 3, 033016. – URL <https://doi.org/10.1088/0029-5515/55/3/033016>
- [Takeda and Tokuda 1991] TAKEDA, Tatsuoki ; TOKUDA, Shinji: Computation of MHD equilibrium of tokamak plasma. In: *Journal of Computational Physics* 93 (1991), 1, 1 – 107. – URL <http://www.sciencedirect.com/science/article/pii/002199919190074U>. – ISSN 0021-9991
- [TFR and FOM-ECRH 1988] TFR, Group ; FOM-ECRH, Team: The electron cyclotron resonance experiment on TFR. In: *Nuclear Fusion* 28 (1988), nov, 11, 1995–2025. – URL <https://doi.org/10.1088/0029-5515/28/11/006>
- [Tretinnikov et al. 2021] TRETINNIKOV, P. ; GUSAKOV, E. ; HEURAU, S.: X-mode beam broadening in turbulent plasma. In: *Plasma Physics and Controlled Fusion* 63 (2021), jun, 8, 085003. – URL <https://dx.doi.org/10.1088/1361-6587/abfdd6>
- [Troyon et al. 1984] TROYON, F. ; GRUBER, R. ; SAURENMANN, H. ; SEMENZATO, S. ; SUCCI, S.: MHD-Limits to Plasma Confinement. In: *Plasma Physics and Controlled Fusion* 26 (1984), jan, 1A, 209. – URL <https://dx.doi.org/10.1088/0741-3335/26/1A/319>
- [Tsironis et al. 2021] TSIRONIS, C. ; PAPAGIANNIS, P. ; BAIRAKTARIS, E. ; VALVIS, S. I. ; HIZANIDIS, K.: Modelling effects of edge density fluctuations on electron-cyclotron current drive used for neoclassical tearing mode stabilization. In: *Journal of Plasma Physics* 87 (2021), 1, 905870103
- [Tsironis et al. 2009] TSIRONIS, C. ; PEETERS, A. G. ; ISLIKER, H. ; STRINTZI, D. ; CHATZIANTONAKI, I. ; VLAHOS, L.: Electron-cyclotron wave scattering by edge density fluctuations in ITER. In: *Physics of Plasmas* 16 (2009), 11, 112510. – URL <https://doi.org/10.1063/1.3264105>
- [UNDP (United Nations Development Programme) 2022] UNDP (UNITED NATIONS DEVELOPMENT PROGRAMME): Human Development Report 2021-22. In: *UNDP (United Nations Development Programme) (2022)*. – URL <http://report.hdr.undp.org>
- [Villard et al. 2002] VILLARD, L. ; BOTTINO, A. ; SAUTER, O. ; VACLAVIK, J.: Radial electric fields and global electrostatic microinstabilities in tokamaks and stellarators. In: *Physics of Plasmas* 9 (2002), 6, 2684–2691. – URL <https://doi.org/10.1063/1.1477921>

- [Weber et al. 2015] WEBER, H. ; MAJ, O. ; POLI, E.: Scattering of diffracting beams of electron cyclotron waves by random density fluctuations in inhomogeneous plasmas. In: *EPJ Web of Conferences* 87 (2015), 01002. – URL <https://doi.org/10.1051/epjconf/20158701002>
- [Weisen et al. 2023] WEISEN, H. ; BLANCHARD, P. ; VALLAR, M. ; KARPUSHOV, A. N. ; DUBRAY, J. ; MERLE, A. ; DUVAL, B. P. ; CAZABONNE, J. ; TESTA, D. ; ELAIAN, H. H. ; ; TCV TEAM the ; ŽOHAR, A. ; SNOJ, L. ; KOS, B. ; FORTUNA, M. ; ČUFAR, A. ; TESSE, F. ; FONTANA, F. ; GLOOR, C. ; IANNARELLI, R. ; PALACIOS, H. ; TILLE, C. ; MOLteni, M.: TCV Tokamak Neutron Shielding Upgrade for Dual NBI Operation. In: *Fusion Science and Technology* 0 (2023), 0, 1–13. – URL <https://doi.org/10.1080/15361055.2023.2209490>
- [Westerhof 1997] WESTERHOF, E: Wave propagation through an electron cyclotron resonance layer. In: *Plasma Physics and Controlled Fusion* 39 (1997), 6, 1015–1029. – URL <https://doi.org/10.1088/0022-3778/39/6/1015>
- [Westerhof and Peeters 1996] WESTERHOF, E. ; PEETERS, A.G.: A model for bootstrap current calculations with bounce averaged Fokker-Planck codes. In: *Computer Physics Communications* 95 (1996), 2, 131–138. – URL <https://www.sciencedirect.com/science/article/pii/0010465595001433>. – ISSN 0010-4655
- [Williams et al. 2014] WILLIAMS, T R N. ; KÖHN, A ; O'BRIEN, M R. ; VANN, R G L.: Propagation in 3D of microwaves through density perturbations. In: *Plasma Physics and Controlled Fusion* 56 (2014), may, 7, 075010. – URL <https://dx.doi.org/10.1088/0741-3335/56/7/075010>
- [Wootton et al. 1990] WOOTTON, A. J. ; CARRERAS, B. A. ; MATSUMOTO, H. ; MCGUIRE, K. ; PEEBLES, W. A. ; RITZ, Ch. P. ; TERRY, P. W. ; ZWEBEN, S. J.: Fluctuations and anomalous transport in tokamaks. In: *Physics of Fluids B: Plasma Physics* 2 (1990), 12, 2879–2903. – URL <https://doi.org/10.1063/1.859358>
- [Yang et al. 2018] YANG, H. Y. ; CHEN, Z. Y. ; HUANG, D. W. ; TONG, R. H. ; YAN, W. ; WEI, Y. N. ; LIN, Z. F. ; DAI, A. J. ; GAO, H. L. ; WANG, X. L. ; LI, Y. ; LI, W. ; HUANG, Y. ; HU, J. ; WANG, D. Q. ; YANG, Z. J. ; JIANG, Z. H.: Vertical fast electron bremsstrahlung diagnostic on J-TEXT tokamak. In: *Review of Scientific Instruments* 89 (2018), 10, 10F126. – URL <https://doi.org/10.1063/1.5035185>
- [Zhang et al. 2014] ZHANG, Xinguang ; LI, S. ; JIANG, H. ; REN, Z. ; XU, C.: Optimal Tracking for a Divergent-Type Parabolic PDE System in Current Profile Control. In: *Abstract and Applied Analysis* 2014 (2014), 940965. – URL <https://doi.org/10.1155/2014/940965>. – ISSN 1085-3375
- [Zhang et al. 2021] ZHANG, Y. P. ; MAZON, D. ; ZHANG, J. ; ZHANG, P. F. ; MALARD, P. ; XU, H. B. ; ZHOU, J. ; PEYSSON, Y. ; ZOU, X. L. ; YANG, J. W. ; YUAN, G. L. ; ISOBE, M. ; SONG, X. Y. ; LI, X. ; LIU, Yi ; SHI, Z. B. ; XU, M. ; DUAN, X. R. ; HL-2A TEAM the: A Hard X-Ray Pinhole Camera System for Fast Electron Bremsstrahlung Measurements in the HL-2A Tokamak. In: *Fusion Science and Technology* 77 (2021), 1, 1–8. – URL <https://doi.org/10.1080/15361055.2020.1829457>

## Bibliography

---

- [Zhou et al. 2019] ZHOU, R. J. ; ZHONG, G. Q. ; HU, L. Q. ; TARDOCCHI, M. ; RIGAMONTI, D. ; GIACOMELLI, L. ; NOCENTE, M. ; GORINI, G. ; FAN, T. S. ; ZHANG, Y. M. ; HU, Z. M. ; XIAO, M. ; LI, K. ; ZHANG, Y. K. ; HONG, B. ; ZHANG, Y. ; LIN, S. Y. ; ZHANG, J. Z.: Development of gamma ray spectrometer with high energy and time resolutions on EAST tokamak. In: *Review of Scientific Instruments* 90 (2019), 12, 123510. – URL <https://doi.org/10.1063/1.5120843>

# Acknowledgements

Disclaimer: this work would not have been possible without the help and support at all levels from a lot of people, and I hope I did not forget anyone in these acknowledgments. Additional disclaimer: this section is written in a shameless mix of English and French, with a drop of other languages.

Scientific research aims at meticulously extending humankind knowledge by formulating hypotheses and providing data and information to test and assess these hypotheses. One of the most important cross-field research area is the search for funding. Therefore, it is important to acknowledge that this work was supported in part by the Swiss National Science Foundation. This work has been carried out within the framework of the EUROfusion Consortium, partially funded by the European Union via the Euratom Research and Training Programme (Grant Agreement No 101052200 — EUROfusion). The Swiss contribution to this work has been funded by the Swiss State Secretariat for Education, Research and Innovation (SERI). Views and opinions expressed are however those of the author(s) only and do not necessarily reflect those of the European Union, the European Commission or SERI. Neither the European Union nor the European Commission nor SERI can be held responsible for them.

First and foremost, I would like to thank my supervisor, Stefano Coda. Stefano, you have been a great support throughout this period. You always find the time to answer questions and provide comments on the work, even though you have to deal with a lot of other responsibilities. Your calm and your patience are truly reassuring, in particular when facing stressful<sup>1</sup> situations. You let me a lot of independence, without letting me getting lost, which I think significantly contributes to make me a better scientist. *Quindi, grazie mille Stefano!*

The next person I would like to thank is Joan Decker. Joan, you have been acting like a co-supervisor, and I am glad that this status becomes official for the following of the project. Your help in handling the codes was precious, and discussing with you was always interesting. You are always keen to share your deep knowledge on Fokker-Planck simulations and fast electron physics, even if you are very busy with your other tasks. *Merci encore à toi Joan !*

The other person who need to be thanked is Peter Donnel. Peter, your contribution to this thesis work is huge, and the final work would not have been the same without you. Besides

---

<sup>1</sup>It is important to note that the quality of the adjective "stressful" depends on the observer.



## Acknowledgements

---

this contribution, your positive attitude and constant support helped me so much to keep going further. *Tu n'es pas seulement un collègue, mais un ami, et travailler avec toi est un réel plaisir. Merci !*

I want to thank the Swiss Plasma Center and its director, Prof. Ambrogio Fasoli, for giving me the opportunity to take part of the challenge nuclear fusion research represents, and to provide my modest contribution to this huge project. *Un grand merci à l'équipe administrative également, en particulier Roxane et Edith. Vous êtes toujours disponible pour aider, et vous nous offrez le luxe de ne pas nous inquiéter des soucis administratifs.* At the Swiss Plasma Center, we also have the chance of having a lot of different experts that are keen to help any PhD student, keeping their door open to answer to questions, and providing useful feedback on the work we present. In particular, thank you Laurent, Stephan, Stefano A., Laurie and Basil<sup>2</sup> for sharing your expertise.

The experimental part of this thesis was only possible thanks to the tremendous work of the whole TCV team<sup>3</sup> and of the technical services. *Un immense merci notamment à Severino, Maxime, Eve, Pierre L., Blaise et Olivier de m'avoir si chaleureusement accueilli dans le labo d'électronique<sup>4</sup>. Merci également à l'équipe du vide, Stefano B., Omar B. et Fred, ainsi qu'au service informatique, Pierre E., Mateusz et Cenk. Et un grand merci aux pilotes, GdJ, PdJ et DdJ.* Thank you all!

For the numerical part, two persons in particular helped me a lot at the beginning of this thesis journey. So, thank you Dahye and Oulfa for your help and your patience, and for teaching me all the basics! I would also like to thank Dr. Omar Maj. Thank you Omar for your work. I am sorry that it was not possible to include WKBeam simulations in this thesis work, but I am sure that the future of the project will benefit a lot from your contribution. Finally, I want to thank Dr. Yves Peysson for his help with LUKE.

Working at EPFL offers the great opportunity of taking part of the education system, by assisting teachers in their courses and helping bachelor and master students fulfilling their objectives. I would like to thank the "Global Issues" team: thank you Ivo, Ambrogio, Ludovic, Davide G., Duccio and the others. A special thank goes to Duccio, for having given me the first occasion of working at the Swiss Plasma Center. *Grazzie Duccio!* I also want to thank Jean-Philippe. Your commitment to teaching is an inspiration and it has been a pleasure to work with you, even when we had to setup the remote courses during the COVID-19 pandemic (thank you Guillaume, Curdin and Christine: you saved the semester of many students). And, also, thank you for having taken the time to read this thesis.

The Swiss Plasma Center is an international environment where it is possible to interact with about 40 to 50 PhD students and 20 to 30 Postdocs from all around the world. I would like to thank you all for the deep discussions and the laughter, and for your contribution in making

---

<sup>2</sup>Interestingly, it is possible to be helpful and sarcastic at the same time.

<sup>3</sup>See the very long author list of Reimerdes H *et al* 2022, *Nucl. Fusion* **62** 042018

<sup>4</sup>Désolé pour les bruits de ventilateurs et pour les LED clignotantes dans les yeux de Maxime.

this place such a pleasant place.

When I first arrived at SPC, I was not even a PhD candidate, and my first contact with Switzerland was with a Swiss guy smoothly deriving horrendously complicated equations all day long. Thank you Baptiste, and remember this nice summer in the PPB-110 oven. Then, I eventually got accepted as a PhD student, and I was sent to a visitor office<sup>5</sup>, where I met new friends. Thank you Simon, for all the discussions we had: an Italian guy once said "*Horum omnium fortissimi sunt Belgae*" and now I understand. Thank you also Antoine B. for all the fun we had, and for having shared with Simon and me, the experience of the first scientific conference. Lesson learned: never chose a hotel because of its funny name<sup>6</sup>. Thank you Arsène, your energy is contagious, and you have been a great support throughout this thesis. Thank you also Aylwin, Mike, Guillermo and André.

At some point, I moved to another visitor office, same as the previous one, but with a carpet<sup>7</sup>. Thank you Peter, Andreas and Lavinia! Finally, I got to my final office, PPH-273<sup>8</sup>. At the beginning, I shared it with finishing PhD students, warning me about how stressful and difficult is the end of the PhD thesis. Thank you Mengdi, Mirko, Lorenzo S., Francesco C. and Fabian for all the advices and nice discussions. Time passing by, I became the old guy, an newcomers entered the office. Thank you Cassandre, Massimo, Guangyu, Francesco, Antonia, Emanuel and António (don't worry, I did not mind the white noise produced by your computer trying to understand stellarator configurations). You all set a really good vibe in the office, and I trully enjoyed discussing with each of you. People tend to neglect how important it is to work in such a friendly environment.

Although PPH-273 is unambiguously the best office at SPC, I would also like to thank friends and neighbors from PPH-277. Thank you Claudia, Lorenzo M., Guillaume, Filippo, Sophie, Curdin, Stefano M., and also the old guys Federico P, Hugo and Jérémy. I am very grateful for the invitation to the special PPH-277 Wednesday meetings. Thank you Antoine H. for the interesting political discussions, together with Cassandre. And thank both of you for representing PhD students interests to the school assembly. Thank you Umesh for having spent hours with me in the control room. And thank you Ewout for continuing this work, you'll do great! Thank you Alessandro B., Alessandro G., Arno, Benjamin, Cyrille, Davide M., Garance, Giovanni, Jean-Baptiste, Jésus, Jia, Joachim, Joel, Kenneth, Kyungtak, Louis, Luke, Mack, Matteo, Margherita, Margot, Marta, Martim, Mohan, Oleg, Olivier F., Pedro, Reinart, Renat, Samuele, Simon V., Vincent, Yuri and many others!

During this PhD thesis, some people gave me the opportunity to fulfill my teenage dream of being a member of a metal band, and of giving a live concert. Thank you so much to my friends and fellow members of *Quench'em all*: Francesco, Lorenzo V., Lyes and Mathias. The memory of people pogoing in the SPC hall is now carved into my mind.

---

<sup>5</sup>Remember, 40 to 50 PhD students and 20 to 30 Postdocs. They take some space.

<sup>6</sup>The Hotel California in Zurich is not that nice (it is cheap though).

<sup>7</sup>At that moment, I started undergoing ESD each time I touched a metallic surface. Coincidence?

<sup>8</sup>The ESD stopped.

## Acknowledgements

---

*Merci à mes amis d'enfance, de collège et de lycée restés en France (enfin, pour certains au Canada). Vous revoir est à chaque fois une bouffée d'air frais, dommage que ce ne soit pas possible plus souvent ! Merci aux amis d'école d'ingénieur, j'aimerais aussi avoir plus d'occasion de vous revoir. Et merci aux amis de Neuchâtel (et de Berne) pour le soutien.*

*Merci Camille. D'abord, merci pour les cours de rappel d'électronique discrète et pour l'aide sur la fonction de transfert du HXRS. Mais, surtout, merci d'avoir été en première ligne pendant ces plus de quatre ans et demi de thèse, et d'être toujours là pour m'épauler, depuis maintenant plus de huit ans. Merci aussi à ta famille pour l'accueil bienveillant et pour nous permettre de nous ressourcer, le temps d'un week-end ou d'une semaine, aussi bien dans les Vosges qu'au pied du massif des Maures.*

*Pour finir, je voudrais remercier ma famille pour leur soutien aveugle depuis le début. Merci à mon frère Antoine. Grâce à toi, je suis certain de ne jamais avoir la grosse tête. Et merci Dorine de l'empêcher, lui, d'avoir la grosse tête. Blague à part, merci pour tout ! Et enfin, merci à mes parents de m'avoir permis de faire ce que je voulais, sans obstacle, et de m'avoir encouragé dans mes choix. La personne que je suis devenu aujourd'hui vous doit beaucoup à tous les deux.*

Neuchâtel, the 7th of October 2023

Jean

# Curriculum Vitae

## List of publications

- J. Cazabonne *et al* 2023, submitted to *Nucl. Fusion*: "Impact of microwave beam scattering by density fluctuations on the Electron-Cyclotron power deposition profile in tokamaks".
- J. Cazabonne *et al* 2023, *Plasma Phys. Control. Fusion* **65** 10
- H. Weisen *et al* 2023, *Fusion Science Techno.* 11-13
- P. Donnel *et al* 2022, *Plasma Phys. Control. Fusion* **64** 9
- P. Donnel *et al* 2021, *Plasma Phys. Control. Fusion* **63** 6
- D. Choi *et al* 2020, *Plasma Phys. Control. Fusion* **62** 11

## Conference participation

- 49th EPS Conference on Plasma Physics, Bordeaux, France, 3-7 Jul. 2023: Poster presentation, shortlisted for the Itoh Project Prize, attributed by the University of Kyushu (Japan).
- Joint Varenna-Lausanne Workshop on the Theory of Fusion Plasma, Varenna, Italy, 12-16 Sep. 2022: Poster presentation.
- 48th EPS Conference on Plasma Physics, Maastricht, Netherlands, 27 Jun. - 1 Jul. 2022 (remote): Contributed Oral.
- 47th EPS Conference on Plasma Physics, Stiges, Spain, 21-25 Jun. 2021 (remote): Poster presentation.
- Joint Annual Meeting of the Swiss and Austrian Physical Societies, Zürich, Switzerland, 26-30 Aug. 2019: Poster presentation.



# Jean CAZABONNE

*Ph.D. student in plasma physics*

 <https://orcid.org/0000-0001-7629-1375>

 [jean.cazabonne@epfl.ch](mailto:jean.cazabonne@epfl.ch)

## EDUCATION

**2019 – 2023:** Ph.D.

Plasma Physics

(ongoing)

*Ecole Polytechnique*

*Fédérale de Lausanne*

**2017 – 2018:** M.Sc.

Fusion and Plasma

Physics

*Paris-Saclay University*

**2015 – 2017:** M.Sc.

Energy and Nuclear

Engineering

*Grenoble IT – Phelma*

## LANGUAGES

- French (native)
- English (fluent)

## CODING

- MATLAB (expert level)
- PYTHON (basic level)
- C (basic level)

## SOFTWARES

- COMSOL
- LUKE/C3PO
- SUPERMAGNET suite
- TRIPOLI4/MCNP

## INTERESTS

- **Reading** from SF and fantasy novels to archaeology treatises
- **Music**: playing bass in a band, learning guitar
- **Photography**

## WORK EXPERIENCE

**2019 – Present:** Doctoral researcher in plasma physics

*Ecole Polytechnique Fédérale de Lausanne – Swiss Plasma Center*

- **Ph.D. thesis preparation:** “Investigation of the interplay between Electron-Cyclotron waves, suprathermal electrons and turbulence in tokamak plasmas”
- **Diagnostic operation:** responsible for the hard X-ray spectrometer of the *Tokamak à Configuration Variable* (TCV)
- **Code development and modeling:** LUKE, COMSOL
- **Teaching assistant:** general physics, transverse course on energy

**2018 Mar – Sep:** Research intern in plasma physics and neutron physics

*Ecole Polytechnique Fédérale de Lausanne – Swiss Plasma Center*

- Neutron emission estimation and shielding studies for the local tokamak TCV, when using neutral beam heating

**2017 Mar – Sep:** R&D intern in cryogenics

*CEA Cadarache – IRFM*

- Numerical analysis of the quench tests of the toroidal field coils of the tokamak JT-60SA

**2016 May – Sep:** R&D intern in neutron physics

*CEA Cadarache – Direction d’Etude des Réacteurs*

- Monte-Carlo studies for the conception of a reactivity-controlling system for future experimental reactors

## PUBLICATION CONTRIBUTION

- J. Cazabonne *et al*, submitted to *Nucl. Fusion* (2023) “Impact of microwave beam scattering by density fluctuations on the Electron-Cyclotron power deposition profile in tokamaks”
- J. Cazabonne *et al*, *Plasma Phys. Control. Fusion* **65** 10 (2023) “Experimental and numerical investigations of electron transport enhancement by Electron-Cyclotron plasma-wave interaction in tokamaks”
- H. Weisen *et al*, *Fusion Science and Technology* 1-13 (2023) “TCV Tokamak Neutron Shielding Upgrade for Dual NBI Operation”
- P. Donnel *et al*, *Plasma Phys. Control. Fusion* **64** 9 (2022) “Electron-cyclotron resonance heating and current drive source for flux-driven gyrokinetic simulations of tokamaks”
- P. Donnel *et al*, *Plasma Phys. Control. Fusion* **63** 6 (2021) “Quasilinear treatment of wave-particle interactions in the electron cyclotron range and its implementation in a gyrokinetic code”
- D. Choi *et al*, *Plasma Phys. Control. Fusion* **62** 11 (2020) “Study of suprathermal electron dynamics during electron cyclotron current drive using hard x-ray measurements in the TCV tokamak”
- S. Nicollet *et al*, *IEEE Trans. Applied Supercond.* **28** 3 (2018) “Parametric Analyses of JT-60SA TF Coils in the Cold Test Facility With SuperMagnet Code”